TECHNISCHE UNIVERSITÄT BERLIN

HABILITATIONSSCHRIFT

Material Modeling of Microstructured Solids
—Theory, Numeric and Applications—

an der Fakultät für Verkehrs- und Maschinensysteme der TU Berlin
zur Erlangung der venia legendi im Fach Mechanik
eingereicht von Dr.-Ing. Kerstin Weinberg

Habilitationsantrag: 12. April 2006
Lehrprobe: 26. Juli 2006
Habilitationskolloquium: 25. Juni 2007

Gutachter:

Prof. Dr. rer. nat. W. H. Müller, TU Berlin
Prof. Dr.-Ing. W. Brocks, GKSS Geesthacht b. Hamburg
Prof. Dr.-Ing. C. Miehe, Universität Stuttgart

Berlin 2007
D 83

This work presents a systematic approach to incorporate microstructural changes in the constitutive modeling of the macroscopic material behavior. In particular we consider materials that are in its virgin state isotropic and develop a microstructure as a consequence of mechanical or thermal loading. To provide purely heuristic theories with a more refined background a mesoscopic theory will be introduced. Mesoscopic theories fall somewhere in between microscopic and macroscopic theories in the sense that no microscopic interactions between atoms and molecules are considered. Rather mesoscopic field equations contain additional variables which have to do with microstructural changes of the material.

The focus of this work is on modeling the material in a way that enables a *numerical computation* of engineering or biological structures. Special emphasis is put on dynamically loaded structures undergoing large deformations. The theoretical framework is based on (local and instantaneous) energy-minimizing principles. In consequence, the presented algorithms for numerical simulations are strictly variational. Exemplarily the fragmentation of ductile metal structures, the assessment of damage in microelectronic components and the shock wave induced damage in a human kidney are analyzed.

Diese Arbeit präsentiert einen systematischen Ansatz um mikromechanische Änderungen in der makroskopischen Modellierung des Materialverhaltens zu berücksichtigen. Dazu betrachten wir Materialien die zunächst isotrop sind, im Verlaufe der Belastung aber eine gewisse Mikrostruktur entwickeln. Wesentliche Effekte dieser mikrostrukturellen Entwicklung werden mit Hilfe einer mesoskopischen Theorie im makroskopischen Materialgesetz berücksichtigt.

Insbesondere geht es bei dieser Modellierung darum die Materialgesetze so zu formulieren, dass sie eine numerische Berechnung komplexer Strukturen ermöglichen. Solche Strukturen erfahren dabei große Verformungen und schnelle Belastungen. Sämtliche Formulierungen basieren daher auf (lokaler und zeitinkrementeller) Energieminimierung, und die vorgestellten Algorithmen sind folglich variationell. Beispielhaft werden die Zersprengung eines duktilen Metallrings, die Schädigung eines mikroelektronischen Verbindungsbauteils und die Schockwellenbehandlung einer menschlichen Niere simuliert und analysiert.

Contents

Introduction

Should an engineer be bothered by the microstructure of the material in his designed structures? There are characteristic strength, limit loads and safety factors to guarantee that, theoretically, nothing catastrophic is ever going to happen. Never? Indeed, in practice things might be a little different. Once the loading of a solid exceeds the elastic range — whether by simple overloading, by fatigue, or by a sudden impact — the material deteriorates with a certain microstructure. Typical examples are damage by micro-cracks, cavities and shear bands but also local movements in the metal's crystal lattice, phase separations and grain coarsening. This work presents a systematic approach to incorporate microstructural changes in the constitutive modeling of the macroscopic material behavior. The theoretical framework is based on (local and instantaneous) energy-minimizing principles. In consequence, the algorithms for numerical simulations are strictly variational.
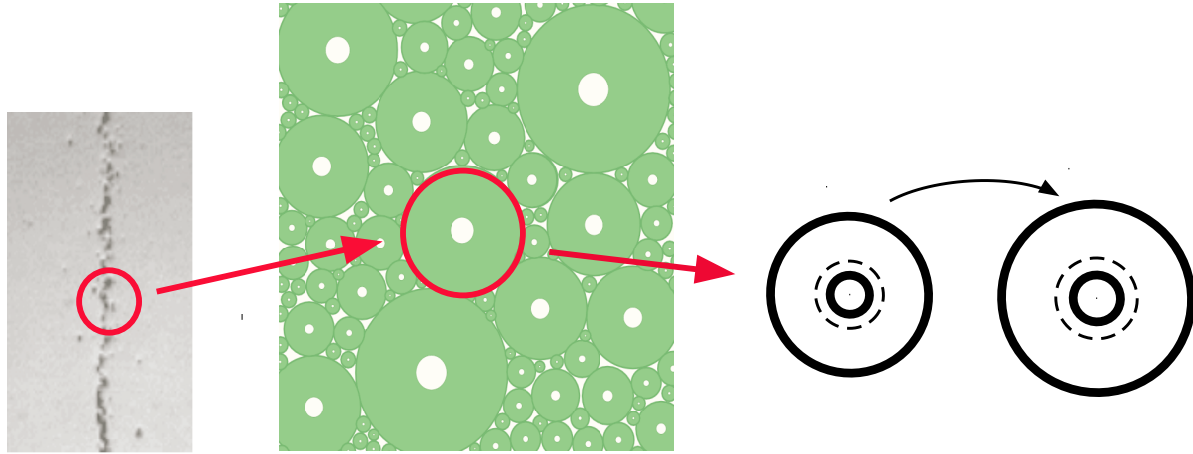
Figure I.1.: Modelling of dynamic void growth as a typical failure mechanism in metal spallation [29].

Following these general ideas we consider materials that are in its virgin state isotropic and develop a microstructure as a consequence of mechanical or thermal loading. We do
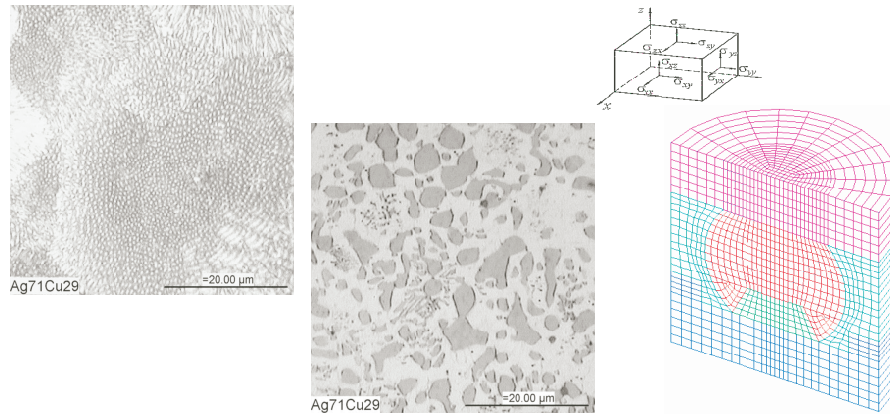
Figure I.2.: Microstructural changes in an Ag-Cu alloy before and after aging [42], and finite element analysis of a solder ball.

not study the detailed microscopic background. Instead we focus on phenomenological theories enabling a numerical computation of the specific response of an engineering or a biological structure to a certain loading regime. Special emphasis is put on dynamically loaded structures undergoing large deformations.

The figures in this introduction illustrate the general approach. A (simplified) model of the particular microstructure is employed to describe its essential features and to deduce the consequences to the overall material behavior, induced, e.g., by void growth in a ductile metal (Figure I.1), by phase separation in metal alloys (Figure I.2) or by cavitation of bubbles in a biological tissue (Figure I.3). To provide the purely heuristic macroscopic theory with a more refined background a mesoscopic theory will be introduced. Mesoscopic theories fall somewhere in between microscopic and macroscopic theories in the sense that no microscopic interactions between atoms and molecules are considered. Rather mesoscopic field equations contain additional variables which have to do with microstructural changes of the material.

This book is divided into three parts, the first part contains the theoretical foundation together with special aspects of numerical solution procedures. The second part describes three different applications of the presented theories illustrating the possibilities (and limits) of numerical simulations of such complex problems. The third part consists of an appendix which summarizes some formal and mathematical details.

Part I, Theory and Numerics, starts with two chapters which introduce the fundamental relations of finite kinematics and the classical balance equations of continuum mechanics. In Chapter 3 the general prerequisites for constitutive equations are summarized and some examples for elastic constitutive relations are given.

2
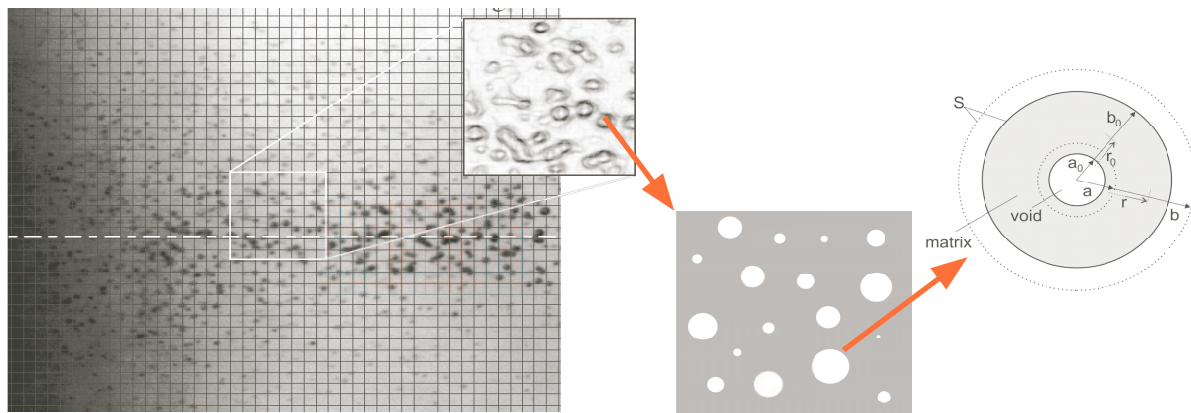
Figure I.3.: Bubble caviation in a soft tissue, material model motivated by experimental observations [11].

With a view to formulate finite element approximations we restate in Chapter 4 the introduced relations in a variational form and explain methods of space and time discretization which preserve a variational structure. Chapter 5.2 provides a short outline on the numerical solution techniques. The variational structure of Newmark's algorithms for time-discretization is pointed out and some basics of finite element discretization are given.

Chapter 6 presents the fundamentals of irreversible, i.e., plastic material behavior. The classical plasticity is extended here to the finite range, resulting in the so-called J_2-theory of finite plasticity.

The main theoretical contributions of the author are formulated in Chapter 7. Here the established theory of elasto-plasticity of finite deformations is extended to materials with a certain porosity. For our analysis we assume the material to be a conglomerate of (initially very small) spherical pores each surrounded by matrix material. This model of a porous composite enables us to link the mechanism of pore expansion and global softening in a solid to parameters which describe the micromechanical mechanisms of the material. In Chapter 7 we first explain the underlying model and provide the basic equations of the mesoscopic framework. The constitutive models of void growth in an elastic as well as in a visco-plastic material are derived in detail and numerical results on void growth and void distribution function are also provided there. Then, starting from this mesoscopic concept, we introduce a variational formulation of constitutive updates for porous visco-elastic plastic materials. The material model combines finite elasticity and plasticity with irreversible volumetric expansion as induced, e.g., by growth of voids and defects in metals or by cavitation of bubbles in soft tissue. Dynamic effects such

as micro-inertia and rate sensitivity are included. For numerical computation we derive the time-discretized constitutive updates of a general porous visco-elastic plastic material with special emphasis on a strictly variational setting.

Chapter 8 deals with different concepts of damage in continuum mechanics. Roughly spoken — damage means an irreversible change of the microstructure of the material resulting in a reduced load carrying capacity. Beyond the already discussed forms of (local) plastic zones and irreversible pore growth, examples of such microstructural evolutions considered here are fracture and fragmentation, shear bands, fatigue, and phase separation in metallic alloys and other mixtures. Moreover, a damage localisation technique is provided to enable finite-element computations of fragmented structures, Figure I.4-6.
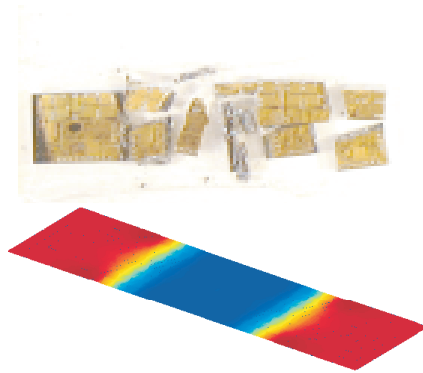
Fig.I.4.: Silicon die fragmented in a 4-point bending test and computed stress state.

The first chapter of the **Part II, Applications,** Chapter 9, employs the variational formulation of the constitutive updates of Chapter 7 and the damage localization technique of Chapter 8 for porous visco-elastic plastic metals. The underlying computational model combines von Mises plasticity and void growth in a fully variational manner. Numerical examples, e.g., the Taylor impact test, illustrate the range of behavior predicted by the model. The performance of the variational update is demonstrated by its application to the forced expansion and fragmentation of U-6%Nb rings.

The fatigue performance of components in microelectronic circuit boards is analyzed in Chapter 10. Thermal fatigue of solder joints and plated-through vias are a subject of great concern, in particularly when the circuit unit is exposed to high operating temperatures (associated, e.g., with automotive applications). The performance of different types of solder balls and copper vias in different positions of a printed circuit board is analyzed. To this end a multi-scale finite element analysis under the loading conditions of thermal cycling is employed. The material model for the electrolytically deposited copper considers large elastic and plastic deformations and, additionally, the growth of pores within the material. The main concern in the solder alloys is the determination of the basic material parameters as well as phase separation and grain coarsening of the brazing material. It is common practice to extrapolate the plastic straining computed within few steps of thermal cycling by means of Coffin-Manson like equations. We critically examine this strategy for the copper via and show that an extrapolation of the

4

Figure I.5.: Numerical simulation of the fragmentation of a metal ring, meshing technique, finite element result and necking experimentally observed in [249].

computed porosity up to critical values allows similar conclusions.
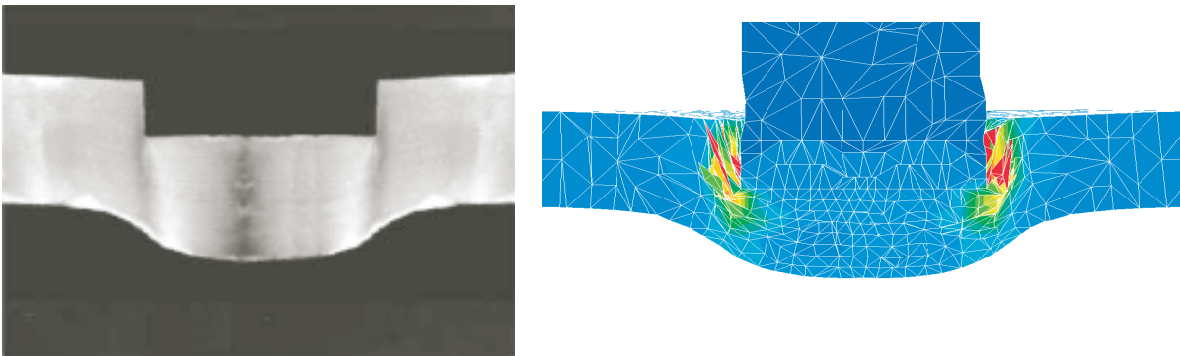
Figure I.6.: Shear plug formation in steel by a cylindrical indenter, experiments [45] and numerical results [228].

The final Chapter 11 deals with a soft biological material, namely kidney tissue. In a common medical procedure to destroy kidney stones hypersonic waves are generated outside the body and focused at the kidney stone. The shock waves are supposed to fragment the stone but they also lead to injuries of the surrounding kidney tissue. To understand, predict and estimate the underlying damaging mechanisms we develop a mechanical model for the response of soft tissue to the exposure of shock waves. The material model accounts for shear induced damage and irreversible volumetric expansion as induced, e.g., by cavitating bubbles. Finite element simulations allow to localize the

damage in the human kidney in good agreement to clinical and experimental studies.

Finally, the **Appendix** explains the notation, some rules of tensor algebra and the exponential and logarithmic mapping technique.

Part I.

Theory and Numeric

1. Kinematics of Deformation

In this chapter we briefly summarize the fundamental relations of the kinematics of large deformations, restricting ourselves to the applications we have in mind. For concise treatments we refer to the literature on continuum mechanics, e.g., the monographs of Altenbach [5], Becker and Bürger [23], Betten [35], Chadwick [80], Gurtin [138], Malvern [204], Truesdell and Noll [339] as well as the recent works of Bertram [32], Haupt [148] and Holzapfel [152].

Our description focuses initially on **(elastic) bodies**, Figure 1.1. For continuum-mechanical description a body is a set whose elements are in one-to-one correspondence with points of a region $\mathcal{B} \subset \mathbb{R}^3$ and we partition its boundary $\mathcal{S} = \partial\mathcal{B}$ into two parts, $\mathcal{S} = \mathcal{S}_1 \cup \mathcal{S}_2$, where displacements are prescribed or mechanical traction is applied, respectively, $\mathcal{S}_1 \cap \mathcal{S}_2 = 0$. Moreover, the body is of a size which allows to neglect its microscopic composition. Elasticity means that the processes under consideration are reversible. Consequently, elastic materials show no internal processes, no time dependence, no hysteresis and no dissipation. Note that elasticity as it is defined here does not mean linearity[1]. Elastic

Figure 1.1.: Solid body $\mathcal{B}$.

materials can be nonlinear because of large deformations as well as of nonlinear material laws, and, on the other hand linear materials can be inelastic, e.g. viscoelastic. Inelastic materials are subject of subsequent chapters.
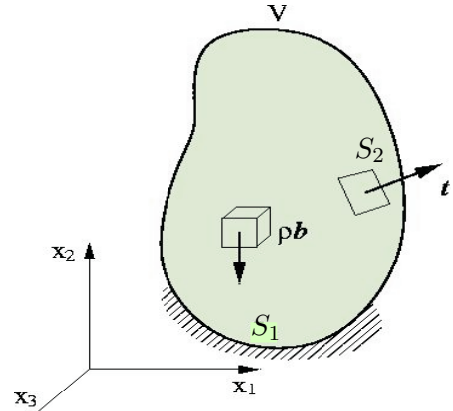
1.1. Deformation and motion

We consider a body whose particles occupy a region $\mathcal{B} \subset \mathbb{R}^3$ in a certain **reference configuration**. We label the material particles $P \in \mathcal{B}$ by their position vectors $\boldsymbol{X}(P)$. Without loss of generality these position vectors may be defined by their components

---

[1]Note that the definition of elasticity may differ in literature.
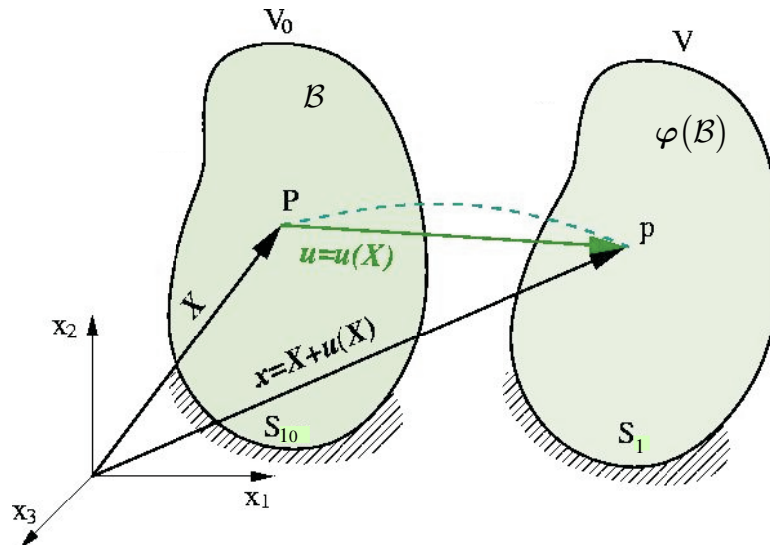
Figure 1.2.: Lagrangian point of view: $\boldsymbol{x} = \boldsymbol{\varphi}(\boldsymbol{X})$

$\{X_1, X_2, X_3\}$ relative to some coordinate system with orthonormal basis $\boldsymbol{E}_1, \boldsymbol{E}_2, \boldsymbol{E}_3$ centered at some convenient origin O, $\boldsymbol{X} = X_i \boldsymbol{E}_i$. We will refer to this reference system as the material reference frame and to components relative to this frame as *material* or *Lagrangian coordinates*. The reference configuration is commonly (but not necessarily) identified with the initial, undeformed configuration of the body, see Figure 1.2.

The body $\mathcal{B}$ subsequently deforms and moves over a period of time $t \in \mathbb{R}^+$. A **deformation** of a body $\mathcal{B}$ is an injective mapping $\boldsymbol{\varphi} : \mathcal{B} \to \mathbb{R}^3$. The condition that the deformation mapping $\boldsymbol{\varphi}$ defines an injective function excludes deformation involving tearing and interpenetration of matter of the body.

The region $\boldsymbol{\varphi}(\mathcal{B})$ is the **current** or **deformed configuration** of the body. The material point $P \in \varphi(\mathcal{B})$ is labelled now by a position vector $\boldsymbol{x}(P)$. The components $\{x_1, x_2, x_3\}$ of the position vector are relative to a coordinate system with orthonormal basis $\boldsymbol{e}_1, \boldsymbol{e}_2, \boldsymbol{e}_3$ centered at o, $\boldsymbol{x} = x_i \boldsymbol{e}_i$. We will refer to this configuration as the spatial reference frame. The components relative to this frame are *spatial* or *Eulerian coordinates*, see Figure 1.3.

In the following we presume the origins O, o and the basis vectors of material and spacial frame to coincide, i.e., the basis $\boldsymbol{E}_i$ is identical to $\boldsymbol{e}_i$. We refer to tensorial quantities in the reference configuration by using capitals letters, whereas the current configuration is denoted by lowercase letters. To reduce conflicts in notation we employ a subscript 0 for some quantities when they refer to the initial (reference) configuration and omit the subscript in the current configuration. Moreover, we identify the material particles
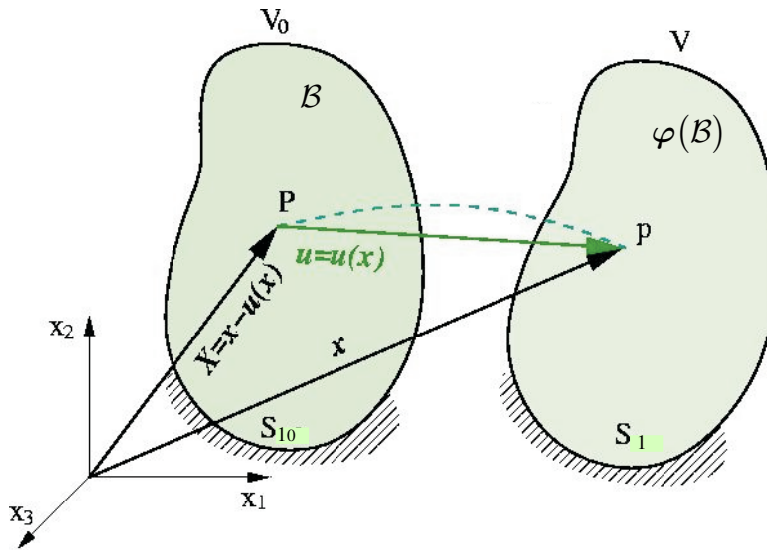
Figure 1.3.: Eulerian point of view $\boldsymbol{X} = \boldsymbol{\varphi}^{-1}(\boldsymbol{x})$

$P \in \mathcal{B}$ by their position vectors $\boldsymbol{X}(P)$ and $\boldsymbol{x}(P)$, respectively.

In coordinates, the deformation mapping takes the form

$$x_i = \varphi_i(\boldsymbol{X}), \qquad \boldsymbol{X} \in \mathcal{B}. \tag{1.1}$$

Since, by assumption, $\boldsymbol{\varphi}$ is injective, the **inverse deformation mapping $\boldsymbol{\varphi}^{-1} : \boldsymbol{\varphi}(\mathcal{B}) \to \mathcal{B}$** is well defined.

Unlike to small strain approaches the total deformation of a body cannot be understood as an additive superposition of displacement vector fields. To illustrate this, let $\boldsymbol{\varphi}_1 : \mathcal{B} \to \mathbb{R}^3$ and $\boldsymbol{\varphi}_2 : \mathcal{B} \to \mathbb{R}^3$ be two successive deformations of the body $\mathcal{B}$, see Figure 1.4. The total or **combined deformation** of the body is

$$\boldsymbol{\varphi}(\boldsymbol{X}, t) = \boldsymbol{\varphi}_2(\boldsymbol{\varphi}_1(\boldsymbol{X}, t), t) \equiv \boldsymbol{\varphi}_2 \circ \boldsymbol{\varphi}_1(\boldsymbol{X}, t). \tag{1.2}$$

where $\circ$ denotes the composition. Evidently, the total deformation follows by a composition of mappings. The composition of deformation mappings has a multiplicative group structure [206].

A **motion** of a body during a time interval $[t_1, t_2]$ is a function $\boldsymbol{\varphi} : \mathcal{B} \times [t_1, t_2] \to \mathbb{R}^3$ such that the mappings $\boldsymbol{\varphi}(\cdot, t)$, $t \in [t_1, t_2]$, are injective. In other words, a motion defines a one parametric sequence of deformation mappings indexed by time, $\boldsymbol{x} = \boldsymbol{\varphi}_t(\boldsymbol{X}) = \boldsymbol{\varphi}(\boldsymbol{X}, t)$. This describes for every material point $P \in \mathcal{B}$ a path or trajectory in $\mathbb{R}^3$.
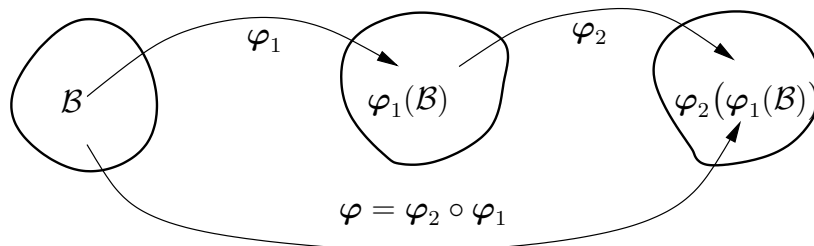
Figure 1.4.: Composition of deformations.

To describe the motion of a particle we may distinguish between a direct (or spatial) motion and a inverse (or material) motion problem. The **direct motion problem** is based on the idea of following material particles from a fixed position $\boldsymbol{X}$ along their trajectories through the ambient space. Because attention is paid to the particles (we observe what happens to the particles when they move), this point of view is denoted as the *material* or *Lagrangian* setting. In contrast to this, within the **inverse motion problem**, physical particles are followed through the ambient material at a fixed spatial position $\boldsymbol{x}$. The observer takes the *spatial* or *Eulerian* point of view.

The **displacement field $\boldsymbol{U}$** of a particle relates its position in the undeformed configuration to its position in the deformed configuration at time t. In the *Lagrangian* setting we write

$$\boldsymbol{U}(\boldsymbol{X}, t) = \boldsymbol{x}(\boldsymbol{X}, t) - \boldsymbol{X}, \tag{1.3}$$

whereas the *Eulerian* form of equation(1.3) reads

$$\boldsymbol{u}(\boldsymbol{x}, t) = \boldsymbol{x} - \boldsymbol{X}(\boldsymbol{x}, t). \tag{1.4}$$

Both settings are related by the inverse deformation mapping,

$$\boldsymbol{U}(\boldsymbol{X}, t) = \boldsymbol{U}\big(\boldsymbol{\varphi}^{-1}(\boldsymbol{x}, t)\big) = \boldsymbol{u}(\boldsymbol{x}, t). \tag{1.5}$$

The **instantaneous velocity** of a material point is the *material* or *Lagrangian velocity* field

$$\boldsymbol{V}(\boldsymbol{X}, t) = \frac{\partial \boldsymbol{\varphi}_i}{\partial t}(\boldsymbol{X}, t). \tag{1.6}$$

On the other hand, in the Eulerian setting the velocity follows by a composition of material velocity and the inverse deformation mapping. Thus, the **velocity at a spacial position** is described by the *spacial* or *Eulerian velocity* field

$$\boldsymbol{v}(\boldsymbol{x}, t) = \boldsymbol{V}\big(\boldsymbol{\varphi}(\boldsymbol{X}, t), t\big) = \frac{\partial \boldsymbol{\varphi}}{\partial t}\big(\boldsymbol{\varphi}^{-1}(\boldsymbol{x}, t), t\big) = \big(\boldsymbol{V} \circ \boldsymbol{\varphi}^{-1}\big)(\boldsymbol{x}, t). \tag{1.7}$$

Analogously, the **instantaneous acceleration** of the material point $\boldsymbol{X}$ at time t is represented by the *material* or *Lagrangian acceleration* field

$$\boldsymbol{A}(\boldsymbol{X}, t) = \frac{\partial \boldsymbol{V}}{\partial t}(\boldsymbol{X}, t). \tag{1.8}$$

The *spacial* or *Eulerian acceleration* field represents the **acceleration of** the material point occupying the **spatial position** $\boldsymbol{x}$ at time t.

$$\boldsymbol{a}(\boldsymbol{x}, t) \;\; = \;\; \boldsymbol{A}\big(\boldsymbol{\varphi}(\boldsymbol{X}, t), t\big) = \frac{\partial \boldsymbol{V}}{\partial t}\big(\boldsymbol{\varphi}^{-1}(\boldsymbol{x}, t), t\big) = \big(\boldsymbol{A} \circ \boldsymbol{\varphi}^{-1}\big)(\boldsymbol{x}, t) \tag{1.9}$$

The material time-derivative (1.9) of a smooth spatial vector field $\boldsymbol{v}(\boldsymbol{x}, t)$ may be evaluated to give

$$\boldsymbol{a}(\boldsymbol{x}, t) = \frac{\partial \boldsymbol{v}(\boldsymbol{x}, t)}{\partial t} + \operatorname{grad} \boldsymbol{v}(\boldsymbol{x}, t) \cdot \boldsymbol{v}(\boldsymbol{x}, t). \tag{1.10}$$

Evidently, a material time derivative $\boldsymbol{a}(\boldsymbol{x}, t) = \dot{\boldsymbol{v}}(\boldsymbol{x}, t)$ is distinct from a 'normal' time-derivative because of its structure. The first term in equation(1.10) describes the local acceleration (i.e., the local rate of change in the velocity field), the second term describes a convective acceleration field. It plays an important role in fluid mechanics, because by equation (1.10) the spatial acceleration can be determined without knowing the motion explicitly.

In solid mechanics the constitutive behavior of materials is commonly given in terms of material coordinates. This motivates us to restrict our attention in the following to the direct motion problem formulated in the *Lagrangian* setting. However, we keep in mind that the kinematic equations in the direct and in the inverse motion problem correspond to each other.

1.2. Kinematics of local deformations

Let $dV_0 \subset \mathcal{B}$ be the volume of an infinitesimal material neighborhood of point $\boldsymbol{X} \in \mathcal{B}$ and let dV be the volume of the corresponding infinitesimal spatial neighborhood. Consider now a material point at position $\boldsymbol{X} \in \mathcal{B}$ and let $\boldsymbol{X} + d\boldsymbol{X}$ be a neighboring material point within dV_0. The corresponding spatial point be $\boldsymbol{x} + d\boldsymbol{x}$, see Figure 1.5. With deformation (1.1) we know for the components of $\boldsymbol{x} + d\boldsymbol{x}$,

$$x_i + dx_i = \varphi_i\big(\boldsymbol{X} + d\boldsymbol{X}, t\big), \tag{1.11}$$
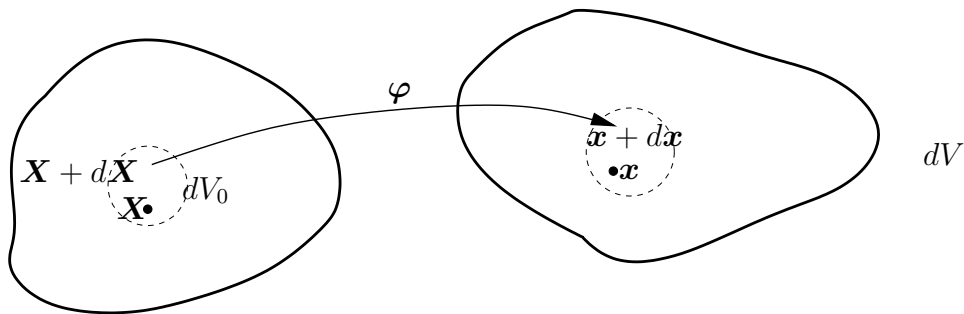
Figure 1.5.: Local deformation of a material neighborhood.

which may be expanded in a Taylor series[2] at position $\boldsymbol{X}$ to give

$$\varphi_i\big(\boldsymbol{X} + d\boldsymbol{X}, t\big) \;=\; \varphi_i\big(\boldsymbol{X}, t\big) + \frac{\partial \varphi_i}{\partial X_J}\big(\boldsymbol{X}, t\big)\, dX_J + o(d\boldsymbol{X}). \tag{1.12}$$

The expression $o(d\boldsymbol{X})$ denotes terms of higher order that tend to zero faster than $d\boldsymbol{X}$. Neglecting these terms we obtain from (1.12) the **linearized** differential relation

$$x_i + dx_i \simeq x_i + \frac{\partial \varphi_i}{\partial X_J}\big(\boldsymbol{X}, t\big)\, dX_J \quad \Rightarrow \quad dx_i = \frac{\partial \varphi_i}{\partial X_J}\big(\boldsymbol{X}, t\big)\, dX_J \tag{1.13}$$

and we define the **deformation gradient** $\boldsymbol{F}$ with components

$$F_{iJ}\big(\boldsymbol{X}, t\big) \;=\; \frac{\partial \varphi_i}{\partial X_J}\big(\boldsymbol{X}, t\big) \quad \Rightarrow \quad dx_i = F_{iJ}\big(\boldsymbol{X}, t\big)\, dX_J \tag{1.14}$$

The deformation gradient $\boldsymbol{F}$ is fundamental in non-linear continuum mechanics. It is a primary measure of deformation. The quantity provides a full determination of the deformation mapping at time t on an infinitesimal material neighborhood $d\boldsymbol{X}$ of $\boldsymbol{X}$.

The deformation gradient is a linear operator by definition. Therefore, $\boldsymbol{F}(\boldsymbol{X}, t)$ may regarded to be a member of the linear group of all linear, second-order tensor transformations $\mathbb{R}^{3 \times 3}$, i.e., GL(3, $\mathbb{R}$), cf. Appendix 1 and 4.

Consider now an **infinitesimal** material neighborhood $\boldsymbol{X} + d\boldsymbol{X}$ of **volume** dV_0, which is given by the parallelepipedic product $dV_0 = (d\boldsymbol{X}^{(1)} \times d\boldsymbol{X}^{(2)}) \cdot d\boldsymbol{X}^{(3)}$. Let dV be the volume of the corresponding spatial neighborhood at time t and write

$$\begin{aligned} dV &= \big(d\boldsymbol{x}^{(1)} \times d\boldsymbol{x}^{(2)}\big) \cdot d\boldsymbol{x}^{(3)} = \big(F_{1i}\, dX_i^{(1)} \times F_{2i}\, dX_i^{(2)}\big) \cdot F_{3i}\, dX_i^{(3)} \\ &= \det \boldsymbol{F}\big(d\boldsymbol{X}^{(1)} \times d\boldsymbol{X}^{(2)}\big) \cdot d\boldsymbol{X}^{(3)} = \det \boldsymbol{F}\, dV_0. \end{aligned} \tag{1.15}$$

---

[2]This derivation implicitly presumes differentiability of the fields. Other derivations are as well possible but less intuitively.

Consequently, the following relation holds

$$\frac{dV}{dV_0} = J(\boldsymbol{X}, t), \tag{1.16}$$

where

$$J(\boldsymbol{X}, t) = \det\big(\boldsymbol{F}(\boldsymbol{X}, t)\big) \tag{1.17}$$

is the **Jacobian of the deformation**. Evidently, the Jacobian J provides a measure of the local volumetric deformation. From the inverse mapping theorem follows that the deformation mapping is locally one-to-one at $\boldsymbol{X}$ and time t if and only if

$$J(\boldsymbol{X}, t) > 0. \tag{1.18}$$

Therefore, we may interpret this condition as a local invertibility condition. (Note that conditions for global invertibility are considerably harder to define.)

The following transformation relates **elements of oriented area** in the undeformed and deformed configurations. Let $dS \subset \partial\mathcal{B}$ denote an infinitesimal (surface) area containing $\boldsymbol{X}$ with the corresponding outward unit normal $\boldsymbol{N}$, see Figure 1.6. Let ds be the deformed area on $\boldsymbol{\varphi}(S, t)$ and $\boldsymbol{n}$ its corresponding outward unit normal. Then, for the components of the outward unit normal holds

$$n_i ds = J(\boldsymbol{X}, t) F_{Ji}^{-1}(\boldsymbol{X}, t) N_J dS. \tag{1.19}$$

Figure 1.6.: Oriented area.

This relation is known as **Nanson's formula** and may easily be verified by equation (1.16) and $dV = d\boldsymbol{x} \cdot \boldsymbol{n}\, ds = J dV_0 = J d\boldsymbol{X} \cdot \boldsymbol{N}_e\, dS$. Shortly we may write

$$\boldsymbol{n}\, ds = J \boldsymbol{F}^{-T} \boldsymbol{N}_e\, dS. \tag{1.20}$$

To illustrate the composition of deformations let $\boldsymbol{\varphi}_1 : \mathcal{B} \to \mathbb{R}^3$ and $\boldsymbol{\varphi}_2 : \mathcal{B} \to \mathbb{R}^3$ be two successive deformations of $\mathcal{B}$, cf. Figure 1.4. Let $\boldsymbol{F}_1(\boldsymbol{X}, t)$ and $\boldsymbol{F}_2(\boldsymbol{X}, t)$ be the corresponding deformation gradients at material point $\boldsymbol{X}$ and time t. Then, the total or combined local deformation gradient follows by multiplication of the incremental deformation gradients

$$\boldsymbol{F}(\boldsymbol{X}, t) = \boldsymbol{F}_2\big(\boldsymbol{\varphi}_1(\boldsymbol{X}, t), t\big) \boldsymbol{F}_1(\boldsymbol{X}, t). \tag{1.21}$$

Composition rule (1.21) together with the invertibility condition (1.18) confers the set of (all admissible) deformation gradients a **multiplicative group** structure. It may be identified with a subgroup of the general linear group of orientation-preserving transformations, i.e., $\mathrm{GL}^+(3, \mathbb{R}) = \{\boldsymbol{F} \in \mathrm{GL}(3, \mathbb{R}) \mid \det(\boldsymbol{F}) > 0\}$.
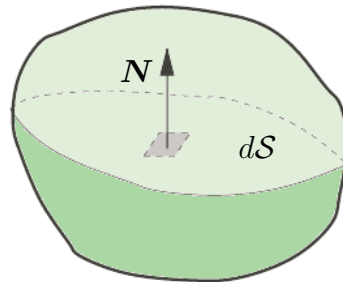
1.3. Decomposition of deformations

The deformation gradient $\boldsymbol{F}$ contains the full information about the (linearized) deformation $\boldsymbol{\varphi}(\boldsymbol{X}, t)$ at a local material point. However, it is a "two-point tensor", i.e., it works between current and reference configuration. Strain measures are required to refer to either the reference or the current configuration and, moreover, to be not affected by rigid body rotations. In this section we will extract the information of interest out of the deformation gradient and, then, introduce some common strain tensors.

The natural way of splitting the deformation gradient into different parts is, because of its multiplicative group structure, a **multiplicative decomposition**. Let $\boldsymbol{F}$ by a given state of deformation, and let one part of the full deformation be associated with reason A (e.g., volume preserving deformation or irreversible stretching) and another part be related to reason B (e.g., pressure induced dilatation or purely elastic stretching). Then, the decomposition of the deformation gradient reads[3]

$$\boldsymbol{F} = \boldsymbol{F}^B \, \boldsymbol{F}^A. \tag{1.22}$$

This type of decomposition goes back to Lee [187].

In that sense we separate the straining from the rigid rotation at a material point and employ the **polar decomposition**. Any deformation gradient $\boldsymbol{F}$ factors as the product

$$\boldsymbol{F} \;=\; \boldsymbol{R}\boldsymbol{U}, \tag{1.23}$$

with

$$\boldsymbol{U} \;=\; \boldsymbol{U}^\top \tag{1.24}$$
$$\boldsymbol{R}^{-1} \;=\; \boldsymbol{R}^\top. \tag{1.25}$$

The positive definite tensor $\boldsymbol{U}$ is the (right) stretch tensor, the orthogonal tensor $\boldsymbol{R}$ describes a rotation. Tensor $\boldsymbol{R}$ may be regarded as a member of the group of rotations SO(3), where SO(3) is the Lie-group $\{\boldsymbol{R} \in \mathbb{R}^{3\times3}, \boldsymbol{R}^T\boldsymbol{R} = \boldsymbol{I}, \det \boldsymbol{R} = 1\}$. The polar decomposition is always unique. (The proof is easily done by contradiction, see, e.g. [32].)

The eigenvalues of the stretch tensor $\boldsymbol{U}$, denoted as λ_α, $\alpha = 1, 2, 3$, fulfill the relation

$$\boldsymbol{U}\vec{\boldsymbol{N}}_{e\alpha} \;=\; \lambda_\alpha \vec{\boldsymbol{N}}_{e\alpha} \quad \text{with} \quad |\vec{\boldsymbol{N}}_{e\alpha}| = 1. \tag{1.26}$$

---

[3]For brevity we omit in this section the arguments of $\boldsymbol{F}$.
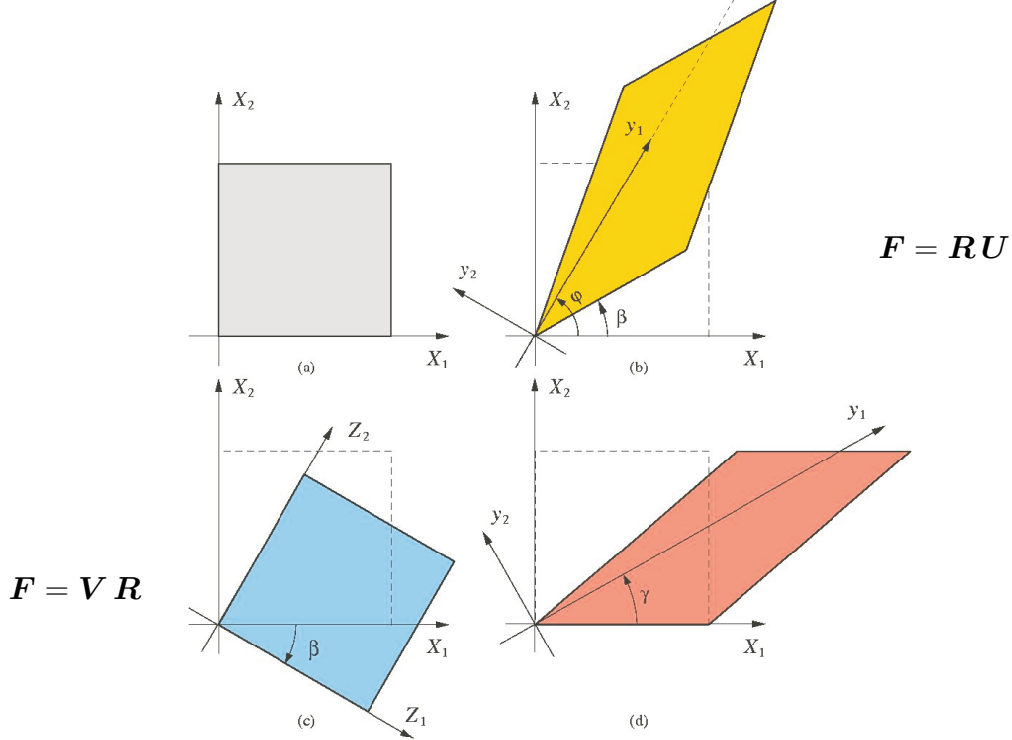
Figure 1.7.: Illustration of the polar decomposition.

The (real and positive) eigenvalues λ_α represent the principal stretches of the deformation, whereas the orthonormal eigenvectors $\vec{N}_{e\alpha}$ are the principal referential axis, i.e., the principal directions in the reference configuration.

There exists also a unique left polar decomposition of the form

$$\boldsymbol{F} = \boldsymbol{V}\,\boldsymbol{R}, \tag{1.27}$$

where again $\boldsymbol{R} \in \mathrm{SO}(3)$ and with the stretch tensor

$$\boldsymbol{V} = \boldsymbol{V}^\top \tag{1.28}$$

orthogonal to $\boldsymbol{U}$. (Please excuse the ambiguous notation, here and in Section 1.4 the letter $\boldsymbol{V}$ denotes the left stretch tensor, in the remaining of the text it is the vector of material velocity.)

The eigenvalues and eigenvectors of the left stretch tensor $\boldsymbol{V}$, are

$$\boldsymbol{V}\vec{n}_\alpha \;=\; \lambda_\alpha \vec{n}_\alpha \quad \text{with} \quad |\vec{n}_\alpha| = 1. \tag{1.29}$$

16

The eigenvalues λ_α represent here the principal stretches in the current configuration and the orthonormal eigenvectors $\vec{n}_\alpha$ are the corresponding principal directions. In other words, the eigenvectors of $\boldsymbol{V}$ are those of $\boldsymbol{U}$ rotated by $\boldsymbol{R}$, $\vec{n}_\alpha = \boldsymbol{R}\vec{N}_{e\alpha}$.

To illustrate the nature of rotation $\boldsymbol{R}$ we write the spectral decomposition of (1.24) and (1.28) as follows.

$$
\boldsymbol{U} = \sum_{\alpha=1}^{3} \lambda_\alpha \vec{N}_{e\alpha} \otimes \vec{N}_{e\alpha} \tag{1.30}
$$

$$
\boldsymbol{V} = \sum_{\alpha=1}^{3} \lambda_\alpha \vec{n}_\alpha \otimes \vec{n}_\alpha \tag{1.31}
$$

Then, the rotation tensor $\boldsymbol{R}$ may be decomposed as

$$
\boldsymbol{R} = \sum_{\alpha=1}^{3} \vec{n}_\alpha \otimes \vec{N}_{e\alpha}. \tag{1.32}
$$

Another useful decomposition of the deformation gradient $\boldsymbol{F}$ separates the deformation along a tangential plane from the deformation normal to that plane, cf. Section 8.3,

$$
\boldsymbol{F} = \boldsymbol{F}^{\parallel} \boldsymbol{F}^{\perp}, \tag{1.33}
$$

where $\boldsymbol{F}^{\parallel}$ denotes the **in-plane part** of the deformation gradient (or membrane deformation) and $\boldsymbol{F}^{\perp}$ the **out-of-plane part** of the deformation gradient (or transversal deformation). The in-plane part satisfies the identity

$$
\boldsymbol{F}^{\parallel} \boldsymbol{N}_e = \boldsymbol{N}_e, \tag{1.34}
$$

where $\boldsymbol{N}_e$ is the unit normal to the tangential plane in the reference configuration. With a vector $\boldsymbol{a} \in \mathbb{R}^3$ and by Hadamard's compatibility condition (see, e.g. [327]), the out-of-plane part of the deformation gradient has the form

$$
\boldsymbol{F}^{\perp} = \boldsymbol{I} + \boldsymbol{a} \otimes \boldsymbol{N}_e. \tag{1.35}
$$

1.4. Strain measures

The crucial demand on a **strain measure** is that it represents strain but vanishes for rigid body rotations. This in turn requires symmetry of the strain tensors. Thus, the **right Cauchy-Green tensor** is defined by

$$
\begin{aligned}
\boldsymbol{C} &= \boldsymbol{F}^\top \boldsymbol{F} \\
&= \boldsymbol{U}^\top \boldsymbol{U} = \boldsymbol{U}^2,
\end{aligned} \tag{1.36}
$$

The six independent components of tensor $\boldsymbol{C}$, $C_{JL} = F_{Ji}F_{iL}$, refer to the reference configuration and can uniquely be determined by the nine components of $\boldsymbol{F}$ (but not vice versa). The **Green-Lagrange strain tensor**

$$\boldsymbol{E} = \frac{1}{2}\left(\boldsymbol{F}^\top \boldsymbol{F} - \boldsymbol{I}\right) \tag{1.37}$$

has additionally the property to be zero in all components in case of no deformation. Frequently used is the **logarithmic strain**

$$\boldsymbol{\epsilon} = \frac{1}{2}\ln \boldsymbol{C} \tag{1.38}$$

which is also known as **Hencky strain tensor**[4]

$$\boldsymbol{H} = \ln \boldsymbol{U}. \tag{1.39}$$

Analogously the **left Cauchy-Green tensor** or **Finger tensor** is defined by

$$\begin{aligned} \boldsymbol{b} &= \boldsymbol{F}\,\boldsymbol{F}^\top \\ &= \boldsymbol{V}^\top \boldsymbol{V} = \boldsymbol{V}^2 = \boldsymbol{R}\,\boldsymbol{C} \end{aligned} \tag{1.40}$$

and the **Euler-Almansi strain tensor** is

$$\boldsymbol{e} = \frac{1}{2}\left(\boldsymbol{I} - \boldsymbol{b}^{-1}\right) = \frac{1}{2}\left(\boldsymbol{I} - \boldsymbol{F}^{-\top}\boldsymbol{F}^{-1}\right), \tag{1.41}$$

which both refer to the current configuration.

In linear theory small deformations are presumed. Consequently, reference and current configuration coincide. Strains are small enough so that a linearized strain measure accurately approximates the more rigorous nonlinear measures. This condition is fulfilled in virtually all solid materials under sufficiently small loads. By linearization of (1.37) or (1.41) we get the **infinitesimal strain tensor** as

$$\boldsymbol{\epsilon} = \frac{1}{2}\left(\operatorname{grad}\boldsymbol{u} + \operatorname{grad}\boldsymbol{u}^\top\right). \tag{1.42}$$

---

[4]To distinguish the logarithmic strain and the infinitesimal strain we denote the first by H but we will go back later to use definition (1.38).

Remark

The following general formula may illustrate the different strain measures for the simple case of uniaxial deformation. Let λ denote the ratio of current to initial length of the specimen and let the only nonzero entry in the strain tensors be ε. Now we write (following Seth [300], see also [32, 306])

$$\varepsilon = \frac{1}{\alpha}\bigl(1 - \lambda^{-\alpha}\bigr). \tag{1.43}$$

Then, assuming various values of constant α we obtain:

$$
\begin{array}{llll}
\alpha = -2 & \varepsilon = \frac{1}{2}\bigl(\lambda^2 - 1\bigr) & \varepsilon \in \bigl[-\tfrac{1}{2}, \infty\bigr] & \text{Green-Lagrange strain} \\
\alpha = -1 & \varepsilon = \lambda - 1 & \varepsilon \in [-1, \infty] & \text{infinitesimal strain} \\
\alpha = 0 & \varepsilon = \ln(\lambda) & \varepsilon \in [-\infty, \infty] & \text{logarithmic strain} \\
\alpha = 2 & \varepsilon = \frac{1}{2}\bigl(1 - \lambda^2\bigr) & \varepsilon \in \bigl[-\infty, \tfrac{1}{2}\bigr] & \text{Euler-Almansi strain}
\end{array}
$$

The first three measures are plotted in Figure 1.8 and we observe a very different behavior at large strains. A strain measuring function $f : \mathbb{R} \mapsto \mathbb{R}$ is called additively symmetric with respect to lengthening and shortening if the following condition holds

$$f\Bigl(\frac{1}{\lambda}\Bigr) = -f\bigl(\lambda\bigr). \tag{1.44}$$

Among the four strain measures only the (uniaxial) logarithmic strain satisfies this requirement. Note that the stretch λ itself is multiplicatively symmetric with respect to lengthening and shortening but not additively. Moreover there exist other valid strain measures with no symmetry at all [340]. Consequently, it is up to the reader to decide as to whether satisfying (1.44) makes the logarithmic strain (1.38) a "better" measure.

Figure 1.8.: Strain measures.

1.5. Strain rates

To finally determine a rate of deformation measure we note the **velocity gradient**

$$\boldsymbol{l} \;=\; \frac{\partial \boldsymbol{v}}{\partial \boldsymbol{x}}. \tag{1.45}$$

The velocity appears here as a function of time for a given particle at $\boldsymbol{X}$. The velocity gradient (1.45) may be evaluated in terms of the deformation gradient as

$$\boldsymbol{l} \;=\; \dot{\boldsymbol{F}} \cdot \boldsymbol{F}^{-1}. \tag{1.46}$$

The **rate-of-deformation tensor** is now defined as the symmetric part of tensor $\boldsymbol{l}$

$$\boldsymbol{d} = \frac{1}{2}\big(\boldsymbol{l} + \boldsymbol{l}^{\top}\big), \tag{1.47}$$

whereas the antisymmetric part of $\boldsymbol{l}$ is known as **spin tensor**.

$$\boldsymbol{w} = \frac{1}{2}\big(\boldsymbol{l} - \boldsymbol{l}^{\top}\big), \tag{1.48}$$

The rate-of-deformation tensor measures the rate of change of the square of the length of material line segments $d\boldsymbol{x}$. However, in general, the integral of the rate-of-deformation does not vanish in a reversible cycle of deformation. Consequently, the rate-of-deformation tensor is path-dependent. Although it is commonly used the rate-of-deformation (1.47) is not necessarily a physical meaningful measure of deformation.

1.6. Examples

Kinematic equations for some simple deformations are summarized here for later reference. At first we consider homogeneous deformations, i.e., deformations with constant affine boundary conditions. In a homogeneous state of deformation the gradient $\boldsymbol{F}$ is independent of the position of the material point $\boldsymbol{X}$ or $\boldsymbol{x}$, respectively, and, in consequence, we can derive one deformation gradient, $\boldsymbol{F} \in \mathrm{GL}^{+}(3, \mathbb{R})$, which is valid for all points of the body $\mathcal{B}$.

To write down the components of $\boldsymbol{F}$ explicitly, we presume volume preserving deformations with $\det \boldsymbol{F} = 1$. As above we employ cartesian coordinate systems.
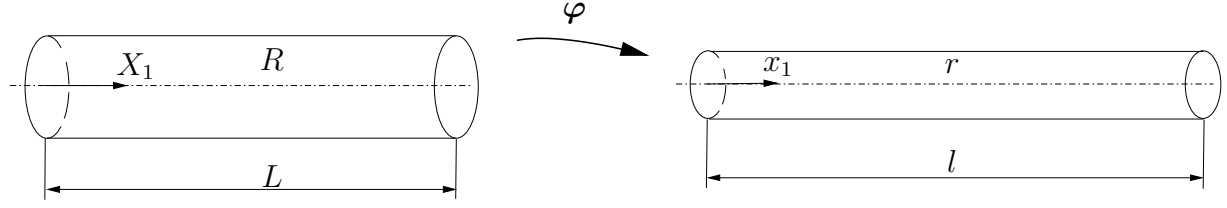
Figure 1.9.: Uniaxial tension of a rod made of an incompressible material.

Uniaxial tension.

A rod with circular (or quadratic) cross section is pulled from initial length L to current length l, see Figure 1.9. The components of the deformation gradient $\boldsymbol{F} = \partial \boldsymbol{x}/\partial \boldsymbol{X}$ in this uniaxial case read

$$\boldsymbol{F} = \begin{pmatrix} l/L & 0 & 0 \\ 0 & r/R & 0 \\ 0 & 0 & r/R \end{pmatrix}, \tag{1.49}$$

with initial and current radius R and r, respectively.

We define now the axial **stretch ratio** $\lambda = l/L$ and assume the material of the rod to be incompressible. From the preserved volume of the deformation follows

$$\pi R^2 L = \pi r^2 l, \tag{1.50}$$

and for the transverse stretch ratio we can write

$$\frac{l}{L} = \left(\frac{R}{r}\right)^2 = \lambda. \tag{1.51}$$

The deformation gradient $\boldsymbol{F}$ now follows as

$$\boldsymbol{F} = \begin{pmatrix} \lambda & 0 & 0 \\ 0 & 1/\sqrt{\lambda} & 0 \\ 0 & 0 & 1/\sqrt{(\lambda)} \end{pmatrix}. \tag{1.52}$$

Note that for a compressible material with a Poisson ratio ν and for small-strain kinematics (1.42) the deformation gradient can be evaluated from linear theory and expression (1.49) as

$$\boldsymbol{F} = \begin{pmatrix} 1 + \varepsilon & 0 & 0 \\ 0 & 1 - \nu\varepsilon & 0 \\ 0 & 0 & 1 - \nu\varepsilon \end{pmatrix}. \tag{1.53}$$
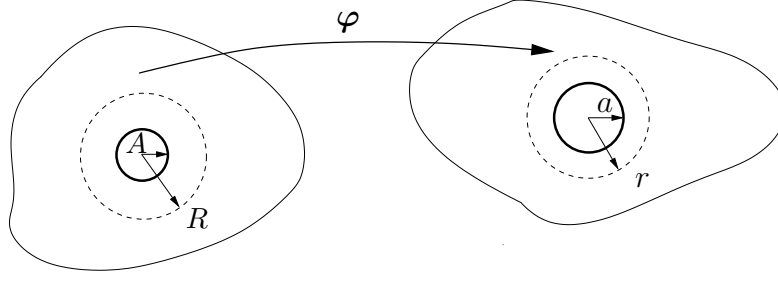
Figure 1.10.: Void expansion in an incompressible body.

Here we employ ε in its common uniaxial definition $\varepsilon = \frac{l-L}{L}$. Note that in the incompressible limit follows $1 - \nu\varepsilon = 1 - \frac{1}{2}\varepsilon = \frac{1}{2}(3 - \lambda)$ which is the linearization of the function $1/\sqrt{\lambda}$.

Expansion of a void in an infinite body.

A spherical void with initial radius A is expanding to the current radius a. Material spheres surrounding the void with radii R and r, respectively, deform with the body. From the volume constraint follows

$$\frac{4\pi}{3}(R^3 - A^3) = \frac{4\pi}{3}(r^3 - a^3), \tag{1.54}$$

and, consequently, the deformation mapping $r = \varphi(R)$ reads

$$r = \left(a^3 - A^3 + R^3\right)^{1/3}. \tag{1.55}$$

Clearly, this deformation is not homogeneous. However, for any point located on the void surface we can compute the deformation gradient as

$$\boldsymbol{F} = \begin{pmatrix} a/A & 0 & 0 \\ 0 & a/A & 0 \\ 0 & 0 & a/A \end{pmatrix}. \tag{1.56}$$

2. Balance Equations

In this chapter we provide in short form the classical balance principles. For detailed studies and consequences of these relations in continuum mechanics we refer to the fundamental works of Coleman, Truessdell and Noll [93, 339, 340], and to comprehensive textbooks as, e.g., [32, 80, 152, 231].

In classical solid mechanics the wanted fields determined by the balance equations are defined on time $t \in \mathbb{R}^+$ and position $\boldsymbol{x} \in \mathbb{R}^3$ of a set of particles $\mathcal{P}$ occupying a region $\mathcal{B} \subset \mathbb{R}^3$. The hypothesis of a continuum states that a volume element dV is associated with each event in space-time $(\boldsymbol{x}, t)$; this allows to define macroscopic fields with a certain continuity. Primarily we focus on bodies or systems of sub-bodies, respectively, which are modeled as closed systems. In a closed system the mass of the bodies remains constant under all deformation. This excludes processes of mass growth and loss for which the system is commonly modeled as open, assuming a constant volume instead, see Section 2.7.

The solids under consideration in this work deform and move over a period of time under the action of a system of externally applied forces and prescribed displacements. The forces may consist of body forces which are the result of interaction at a distance, as well as of traction acting on the surface of the body. By $\bar{\boldsymbol{B}} : \mathcal{B} \to \mathbb{R}^3$ we denote the **material body force** field per unit mass and by $\bar{\boldsymbol{b}} : \boldsymbol{\varphi}(\mathcal{B}) \to \mathbb{R}^3$ the **spatial body force** field per unit mass. A relation between the two fields may be established considering an infinitesimal neighborhood of mass dm and letting $d\boldsymbol{f}$ be the resultant body force acting on the neighborhood. With the deformation mapping $\boldsymbol{x} = \boldsymbol{\varphi}(\boldsymbol{X}, t)$ we may write

$$d\boldsymbol{f} = \bar{\boldsymbol{B}}(\boldsymbol{X}, t)\, dm = \bar{\boldsymbol{b}}(\boldsymbol{x}, t)\, dm. \tag{2.1}$$

Thus we get $\bar{\boldsymbol{b}} \circ \boldsymbol{\varphi} = \bar{\boldsymbol{B}}$. Let us mention that here and in the remaining of this text we silently presume the **principle of local action** to be valid. This principle states that the internal energy density of a material point $\boldsymbol{X} \in \mathcal{B}$ depends only on the local state of an infinitesimal material neighborhood containing the point.

Analogously, we denote by $\bar{\boldsymbol{T}} : \mathcal{S} \to \mathbb{R}^3$ the **material surface traction** field per unit reference area, and by $\bar{\boldsymbol{t}} : \boldsymbol{\varphi}(\mathcal{S}) \to \mathbb{R}^3$ the **spatial surface traction** field per
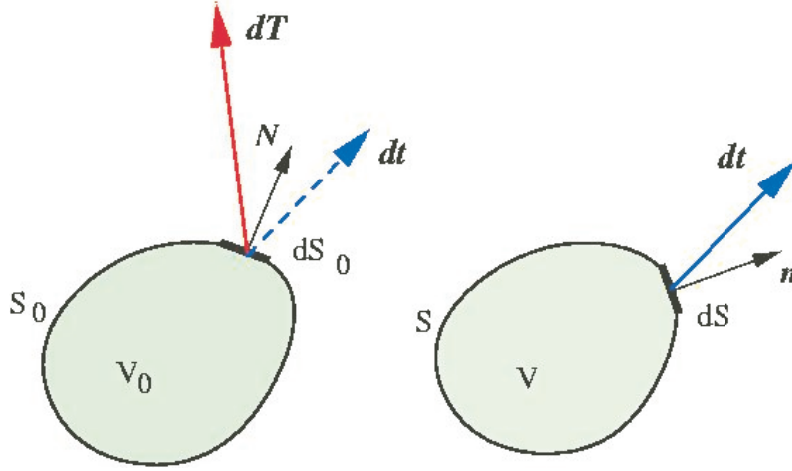
Figure 2.1.: Piola transformation.

unit deformed area. Denote by dS and ds the infinitesimal areas containing $\boldsymbol{X}$ and $\boldsymbol{x}$, respectively, and let $\boldsymbol{N}$ and $\boldsymbol{n}$ be the corresponding outward unit normals, Figure 2.1. Then, the total force acting on an element of area is

$$d\boldsymbol{f} = \bar{\boldsymbol{T}}(\boldsymbol{X},t)\,dS = \bar{\boldsymbol{t}}(\boldsymbol{x},t)\,ds. \tag{2.2}$$

We employ **Cauchy's tetrahedron** theorem from which it follows that the traction depends linearly on the corresponding unit normal, i.e.,

$$\bar{\boldsymbol{t}}(\boldsymbol{x},t) = \boldsymbol{\sigma}(\boldsymbol{x},t)\boldsymbol{n}(\boldsymbol{x},t) \tag{2.3}$$

where $\boldsymbol{\sigma} : \boldsymbol{\varphi}(\mathcal{B}) \to \mathbb{R}^{3\times3}$ is the **Cauchy stress tensor** comprising the "true" stress at the deformed material point. Correspondingly, we may formulate these relations for the reference configuration,

$$\bar{\boldsymbol{T}}(\boldsymbol{X},t) = \boldsymbol{P}(\boldsymbol{X},t)\boldsymbol{N}(\boldsymbol{X},t), \tag{2.4}$$

where $\boldsymbol{P} : \mathcal{B} \to \mathbb{R}^{3\times3}$ is the **first Piola-Kirchhoff stress tensor**. Inserting (2.3) and (2.4) in (2.2) and applying Nanson's formula (1.20) yields the following relation between the stress tensors,

$$\boldsymbol{\sigma} = J^{-1}\boldsymbol{P}\boldsymbol{F}^{\top}. \tag{2.5}$$

Relation (2.5) is known as **Piola transformation**. Written in components it reads

$$\sigma_{ij} \;=\; J^{-1}(\boldsymbol{X},t)\,P_{iJ}(\boldsymbol{X},t)\,F_{Jj}(\boldsymbol{X},t) \quad\Leftrightarrow\quad P_{iJ} = J(\boldsymbol{X},t)\,\sigma_{ij}(\boldsymbol{X},t)\,F_{jJ}^{-1}(\boldsymbol{X},t),$$

where the indices emphasize that $\boldsymbol{\sigma}$ is defined on the current configuration whereas $\boldsymbol{P}$ is a two-point tensor, i.e., it works between current and reference configuration.

Additionally, we introduce a symmetric tensor measuring the stress with respect to the reference configuration, namely, the **second Piola-Kirchhoff stress tensor**, $\boldsymbol{S} : \mathcal{B} \to \mathbb{R}^{3\times 3}$. The following relations hold

$$\boldsymbol{\sigma} = J^{-1}\boldsymbol{F}\boldsymbol{S}\boldsymbol{F}^{\top} \tag{2.6}$$

$$\boldsymbol{P} = \boldsymbol{F}\boldsymbol{S}, \tag{2.7}$$

and, vice versa,

$$\boldsymbol{S} = J\boldsymbol{F}^{-1}\boldsymbol{\sigma}\boldsymbol{F}^{-\top} \tag{2.8}$$

$$= \boldsymbol{F}^{-1}\boldsymbol{P}. \tag{2.9}$$

2.1. Conservation of mass

Let $\varrho_0(\boldsymbol{X}, t)$ be the mass density per unit undeformed volume and $\varrho(\boldsymbol{x}, t)$ the corresponding mass density per unit of deformed volume. Now we consider an infinitesimal neighborhood of $\boldsymbol{X} \in \mathcal{B}$ at time t of volume dV_0 and let dV be the volume of the corresponding spatial neighborhood. Since both material volumes are in correspondence by the deformation mapping, the total mass contained in them must be identical, i.e.

$$dm = \varrho_0(\boldsymbol{X}, t)dV_0 = \varrho(\boldsymbol{x}, t)dV. \tag{2.10}$$

Combining this relation with (1.16) gives the simple algebraic equation[1]

$$\varrho_0 = J\varrho, \tag{2.11}$$

which is the *Lagrangian local form of mass balance*. Within the *Eulerian* frame we obtain a partial differential equation known as continuity equation, see Table 2.1.

2.2. Conservation of linear momentum

The total linear momentum $\boldsymbol{L}$ of the body expressed in material form is

$$\boldsymbol{L} = \int_{\mathcal{B}} \varrho_0 \boldsymbol{V} \, dV, \tag{2.12}$$

---

[1]For brevity we omit in the following the arguments but we silently understand all relevant quantities to depend on position and time.

where $\boldsymbol{V}$ denotes the material velocity. Likewise the resultant of the forces acting on the body $\bar{\boldsymbol{F}}$ may be written in the form

$$\bar{\boldsymbol{F}} = \int_{\mathcal{B}} \varrho_0 \bar{\boldsymbol{B}} \, dV + \int_{\mathcal{S}} \boldsymbol{P} \boldsymbol{N} dS, \tag{2.13}$$

with the first Piola-Kirchhoff tensor $\boldsymbol{P}$ and the outward unit normal $\boldsymbol{N}$ as above. Then, the principle of linear momentum (or Newtons second law) simply states

$$\frac{d\boldsymbol{L}}{dt} = \bar{\boldsymbol{F}}. \tag{2.14}$$

Inserting the corresponding integral expressions equation (2.14) reads

$$\int_{\mathcal{B}} \varrho_0 \boldsymbol{A} dV = \int_{\mathcal{B}} \varrho_0 \bar{\boldsymbol{B}} dV + \int_{\mathcal{S}} \boldsymbol{P} \boldsymbol{N} dS, \tag{2.15}$$

where $\boldsymbol{A}$ is the material acceleration defined by (1.8). Here and further on we assume the material mass density ϱ_0 to be constant in time. An application of the divergence theorem gives[2]

$$\int_{\mathcal{B}} \big(\varrho_0 (\boldsymbol{A} - \bar{\boldsymbol{B}}) - \operatorname{Div} \boldsymbol{P} \big) \, dV = 0. \tag{2.16}$$

The balance equation applies to the body as well as to all 'sub-bodies' of $\mathcal{B}$, i.e., an identical identity must hold for every open subset $\Omega \subset \mathcal{B}$. This in turn requires the integrand in (2.15) to equal zero.

$$\varrho_0 \boldsymbol{A} = \varrho_0 \bar{\boldsymbol{B}} + \operatorname{Div} \boldsymbol{P} \qquad \text{a.e. in } \mathcal{B}, \tag{2.17}$$

Equation (2.17) states the *Lagrangian local form of linear momentum balance*. In quasi-static deformations, i.e, deformations with negligible influence of acceleration, the left hand side of equation (2.17) vanishes and the remaining terms state the local *equilibrium* condition.

2.3. Conservation of angular momentum

The total angular momentum $\boldsymbol{G}$ of the body reads in material form

$$\boldsymbol{G} = \int_{\mathcal{B}} \boldsymbol{x} \times (\varrho_0 \boldsymbol{V}) \, dV. \tag{2.18}$$

---

[2]By $\operatorname{Div}(\cdot)$ and $\operatorname{Grad}(\cdot)$ we denote the divergence and the gradient with respect to the material frame, respectively, see Appendix 2.

Likewise, the resultant moment $\boldsymbol{M}$ acting on the body may be expressed in the form

$$\boldsymbol{M} = \int_{\mathcal{B}} \boldsymbol{x} \times (\varrho_0 \bar{\boldsymbol{B}}) \, dV + \int_{\mathcal{S}} \boldsymbol{x} \times (\boldsymbol{PN}) \, dS. \tag{2.19}$$

Under these conditions conservation of angular momentum means

$$\frac{d\boldsymbol{G}}{dt} = \boldsymbol{M}. \tag{2.20}$$

Equation (2.19) applied to a deformed (non-polar) material element simply requires the Cauchy stress tensor to be symmetric,

$$\boldsymbol{\sigma} = \boldsymbol{\sigma}^\top \qquad \text{in } \boldsymbol{\varphi}(\mathcal{B}), \tag{2.21}$$

which is the *spatial local form of conservation of angular momentum*. Pulled back into the reference configuration by virtue of (2.5) it follows the *Lagrangian local form of angular momentum*,

$$\boldsymbol{PF}^\top = \boldsymbol{FP}^\top \qquad \text{in } \mathcal{B}. \tag{2.22}$$

2.4. The deformation power identity

The **kinetic energy** of the body written in Lagrangian form is

$$K = \frac{1}{2} \int_{\mathcal{B}} \varrho_0 |\boldsymbol{V}|^2 \, dV. \tag{2.23}$$

The **external power** P^E is the power of all externally applied force fields, i.e., the sum of resulting body forces and traction.

$$P^E = \int_{\mathcal{B}} \varrho_0 \, \bar{\boldsymbol{B}} \cdot \boldsymbol{V} \, dV + \int_{\mathcal{S}} \boldsymbol{PN} \cdot \boldsymbol{V} \, dS. \tag{2.24}$$

The deformation power P^D is by definition the amount of the external power supply which is not converted into kinetic energy of the body,

$$P^D = P^E - \dot{K}. \tag{2.25}$$

Inserting (2.23) and (2.24) in (2.25) gives

$$P^D = \int_{\mathcal{B}} \varrho_0 \, \bar{\boldsymbol{B}} \cdot \boldsymbol{V} \, dV + \int_{\mathcal{S}} \boldsymbol{PN} \cdot \boldsymbol{V} \, dS - \int_{\mathcal{B}} \varrho_0 \boldsymbol{A} \cdot \boldsymbol{V} \, dV. \tag{2.26}$$

By application of the divergence theorem we get

$$P^D = \int_{\mathcal{B}} \left(\varrho_0 (\bar{\boldsymbol{B}} - \boldsymbol{A}) + \operatorname{Div} \boldsymbol{P} \right) dV + \int_{\mathcal{B}} \boldsymbol{P} \cdot \operatorname{Grad} \boldsymbol{V} \, dV, \tag{2.27}$$

and simple algebra gives $\operatorname{Grad}(\boldsymbol{V}) = \dot{\boldsymbol{F}}$. If the motion satisfies the linear momentum balance the first integral in (2.27) vanishes. Then, the **deformation power** follows as,

$$P^D = \int_{\mathcal{B}} \boldsymbol{P} \cdot \dot{\boldsymbol{F}} \, dV. \tag{2.28}$$

Equation (2.28) shows, that the Piola-Kirchhoff stress tensor $\boldsymbol{P}$ and the deformation gradient $\boldsymbol{F}$ are *work-conjugate* variables, i.e., their scalar product defines a rate of internal mechanical work. With the definitions of Section 1.4 other work-conjugate expressions are given by

$$\boldsymbol{P} \cdot \dot{\boldsymbol{F}} = \boldsymbol{S} \cdot \dot{\boldsymbol{E}} = J \boldsymbol{\sigma} \cdot \boldsymbol{d} = \boldsymbol{\tau} \cdot \boldsymbol{d}. \tag{2.29}$$

The Tensor $\boldsymbol{\tau}$ is the frequently used **Kirchhoff-stress tensor**, $\boldsymbol{\tau} : \mathcal{B} \to \mathbb{R}^{3 \times 3}$ with $\boldsymbol{\tau} = J \boldsymbol{\sigma}$.

2.5. Conservation of mechanical energy

Let $U : \mathcal{B} \mapsto \mathbb{R}$ denote the **internal energy density** per unit undeformed volume and

$$E = \int_{\mathcal{B}} U dV = \int_{\boldsymbol{\varphi}(\mathcal{B})} J^{-1} U dV \tag{2.30}$$

the total internal energy of the body. For elastic bodies (or reversible deformations) the conservation of energy demands

$$P^E = \dot{E} + \dot{K}, \tag{2.31}$$

i.e., the external power will be converted, without gains or losses, into internal or kinetic energy. By the definition of deformation power (2.25) and the deformation-power identity (2.28) this reduces to the tautology $\dot{E} = P^D$:

$$\int_{\mathcal{B}} \varrho_0 \, \bar{\boldsymbol{B}} \cdot \boldsymbol{V} \, dV + \int_{\mathcal{S}} \bar{\boldsymbol{T}} \cdot \boldsymbol{V} dS = \int_{\mathcal{B}} \boldsymbol{P} \cdot \dot{\boldsymbol{F}} dS + \int_{\mathcal{B}} \varrho_0 \boldsymbol{A} \cdot \boldsymbol{V} dV. \tag{2.32}$$

Writing the *conservation of mechanical energy in Lagrangian local form* results in

$$\dot{U} = \boldsymbol{P} \cdot \dot{\boldsymbol{F}}. \tag{2.33}$$

Equation (2.33) does not furnish a new field equation.

Table 2.1 summarizes the local balance equations in material and spacial form.

mass:	$\varrho_0 = J\varrho$	$\frac{d\varrho}{dt} = \varrho\frac{dv_i}{dx_i}$
linear momentum:	$\varrho_0 A_i = \varrho_0 \bar{B}_i + P_{iJ,J}$	$\varrho a_i = \varrho \bar{b}_i + \sigma_{iJ,J}$
angular momentum:	$\sigma_{ij} = \sigma_{ij}$	$P_{iJ}F_{jJ} = P_{jJ}F_{iJ}$
mechanical energy:	$\dot{U} = P_{iJ}\dot{F}_{iJ}$	$\dot{U} = J\sigma_{iJ}d_{iJ}$
thermal energy:	$\dot{U} = P_{iJ}\dot{F}_{iJ} - \frac{\partial Q_L}{\partial X_L} + R$	$J^{-1}\dot{U} = \sigma_{iJ}d_{iJ} - \frac{\partial q_L}{\partial x_L} + r$

Table 2.1.: Local balance equation in *Lagrangian* and *Eulerian* form.[3]

2.6. Thermal energy

In this section we deviate from the restriction to reversible (and thus adiabatic) processes and consider both mechanical and thermal energy. For later reference we state here the fundamental laws of thermodynamics.

First law of thermodynamics

Let $Q : \mathcal{B} \mapsto \mathbb{R}$ be the **thermal power** or the rate of thermal work. With the vector of **heat flux** per unit time and per unit reference and current surface $\boldsymbol{Q}$ and $\boldsymbol{q}$, respectively, and with the **heat source** R and r per unit reference and current volume, the thermal work is determined to be

$$Q = \int_{\mathcal{B}} R\, dV - \int_{\mathcal{S}} \boldsymbol{Q} \cdot \boldsymbol{N}\, dS = \int_{\boldsymbol{\varphi}(\mathcal{B})} r\, dV - \int_{\boldsymbol{\varphi}(\mathcal{S})} \boldsymbol{q} \cdot \boldsymbol{n}\, dS. \qquad (2.34)$$

In a thermomechanical system the conservation of energy demands

$$P^E + Q = \dot{E} + \dot{K}\,. \qquad (2.35)$$

The thermal power will, additionally to the external (mechanical) power, completely be invested to raise the internal or kinetic energy of the body. Thus, the first law of

---

[3]Written in components, here and subsequently, a comma denotes partial differentiation.

thermodynamics in material form reads

$$\int_{\mathcal{B}} \left(\varrho_0 \, \bar{\boldsymbol{B}} \cdot \boldsymbol{V} + R \right) dV + \int_{\mathcal{S}} \left(\bar{\boldsymbol{T}} \boldsymbol{V} - \bar{\boldsymbol{Q}} \cdot \boldsymbol{N} \right) dS = \int_{\mathcal{B}} \dot{U} \, dV + \int_{\mathcal{B}} \varrho_0 \boldsymbol{A} \cdot \boldsymbol{V} \, dV. \quad (2.36)$$

Following arguments as above we find the *Lagrangian local form of thermal energy balance* to have the form

$$\dot{U} = \boldsymbol{P} \cdot \dot{\boldsymbol{F}} - \operatorname{Div} \boldsymbol{Q} + R. \quad (2.37)$$

Second law of thermodynamics

Let $S : \mathcal{B} \to \mathbb{R}$ denote the entropy per unit reference volume. Let $\Sigma : \mathcal{B} \to \mathbb{R}^+$ be the total production of entropy within the body, i.e., the difference between the rate of change of entropy and the rate of entropy input into the body. The second law of thermodynamics states that in a thermodynamic process the total entropy production can never be negative,

$$\Sigma \geq 0. \quad (2.38)$$

A *reversible* thermodynamic process is not accompanied by any entropy production, i.e., $\Sigma = 0$, whereas a process is called *irreversible* if $\Sigma > 0$.

We present the second law of thermodynamics in form of the **Clausius-Duhem inequality**. This approach links (under the presumption of uniformly distributed temperature, cf. [106]) the thermal quantities heat flux $\boldsymbol{Q}$ and heat source R via the absolute temperature T to the entropy flux $\boldsymbol{Q}/T$ and entropy source R/T, respectively. Consequently, the material form the Clausius-Duhem inequality reads

$$\Sigma = \int_{\mathcal{B}} \dot{S} \, dV + \int_{\mathcal{S}} \frac{\boldsymbol{Q}}{T} \cdot \boldsymbol{N} \, dS - \int_{\mathcal{B}} \frac{R}{T} \, dV \geq 0. \quad (2.39)$$

In an adiabatic closed system, i.e., in a system without heat source and without heat flux, $R = 0$, $\boldsymbol{Q} = \boldsymbol{0}$, equation (2.39) simplifies to

$$\dot{S} \geq 0. \quad (2.40)$$

Roughly speaking, the entropy measures the probability of a state, i.e., in equilibrium the state with the highest entropy is the most likely one. The fact that the entropy can only rise defines a direction for irreversible processes.

Let $A : \mathcal{B} \to \mathbb{R}$ denote the **Helmholtz free energy density**

$$A = U - ST. \quad (2.41)$$

The Helmholtz free energy density defines the internal energy density which may be converted into mechanical work at a constant temperature and is sometimes named as "work content". With this definition we can formulate equation (2.37) as

$$\dot{A} = \boldsymbol{P} \cdot \dot{\boldsymbol{F}} - \operatorname{Div} \boldsymbol{Q} + R - \dot{S}T - S\dot{T}, \tag{2.42}$$

and we derive a *local form* of (2.39)

$$\dot{A} + S\dot{T} - \boldsymbol{P} \cdot \dot{\boldsymbol{F}} + \frac{\boldsymbol{Q}}{T} \cdot \operatorname{Grad} T \leq 0. \tag{2.43}$$

The inequality (2.43) is often referred to as **Clausius-Planck inequality**, the terms on the left hand side describe the internal dissipation D^{int}. At constant temperature (2.43) reduces to

$$D^{int} = \boldsymbol{P} \cdot \dot{\boldsymbol{F}} - \dot{A} \geq 0. \tag{2.44}$$

For completeness we define here also the **Gibbs free energy density**, $G : \mathcal{B} \to \mathbb{R}$

$$G = U - ST + pV, \tag{2.45}$$

which is a thermodynamic potential and, correspondingly, a state function of a thermodynamic system. (For simplicity in notation we denote here with pV the volume work per unit volume.)

In the variational approaches favored in this work we will repeatedly exploit the idea, that a system seeks to archive a minimum of its free energy function.

2.7. General balance equations in a Schottky system

A domain $\Omega(t)$ exchanging heat, power and material with its environment is commonly defined to be a **Schottky system** [234, 230], see Figure 2.2 left. A Schottky system is, therefore, an extension of the above defined body with constant mass $\mathcal{B}$. Let now $\Psi(\boldsymbol{x}, t)$ be an extensive quantity in a Schottky system $\Omega(t)$. A change of quantity Ψ can be invoked by a production or source within the volume, here both denoted by Π^{ψ}, by a supply Σ^{ψ} and by a flux of quantity Ψ over the boundaries of the volume. The latter is written as the vector of outward flux per unit time and unit surface $\boldsymbol{J}^{\psi}$ in direction of the normal $\boldsymbol{n}$ of surface $S \equiv \partial\Omega$. Then the **generic form of a global balance equation** reads in spacial form

$$\begin{aligned}
\frac{d\Psi}{dt} &= \frac{d}{dt} \int_{\Omega(t)} \rho\psi(\boldsymbol{x}, t) dV \\
&= -\int_{\partial\Omega(t)} \boldsymbol{J}^{\psi}(\boldsymbol{x}, t) \cdot \boldsymbol{n} \, dS + \int_{\Omega(t)} (\Pi^{\psi}(\boldsymbol{x}, t) + \Sigma^{\psi}(\boldsymbol{x}, t)) dV \, , \tag{2.46}
\end{aligned}$$

where $\rho\psi$ is the quantity $\Psi(\boldsymbol{x}, t)$ per unit volume.
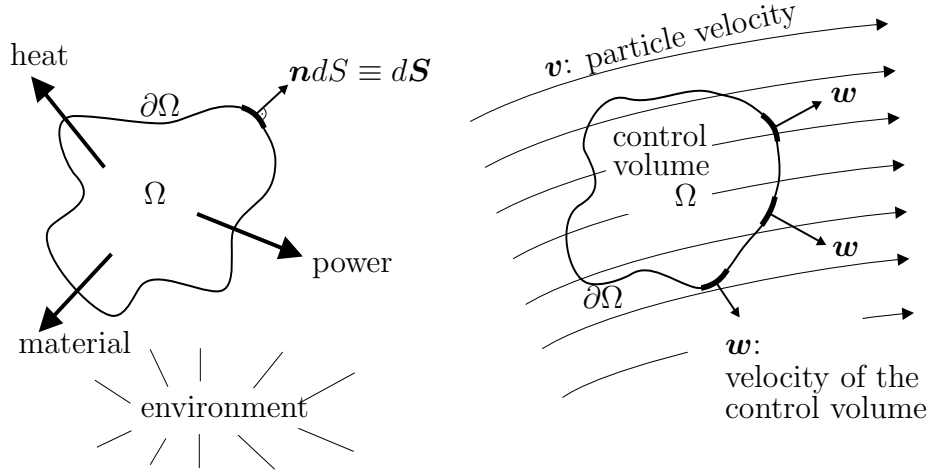
Figure 2.2.: Definition of a Schottky system Ω with boundary $\partial\Omega$, velocity $\boldsymbol{w}$ and particle velocity $\boldsymbol{v}$.

If the domain $\Omega(t)$ of a Schottky system coincides with a body (i.e., the system is a closed system), there is no particle transfer over the boundary $\partial\Omega$. The total mass contained in it remains constant and equation (2.10) holds, in other words

$$\frac{d}{dt}\int_{\Omega(t)}\rho(\boldsymbol{x}, t)dV = 0. \tag{2.47}$$

Equation (2.47) represents a special case of equation (2.46) with $\psi \equiv 1$, $\boldsymbol{J}^{\psi} = \Pi^{\psi} = \Sigma^{\psi} \equiv 0$. On the other hand, a Schottky system may be modeled as open presuming a constant volume moving with velocity $\boldsymbol{w}$ (right in Figure 2.2). The velocity $\boldsymbol{w}$ is superposed to the material velocity $\boldsymbol{v}(\boldsymbol{x}, t)$ of the particles $\mathcal{P}$. Then holds $\boldsymbol{J}^{\psi} \equiv \boldsymbol{J}^1 = \boldsymbol{J}$ and we notify

$$\frac{d}{dt}\int_{\Omega(t)}\rho(\boldsymbol{x}, t)dV = -\int_{\partial\Omega(t)}\boldsymbol{J}(\boldsymbol{x}, t)d\boldsymbol{S} \neq 0 \quad, \tag{2.48}$$

where the flux of mass is given by

$$\boldsymbol{J} = \rho(\boldsymbol{v} - \boldsymbol{w}). \tag{2.49}$$

Note that in a control volume the total outward flux $\boldsymbol{J}^{\psi}$ of quantity ψ is the sum of a convective (mass related) part $\rho(\boldsymbol{v} - \boldsymbol{w})\psi$ and a conductive part $\boldsymbol{J}^{\psi}_{\text{cond}}$. Clearly, if domain Ω is a body the convective part of the flux vanishes, i.e., $\boldsymbol{v} = \boldsymbol{w}$.

With the same arguments as before and by applying the divergence theorem and Reynolds' transport theorem (see Appendix, equation A 2.67) we obtain the **local form of the generic balance equation** in regular points, (cf. [231])

$$\frac{\partial \rho \psi}{\partial t} + \boldsymbol{\nabla} \cdot \left(\boldsymbol{w}\, \rho\, \psi + \boldsymbol{J}^{\psi} \right) = \Pi^{\psi} + \Sigma^{\psi} \ . \tag{2.50}$$

The specific balances of mass, momentum, total and internal energy follow by inserting the known expressions (here stated in spatial form):

- *mass*:
$$\psi \equiv 1 \ , \ \boldsymbol{J}^{1} \equiv \rho(\boldsymbol{v} - \boldsymbol{w}) \ , \ \Pi^{1} \equiv 0 \ , \ \Sigma^{1} \equiv 0. \tag{2.51}$$

- *momentum*:
$$\psi \equiv \boldsymbol{v} \ , \ \boldsymbol{J}^{\boldsymbol{v}} \equiv \rho(\boldsymbol{v} - \boldsymbol{w})\boldsymbol{v} - \boldsymbol{\sigma}^{T} \ , \ \Pi^{\boldsymbol{v}} \equiv 0 \ , \ \Sigma^{\boldsymbol{v}} \equiv \rho\bar{\boldsymbol{b}}. \tag{2.52}$$

- *total energy*:
$$\psi \equiv e \ , \ \boldsymbol{J}^{e} \equiv \rho(\boldsymbol{v} - \boldsymbol{w})e - \boldsymbol{\sigma}^{T} \cdot \boldsymbol{v} + \boldsymbol{q} \ , \ \Pi^{e} \equiv 0 \ , \ \Sigma^{e} \equiv \rho\bar{\boldsymbol{b}} \cdot \boldsymbol{v} + r. \tag{2.53}$$

- *internal energy*:
$$\psi \equiv u \ , \ \boldsymbol{J}^{u} \equiv \rho(\boldsymbol{v} - \boldsymbol{w})u + \boldsymbol{q} \ , \ \Pi^{u} \equiv \boldsymbol{\nabla}\boldsymbol{v} : \boldsymbol{\sigma} \ , \ \Sigma^{u} \equiv \rho r. \tag{2.54}$$

Note that the internal energy balance is not a conservation law, because of the nonzero production Π^{u}.

2.8. Jump conditions

In the foregoing we presented the global balance equations for the extensive quantities mass, momentum and energy, and we assumed continuity to derive the local, differential form. In some problems the considered fields are not smooth but only piecewise continuous. Let Λ be a surface discontinuity within a body $\mathcal{B}$ invoking (finite) jumps in some fields quantities. Assume this singular surface travels through the body with velocity $\boldsymbol{v}^{\Lambda} \neq \boldsymbol{v}$. Then, the body is divided into two sub-bodies $\mathcal{B}^{+}(t)$ and $\mathcal{B}^{-}(t)$ such that $\mathcal{B}^{+} \cup \mathcal{B}^{-} = \mathcal{B}$ and $\mathcal{B}^{+} \cap \mathcal{B}^{-} = \Lambda$. Indicate the values of a field quantity Ψ on the positive side of Λ by + and on the negative side by -. On Λ we define the jump in Θ as the difference of the limits Θ^{+} and Θ^{-} and we write

$$[\![\Psi]\!] = \Psi^{-} - \Psi^{+}. \tag{2.55}$$

To compute the time rate of a field quantity Ψ Reynolds' transport theorem (2.67) now needs to be applied to the domains of both sub-bodies, $\Omega(\mathcal{B}^+, t)$ and $\Omega(\mathcal{B}^-, t)$, and, moreover, to the surface Λ where the quantity Ψ jumps. The latter results in an additional term in equation (A 2.67), which is of the form

$$\int_\Lambda [\![\Psi \cdot (\boldsymbol{v}^\Lambda - \boldsymbol{v})]\!] \cdot \boldsymbol{n} \, dS. \tag{2.56}$$

Consequently, the generic form of the balance equations for a body with a discontinuous surface, i.e., the **general global jump balance equation**, reads in spacial form

$$\frac{d}{dt} \int_{\Omega^+(t) \cup \Omega^-(t)} \rho\psi(\boldsymbol{x}, t) \, d\Omega = - \int_{(\partial\Omega^+ \cup \partial\Omega^-) \backslash \Lambda} \boldsymbol{J}^\psi(\boldsymbol{x}, t) \cdot \boldsymbol{n} \, dS + \int_{\Omega^+(t) \cup \Omega^-(t)} (\Pi^\psi + \Sigma^\psi) \, d\Omega$$

$$+ \int_\Lambda [\![\rho\psi(\boldsymbol{x}, t) \cdot (\boldsymbol{v}^\Lambda - \boldsymbol{v})]\!] \cdot \boldsymbol{n} \, dS, \tag{2.57}$$

with the physical field quantities, flux and source terms of equations (2.52–2.54).

The local form of equation (2.57) yields to local forms for both sub-bodies $\mathcal{B}^+$ and $\mathcal{B}^-$, respectively, and to an *Eulerian local jump balance equation* on surface Λ,

$$[\![\rho\psi \cdot (\boldsymbol{v}^\Lambda - \boldsymbol{v}) - \boldsymbol{J}^\psi]\!] \cdot \boldsymbol{n} = 0. \tag{2.58}$$

Note that we neglect here all sources and sinks on the singular surfaces, otherwise there would be a source term on the right-hand side of equation (2.58) reflecting a possible area-distributed production onto the singular surface. The analogous *Lagrangian local jump balance equation* on surface Λ reads

$$[\![\rho\psi \, V_N^\Lambda]\!] - [\![\boldsymbol{J}^\psi \cdot \boldsymbol{N}]\!] = 0, \tag{2.59}$$

where V_N^Λ is the normal component of the material velocity of the travelling front Λ, i.e., $V^\Lambda = \boldsymbol{V} \cdot \boldsymbol{N}|_\Lambda$.

3. Constitutive Equations

The kinematic equations introduced in Chapter 1 are essential to describe motion and deformation of a body, whereas the local balance equations of Chapter 2 are the differential equations that determine the time evolution of the wanted fields. Altogether they are not yet a closed set of equations, since they do not distinguish one material from another. In addition, constitutive laws[1] are required which should in appropriate form specify the material behavior as a function of strain and stress state. Here we make no attempt to review the huge body of constitutive theories available in continuum mechanics but restrict ourself to some essential equations; for more details see [32, 152, 229, 247] and others. In this chapter we will summarize the general prerequisites for constitutive equations and we will introduce some elastic material models.

3.1. Elasticity

Let us consider an infinitesimal material neighborhood undergoing a deformation along a path Γ. The deformation is defined by a defomation gradient $\boldsymbol{F} : [t_1, t_2] \to \mathrm{GL}^+(3, \mathbb{R})$. Then, the work of deformation associated with this path is

$$W = \int_{t_1}^{t_2} \boldsymbol{P}(t) \cdot \boldsymbol{F}(t) \, dt. \tag{3.1}$$

A material is said to be an **elastic material** if the work of deformation is path independent. Consequently holds

$$\int_{\Gamma'} P_{iJ} dF_{iJ} = \int_{\Gamma''} P_{iJ} dF_{iJ}$$

for all paths of deformation $\Gamma', \Gamma'' \in \mathrm{GL}^+(3, \mathbb{R})$ defined by functions $\boldsymbol{F}', \boldsymbol{F}'' : [t_1, t_2] \to \mathrm{GL}^+(3, \mathbb{R})$ such that $\boldsymbol{F}'(t_1) = \boldsymbol{F}''(t_1)$ and $\boldsymbol{F}'(t_2) = \boldsymbol{F}''(t_2)$. For all closed paths of deformation the work of deformation is zero.

---

[1]which are not given by law but are assumptions basing on observation and generalization

3.1.1. Variational form

The definition of elasticity implies that for any deformation path Γ starting at a fixed reference configuration and terminating at $\boldsymbol{F}$ the **strain energy density** W is of the form

$$W(\boldsymbol{F}) = \int_\Gamma \boldsymbol{P} \, d\boldsymbol{F}. \tag{3.2}$$

Clearly, the elastic strain energy density is a function of the deformation only. In addition we know the gradient, i.e., the work conjugate stress tensor

$$P_{iJ}(\boldsymbol{F}) = \frac{\delta W}{\delta \boldsymbol{F}} \equiv \frac{\partial W}{\partial F_{iJ}}(\boldsymbol{F}). \tag{3.3}$$

The strain energy density acts as a potential for the stress tensor. Relation (3.3) is, therefore, the general *variational form* of elastic **constitutive laws**. Elastic materials with variational constitutive relations like (3.3) are also called **hyperelastic** materials.

In contrast to that, models with an *ad hoc* formulation of the elastic constitutive law are called **hypoelastic** materials. The hypoelastic constitutive relation is formulated in rate form, i.e., the stress rate is defined. In original hypoelastic theory [339], the stress rate is a function of the rate of deformation tensor (1.47) and additional contributions, e.g., the stress itself $f(d_{kl}, \sigma_{ij}, \dots)$. However, such constitutive relations (which are not elastic in the sense of the above definition) are not employed in modern constitutive theories. Instead, the name hypoelastic mostly refers to a rate formulation of the elastic law, e.g.,

$$\hat{\boldsymbol{\sigma}}(\boldsymbol{F}) = \overset{<4>}{C}(\boldsymbol{F}) \, \boldsymbol{d}(\boldsymbol{F}), \tag{3.4}$$

where $\hat{\boldsymbol{\sigma}}$ denotes a physical meaningful (objective) time derivative of the Cauchy stress tensor. The components of the stiffness tensor $\overset{<4>}{C}(\boldsymbol{F})$ are expressions of the elastic constants which in turn depend on the actual definition of the stress rate (and thus on the deformation). Because of the properties of the rate of deformation tensor (cf., Section 1.5) hypoelastic constitutive laws do not strictly reflect the path independence of elasticity. Moreover, the derivation of objective rates of stress tensors and the corresponding stiffness tensors is not trivial, see, e.g. [32].

From the theoretical point of view there is no reason to work with hypoelastic constitutive relations. However, the majority of commercial finite element programs still applies constitutive relations like (3.4). For this reason this approach is mentioned here. In the remaining of this text we speak about elasticity meaning the constitutive equations in its variational form (3.2–3.3).

3.1.2. Internal energy, stresses and elasticity tensor

The strain-energy function $W(\boldsymbol{F})$ of an elastic material may be given by the Helmholtz free energy density introduced in Chapter 2. To be more precise, inserting (3.3) into the mechanical energy balance equation (2.33) gives the identity

$$U = W(\boldsymbol{F}) = A(\boldsymbol{F}) \tag{3.5}$$

which states that the internal energy density of an elastic body coincides (up to an inconsequential additive constant) with the strain energy density.

From the definition of elasticity it follows that a material is elastic if and only if for all closed paths of deformation the rate of free energy vanishes, i.e., if the deformation of the material does not entail dissipation or hysteresis. This yields the definition of elasticity in terms of continuum thermodynamics where a material is said to be elastic if it produces *no entropy*. The second law of thermodynamics degenerates to an equation. Following a strategy known as Coleman-Noll procedure we expand the Clausius-Planck inequality (2.44) to write

$$\boldsymbol{P} \cdot \dot{\boldsymbol{F}} - \dot{A} = \left(\boldsymbol{P} - \frac{\partial \dot{A}}{\partial \boldsymbol{F}}\right) \cdot \dot{\boldsymbol{F}} = 0. \tag{3.6}$$

Only if the term in brackets vanishes equation (3.6) holds for every rate of deformation. In consequence this relates the stresses to the energy function as in the constitutive relation (3.3).

In order to obtain numerical solutions of nonlinear finite-deformation problems the linearized stress state is of central importance. Therefore we proceed expressing relation (3.3) in an incremental from. This can be accomplished in a number of mathematically equivalent ways. For instance taking differentials of (3.3) gives

$$dP_{iJ} = C_{iJkL}(\boldsymbol{F}) \, dF_{kL}, \tag{3.7}$$

where $C_{iJkL}(\boldsymbol{F})$ are the *Lagrangian elastic moduli*. The elastic moduli are the components of the fourth-order **elasticity tensor** $\overset{<4>}{C}$

$$\overset{<4>}{C} \;=\; C_{iJkL}\boldsymbol{e}_i \otimes \boldsymbol{e}_J \otimes \boldsymbol{e}_k \otimes \boldsymbol{e}_L \quad \text{with} \quad C_{iJkL}(\boldsymbol{F}) = \frac{\partial^2 W}{\partial F_{iJ}\partial F_{kL}}(\boldsymbol{F}). \tag{3.8}$$

The elasticity tensor is always symmetric in its first and second and in its third and fourth index. This symmetry is known as *minor symmetry*,

$$C_{iJkL} = C_{JikL} = C_{iJLk} = C_{JiLk}. \tag{3.9}$$

37

If derived from a scalar-valued energy function as presumed here by (3.8), the tensor $\overset{<4>}{C}$ also possesses *major symmetry*, i.e., it is symmetric in the sense

$$C_{iJkL} \;=\; C_{kLJi} \qquad \Leftrightarrow \qquad \overset{<4>}{C} = \overset{<4>}{C}{}^{\top} .\qquad (3.10)$$

A standard exercise shows that a fourth-order tensor with major and minor symmetry has only 21 independent components.

3.2. General requirements on the strain-energy function

Throughout this text we focus for simplicity on homogeneous (or homogenized) materials. A material is said to be **homogeneous** when the distribution of the internal structure is such that every material point has the same mechanical behavior. On the other hand, in a **heterogeneous** material the strain-energy function will additionally depend on the position of the material point in the reference configuration $\boldsymbol{X}$. (A common approach to simplify that situation is to homogenize the material by "averaging" over the internal structure, see Chapter 7.1.)

Hence, the strain-energy density is a postulated scalar-valued function of one tensorial variable, namely the deformation gradient $\boldsymbol{F}$. For convenience we require this function to vanish in the reference configuration where $\boldsymbol{F} = \boldsymbol{I}$, i.e., the reference configuration is stress free. From physical observations we conclude that the strain energy increases monotonically with the deformation,

$$W(\boldsymbol{I}) = 0 \qquad \text{and} \qquad W(\boldsymbol{F}) \geq 0. \qquad (3.11)$$

The strain energy function attains a global minimum for $\boldsymbol{F} = \boldsymbol{I}$ at the stress free state.

Moreover, let us require that an infinite amount of energy is necessary to expand a body infinitely and to compress a body to zero volume, respectively.

$$W(\boldsymbol{F}) \to \infty \quad \text{as} \quad \det \boldsymbol{F} \to \infty \qquad (3.12)$$
$$W(\boldsymbol{F}) \to \infty \quad \text{as} \quad \det \boldsymbol{F} \to 0. \qquad (3.13)$$

The strain-energy density $W(\boldsymbol{F})$ and the resulting constitutive equation must, of course, fulfill some requirements which arise from mathematical theory as well as from the physical nature of the material under consideration.

3.2.1. Polyconvexity

From a mathematical prospective the fundamental issue is to guarantee the existence of a (unique) solution for a given constitutive model. Local existence and uniqueness theorems in nonlinear elastostatics and elastodynamics are based on **ellipticity**. The ellipticity condition states that an energy function $W(\boldsymbol{F})$ leads to an elliptic system if and only if the well known Legendre-Hadamard condition holds,

$$\frac{\partial^2 W}{\partial \boldsymbol{F} \partial \boldsymbol{F}}(\boldsymbol{F}) \geq 0 \tag{3.14}$$

for all $\boldsymbol{F}(\boldsymbol{X}) \in \mathrm{GL}^+(3, \mathbb{R})$, $\boldsymbol{X} \in \mathbb{R}^3$. If the inequality holds we say that W is strongly elliptic or uniform rank-1 convex.

Originally, global existence theory for elastic problems was based on **convexity** of the free energy function. A scalar function is said to be convex if, for all $\boldsymbol{x}_1, \boldsymbol{x}_2 \in \mathbb{R}^3$, holds

$$\phi(\lambda \boldsymbol{x}_1 + (1 - \lambda)\boldsymbol{x}_2) \leq \lambda \phi(\boldsymbol{x}_1) + (1 + \lambda)\phi(\boldsymbol{x}_2) \qquad \lambda \in (0, 1). \tag{3.15}$$

However, from a physical point of view this condition may be too strong. As pointed out by Ball [12] convexity precludes some special but eminent physical phenomena as, e.g., buckling or wrinkling of structures. This leads to the important concept of **quasiconvexity**, introduced by Morrey in [226]. On a fixed domain Ω a function W is quasiconvex if

$$\int_\Omega \big(W(\boldsymbol{F} + \operatorname{grad} \boldsymbol{u})dx \geq \int_\Omega W(\boldsymbol{F})dx \qquad \forall \, \boldsymbol{F} \in \mathrm{GL}^+(3, \mathbb{R}), \, \boldsymbol{u} \in C_0^\infty. \tag{3.16}$$

Morrey showed that (under suitable growth conditions) quasiconvexity is a necessary and sufficient condition for a functional to be weakly lower semi-continuous, i.e., $W(\boldsymbol{F}) \geq \alpha$. Thus, quasiconvexity is closely related to the existence of minimizers of an energy function.

Unfortunately, condition (3.16) is a global one and, therefore, complicated to handle. A concept of greater practical importance is that of **polyconvexity**. Following Ball [12], see also [206], we define an energy function $W(\boldsymbol{F})$ to be polyconvex if and only if there exits a function ϕ which has arguments $\boldsymbol{F}$, $\operatorname{cof}(\boldsymbol{F})$ and $\det(\boldsymbol{F})$ and is convex, such that

$$W(\boldsymbol{F}) \;\; = \;\; \phi\big(\boldsymbol{F}, \operatorname{cof}(\boldsymbol{F}), \det(\boldsymbol{F})\big). \tag{3.17}$$

The polyconvexity condition has an additive nature, i.e., if the functions ϕ_i are all convex in their respective arguments then the function $W(\boldsymbol{F}) = \phi_1(\boldsymbol{F}) + \phi_2(\operatorname{cof}(\boldsymbol{F})) + \phi_3(\det \boldsymbol{F})$

is polyconvex. This property turns out to be very useful to establish constitutive models because it permits to construct energy functions out of simpler ones.

Finally, as shown in [206], the following implication chain relates all introduced concepts

convexity $\Rightarrow$ polyconvexity $\Rightarrow$ quasiconvexity $\Rightarrow$ rank-1-convexity (ellipticity) .

For homogenous and isotropic elastic materials we commonly require the strain energy function to be a convex potential. However, non-convex energy functions are encountered in many applications such as phase transitions in shape memory alloys [36, 279], in phase field theory (see Section 8.4) and, in particular, in dissipative materials under finite deformations. Non-convex potentials govern the microstructural development of a priori heterogeneous materials (such as textured materials or single crystals, [61, 163, 200]) as well as deformation phase decompositions in initially homogeneous materials.

Material instability phenomena can be interpreted as deformation microstructures, they are also associated with non-convex potentials. Such microstructures may be resolved by relaxation techniques based on a convexification of the (incremental) potential, whereby the relaxed problem then allows for a well-posed numerical analysis. For a concise mathematical background of the subject see [100, 232], mathematical treatments in the continuum mechanical context can be found in [19, 59, 75] and applications to special problems of metal plasticity and biological tissues are reported, e.g., in [60, 62, 173] and [15, 14, 297], respectively.

3.2.2. Objectivity and material frame indifference

It is obvious to claim that the deformation and consequently the strain energy density of a material point must not depend on the position of the observer who records the motion. In other words, two observers located at different positions in space should see at one instance an identical response of the material point. This requirement is called **observer invariance** or **objectivity**. If a physical quantity depends on the position of the observer than a change of observer, or, in mathematical terms, an action of a Euclidean group, induces a transformation of motion $\boldsymbol{\varphi}$ into $\hat{\boldsymbol{\varphi}}$. The second observer records the motion as being shifted by a vector $\boldsymbol{c}(t)$ and rotated by a finite rotation $\boldsymbol{Q} \in \mathrm{SO}(3)$, i.e.,

$$\boldsymbol{x} = \boldsymbol{\varphi}(\boldsymbol{X}, t) \tag{3.18}$$
$$\Rightarrow \quad \boldsymbol{Q}(t)\,\boldsymbol{\varphi}(\boldsymbol{X}, t) + \boldsymbol{c}(t) = \hat{\boldsymbol{\varphi}}(\boldsymbol{X}, t) = \boldsymbol{Q}(t)\,\boldsymbol{x} + \boldsymbol{c}(t),$$

where we assume the initial configuration to be observer independent.

Closely related to observer invariance is the expectation that the energy of a deformed elastic body remains unchanged when a rigid-body motion is superposed on an existing deformation. This requirement leads to the **principle of material-frame indifference**. Material-frame indifference is a somewhat questionable requirement because in some — rare — cases it might be physical meaningful that material properties change with, e.g., superposed fast rotations. The validity of this principle, its physical interpretation and the fundamental differences of the principles of objectivity and of material-frame indifference are subject of extensive discussions in theoretical literature, see, e.g., [33, 34, 235]. We consider here only common, acceleration-independent solid materials. In this case both, the agreement among observers about the perceived material response, i.e., objectivity, and the invariance of material response to superposed rigid body motions, i.e., material-frame indifference, coincide de facto. For more theoretical details we refer to the cited literature.

With (3.18) we can now derive the action of an Euclidean group on other kinematic quantities, primarily on the deformation gradient $\boldsymbol{F}(\boldsymbol{X}, t)$,

$$\hat{\boldsymbol{F}} = \frac{\partial \hat{\boldsymbol{\varphi}}}{\partial \boldsymbol{X}} = \frac{\partial \hat{\boldsymbol{\varphi}}}{\partial \boldsymbol{x}} \frac{\partial \boldsymbol{x}}{\partial \boldsymbol{X}} = \boldsymbol{Q}\boldsymbol{F}. \tag{3.19}$$

With the polar decomposition (1.23) and (1.27) follows immediately

$$\hat{\boldsymbol{U}} = \boldsymbol{U} \tag{3.20}$$
$$\hat{\boldsymbol{R}} = \boldsymbol{Q}\boldsymbol{R} \tag{3.21}$$
$$\hat{\boldsymbol{V}} = \boldsymbol{Q}\boldsymbol{V}\boldsymbol{Q}^{\top}. \tag{3.22}$$

By presuming the strain-energy density being solely a function of the deformation gradient, invariance upon translation is ensured. This leads to the following definition: An elastic material is said to be **objective** (and material frame indifferent) if its strain-energy density is invariant upon rotations. It holds for $\boldsymbol{Q} \in \mathrm{SO}(3)$

$$W(\boldsymbol{Q}\boldsymbol{F}) = W(\boldsymbol{F}) \tag{3.23}$$

for all $\boldsymbol{F} \in \mathrm{GL}^{+}(3, \mathbb{R})$. A strain-energy density function is objective if and only if it can be expressed as a function of the right Cauchy-Green tensor $\boldsymbol{C} = \boldsymbol{F}^T\boldsymbol{F} = \boldsymbol{U}^2$, equation (1.36). It is clear from (3.19) and (3.20) that a function of the form $W(\boldsymbol{U}^2) = W(\boldsymbol{C})$ is objective. To prove the necessity condition, assume, conversely, that $W(\boldsymbol{F})$ is objective. Let $\boldsymbol{F} = \boldsymbol{R}\boldsymbol{U}$ be the polar decomposition of $\boldsymbol{F}$ and $\boldsymbol{Q} \equiv \boldsymbol{R}^{-1}$. Then, by

definition (3.23) is[2]

$$
\begin{aligned}
W(\boldsymbol{F}) &= W(\boldsymbol{R}^{-1}\boldsymbol{F}) \\
&= W(\boldsymbol{U}) = W(\boldsymbol{C}).
\end{aligned}
\tag{3.24}
$$

Transformation rules for the stresses and the elastic moduli follow. Let $W(\boldsymbol{F})$ be objective and imagine perturbing it by an infinitesimal deformation $d\boldsymbol{F}$. Then definition (3.23) demands

$$
W\big(\boldsymbol{Q}(\boldsymbol{F}+d\boldsymbol{F})\big) = W\big(\boldsymbol{F}+d\boldsymbol{F}\big).
\tag{3.25}
$$

Expand this expression to employ the definition of the stresses (3.3).

$$
W\big(\boldsymbol{Q}\boldsymbol{F}\big) + \frac{\partial W}{\partial F_{iJ}}\big(\boldsymbol{Q}\boldsymbol{F}\big)Q_{ij}dF_{jJ} = W\big(\boldsymbol{F}\big) + \frac{\partial W}{\partial F_{iJ}}\big(\boldsymbol{F}\big)dF_{iJ}
$$

By virtue of (3.23) and with (3.3) this identity reduces to

$$
P_{iJ}(\boldsymbol{Q}\boldsymbol{F})Q_{ij}dF_{jJ} = P_{jJ}(\boldsymbol{F})dF_{iJ}.
\tag{3.26}
$$

Because $d\boldsymbol{F}$ is arbitrary we conclude that

$$
Q_{ij}P_{iJ}\big(\boldsymbol{Q}\boldsymbol{F}\big) = P_{jJ}(\boldsymbol{F}),
\tag{3.27}
$$

or, taking $\boldsymbol{Q}$ to the right-hand side of this equation

$$
\boldsymbol{P}(\boldsymbol{Q}\boldsymbol{F}) = \boldsymbol{Q}\boldsymbol{P}(\boldsymbol{F}) \qquad \forall\, \boldsymbol{Q} \in \mathrm{SO}(3)\,.
\tag{3.28}
$$

To establish the transformation rule for the elastic moduli we start with equation (3.28) and imagine perturbing it by an infinitesimal deformation $d\boldsymbol{F}$. By objectivity of the stress tensor holds

$$
P_{iJ}\big(\boldsymbol{Q}(\boldsymbol{F}+d\boldsymbol{F})\big) = Q_{ij}P_{jJ}\big(\boldsymbol{F}+d\boldsymbol{F}\big).
\tag{3.29}
$$

Expanding this expression gives

$$
P_{iJ}\big(\boldsymbol{Q}\boldsymbol{F}\big) + \frac{\partial^2 W}{\partial F_{iJ}\partial F_{kL}}\big(\boldsymbol{Q}\boldsymbol{F}\big)Q_{kl}\,dF_{lL} = Q_{ij}P_{jJ}\big(\boldsymbol{F}\big) + Q_{ij}\frac{\partial^2 W}{\partial F_{jJ}\partial F_{kL}}\big(\boldsymbol{F}\big)\,dF_{kL}.
$$

By the presumed objectivity of stress tensor and by the definition of the tangent moduli (3.8) this identity reduces to

$$
C_{iJkL}(\boldsymbol{Q}\boldsymbol{F})Q_{kl}\,dF_{lL} = Q_{ij}C_{jJkL}(\boldsymbol{F})\,dF_{kL}.
\tag{3.30}
$$

Again, $d\boldsymbol{F}$ is arbitrary, and we conclude for the tangential moduli

$$
C_{iJkL}(\boldsymbol{Q}\boldsymbol{F}) = Q_{ij}Q_{kl}\,C_{jJlL}(\boldsymbol{F}).
\tag{3.31}
$$

---

[2]By minor abuse of notation we write subsequently $W(\boldsymbol{F})$ and $\boldsymbol{P}(\boldsymbol{F})$ etc., meaning the corresponding function of argument $\boldsymbol{F}^{\top}\boldsymbol{F} = \boldsymbol{C}$. Furthermore, we write the functions without additionally indicating the different forms, depending on the specific arguments.

3.2.3. Material symmetry

Further constraints to the form of the strain-energy density function arise from material symmetry. If the material response in some preferred directions is identical, the strain-energy function is expected to reflect that property. A finite rotation $\boldsymbol{Q} \in \mathrm{SO}(3)$ is said to be a material **symmetry transformation** of a solid elastic material if for all $\boldsymbol{F} \in \mathrm{GL}^+(3, \mathbb{R})$ holds

$$W(\boldsymbol{F}\boldsymbol{Q}) = W(\boldsymbol{F}). \tag{3.32}$$

In general, not all finite rotations $\boldsymbol{Q} \in \mathrm{SO}(3)$ are symmetry transformations. Nonetheless the set of all symmetry transformations of a material defines a subgroup $S \subset \mathrm{SO}(3)$. To prove this consider a rotation $\boldsymbol{Q}_1 \in S$. Then, by (3.32),

$$W\big(\boldsymbol{F}\boldsymbol{Q}_1^{-1}\big) = W\big((\boldsymbol{F}\boldsymbol{Q}_1^{-1})\boldsymbol{Q}_1\big) = W(\boldsymbol{F}), \tag{3.33}$$

and, hence, $\boldsymbol{Q}_1^{-1} \in S$. Now let $\boldsymbol{Q}_1, \boldsymbol{Q}_2 \in S$. By the same argument is

$$W\big(\boldsymbol{F}(\boldsymbol{Q}_1\boldsymbol{Q}_2)\big) = W\big((\boldsymbol{F}\boldsymbol{Q}_1)\boldsymbol{Q}_2\big) = W\big(\boldsymbol{F}\boldsymbol{Q}_1\big) = W(\boldsymbol{F}), \tag{3.34}$$

and, $\boldsymbol{Q}_1\boldsymbol{Q}_2 \in S$. Consequently, S defines a group.

To deduce the **transformation rules** for the stresses and the elastic modulus we apply the same procedure as above. Let $\boldsymbol{Q} \in S$ be an arbitrary finite rotation, $\boldsymbol{F} \in \mathrm{GL}^+(3, \mathbb{R})$ be a local deformation, and imagine perturbing it by an arbitrary infinitesimal deformation $d\boldsymbol{F}$. Then symmetry demands that

$$W\big((\boldsymbol{F} + d\boldsymbol{F})\boldsymbol{Q}\big) = W\big(\boldsymbol{F} + d\boldsymbol{F}\big). \tag{3.35}$$

Expand this expression to employ relation (3.3)

$$W\big(\boldsymbol{F}\boldsymbol{Q}\big) + \frac{\partial W}{\partial F_{iJ}}\big(\boldsymbol{F}\boldsymbol{Q}\big)dF_{jI}Q_{IJ} = W\big(\boldsymbol{F}\big) + \frac{\partial W}{\partial F_{iJ}}\big(\boldsymbol{F}\big)dF_{iJ}.$$

By symmetry of the material we get

$$P_{iJ}(\boldsymbol{F}\boldsymbol{Q})dF_{jJ}Q_{IJ} = P_{iJ}\big(\boldsymbol{F}\big)dF_{iJ}, \tag{3.36}$$

and, because $d\boldsymbol{F}$ is arbitrary,

$$P_{iI}\big(\boldsymbol{F}\boldsymbol{Q}\big)Q_{JI} = P_{iJ}(\boldsymbol{F}). \tag{3.37}$$

Equivalently we may write

$$\boldsymbol{P}(\boldsymbol{F}\boldsymbol{Q}) = \boldsymbol{P}(\boldsymbol{F})\boldsymbol{Q}. \tag{3.38}$$

Further, from the material symmetry of the stress tensor follows that

$$P_{iJ}\big((\boldsymbol{F}+d\boldsymbol{F})\boldsymbol{Q}\big) = P_{jI}\big(\boldsymbol{F}+d\boldsymbol{F}\big)Q_{IJ}. \tag{3.39}$$

Expanding this expression, applying (3.38) and the definition of the elastic moduli (3.8) gives

$$\begin{aligned} P_{iJ}\big(\boldsymbol{FQ}\big) + \frac{\partial^2 W}{\partial F_{iJ}\partial F_{kL}}\big(\boldsymbol{FQ}\big)dF_{kK}Q_{KL} &= P_{iI}\big(\boldsymbol{F}\big)Q_{IJ} + \frac{\partial^2 W}{\partial F_{iI}\partial F_{kL}}\big(\boldsymbol{F}\big)dF_{kL}Q_{IJ} \\ C_{iJkL}\big(\boldsymbol{FQ}\big)dF_{kK}Q_{KL} &= C_{iIkL}\big(\boldsymbol{F}\big)dF_{kL}Q_{IJ}, \end{aligned} \tag{3.40}$$

and, we conclude

$$\begin{aligned} C_{iJkL}\big(\boldsymbol{FQ}\big)Q_{LK} &= C_{iIkL}\big(\boldsymbol{F}\big)Q_{IJ} \tag{3.41} \\ \Leftrightarrow \qquad C_{iJkL}\big(\boldsymbol{FQ}\big) &= C_{iIkK}\big(\boldsymbol{F}\big)Q_{IJ}Q_{KL}. \tag{3.42} \end{aligned}$$

For the strain-energy function of materials with symmetry exists representation theorems. These theorems (which state that a scalar function of any number of tensor invariants under a symmetry group can be expressed as a function of a finite number of scalar invariants, none of which is expressible as a function of the remaining ones) are fundamental for the definition of the strain-energy function.

3.3. Isotropy

A special but very important class of materials are isotropic materials. From the physical point of view isotropic materials are materials without any preferred direction. In terms of material symmetry an elastic material is said to be isotropic if its symmetry group is $S \equiv \mathrm{SO}(3)$. It is said to be anisotropic otherwise.

For isotropic materials the strain-energy function can be represented as a function of the invariants of the right Cauchy-Green tensor

$$W(\boldsymbol{C}) = W\big(I_1^C, I_2^C, I_3^C\big) \tag{3.43}$$

with (see also Appendix III)

$$\begin{aligned} I_1^C &= \mathrm{tr}(\boldsymbol{C}) \\ I_2^C &= \frac{1}{2}\big(\mathrm{tr}(\boldsymbol{C}^2) - \mathrm{tr}(\boldsymbol{C})^2\big) \tag{3.44} \\ I_3^C &= \det(\boldsymbol{C}). \end{aligned}$$

Note that this representation follows from the strain-energy function being invariant under rotations and, thus, equation (3.43) may equivalently be written in terms of the invariants of the left Cauchy-Green tensor $W(\boldsymbol{b}) = W(I_1^b, I_2^b, I_3^b)$ or its related strain measures.

With similar arguments the strain-energy function of an isotropic material can be expressed as a symmetric function of the eigenvalues of the right Cauchy-Green tensor.

$$W(\boldsymbol{C}) = W(\lambda_1^2, \lambda_2^2, \lambda_3^2) \tag{3.45}$$

Here we made use of the fact that the eigenvalues of tensor $\boldsymbol{C}$, λ_α^2, $\alpha = 1, 2, 3$, are the squares of the eigenvalues of tensor $\boldsymbol{U}$, λ_α. Moreover, in isotropic materials the principal directions of stress tensor and work conjugate deformation tensor coincide.

In order to express the constitutive relation in terms of strain invariants we exploit the fact, that the stress-strain relation is given by an isotropic tensor function,

$$\boldsymbol{Q}W(\boldsymbol{C})\boldsymbol{Q}^\top = W(\boldsymbol{Q}\boldsymbol{C}\boldsymbol{Q}^T), \tag{3.46}$$

which can easily be derived from equations (3.22), (3.28) and (3.38) and is not restricted to isotropic materials. An isotropic tensor function $W(\boldsymbol{C})$ can explicitly be represented as

$$\frac{\partial W(\boldsymbol{C})}{\partial \boldsymbol{C}} = \alpha_1 \boldsymbol{I} + \alpha_2 \boldsymbol{C} + \alpha_3 \boldsymbol{C}^2, \tag{3.47}$$

where the α_i, are scalar coefficients (so-called response coefficients), which may be evaluated for each material law in terms of tensor $\boldsymbol{C}$, $\alpha_i = \alpha_i(I_1^b, I_2^b, I_3^b)$. Equation (3.47) is known as **Richter representation** or first representation theorem for isotropic tensor functions. By some algebra (see, e.g., [138, 204]) it can alternatively be formulated as

$$\frac{\partial W(\boldsymbol{C})}{\partial \boldsymbol{C}} = \hat{\alpha}_0 \boldsymbol{I} + \hat{\alpha}_1 \boldsymbol{C} + \hat{\alpha}_2 \boldsymbol{C}^{-1}, \tag{3.48}$$

which is known as the **alternative Richter representation** or second representation theorem for isotropic tensor functions. The fundamental message of these theorems is that the stress response on the straining of an isotropic material is uniquely determined by only three parameters.

3.4. Elastic material models

The stress-strain relation of an elastic material follows by equation (3.3) from a strain-energy potential, which, of course, should map the physical properties for every specific

material under consideration. Consequently there exists a huge number of strain-energy functions and corresponding constitutive theories. The aim of this section is to summarize some well established and frequently employed models for reference.

3.4.1. Linear elastic materials

In linear elasticity the constitutive relation is given by **Hooke's law**. The linearized or incremental strain tensor $\boldsymbol{\epsilon}$ (1.42) and the corresponding stresses $\boldsymbol{\sigma}$ are related via the linear equation

$$\boldsymbol{\sigma} = \overset{<4>}{C} \boldsymbol{\epsilon}. \tag{3.49}$$

The elasticity tensor $\overset{<4>}{C}$ is a function of Young's modulus, E, and Poisson number, ν, or of the Lamè constants, μ and λ, respectively. For isotropic material these moduli are related by:

$$\lambda = \frac{E\nu}{(1+\nu)(1-2\nu)} \qquad \mu = \frac{E}{2(1+\nu)}. \tag{3.50}$$

The material parameters are presumed to depend on temperature but not on the deformation. Then the corresponding (isothermal) strain-energy density may be written as

$$W(\boldsymbol{\epsilon}) = \frac{\lambda}{2}\left(\mathrm{tr}\boldsymbol{\epsilon}\right)^2 + \mu\mathrm{tr}\boldsymbol{\epsilon}^2, \tag{3.51}$$

where $\mathrm{tr}(\cdot)$ denotes the trace of a tensor. The stress-strain relation (3.49) assumes with (3.3) the well known form

$$\boldsymbol{\sigma} = \lambda\,\mathrm{tr}\boldsymbol{\epsilon}\,\boldsymbol{I} + 2\mu\boldsymbol{\epsilon}. \tag{3.52}$$

With bulk modulus κ,

$$\kappa = \frac{E}{3(1-2\nu)} = \lambda + \frac{2}{3}\,\mu, \tag{3.53}$$

equation (3.51) can alternatively be formulated as

$$W(\boldsymbol{\epsilon}) = \frac{1}{2}\kappa\left(\mathrm{tr}\boldsymbol{\epsilon}\right)^2 + \mu\|\boldsymbol{\epsilon}\|^2. \tag{3.54}$$

Here $\|\cdot\|$ defines the deviatoric norm of a strain tensor by $\sqrt{\frac{2}{3}\,\mathrm{dev}(\cdot)\cdot\mathrm{dev}(\cdot)}$, see Appendix.

For later reference we also formulate a temperature dependent version of the elastic strain-energy density

$$W^e(\boldsymbol{\epsilon}, T) = \frac{\kappa}{2}\left(\mathrm{tr}\boldsymbol{\epsilon} - 3\alpha(T-T_0)\right)^2 + \varrho_0 c_v T\left(1 - \ln\frac{T}{T_0}\right) + \mu\|\boldsymbol{\epsilon}\|^2, \tag{3.55}$$

where α is the thermal expansion coefficient, T_0 is a reference absolute temperature, ϱ_0 is the mass density per unit undeformed volume, and c_v is the specific heat per unit mass at constant volume (which is assumed to not depend on strain). The first term in (3.54) and (3.55) represents the volumetric part of the elastic energy density and implies the equation of state of the material. The corresponding pressure follows as

$$p(\boldsymbol{\epsilon}, T) = \kappa \left(\mathrm{tr}\boldsymbol{\epsilon} - 3\alpha(T - T_0)\right). \tag{3.56}$$

As a matter of course, the linear elastic constitutive theory has major limitations. It can only be used to model small deformations, because it is based on the linearized deformation measure (1.42) and, even if the strains are small, it can only model a linear stress-strain behavior. For many practical purposes these restrictions are of no concern. Most engineering materials show elastic behavior for modest strains and the stresses are observed to be proportional to the strains in this range. In this text, however, we focus on large deformations. The easiest way to extend the linear elastic material behavior to finite kinematics is by simply replacing the infinitesimal strain $\boldsymbol{\epsilon}$ in (3.51) by the Green-Lagrange strain tensor $\boldsymbol{E}$. The result is known as the **Saint-Vernant Kirchhoff** material

$$W\left(\boldsymbol{E}\right) = \frac{\lambda}{2}\left(\mathrm{tr}(\boldsymbol{E})\right)^2 + \mu\mathrm{tr}\boldsymbol{E}^2 \tag{3.57}$$

where λ and μ are again the Lamè constants (3.50). With

$$\boldsymbol{S} = \frac{\partial W}{\partial \boldsymbol{E}} = 2\frac{\partial W}{\partial \boldsymbol{C}} \tag{3.58}$$

follows the stress-strain relation for the second Piola-Kirchhoff stress tensor $\boldsymbol{S}$,

$$\boldsymbol{S} = \lambda \boldsymbol{I}\,\mathrm{tr}\boldsymbol{E} + 2\mu\boldsymbol{E}. \tag{3.59}$$

Unfortunately, the energy function (3.57) fails to be polyconvex as we shall see in the next paragraph. In particular, (3.57) does not give a reasonable limit in compression because as $\det \boldsymbol{F} \to 0$, i.e., $\boldsymbol{E} \to -\frac{1}{2}\boldsymbol{I}$, the stresses vanishes. Consequently, from the theoretical point of view, this constitutive relation should be avoided. (Nonetheless the Saint-Vernant Kirchhoff model is very common, especially for metals where the range of elastic strains is relatively small.)

3.4.2. Rubbery and biological materials

More sophisticated elastic models are required for organic materials. Some of them exhibit a nonlinear stress-strain behavior even at modest strains. More importantly,

there is a wide range of polymers and also biological tissues which are elastic up to huge strains. These materials show complex (and very different) nonlinear stress-strain behavior. Specific strain energy-functions are designed to account for these phenomena.

The typical example for a material undergoing large strains is natural rubber. Many polymers also show (above a critical temperature) a *rubbery* behavior – the response is elastic without much rate or history dependence. Polymers with a heavily cross-linked molecular structure (elastomers) are the most likely to behave like ideal rubber, but also soft biological tissue shows rubbery behavior. Besides being elastic, the following feature is typical of rubbery materials: the material strongly resists volume changes. The bulk modulus (3.53) is comparable to that of metals. On the other hand, rubbery material is very compliant in shear, the shear modulus μ is of orders of magnitudes smaller than the shear resistance of most metals. This observation motivates the modelling of rubbery materials as being incompressible, i.e., the volume remains constant during deformation, $\det \boldsymbol{F} = 1$.

To assure **incompressibility** of an elastic material the strain-energy function is postulated to be of the form

$$W^{isochor} = W(\boldsymbol{C}) - p\left(\det \boldsymbol{F} - 1\right) \tag{3.60}$$

where p plays the role of a Lagrangian multiplier. By equation (3.3) follows for the first Piola-Kirchhoff stress tensor

$$\boldsymbol{P} \;=\; p\,\boldsymbol{F}^{-\top} + \frac{\partial W}{\partial \boldsymbol{F}} \tag{3.61}$$

and for the second Piola-Kirchhoff stresses and the Cauchy stresses

$$\boldsymbol{S} \;=\; -p\,\boldsymbol{F}^{-1}\boldsymbol{F}^{-\top} + \boldsymbol{F}^{-1}\frac{\partial W}{\partial \boldsymbol{F}} = -p\,\boldsymbol{C}^{-1} + 2\frac{\partial W}{\partial \boldsymbol{C}} \tag{3.62}$$

$$\boldsymbol{\sigma} \;=\; -p\,\boldsymbol{I} + \frac{\partial W}{\partial \boldsymbol{F}}\boldsymbol{F}^{\top} = -p\,\boldsymbol{I} + \boldsymbol{F}\left(\frac{\partial W}{\partial \boldsymbol{F}}\right)^{\top}. \tag{3.63}$$

These relations illustrate that the pressure p can not be determined from the materials response but only from additional equilibrium equations and boundary conditions.

To account later for both, volume preserving as well as volumetric deformations, we decompose the deformation gradient according to relation (1.22) into an isochoric (or unimodular) part $\boldsymbol{F}^{isochor}$ and a volume related part $\boldsymbol{F}^{vol} = \sqrt[3]{\det(\boldsymbol{F})}\,\boldsymbol{I}$,

$$\boldsymbol{F} \;=\; \boldsymbol{F}^{isochor}\boldsymbol{F}^{vol} = J^{\frac{1}{3}}\boldsymbol{F}^{isochor}. \tag{3.64}$$
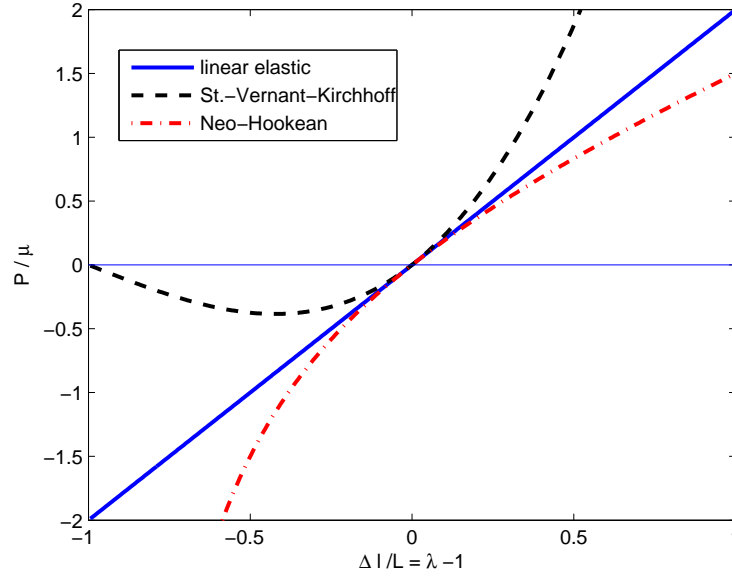
Figure 3.1.: Stress-strain relations in uniaxial tension.

Let us now summarize the classical strain-energy functions for incompressible materials $W(\boldsymbol{F}^{isochor})$ but omit the superscript *isochor* for simplicity. As before, I_i^C denotes the i-th principle invariant of the (isochoric part of) tensor $\boldsymbol{C}$, equation (3.44).

The simplest model is the **Neo-Hookean** solid,

$$W(\boldsymbol{C}) = \frac{\mu}{2}(I_1^C - 3). \tag{3.65}$$

First used by Treloar [338], the parameter μ was originally determined from an elementary statistical mechanics treatment predicting that $\mu = \frac{N}{2}kT$, where N is the number of polymer chains per unit volume, k is the Boltzmann constant and T is the temperature. Today this model is widely used with shear modulus μ determined by experiments. The stress-strain relation follows from (3.61- 3.63).

In Figure 3.1 the stress-strain relations in uniaxial tension are displayed. The dash-dotted line shows the Neo-Hookean model (3.65) whereas the dashed line results from the Saint-Vernant Kirchhoff model (3.59). In the undeformed configuration the tangent on both curves is the straight line of the Hookean law (3.52). The limited validity of the Saint-Vernant Kirchhoff model (3.59) is clearly visible. If $\Delta l/L < -0.4226$ an instability occurs, thence for rising compression a reduced stress is observed. Clearly,

the model makes sense only for small compressive strains. (The critical strain value does not depend on the material data.). On the other hand, the Neo-Hookean model captures the (principal) physics for the full range of straining. From experiments we know that for rubbery materials under moderate straining up to 30 - 70 % the Neo-Hookean model usually fits the material behavior with sufficient accuracy.

To model rubber at high strains the one-parametric Neo-Hookean model (3.65) is in most models replaced by a more sophisticated development of **Ogden** [291, 292]. Instead of using strain invariants this model expresses the strain energy density in terms of principal stretches λ_α, $\alpha = 1, 2, 3$,

$$W = \sum_{p=1}^{N} \frac{\mu_p}{\alpha_p} (\lambda_1^{\alpha_p} + \lambda_2^{\alpha_p} + \lambda_3^{\alpha_p} - 3), \tag{3.66}$$

where N, μ_p and α_p are material constants. In general, the shear modulus results from

$$2\mu = \sum_{p=1}^{N} \mu_p \alpha_p. \tag{3.67}$$

The three principal values of the Cauchy stresses can be computed from (3.66) as

$$\sigma_\alpha = p + \lambda_\alpha \frac{\partial W}{\partial \lambda_\alpha} \qquad \alpha = 1, 2, 3 \text{ (no summation)}, \tag{3.68}$$

and the principal first and second Piola-Kirchhoff stresses follow by

$$P_\alpha = \lambda_\alpha^{-1} \sigma_\alpha \quad \text{and} \quad S_\alpha = \lambda_\alpha^{-2} \sigma_\alpha. \tag{3.69}$$

With $N = 3$ and values summarized in Table 3.1 the Ogden material reaches an almost perfect agreement to the experimental data of Treloar. Therefore and because it is computational simple, equation (3.66) is *the* reference material law for natural rubber.

Neo-Hookean	$\alpha_1 = 2.0$	$\mu = 4.225 \cdot 10^5 \text{N/m}^2$
Ogden	$\alpha_1 = 1.3$	$\mu_1 = 6.3 \cdot 10^5 \text{ N/m}^2$
	$\alpha_2 = 5.0$	$\mu_2 = 0.012 \cdot 10^5 \text{ N/m}^2$
	$\alpha_3 = -2.0$	$\mu_3 = -0.1 \cdot 10^5 \text{ N/m}^2$
Mooney-Rivlin	$\alpha_1 = 2.0$	$\mu_1 = 3.6969 \cdot 10^5 \text{ N/m}^2$
	$\alpha_2 = -2.0$	$\mu_2 = -0.5281 \cdot 10^5 \text{ N/m}^2$
Arruda-Boyce	$\lambda_{lock} = 3$	$\mu_0 = 3.380 \cdot 10^5 \text{ N/m}^2$
Blatz-Ko	$\nu = 0.45$	$\mu = 4.225 \cdot 10^5 \text{N/m}^2$
St.Vernant-Kirchhoff	$\nu = 0.45$	$\mu = 4.225 \cdot 10^5 \text{N/m}^2$

Table 3.1.: Material parameters.

For special values of material constants the Ogden model (3.66) will reduce to either the Neo-Hookean solid ($N = 1$, $\alpha = 2$) or the Mooney-Rivlin material. The **Mooney-Rivlin** material can be derived from (3.66) with $N = 2$ and $\alpha_1 = 2$, $\alpha_2 = -2$, or, in other form

$$W(\boldsymbol{C}) = \frac{\mu_1}{2}(I_1^C - 3) - \frac{\mu_2}{2}(I_2^C - 3), \tag{3.70}$$

together with equation (3.67). The Mooney-Rivlin material was originally also developed for rubber but is today often applied to model (incompressible) biological tissue, e.g., in [219, 220, 239].

In polymers or industrial rubbers the shear modulus μ usually depends on the deformation. Earlier as natural rubber these materials exhibit a rising resistance against straining. A physically inspired model for carbon filled rubber is the **Arruda-Boyce** model. It is also sometimes called the **8-chain model** because it was derived by idealizing a polymer as 8 elastic chains inside a box [7]. This constitutive law has a strain energy density given by

$$W(\boldsymbol{C}) \;=\; \mu_0 \sum_{p=1}^{N} \frac{c_p}{\lambda_{lock}^{2p-2}}\big((I_1^C)^p - 3^p\big). \tag{3.71}$$

Here, μ_0 is the (initial) shear modulus, c_p are constants following from statistical theory, λ_{lock} and N are material constants of the underlying chain model, namely the limiting chain extensibility and the number of rigid links, (see [152] for illuminating explanations). Evaluating the first three terms of expression (3.71) gives

$$W(\boldsymbol{C}) \;=\; \mu_0\Big(\frac{1}{2}\big(I_1^C - 3\big) + \frac{1}{20\lambda_{lock}^2}\big((I_1^C)^2 - 9\big) + \frac{11}{1050\lambda_{lock}^4}\big((I_1^C)^3 - 27\big)\Big). \tag{3.72}$$

In the example below the limiting chain extensibility is set to $\lambda_{lock} = 3$ and the initial shear modulus is 80% of the Neo-Hookean shear modulus. The special feature of this model is a high strain resistance at strains $> 300\%$ (controlled by the choice of parameters). In other words, the model has the ability to reflect the dependence of the resulting shear modulus on the deformation.

Porous (or foamed) elastomers cannot be regarded as incompressible anymore. Blatz and Ko [37] proposed, based on theoretical arguments and experimental data for polyurethane rubbers, a strain-energy density of the form

$$W(\boldsymbol{C}) = \frac{\mu}{2}(I_1^C - 3) - \frac{\mu}{2\beta}\big((I_3^C)^{-\beta} - 1\big), \tag{3.73}$$

where β is computed from shear modulus μ and Poisson number ν as $\beta = \frac{\nu}{1-2\nu}$. In the incompressible limit is $I_3^C = 1$ and equation (3.73) reduces to the Neo-Hookean

solid. Here the model is introduced because it is — either as Blatz-Ko model or as Neo-Hookean extended to the compressible range — applied for (porous) biological tissue, see e.g. [118, 111].
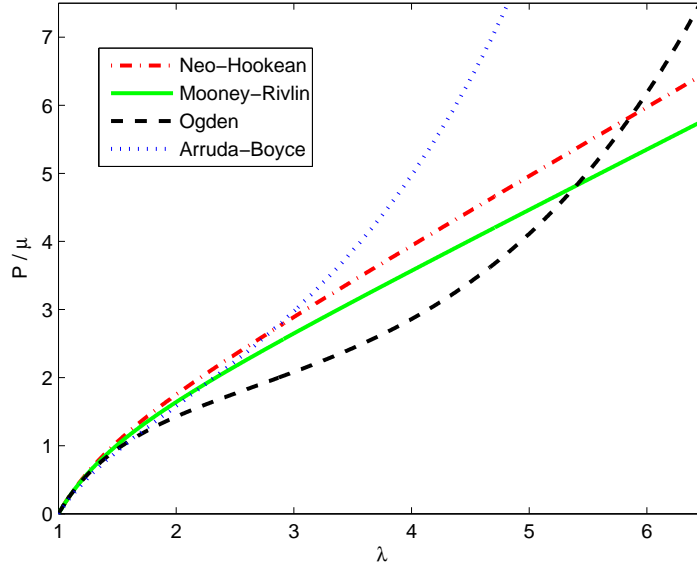

Figure 3.2.: Constitutive relations for rubbery materials in uniaxial tension.

Exemplarily, let us now consider an **incompressible material under uniaxial tension** (cf. Chapter 1.6). In particular, let the stretch ratio $\lambda = l/l_0$ be given. Then we find after differentiation according to (3.68) the principal stresses

$$\sigma_\alpha = p + \sum_{p=1}^{N} \mu_p \lambda_p^{\alpha_p} \tag{3.74}$$

with values from Table 3.1 for Neo-Hookean, Mooney-Rivlin and Ogden material. Pressure p is determined from incompressibility and boundary condition $\sigma_2 = \sigma_3 = 0$. With (3.69) the constitutive equation reduces to a single equation of the form

$$P = \sum_{p=1}^{N} \left(\mu_p \lambda_p^{\alpha_p - 1} - \mu_p \lambda_p^{-\frac{1}{2}\alpha_p - 1} \right). \tag{3.75}$$

For the Arruda-Boyce model (3.71) we get by differentiation

$$P = \mu_0 \left(1 + \frac{1}{5\lambda_{lock}^2}(\lambda^2 + \frac{2}{\lambda}) + \frac{11}{175\lambda_{lock}^4}(\lambda^2 + \frac{2}{\lambda})^2 \right) \left(\lambda_1 - \lambda_1^{-2} \right). \tag{3.76}$$

The Blatz and Ko model coincides in the incompressible case with the Neo-Hookean solid. Figure 3.2 shows the corresponding stress-strain curves for rubbery materials with material data from Table 3.1.

Above we have introduced the classical strain-energy functions for incompressible materials. These isochoric functions may be extended to the **compressible range**, $J = \det \boldsymbol{F} \neq 1$, by replacing the kinematic constraint in (3.60) with a volumetric strain-energy function.

$$W(\boldsymbol{F}) = W(\boldsymbol{F}^{isochor}) + W(\boldsymbol{F}^{vol}) \tag{3.77}$$

The additive decomposition of the strain-energy density (3.77) is postulated for convenience; other formulations are possible but not necessarily better. The easiest way to construct a volumetric addition of the strain energy density $W^{vol} \equiv W(\boldsymbol{F}^{vol}) = W(J)$ is by assuming a linear constitutive relation, and, consequently,

$$W^{vol}(J) \;=\; \frac{\kappa}{2}\big(J^2 - 1\big) = \frac{\kappa}{2}\big((I_3^C) - 1\big), \tag{3.78}$$

with a bulk modulus κ according to (3.53). Unfortunately such a simple extension (which is often applied, e.g., in commercial finite-element codes [161]) fails to be polyconvex. In the limit $J \to 0$ the constitutive relation derived from (3.78) gives non-physical results (compare with the comments to the Saint-Vernant-Kirchhoff material, Figure 3.1).
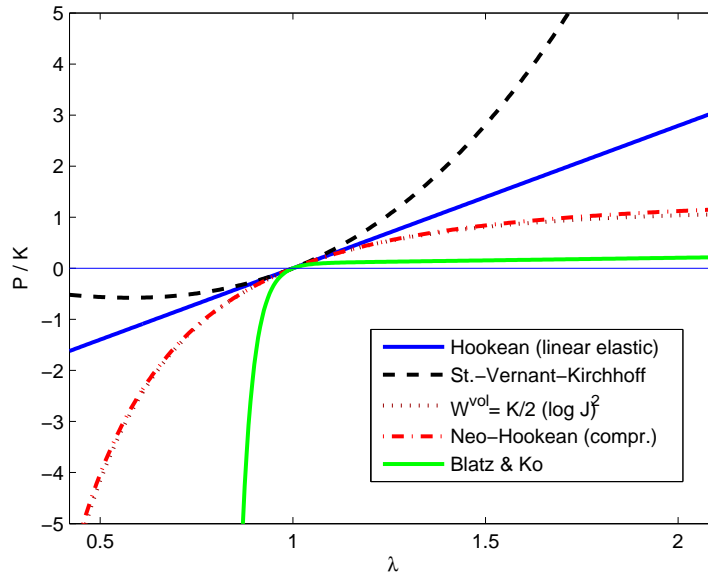

Figure 3.3.: Volumetric constitutive models in pressure and hydrostatic tension.

A standard method to avoid this drawback is to introduce an (additional) logarithmic term of the Jacobian of the deformation, e.g., $\kappa/2\left(\ln J\right)^2$. The term vanishes for small strains, $J \approx 1$, but guarantees a realistic limit of $W^{vol} \to \infty$ for $J \to 0$.

Here we adopt for the volumetric strain-energy function a well known analytical expression of Simo and Miehe [304],

$$W^{vol}(J) = \frac{\kappa}{4}\left(J^2 - 1 - 2\ln J\right), \tag{3.79}$$

which was applied for biological tissue, e.g., by Pandolfi et al. [264]. Equation (3.79) together with (3.65) prescribe a standard form of the Neo-Hookean material extended to the compressible range. A detailed derivation of stress tensors and elastic tangent moduli can be found in [152].

In Figure 3.3 the material parameter of Table 3.1 are applied to compare volumetric constitutive relations. For a hydrostatic pressure and tension test the principal first Piola-Kirchhoff stress divided by the bulk modulus κ is plotted versus the volumetric straining. For small compressions and expansions the curves are close to the linear elastic tangent but in the large strain range the different models diverge significantly.

4. Variational Formulations

In the previous chapters we established a set of kinematic, balance and constitutive equations to describe the motion and deformation of solids. With a view to formulate finite element approximations we restate in this chapter the preceding equations in a variational form.

4.1. Quasistatic deformations

At first we restrict our attention to time-independent deformation mappings and enunciate the **boundary-value problem (BVP)** of elasticity. To this end we consider the elastic body $\mathcal{B}$ of Figure 1.1 with boundary $\mathcal{S} = \mathcal{S}_1 \cup \mathcal{S}_2$, $\mathcal{S}_1 \cap \mathcal{S}_2 = 0$ in a reference configuration. Let the body deform in quasistatic manner under the action of a body-force field $\bar{\boldsymbol{B}} : \mathcal{B} \to \mathbb{R}^3$, prescribed deformations $\bar{\boldsymbol{\varphi}} : \mathcal{S}_1 \to \mathbb{R}^3$, and applied traction $\bar{\boldsymbol{T}} : \mathcal{S}_2 \to \mathbb{R}^3$. The equilibrium condition follows from the balance of linear momentum (2.17). With (1.14) and (2.4) the governing equations can be restated as a function of deformation, $\boldsymbol{\varphi}$, here written in indicial form:

$$\left[P_{iJ}(D\boldsymbol{\varphi}(\boldsymbol{X})) \right]_{,J} - \varrho_0 \bar{B}_i = 0 \quad \text{in } \mathcal{B} \tag{4.1}$$

$$\varphi_i = \bar{\varphi}_i(\boldsymbol{X}) \quad \text{on } \mathcal{S}_1 \tag{4.2}$$

$$P_{iJ}(D\boldsymbol{\varphi}(\boldsymbol{X})) \, N_J = \bar{T}_i \quad \text{on } \mathcal{S}_2 \,. \tag{4.3}$$

Equations (4.1–4.3) define a system of partial differential equations and essential (geometric) and natural (traction) boundary conditions to be solved for $\boldsymbol{\varphi}(\boldsymbol{X})$.

Equivalently (and omitting the arguments), we can write the governing equations in the more familiar spatial notation:

$$\sigma_{ij,j} - \varrho \, b_i = 0 \quad \text{in } \boldsymbol{\varphi}(\mathcal{B}) \tag{4.4}$$

$$\varphi_i = \bar{\varphi}_i \quad \text{on } \boldsymbol{\varphi}(\mathcal{S}_1) \tag{4.5}$$

$$\sigma_{ij} \, n_j = \bar{t}_i \quad \text{on } \boldsymbol{\varphi}(\mathcal{S}_2). \tag{4.6}$$

In both versions the elasticity BVP is usually intractable by analytical means. As a first step towards numerical approximation methods we will transform (4.1-4.3) into a variational setting.

To this end we assume that the admissible configurations of an elastic body belong to a topological vector space $\mathcal{U}$, termed as *displacement space*. (The precise functional nature of this displacement space depends on the constitutive properties of the material and the data of the boundary value problem and will remain unspecified for now.) The deformations which satisfy the geometrical boundary conditions $\bar{\varphi}$ define an affine subspace $\mathcal{U}_\mathcal{S}$ of $\mathcal{U}$, $\mathcal{U}_\mathcal{S} = \{\varphi \in \mathcal{U}$ such that $\varphi - \bar{\varphi} \in \mathcal{U}_0\}$. The translation space $\mathcal{U}_0$ of $\mathcal{U}_\mathcal{S}$ is the space of *admissible displacements*. Thus, by definition, all admissible displacement fields satisfy homogeneous displacement boundary conditions.

We begin by multiplying the equilibrium condition (4.1) with a virtual displacement, i.e., a test function $\eta \in \mathcal{U}_0$. Integrating the result over the domain[1] of body $\mathcal{B}$ we obtain the **weighted-residual form** of (4.1),

$$\int_\mathcal{B} \Big(\big[P_{iJ}(D\varphi(\boldsymbol{X})) \big]_{,J} - \varrho_0 \bar{B}_i \Big) \eta_i \, dV = 0 \qquad \forall \boldsymbol{\eta} \in \mathcal{U}_0. \tag{4.7}$$

Integration by parts gives

$$\int_\mathcal{B} \Big(P_{iJ}(D\varphi(\boldsymbol{X})) \, \eta_{i,J} - \varrho_0 \bar{B}_i \eta_i \Big) \, dV - \int_\mathcal{S} P_{iJ} N_J \, \eta_i \, dS = 0 \qquad \forall \boldsymbol{\eta} \in \mathcal{U}_0, \tag{4.8}$$

which, in view of the traction boundary conditions and the identity $\boldsymbol{\eta}_{|\mathcal{S}_1} = \boldsymbol{0}$, reduces to

$$\int_\mathcal{B} P_{iJ}(D\varphi) \eta_{i,J} \, dV - \int_\mathcal{B} \varrho_0 \bar{B}_i \eta_i \, dV - \int_{\mathcal{S}_2} \bar{T}_i \eta_i \, dS = 0 \qquad \forall \boldsymbol{\eta} \in \mathcal{U}_0, \tag{4.9}$$

$$\stackrel{\text{(def)}}{=} G\big(\varphi, \boldsymbol{\eta}\big)$$

which is the **weak form** of the balance of linear momentum or the **principle of virtual work**.

We now assume that the equations (4.1–4.3) are related to a functional $\Pi : \mathcal{U}_\mathcal{S} \to \mathbb{R}$. Let

$$G\big(\varphi, \boldsymbol{\eta}\big) = D_{,\varphi} \Pi[\varphi](\boldsymbol{\eta}) \qquad \forall \varphi \in \mathcal{U}_\mathcal{S}, \ \forall \boldsymbol{\eta} \in \mathcal{U}_0 \tag{4.10}$$

be the first variation of $\Pi(\varphi)$. That is the case if and only if the integrability condition

$$D_{,\varphi} G\big(\varphi, \boldsymbol{\eta}\big)(\boldsymbol{\xi}) = D_{,\varphi} G\big(\varphi, \boldsymbol{\xi}\big)(\boldsymbol{\eta}) \tag{4.11}$$

---

[1] For simplicity of notation we identify the domain of body $\mathcal{B}$ with its volume $V(\mathcal{B})$.

is satisfied $\forall \boldsymbol{\eta}, \boldsymbol{\xi} \in \mathcal{U}_0$, [215, 285]. Applied to expression (4.9) this condition results in

$$\int_{\mathcal{B}} \frac{\partial P_{iJ}}{\partial F_{kl}}(D\boldsymbol{\varphi}) \, \eta_{i,J} \, \xi_{k,L} \, dV = \int_{\mathcal{B}} \frac{\partial P_{iJ}}{\partial F_{kl}}(D\boldsymbol{\varphi}) \, \xi_{i,J} \, \eta_{k,L} \, dV \quad \forall \boldsymbol{\varphi} \in \mathcal{U}_{\mathcal{S}}, \qquad (4.12)$$

which in turn requires

$$\frac{\partial P_{iJ}}{\partial F_{kl}}(\boldsymbol{F}) = \frac{\partial P_{kL}}{\partial F_{iJ}}(\boldsymbol{F}) \qquad \forall \boldsymbol{F} \in \mathrm{GL}^+(3, \mathbb{R}). \qquad (4.13)$$

This is simply the condition for the existence of a strain-energy density $W(\boldsymbol{F})$ which works as a potential for the stress strain relations (3.3). Consequently, the wanted functional $\Pi(\boldsymbol{\varphi})$ is evaluated to be (up to an inconsequential additive constant), cf., [285],

$$\Pi[\boldsymbol{\varphi}] = \int_0^1 G(\boldsymbol{\varphi}_0 + t(\boldsymbol{\varphi} - \boldsymbol{\varphi}_0), \, \boldsymbol{\varphi} - \boldsymbol{\varphi}_0) \, dt. \qquad (4.14)$$

For a function G as defined in (4.9) this formula gives

$$\Pi[\boldsymbol{\varphi}] = \int_0^1 \left\{ \int_{\mathcal{B}} P_{iJ}(D\boldsymbol{\varphi}_0 + t(D\boldsymbol{\varphi} - D\boldsymbol{\varphi}_0)) \, (\varphi - \varphi_0)_{i,J} \, dV \right.$$
$$\left. - \int_{\mathcal{B}} \varrho_0 \bar{B}_i (\varphi - \varphi_0)_i \, dV - \int_{\mathcal{S}_2} \bar{T}_i (\varphi - \varphi_0)_i \, dS \right\} dt \quad (4.15)$$

Exchanging the order of integration and using (4.13) results in the well known expression

$$\Pi[\boldsymbol{\varphi}] = \int_{\mathcal{B}} \left[W(D\boldsymbol{\varphi}) - \varrho_0 \bar{B}_i \varphi_i \right] dV - \int_{\mathcal{S}_2} \bar{T}_i \varphi_i \, dS. \qquad (4.16)$$

The functional Π in form (4.16) is known as the **potential energy** of the elastic body.

The fundamental result of the preceding treatise is, that the equilibrium equations (4.1-4.2) are the Euler-Lagrange equations corresponding to the variational problem

$$\inf_{\boldsymbol{\varphi} \in \mathcal{U}_{\mathcal{S}}} \Pi[\boldsymbol{\varphi}] \qquad (4.17)$$

which is the **principle of minimum potential energy**.

It should be noted that the insistence on energy minimization stems from the presumption that the stable equilibrium configurations of an elastic body (which are the configurations of interest) are energy minimizers. The minimum principle (4.17) will in Chapter 5.2 be taken as a basis for constructing approximate solutions to the elasticity boundary-value problem.

4.2. Euler-Lagrange equations and internal kinematic constraints

In many cases the problem of energy minimization (4.17) is subjected to additional constraints following from the physical nature of the problem. An internal kinematic constraint is a scalar identity of the form

$$g(\boldsymbol{F}) = 0. \tag{4.18}$$

In order to accommodate internal kinematic constraints we need to enrich the constitutive equations by additional terms. This has been done in Chapter 3.4 for the constraint of material incompressibility, equations (3.60-3.63). To formulate a general minimum principle at the constitutive level, we define the local potential-energy density (3.3) to be a function of the form

$$f(\boldsymbol{F}) = W(\boldsymbol{F}) - \boldsymbol{P} \cdot \boldsymbol{F}. \tag{4.19}$$

As explained above we presume that the equilibrium configurations of elastic bodies, i.e. the configurations of interest, are energy minimizers. The corresponding variational problem than simply reads: Find

$$\min_{\boldsymbol{F} \in \mathrm{GL}^+(3,\mathbb{R})} f(\boldsymbol{F}). \tag{4.20}$$

The corresponding Euler-Lagrange equations are already given by (3.3). Written in components they read

$$\frac{\partial f}{\partial F_{iJ}} = 0 \qquad \Rightarrow \qquad \frac{\partial W}{\partial F_{iJ}} - P_{iJ} = 0. \tag{4.21}$$

This variational structure facilitates the treatment of internal constraints by the **Lagrange-multiplier method**.

Internal kinematic constraints of the form (4.18) pointwise restrict the possible values that may be attained by the deformation gradient. Suppose now that the material is subjected to constraints $g_\alpha(\boldsymbol{F})$, $\alpha = 1, ..., N$, simultaneously. In order to account for the constraints we introduce the Lagrangian function

$$\mathcal{L}(\boldsymbol{F}, \boldsymbol{\Lambda}) = f(\boldsymbol{F}) + \sum_{\alpha=1}^{N} \Lambda_\alpha g_\alpha(\boldsymbol{F}), \tag{4.22}$$

where Λ_α are the Lagrange multipliers. Then we replace problem (4.20) by the saddle point problem (min-max problem)

$$\min_{\boldsymbol{F} \in \mathrm{GL}^+(3,\mathbb{R})} \max_{\boldsymbol{\Lambda} \in \mathbb{R}^N} \mathcal{L}(\boldsymbol{F}, \boldsymbol{\Lambda}). \tag{4.23}$$

The Euler-Lagrange equations follow as

$$\frac{\partial \mathcal{L}}{\partial F_{iJ}} = 0 \quad \Rightarrow \quad \frac{\partial W}{\partial F_{iJ}} - P_{iJ} + \sum_{\alpha=1}^{N} \Lambda_{\alpha} \frac{\partial g_{\alpha}}{\partial F_{iJ}}(\boldsymbol{F}) = 0 \tag{4.24}$$

$$\frac{\partial \mathcal{L}}{\partial \Lambda_{\alpha}} = 0 \quad \Rightarrow \quad g_{\alpha}(\boldsymbol{F}) = 0, \quad \alpha = 1, ..., N \ . \tag{4.25}$$

The corresponding stress tensor is, therefore,

$$P_{iJ} = \frac{\partial W}{\partial F_{iJ}} + \sum_{\alpha=1}^{N} \Lambda_{\alpha} \frac{\partial g_{\alpha}}{\partial F_{iJ}}(\boldsymbol{F}) \ . \tag{4.26}$$

We see from these relations, that, in the presence of constraints, the stresses comprises an unconstrained term and additional terms arising from the constraints (reaction stress).

A typical example for an internal constraint is the incompressibility of a material, hence

$$g(\boldsymbol{F}) = J - 1 = 0. \tag{4.27}$$

For an incompressible material the Lagrangian function (4.22) reads

$$\mathcal{L}(\boldsymbol{F}, \Lambda) = W(\boldsymbol{F}) - P_{iJ}F_{iJ} + \Lambda(J - 1) \ , \tag{4.28}$$

and equation (4.26) evaluates to

$$P_{iJ} = \frac{\partial W}{\partial F_{iJ}} + \Lambda J F_{iJ}^{-1}. \tag{4.29}$$

Equivalently, with (2.5) and pushed forward, we can write the spatial form

$$\sigma_{ij} = \frac{1}{J} \frac{\partial W}{\partial F_{iJ}} F_{jJ} + \Lambda \delta_{ij}. \tag{4.30}$$

Equation (4.30) nicely illustrates that the incompressibility constraint has the effect of introducing an additional term in the trace of the stress tensor, i.e., the Lagrangian variable Λ represents a hydrostatic pressure, cf. Chapter 3.4.

4.3. Multi-field functionals

More general (quasistatic) variational principles then minimizing the potential energy functional (4.16) are multi-field functionals, as, e.g., the **Hu-Washizu principle**, [355].

In such formulations motion, stress tensor and deformation are treated as independent variables. Formulated with (1.1), (1.14) and (2.4) the Hu-Washizu potential of an elastic solid reads

$$
\begin{aligned}
\Pi\big(\boldsymbol{\varphi}, \boldsymbol{F}, \boldsymbol{P}\big) \;=\;& \int_{\mathcal{B}} \big[W(\boldsymbol{F}) + \boldsymbol{P} \cdot (\operatorname{Grad}\boldsymbol{\varphi} - \boldsymbol{F}) - \boldsymbol{\varphi} \cdot \varrho_0 \bar{\boldsymbol{B}}\big]\, dx - \int_{\partial\mathcal{B}_2} \bar{\boldsymbol{T}} \cdot \boldsymbol{\varphi}\, dx \quad (4.31) \\
\;=\;& \int_{\mathcal{B}} \big[W(\boldsymbol{F}) + P_{iJ}(\varphi_{i,J} - F_{iJ}) - \varrho_0 B_i \varphi_i\big]\, dx - \int_{\partial\mathcal{B}_1} P_{iJ} N_J (\varphi_i - \bar{\varphi}_i)\, dx \\
& - \int_{\partial\mathcal{B}_2} \bar{T}_i \varphi_i\, dx\,.
\end{aligned}
$$

The elastic minimum problem (4.17) is now replaced by the search for a stationary solution. Stationarity of $\Pi\big(\boldsymbol{\varphi}, \boldsymbol{F}, \boldsymbol{P}\big)$ demands

$$
\begin{aligned}
D\Pi\big(\boldsymbol{\varphi}, \boldsymbol{F}, \boldsymbol{P}\big) \cdot \boldsymbol{\eta} =& \\
& \int_{\mathcal{B}} \big[P_{iJ}\,\delta\varphi_{i,J} - \varrho_0 B_i\,\delta\varphi_i\big]\, dx - \int_{\partial\mathcal{B}_1} P_{iJ} N_J\,\delta\varphi_i\, dx - \int_{\partial\mathcal{B}_2} \bar{T}_i\,\delta\varphi_i\, dx = 0 \quad (4.32)
\end{aligned}
$$

for all $\boldsymbol{\eta} \in \mathcal{U}_0$, and

$$
\begin{aligned}
D\Pi\big(\varphi, \boldsymbol{F}, \boldsymbol{P}\big) \cdot \delta\boldsymbol{P} =& \\
& \int_{\mathcal{B}} \big[W(\boldsymbol{F}) + P_{iJ}(\varphi_{i,J} - F_{iJ}) - \varrho_0 B_i \varphi_i\big]\, dx - \int_{\partial\mathcal{B}_1} P_{iJ} N_J (\varphi_i - \bar{\varphi}_i)\, dx = 0, \quad (4.33)
\end{aligned}
$$

$$
D\Pi\big(\boldsymbol{\varphi}, \boldsymbol{F}, \boldsymbol{P}\big) \cdot \delta\boldsymbol{F} = \int_{\mathcal{B}} \big[W_{,F_{iJ}}(\boldsymbol{F}) + P_{iJ}\big] \delta F_{iJ}\, dx = 0.
$$
$$(4.34)$$

This is the weak restatement of the field equations and boundary conditions (4.4–4.6).

The special appeal of multi-field principles in the context of finite element approximation is that it allows the independent interpolation of functions with different ansatz spaces, i.e., for mixed finite element formulations. A classical two-field form is the **Hellinger-Reissner principle**, where the displacements $\boldsymbol{u}$ and the infinitesimal stresses $\boldsymbol{\sigma}$ (or the corresponding finite deformation functions) are related independently. A typical three-field functional is the stated Hu-Washizu principle. Other forms involve, e.g., displacements, pressure and the Jacobian of deformation to treat incompressible constitutive laws numerically. The use of the Hu-Washizu principle to formulate mixed finite elements was pioneered by Simo [303]. We will apply it later for finite element formulation.

4.4. Dynamical problems

By nature dynamical problems cannot have a "stable equilibrium" configuration. Consequently no general energy minimum principle can be established to solve the corresponding initial value problems. However, variational principles can be generalized to continuum dynamics by establishing functionals in *position* and *time*.

Assume the Lagrangian density to be of the form

$$\frac{1}{2}\rho_0 V_i V_i - W(\boldsymbol{F}) \tag{4.35}$$

where $\boldsymbol{V}$ is the material velocity, $\rho_0(\boldsymbol{X})$ is the mass density in the undeformed configuration and $W(\boldsymbol{F})$ is the strain energy density. Equivalently, the **Lagrangian** scalar-valued functional[2] can be stated in global form to read

$$\mathcal{L}(\boldsymbol{\varphi}, \dot{\boldsymbol{\varphi}}) = \int_{\mathcal{B}} \frac{1}{2} \varrho_0 |\dot{\boldsymbol{\varphi}}|^2 \, dV - \Pi(\boldsymbol{\varphi}) \tag{4.36}$$

where the first term represents the kinetic energy of the moving elastic body and $\Pi(\boldsymbol{\varphi})$ is the potential energy (4.16).

The motions of the solid can be characterized by recourse to the principle of stationary action. The **action of a motion** within a closed time interval $t \in [t_1, t_2]$ is defined as

$$\mathcal{I}[\boldsymbol{\varphi}] = \int_{t_1}^{t_2} \left\{ \int_{\mathcal{B}} (\mathcal{L} + \rho_0 \bar{\boldsymbol{B}} \cdot \boldsymbol{\varphi}) dV + \int_{\partial \mathcal{B}_2} \bar{\boldsymbol{T}} \cdot \boldsymbol{\varphi} dS \right\} dt. \tag{4.37}$$

The deformation may be required to take on prescribed values over the undeformed displacement boundary $\partial \mathcal{B}_1$,

$$\varphi_i = \bar{\varphi}_i(\boldsymbol{X}, t), \tag{4.38}$$

and it is presumed to be known at times t_1 and t_2. A variational approach known as **Hamilton's principle** requires the motion of the elastic body to optimize the action integral. Stationarity of $\mathcal{I}[\boldsymbol{\varphi}]$ demands the first variation of (4.37) to vanish, i.e.,

$$\delta \mathcal{I}[\boldsymbol{\varphi}] = 0, \tag{4.39}$$

where

$$\delta \mathcal{I}[\boldsymbol{\varphi}] \equiv \left[\frac{d}{d\epsilon} \mathcal{I}[\boldsymbol{\varphi} + \epsilon \boldsymbol{\eta}] \right]_{\epsilon=0} \tag{4.40}$$

---

[2]Please do not confuse with the Lagrangian function of Section 4.2.

for all admissible virtual displacements $\boldsymbol{\eta} \in \mathcal{U}_0$. A straightforward calculation gives

$$\delta\mathcal{I}[\boldsymbol{\varphi}] = \int_{\mathcal{B}}[\rho_0 V_i\eta_{i,t} - P_{iJ}\eta_{i,J} + \rho_0\bar{B}_i\eta_i]dV + \int_{\partial\mathcal{B}_2}\bar{T}_i\eta_i dS = 0 \qquad (4.41)$$

where, again, $P_{iJ} = \partial W/\partial F_{iJ}$ is the first Piola-Kirchhoff stress tensor. From this statement it follows that motions of the solid must satisfy the Euler-Lagrange equations

$$\rho_0 V_{i,t} - P_{iJ,J} = \rho_0 B_i, \qquad \text{in } \mathcal{B} \;, \qquad (4.42)$$
$$P_{iJ}N_J = \bar{T}_i, \qquad \text{on } \partial\mathcal{B}_2 \;, \qquad (4.43)$$

which are the balance of momentum equations and the natural (traction) boundary conditions.

However, if instead of the deformation mapping $\boldsymbol{\varphi}$ (4.38), the initial and final **velocity fields** are required to take on prescribed values at times t_1 and t_2,

$$V_i(\boldsymbol{x}, t_1) = V_i^{(1)}(\boldsymbol{X}), \qquad V_i(\boldsymbol{x}, t_2) = V_i^{(2)}(\boldsymbol{X}), \qquad (4.44)$$

then the virtual displacements $\boldsymbol{\eta}(\boldsymbol{X}, t_1)$ and $\boldsymbol{\eta}(\boldsymbol{X}, t_2)$ are unconstrained and the action integral has to be modified to read

$$\mathcal{I}[\boldsymbol{\varphi}] = \int_{t_1}^{t_2} \left\{ \int_{\mathcal{B}} (\mathcal{L} + \rho_0\boldsymbol{B} \cdot \boldsymbol{\varphi})\, dV + \int_{\partial\mathcal{B}_2} \bar{\boldsymbol{T}} \cdot \boldsymbol{\varphi}\, dS \right\} dt$$
$$+ \int_{\mathcal{B}} \rho_0[V_i^{(1)}(\boldsymbol{X})\varphi_i(\boldsymbol{X}, t_1) - V_i^{(2)}(\boldsymbol{X})\varphi_i(\boldsymbol{X}, t_2)]\, dV \;. \quad (4.45)$$

Stationarity of the action (4.45) now returns (4.44) as natural boundary conditions.

Hamilton's principle of stationary action can alternatively be formulated to result in the well known **Lagrange equations** of structural mechanics [114],

$$\frac{d}{dt}\frac{\partial\mathcal{L}}{\partial\dot{\boldsymbol{q}}} - \frac{\partial\mathcal{L}}{\partial\boldsymbol{q}} = 0, \qquad (4.46)$$

where we write the mechanical system on Euclidean space using vector notation $\boldsymbol{q}, \dot{\boldsymbol{q}} \in \mathbb{R}^n$.

5. Numerical Solution Techniques

Clearly, the variational principles stated in the preceding can be solved analytically only in very rare cases. Numerical solution techniques, however, allow for the solution of rather complex problems. As the finite element method is used to map a continuous mechanical system into a discrete system, time integration schemes are necessary to translate a continuous dynamical process into a step-by-step phenomenon. Starting with the latter we will summarize in this Chapter the employed methods of space and time discretization and explain how they preserve a variational structure.

5.1. Temporal discretization

In the following we consider a Lagrangian of the usual kinetic minus potential energy form (4.35). Using vector-matrix notation we write

$$\mathcal{L}(\boldsymbol{q}, \dot{\boldsymbol{q}}) = \frac{1}{2}\dot{\boldsymbol{q}}^\top \boldsymbol{M}\dot{\boldsymbol{q}} - \Pi(\boldsymbol{q}) \,, \tag{5.1}$$

where $\boldsymbol{q}, \dot{\boldsymbol{q}} \in \mathbb{R}^n$ denote general coordinates and their time derivative, $\boldsymbol{M}$ is a constant symmetric and positive definite mass matrix, and $\Pi(\boldsymbol{q})$ is a given potential energy. Optimizing this energetic expression gives the the corresponding Euler-Lagrange equations which are known to be

$$\boldsymbol{M}\ddot{\boldsymbol{q}} = -D_{,q}\,\Pi(\boldsymbol{q}). \tag{5.2}$$

The most widely used time-stepping algorithms in nonlinear structural dynamics are the algorithm of the Newmark family [244]; general references are [31, 159, 376]. The **Newmark algorithms** are usually written in the following way:
For given $(\boldsymbol{q}_k, \dot{\boldsymbol{q}}_k)$ approximate $(\boldsymbol{q}_{k+1}, \dot{\boldsymbol{q}}_{k+1})$ by

$$\boldsymbol{q}_{k+1} = \boldsymbol{q}_k + \Delta t\dot{\boldsymbol{q}}_k + \frac{\Delta t^2}{2}\Big((1-2\beta)\boldsymbol{a}_k + 2\beta\boldsymbol{a}_{k+1}\Big) \tag{5.3}$$

$$\dot{\boldsymbol{q}}_{k+1} = \boldsymbol{q}_k + \Delta t\big((1-\gamma)\boldsymbol{a}_k + \gamma\boldsymbol{a}_{k+1}\big), \tag{5.4}$$

where β and γ are real numbers between zero and one, and we abbreviate

$$\boldsymbol{a}_k = \boldsymbol{M}^{-1}\big(-D_{,q}\,\Pi(q_k)\big). \tag{5.5}$$

The values of β and γ are directly linked to accuracy and stability of **Newmark's algorithm**. We recall that the integration scheme is second order accurate if and only if $\gamma = 1/2$, otherwise it is only consistent (first order accurate). Thus, one usually chooses $\gamma = 1/2$. (Numerical dissipation may be added in choosing $\gamma > 1/2$.)

The choice of $\beta = 1/4$, $\gamma = 1/2$ leads to a constant average acceleration. This corresponds to a trapezoidal rule and is an unconditionally stable implicit scheme (in linear analyzes).

Moreover, if $\beta = 0$ then equation (5.3) becomes an explicit equation for $\boldsymbol{q}_{k+1}$ in terms of $(\boldsymbol{q}_k, \dot{\boldsymbol{q}}_k)$, so that the case $\beta = 0$, $\gamma = 1/2$, is known as **explicit Newmark** or, equivalently, central difference scheme.

Irritating at first glance but meanwhile established knowledge is the fact that all of the implicit members of the Newmark family are not designed to conserve energy and also fail to conserve momentum [64]; only the central difference scheme, $\beta = 0$, $\gamma = 1/2$, preserves momentum, see [64, 63] or as well [131, 180].
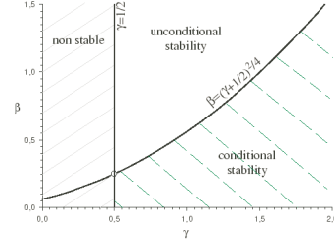
Detailed analyzes of the Newmark algorithm, its stability and energy preserving properties (for linear systems and $\beta = 1/4$) were first provided by Hughes [157, 160]. We

Figure 5.1.: Newmark's parameter.

will proceed here by illuminating the variational structure of Newmarks algorithms following the ideas in [174, 175, 192]. The goal is to show that the Newmark scheme for conservative mechanical systems is variational, and to discuss some of the implications of this fact.

5.1.1. Variational structure of the time integration

The variational nature of the Newmark's scheme and its performance is of particular interest because of its widespread use in finite element codes. Cases in which one has a minimum problem to solve can be used to derive error estimates and mesh optimization techniques. Variational schemes are known to preserve conserved quantities such as linear and angular momentum associated with symmetries provided the discrete Lagrangian has these symmetries. For a given a **displacement space** Q, a **discrete**

Lagrangian is a map $\mathcal{L}_d : Q \times Q \mapsto R$. In practice, a discrete Lagrangian is obtained by approximating the action function associated with a given continuous Lagrangian. The time step information will be contained in $\mathcal{L}_d$ and we regard $\mathcal{L}_d$ as a function of two nearby points $(\boldsymbol{q}_k, \boldsymbol{q}_{k+1}) \in Q \times Q$.

Consider a continuous Lagrangian $\mathcal{L}$ of the standard form (4.35) or (5.1), respectively. Then an associated discrete Lagrangian can be defined by

$$\mathcal{L}_d^\alpha(\boldsymbol{q}_k, \boldsymbol{q}_{k+1}) = \Delta t \, \mathcal{L}\Big((1 - \alpha)\boldsymbol{q}_k + \alpha\boldsymbol{q}_{k+1}, \frac{\boldsymbol{q}_{k+1} - \boldsymbol{q}_k}{\Delta t}\Big), \tag{5.6}$$

where $\Delta t \in R^+$ is the time step and $\alpha \in [0, 1]$ is an interpolation parameter. Using the form of (5.1), this becomes

$$\mathcal{L}_d^\alpha(\boldsymbol{q}_k, \boldsymbol{q}_{k+1}) = \frac{\Delta t}{2}\Big(\frac{\boldsymbol{q}_{k+1} - \boldsymbol{q}_k}{\Delta t}\Big)^\top \boldsymbol{M}\Big(\frac{\boldsymbol{q}_{k+1} - \boldsymbol{q}_k}{\Delta t}\Big) - \Delta t \, \Pi\big((1 - \alpha)\boldsymbol{q}_k + \alpha\boldsymbol{q}_{k+1}\big). \tag{5.7}$$

Another choice of a discrete Lagrangian is a *symmetric version* of expression (5.6) defined by

$$\begin{aligned}
\mathcal{L}_d^{\alpha,sym}(\boldsymbol{q}_k, \boldsymbol{q}_{k+1}) = {}& \frac{\Delta t}{2}\mathcal{L}\Big((1 - \alpha)\boldsymbol{q}_k + \alpha\boldsymbol{q}_{k+1}, \frac{\boldsymbol{q}_{k+1} - \boldsymbol{q}_k}{\Delta t}\Big) \\
& + \frac{\Delta t}{2}\mathcal{L}\Big(\alpha\boldsymbol{q}_k + (1 - \alpha)\boldsymbol{q}_{k+1}, \frac{\boldsymbol{q}_{k+1} - \boldsymbol{q}_k}{\Delta t}\Big),
\end{aligned} \tag{5.8}$$

where, once again, $\Delta t \in R^+$ and $\alpha \in [0, 1]$.

We note that the discrete analog of the action integral (4.37) is the **action sum**. The action sum is defined by

$$\mathcal{I}_d = \sum_{k=0}^{N-1} \mathcal{L}_d(\boldsymbol{q}_k, \boldsymbol{q}_{k+1}) \tag{5.9}$$

where $\boldsymbol{q}_k \in Q$ and for a positive integer N. An **discrete variational principle** now states that the evolution equations extremize the action sum with given fixed end points, $\boldsymbol{q}_0$ and $\boldsymbol{q}_N$. Extremizing $\mathcal{I}_d$ over $\boldsymbol{q}_1, \cdots, \boldsymbol{q}_{N-1}$ leads to the **discrete Euler-Lagrange equations**

$$D_{,1}\mathcal{L}_d(\boldsymbol{q}_{k+1}, \boldsymbol{q}_{k+2}) + D_{,2}\mathcal{L}_d(\boldsymbol{q}_k, \boldsymbol{q}_{k+1}) = 0 \qquad \text{for all } k = 0, \cdots, N-1, \tag{5.10}$$

where $D_{,1}\mathcal{L}_d$ and $D_{,2}\mathcal{L}_d$ denote the derivative of $\mathcal{L}_d$ with respect to its first and second slot, respectively. For the symmetric discrete Lagrangian (5.8) the corresponding discrete

Euler-Lagrange equations have a symmetric form,

$$\frac{1}{\Delta t^2}(\boldsymbol{q}_{k+2} - 2\boldsymbol{q}_{k+1} + \boldsymbol{q}_k) =$$
$$\frac{1}{2}(1-\alpha)\boldsymbol{a}_{k+1+\alpha} + \frac{1}{2}\alpha\boldsymbol{a}_{k+2-\alpha} + \frac{1}{2}\alpha\boldsymbol{a}_{k+\alpha} + \frac{1}{2}(1-\alpha)\boldsymbol{a}_{k+1-\alpha}, \quad (5.11)$$

where we use for abbreviation

$$\boldsymbol{a}_{k+\alpha} := \boldsymbol{M}^{-1}\big[-D_{,q}\Pi((1-\alpha)\boldsymbol{q}_k + \alpha\boldsymbol{q}_{k+1})\big]. \quad (5.12)$$

These equations define a second-order accurate, implicit algorithm for any parameter α. Both algorithms, derived from $\mathcal{L}_d^\alpha$ and $\mathcal{L}_d^{\alpha,sym}$, respectively, preserve the associated discrete symplectic form and the discrete momentum map. (By proper choice of α these two algorithms even recover schemes known elsewhere under different names, cf. [175]).

Now we exemplarily show that **Newmark is variational** with the well known case when $\beta = 0$ and $\gamma = 1/2$, i.e., the explicit Newmark. The explicit Newmark algorithm is the same as the variational algorithm, (5.11), derived from $\mathcal{L}_d^{\alpha,sym}$ with $\alpha = 0$ or $\alpha = 1$. To prove this, we write the algorithm (5.11) in the form

$$\boldsymbol{q}_{k+1} = \boldsymbol{q}_k + \Delta t\dot{\boldsymbol{q}}_k + \frac{\Delta t^2}{2}\big((1-\alpha)\boldsymbol{a}_{k+\alpha} + \alpha\boldsymbol{a}_{k+1-\alpha}\big) \quad (5.13)$$

$$\dot{\boldsymbol{q}}_{k+1} = \dot{\boldsymbol{q}}_k + \Delta t\big(\frac{1}{2}\boldsymbol{a}_{k+\alpha} + \frac{1}{2}\boldsymbol{a}_{k+1-\alpha}\big). \quad (5.14)$$

Now, substituting the specified parameters into the equations (5.3) and (5.4), and into (5.13) we see that in both cases we obtain

$$\boldsymbol{q}_{k+1} = \boldsymbol{q}_k + \Delta t\dot{\boldsymbol{q}}_k + \frac{\Delta t^2}{2}\boldsymbol{a}_k \quad (5.15)$$

$$\dot{\boldsymbol{q}}_{k+1} = \dot{\boldsymbol{q}}_k + \Delta t\boldsymbol{a}_{k+1/2} \quad (5.16)$$

and thus we have equivalence.

Kane et al. analysed in [175] a more general class of Newmark algorithms and considered their action upon a general nonlinear system. By the variational nature of the Newmark algorithm it can be shown that for $\gamma = 1/2$ and $\beta = 1/4$ the Newmark trajectory will be shadowed by a variational trajectory, and vice versa. That means, there is some parameter α so that each point $\boldsymbol{x}_k$ of the Newmark trajectory is equal to the interpolation $(1-\alpha)\boldsymbol{q}_k + \alpha\boldsymbol{q}_{k+1}$ of two points $\boldsymbol{q}_k, \boldsymbol{q}_{k+1}$ of the variational trajectory. In other words, one can regard the 'shadowing' of trajectories as an implicitly defined nonlinear coordinate change and we have that the Newmark scheme and variational algorithms are simply the coordinate transformed versions of each other.

Moreover, it was established in [175] that any Newmark algorithm with $\gamma = 1/2$ is directly variational. The technique to do so is by proving that the Newmark method with $\gamma = 1/2$ and any β gives the discrete Euler-Lagrange equations for some (specially defined) discrete Lagrangian.

These results may be interpreted in different ways. First, one can consider the Newmark and variational schemes to be essentially the same, but only the variational method has the right form to exactly conserve the momenta. A second interpretation is to realize that the Newmark schemes will exactly preserve momenta and a symplectic form, except they will not be quite the obvious ones. It is possible to derive expressions for these momenta and the non-canonical symplectic form conserved by Newmark (but the expressions can be rather unhandy). More useful than actually finding these exactly conserved structures is to use them to conclude the following: For sufficiently small time steps Δt, a regular value of the momentum, and presuming that the solution computed by the Newmark algorithm (5.3–5.4) with $\gamma = 1/2$ are bounded for all time, then the solution will have bounded momentum error, uniformly for all time, and the error will tend to zero as Δt tends to zero.

Note that above remarks in no way guarantee stability of the Newmark method for large time steps. The focus was here on a geometric analysis for nonlinear systems to get results on structure preservation. All the results apply only for some (system dependent) bound on the timestep. Consistent with this, it is also known that the Newmark method can perform badly on some nonlinear systems with moderately large time steps, and it is certainly not unconditionally stable, [157, 160]. This is a reflection of the short time numerical stability behavior of the Newmark scheme, rather than the geometric structure. In practice, of course, one must consider both the numerical accuracy and stability of an integration scheme, as well as its structure preserving qualities.

5.1.2. Minimization structure of the Newmark algorithm

Next we consider a different way of writing the Newmark algorithm as an optimization method following a strategy of [192]. This is particularly useful in order to derive algorithms for dissipative or forced systems, so we include dissipative forces in the formulation here. Let us consider a set of equations of motion of the form:

$$\boldsymbol{M}\ddot{\boldsymbol{q}} + \boldsymbol{f}^{int}(\boldsymbol{q}, \dot{\boldsymbol{q}}) = \boldsymbol{f}^{ext}(t) \tag{5.17}$$

with $\boldsymbol{q}(t) \in \mathbb{R}^n$, and where we regard $\boldsymbol{f}^{ext}(t)$ as a given external force. As for the internal force, we postulate the existence of a conservative potential $\Pi(\boldsymbol{q})$ and a dissipative

potential $R(\boldsymbol{q}, \dot{\boldsymbol{q}})$ such that

$$\boldsymbol{f}^{int}(\boldsymbol{q}, \dot{\boldsymbol{q}}) = \frac{\partial \Pi(\boldsymbol{q}, \dot{\boldsymbol{q}})}{\partial \boldsymbol{q}} + \frac{\partial R(\boldsymbol{q}, \dot{\boldsymbol{q}})}{\partial \dot{\boldsymbol{q}}}. \tag{5.18}$$

Dissipative potentials of this sort are sufficiently general to cover the typical applications of continuum mechanics. Clearly, if with $R = 0$ the energy conserving system is recovered. We now discretize the equations of motion using the Newmark scheme in the following way:

$$\boldsymbol{q}_{k+1} = \boldsymbol{q}_k + \Delta t \dot{\boldsymbol{q}}_k + \frac{\Delta t^2}{2}\Big((1 - 2\beta)\boldsymbol{a}_k + 2\beta\boldsymbol{a}_{k+1}\Big) \tag{5.19}$$

$$\boldsymbol{M}\boldsymbol{a}_{k+1} + \boldsymbol{f}_{k+1}^{int} = \boldsymbol{f}_{k+1}^{ext} \tag{5.20}$$

$$\dot{\boldsymbol{q}}_{k+1} = \boldsymbol{q}_k + \Delta t\big((1 - \gamma)\boldsymbol{a}_k + \gamma\boldsymbol{a}_{k+1}\big). \tag{5.21}$$

By defining an explicitly formulated predictor function

$$\boldsymbol{q}_{k+1}^{pre} = \boldsymbol{q}_k + \Delta t \dot{\boldsymbol{q}}_k + \frac{\Delta t^2}{2}\Big((1 - 2\beta)\boldsymbol{a}_k\Big) \tag{5.22}$$

the first equation in (5.19–5.21) can be written as

$$\boldsymbol{q}_{k+1} = \boldsymbol{q}_{k+1}^{pre} + \beta \Delta t^2 \boldsymbol{a}_{k+1}. \tag{5.23}$$

To close this set of equations we need a relation between $\boldsymbol{f}_{k+1}^{int}$ and $\boldsymbol{q}_{k+1}$. To this end, we introduce the effective incremental potential

$$\Pi_k(\boldsymbol{q}_{k+1}) = \Pi(\boldsymbol{q}_{k+1}) + \Delta t\, R\Big((\boldsymbol{q}_{k+\lambda}), \frac{\boldsymbol{q}_{k+1} - \boldsymbol{q}_k}{\Delta t}\Big), \tag{5.24}$$

where

$$\boldsymbol{q}_{k+\lambda} = (1 - \lambda)\boldsymbol{q}_k + \lambda\boldsymbol{q}_{k+1}, \qquad \lambda \in [0, 1]. \tag{5.25}$$

The internal forces are given by

$$\boldsymbol{f}_{k+1}^{int} = \frac{\partial \Pi_k(\boldsymbol{q}_{k+1})}{\partial \boldsymbol{q}_{k+1}} \tag{5.26}$$

which is consistent with (5.18) as $\Delta t \to 0$ for any choice of λ.

The above algorithm can be recast by combining (5.19) and (5.20) to get

$$\boldsymbol{M}\frac{\boldsymbol{q}_{k+1} - \boldsymbol{q}_{k+1}^{pre}}{\Delta t^2} + \beta \boldsymbol{f}_{k+1}^{int} = \beta \boldsymbol{f}_{k+1}^{ext}. \tag{5.27}$$

Note that this is the Euler-Lagrange equation of the following functional

$$f(\boldsymbol{q}_{k+1}) = \frac{1}{2\Delta t^2}\left(\boldsymbol{q}_{k+1} - \boldsymbol{q}_{k+1}^{pre}\right)^\top \boldsymbol{M}\left(\boldsymbol{q}_{k+1} - \boldsymbol{q}_{k+1}^{pre}\right) + \beta\Pi_k(\boldsymbol{q}_{k+1}) - \beta f^{ext} \cdot \boldsymbol{q}_{k+1}. \quad (5.28)$$

Under appropriate convexity conditions on the potentials Π and R, the updated configuration follows as the solution of the minimum principle:

$$\min_{\boldsymbol{q}_{k+1}} f(\boldsymbol{q}_{k+1}). \quad (5.29)$$

Once $\boldsymbol{q}_{k+1}$ is determined, the internal forces can be computed from (5.26) and subsequently the velocities are updated using (5.21).

Note that the minimization (5.29) operates on the non-explicit part of Newmark's algorithm. Thus, it can be regarded as a two step procedure: first one computes the predictor point by an explicit formula and then, secondly, one corrects this with the minimization principle[1]. In the case of conservative systems (systems without external forces or dissipative potentials) this scheme is literally the Newmark scheme for conservative systems, which, as we have shown above, is equivalent to a variational scheme. Consequently, the introduced scheme has both, it is variational and it obeys a minimum principle.

5.2. Spatial discretization

5.2.1. Triangulation of a body

To analyze the motion, deformation and constitution of general solids we are impelled to employ (piecewise) polynomial interpolation techniques, in particular, the finite element method. Such techniques employ conveniently generated, finite dimensional interpolation spaces basing on a **triangulation** (meshing) of the domain of analysis. In that sense a body is a triangulable set $\mathcal{T} \subset \mathbb{R}^d$, i.e., the body can be represented by a collection of (non-degenerate) elements T. We presume that the solid occupies a Lipschitz domain $\Omega \subset \mathbb{R}^d$ $(d = 1, 2, 3)$ with boundary $\partial\Omega$. Lipschitz domains are locally on one side of their boundary and their boundary is represented by a Lipschitz-continuous function. A mapping $\boldsymbol{\varphi} : \mathbb{R}^d \to \mathbb{R}^d$ is Lipschitz continuous with constant $C > 0$ if

$$|\boldsymbol{\varphi}(x_1) - \boldsymbol{\varphi}(x_2)| \leq C \, \|x_1 - x_2\| \quad (5.30)$$

---

[1]This use of the term *predictor* is special to this formulation. The term is used slightly differently in later sections.

for all $x_1, x_2 \in \mathbb{R}^d$. Let now $\mathtt{V} = \{\boldsymbol{x}_a, a = 0, \ldots, d\}$ be a collection of $d + 1$ points in $\mathbb{R}^d$. An **element** spanned by $\mathtt{V}$ is the set

$$T = \{\boldsymbol{x} = \sum_{a=1}^{d+1} \lambda_a \boldsymbol{x}_a, \ \ 0 \le \lambda_a \le 1, \ \ \sum_{a=1}^{d+1} \lambda_a = 1\}, \tag{5.31}$$

In other words, element $T \subset \mathcal{T}$ is the set of convex combinations of the vertex set $\mathtt{V}$. Elements in that sense are, e.g., a line segment ($d = 1$), a triangle ($d = 2$) and a tetrahedron ($d = 3$).

The triangulable sets defined by the strict definition (5.31) are polyhedra. Intuitively, we would like solids to be 'curved polyhedra' with a well-behaved boundary consisting of interconnected faces, edges and vertices. This may be achieved by (isoparametric) mapping techniques, some remarks on this can be found in the next paragraph. Also, quadrilateral or cubic elements are not included in the strict definition (5.31). However, most statements made below can be extended to other element shapes. For brevity we will restrict here on triangles and tetrahedrons which are sufficient to talk about the concepts of finite element analysis.

Given a point $\boldsymbol{x}$ in a d-dimensional element $T \subset \mathcal{T}$, the numbers λ_a in (5.31) are the **barycentric coordinates** of $\boldsymbol{x}$. They follow from a system of $d + 1$ equations

$$\sum_{a=1}^{d+1} \lambda_a \boldsymbol{x}_a \ = \ \boldsymbol{x} \qquad \text{and} \qquad \sum_{a=1}^{d+1} \lambda_a = 1, \tag{5.32}$$

or, expressed in matrix form

$$\boldsymbol{M}\boldsymbol{\lambda} = \boldsymbol{x}, \tag{5.33}$$

where we write $\boldsymbol{\lambda} = \{\lambda_1, \ldots, \lambda_{d+1}\}$, $\boldsymbol{x} = \{1, x_1, \ldots, x_d\}$ and $\boldsymbol{M}$ with $M_{(d+1)b} = 1$, $M_{ib} = x_{ib}$, $i = 1, \ldots, d$ and $b = 1, \ldots, (d+1)$. The element volume is given by

$$|T| = \frac{1}{d!} |\det(\boldsymbol{M})|. \tag{5.34}$$

An element is said to be **non-degenerate** if $\det(\boldsymbol{M}) \ne 0$, i.e., if it has a nonzero volume. Otherwise, the element is said to be degenerate.

5.2.2. Finite element polynomials

Generally spoken we are interested in approximating functions over their domains of definition by simpler or more convenient functions. Implicit in the notion of approximation is that the approximation function should be close to the original function in some

appropriate sense. In finite element analysis we are particularly interested in interpolating polynomials, i.e., in polynomials which coincide exactly with the function being approximated at selected points.

We begin by considering the case of linear interpolation. Let $p \in \mathcal{P}_1(T)$ be a linear polynomial over T. Then p is uniquely determined by its value at the vertices of T. With $n = d + 1$ we can write

$$p(\boldsymbol{x}) = \sum_{a=1}^{n} p(\boldsymbol{x}_a) N_a(\boldsymbol{x}), \tag{5.35}$$

where $\boldsymbol{N}_e(\boldsymbol{x}) \equiv \{N_a(\boldsymbol{x}), a = 1, \ldots, n\}$ is the collection of **nodal shape functions**. It follows from (5.32) that the barycentric coordinates coincide with the set of linear shape functions. The nodal shape function have the essential property of being one at their corresponding node and zero at all other nodes,

$$N_a(\boldsymbol{x}_b) = \begin{cases} 1 & \text{if } a = b \\ 0 & \text{otherwise.} \end{cases} \tag{5.36}$$

The concept can be transferred to higher order interpolation. The dimension of the set $\mathcal{P}_p(\mathbb{R}^d)$ of polynomials of degree less or equal to p in d independent variables is $n = \binom{d+p}{p}$. Representation (5.35) holds with the corresponding collection of nodal shape functions.

Example 5.1. *Triangular Elements.* A triangle is an element $T \in \mathbb{R}^2$ with area

$$A = \frac{1}{2} \det(\boldsymbol{M}). \tag{5.37}$$

The barycentric coordinates of a point $\boldsymbol{x}$ are defined by $\lambda_i = A_i/A$, where $A = \sum_{i=1}^{3} A_i$. With vertices at positions (x_{1k}, x_{2k}), $k = 1, 2, 3$, this may be written as,

$$\lambda_1(x_1, x_2) = \det \begin{pmatrix} 1 & 1 & 1 \\ x_1 & x_{12} & x_{13} \\ x_2 & x_{22} & x_{23} \end{pmatrix} \Big/ \det \begin{pmatrix} 1 & 1 & 1 \\ x_{11} & x_{12} & x_{13} \\ x_{21} & x_{22} & x_{23} \end{pmatrix}. \tag{5.38}$$

The equations for $\lambda_2(x_1, x_2)$ and $\lambda_3(x_1, x_2)$ follow likewise. The shape functions of a three-node **linear triangle** are

$$N_k = \lambda_k \qquad k = 1, 2, 3. \tag{5.39}$$

The shape functions for the six-node **quadratic triangle** ($p = 2$) follow as

$$
\begin{aligned}
N_1 &= \lambda_1 - \frac{1}{2}N_6 - \frac{1}{2}N_4 \\
N_2 &= \lambda_2 - \frac{1}{2}N_4 - \frac{1}{2}N_5 \\
N_3 &= \lambda_3 - \frac{1}{2}N_5 - \frac{1}{2}N_6 \\
N_4 &= 4\lambda_1\lambda_2 \\
N_5 &= 4\lambda_2\lambda_3 \\
N_6 &= 4\lambda_3\lambda_1
\end{aligned}
\tag{5.40}
$$

where the mid-side node numbers $4, 5, 6$ are on the element sides opposite to node $1, 2, 3$, respectively.

Example 5.2. *Tetrahedral Elements.* A tetrahedron is an element $T \in \mathbb{R}^3$ with volume

$$
V = \frac{1}{6}\det(\boldsymbol{M}).
\tag{5.41}
$$

For a tetrahedron with vertexes at positions x_{ik}, $i = 1, 2, 3$, $k = 1, 2, 3, 4$, equation (5.33) reads

$$
\begin{pmatrix}
1 & 1 & 1 & 1 \\
x_{11} & x_{12} & x_{13} & x_{14} \\
x_{21} & x_{22} & x_{23} & x_{24} \\
x_{31} & x_{32} & x_{33} & x_{34}
\end{pmatrix}
\begin{pmatrix}
\lambda_1 \\ \lambda_2 \\ \lambda_3 \\ \lambda_4
\end{pmatrix}
=
\begin{pmatrix}
1 \\ x_1 \\ x_2 \\ x_3
\end{pmatrix}
\tag{5.42}
$$

The barycenter of a unit tetrahedron is the point with $\boldsymbol{x} = (\frac{1}{4}, \frac{1}{4}, \frac{1}{4})$. The shape functions of a four-node **linear tetrahedron** coincide with the barycentric coordinates (which may be evaluated from (5.33)).

$$
N_k = \lambda_k \qquad k = 1, 2, 3, 4
\tag{5.43}
$$

The shape functions for the ten-node **quadratic tetrahedron** ($p = 2$) are given with

$$\begin{aligned}
N_1 &= \lambda_1 - \frac{1}{2}N_5 - \frac{1}{2}N_7 - \frac{1}{2}N_9 & (5.44) \\
N_2 &= \lambda_2 - \frac{1}{2}N_5 - \frac{1}{2}N_6 - \frac{1}{2}N_{10} \\
N_3 &= \lambda_3 - \frac{1}{2}N_6 - \frac{1}{2}N_7 - \frac{1}{2}N_8 \\
N_4 &= \lambda_4 - \frac{1}{2}N_8 - \frac{1}{2}N_9 - \frac{1}{2}N_{10} \\
N_5 &= 4\lambda_1\lambda_2 & (5.45) \\
N_6 &= 4\lambda_2\lambda_3 \\
N_7 &= 4\lambda_3\lambda_1 \\
N_8 &= 4\lambda_3\lambda_4 \\
N_9 &= 4\lambda_1\lambda_4 \\
N_{10} &= 4\lambda_2\lambda_4 \,,
\end{aligned}$$

where the numbering convention is the same as in Figure 5.2.

Isoparametric elements extend the simple element shapes presented in the foregoing in the sense that they allow for curved boundaries. Consider a standard domain $\hat{T}$ in the form of a d-dimensional element of unit dimension, (5.31), and let $\hat{\boldsymbol{N}}_e = \{\hat{N}_a, a = 1, \ldots, n\}$ be the standard polynomial shape functions of order p over $\hat{T}$. Within the isoparametric concept we use the nodal shape functions to set up a mapping $\boldsymbol{\eta} : \hat{T} \to \mathbb{R}^d$ and identify $T = \boldsymbol{\eta}(\hat{T})$ with the actual domain of the element. The general form of an isoparametric mapping is, therefore,

$$\boldsymbol{x} = \eta_i(\hat{\boldsymbol{x}}) = \sum_{a=1}^{n} x_{ia} \hat{N}_a(\hat{\boldsymbol{x}}) \qquad i = 1 \cdots d \qquad (5.46)$$

where $\{\boldsymbol{x}_a, \ a = 1, \ldots, n\}$ are the positions of the nodes of T in a global coordinate system. For elements in the sense (5.31) the mapping (5.46) defines an invertible affine mapping $\boldsymbol{\eta} : \hat{T} \to T$. For more general elements the mapping (5.46) is usually nonlinear. However, we still require $\boldsymbol{\eta}$ to be one-to-one.

The introduction of an isoparametric mapping has the important consequence of reducing the computation of integrals over the element domains to integrals over standard domains, thus facilitating the use of quadrature rules. The Gauss-point coordinates for numerical integration within triangle and tetrahedral domains can be found in [98] and [165], respectively. The isoparametric concept is quite general and applies to all types of elements which fulfill condition (5.36). We will not go further into detail here but refer

to the standard literature [20, 47, 143, 298, 390]. Other methods of geometrical mapping are described, e.g., in [130, 361, 317].

5.2.3. Finite elements based on the Hu-Washizu principle

Next we introduce a 10-node tetrahedral element where the relation between displacements and deformations is enforced weakly by recourse to the Hu–Washizu principle, cf. Section 4.3. The element arrays are formulated in accordance with the 'assumed-strain' prescription, see, e.g., [158, 377]. Camacho and Ortiz described in [70] a triangular element constructed by assembling linear subtriangles and coupling them to a continuous linear strain field. The assemblage of the tetrahedral element is analogous, the formulation was numerically analyzed in [332].
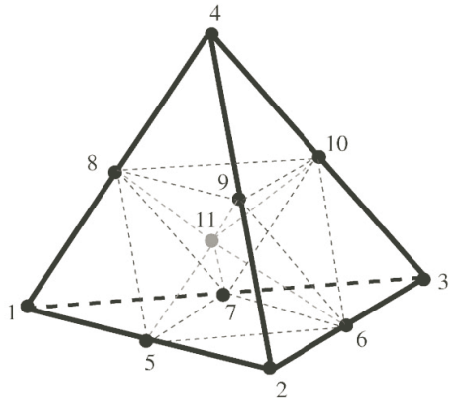
Figure 5.2.: Tetrahedral element.

This so-called **composite element** consists of 12 four-node (linear) sub-elements, Figure 5.2, each of which is equipped with linear displacement interpolation. To ensure that the element possesses all the expected symmetries (in its regular tetrahedral configuration) an auxiliary 11th node is introduced in the barycenter. Note that the element edges need not to be straight. Consequently, the displacements are interpolated in a piecewise linear manner. Independently of the displacement interpolation, an 'assumed' linear representation of the deformation and stress fields with shape functions (5.43) is adopted. Evidently the assumed deformations are not the gradients of the interpolated deformation mapping nor follow the assumed stresses from an application of the constitutive relations. Instead, these relations are enforced weakly in the sense of equations (4.31–4.34)[2]. The resulting tetrahedral element may be obtained from the standard displacement element in Section 5.2.2 by formally replacing the gradients of the material shape function (5.44), $N_{k,J}$, by the array

$$\sum_{b=1}^{4}\sum_{c=1}^{4}\lambda_c\Big[\int_T \lambda_b\lambda_c dV\Big]^{-1}\Big[\int_T \lambda_b N_{k,J}dV\Big] \tag{5.47}$$

where once again λ_i denotes the barycentric coordinates. This substitution can be made at the shape-function routine level, and the remaining structure of the element routine is

---

[2]For the technical details we refer to [332], we summarize here only the resulting shape functions.

identical to that of the displacement finite element. This implementation is in the spirit of Hughes' $\bar{\boldsymbol{B}}$ method for linear elasticity [158], in which the discrete strain operator, or $\boldsymbol{B}$–matrix, is replaced by an assumed matrix $\bar{\boldsymbol{B}}$ in the strain energy density.

The advantages of such an element type arise primarily in explicit time integration and contact-impact problems, where the lumped mass of its mid-side nodes is well matched to its corner node masses. This feature effectively overcomes the difficulties inherent to quadratic tetrahedral elements, for which the row-sum method of lumping (cf., e.g., [390]) results in zero or negative corner masses. Furthermore, the volumetric locking which characterizes linear elements is eliminated. Thus, the composite element appears to combine the best attributes of linear and quadratic tetrahedral elements (including the ease of mesh generation) without their drawbacks. The convergence rates of this element formulation is comparable to those of linear elements.

5.2.4. Local and global interpolation error bounds

In the preceding section we addressed the problem of interpolating a function $\boldsymbol{u}$ over a (spatial) triangulation using polynomials. In general, unless the function $\boldsymbol{u}$ happens to be a polynomial of degree less or equal to p, the interpolation $\boldsymbol{u}_h \in \mathcal{P}_p(\mathcal{T})$ is not exact. A measure of the size of the error function

$$\boldsymbol{e} = \boldsymbol{u} - \boldsymbol{u}_h \tag{5.48}$$

may be taken as an indicator of the quality of the interpolation. We expect this quality to improve when the element size decreases and when the polynomial order of interpolation increases.

The aim is now to obtain a local error estimate for the function (5.48), i.e., a measure of interpolation error over the element $T \in \mathcal{T}$. The strategy to apply is to reduce the problem to a standard domain $\hat{T}$, e.g., a unit triangle, and then use the relations between norms on affine-equivalent domains. If $\boldsymbol{u}_h \in \mathcal{P}_p^d(T)$ interpolates a function $\boldsymbol{u} : T \to \mathbb{R}^d$ over T, then $\hat{\boldsymbol{u}}_h$ is the unique polynomial of degree less or equal to p which interpolates $\hat{\boldsymbol{u}}$ over $\hat{T}$.[3]

We begin by defining some geometrical features. Let a domain $\Omega \in \mathbb{R}^d$ be bounded. The **size** h of Ω is the radius of its minimal circumsphere, i.e., $h = \frac{1}{2}\inf(\operatorname{diam}(S))$, where the infimum is taken over all balls S containing Ω. The **in-radius** ρ of Ω is the radius of its

---

[3]In Appendix 2.3 we introduce some linear spaces and norms naturally to use here. Throughout this section all definitions are given for scalar functions. The analogous definition for vector valued functions are obtained by applying the definition to each one of the components.

maximal inscribed sphere, i.e., $\rho = \frac{1}{2}\sup(\operatorname{diam}(S))$, where the supremum is taken over all balls S contained in Ω. The **aspect ratio** ς is the ratio of its size to its in-radius, i.e., $\varsigma = h/\rho$.

Let now Ω and $\hat{\Omega}$ be two affine-equivalent open subsets of $\mathbb{R}^d$. Let $\eta = \boldsymbol{B}\hat{\boldsymbol{x}} + \boldsymbol{b}$ be the affine mapping which maps Ω to $\hat{\Omega}$. In addition, let $u \in W^{m,p}(\Omega)$, $m \geq 0$; then $\hat{u} \in W^{m,p}(\hat{\Omega})$. We recall that a norm of a matrix $\boldsymbol{B} \in \mathbb{R}^{d \times d}$ is given by

$$\|\boldsymbol{B}\| = \sup_{\boldsymbol{x} \in \mathbb{R}^d/0} \frac{|\boldsymbol{B}\boldsymbol{x}|}{|\boldsymbol{x}|}. \tag{5.49}$$

Then, there are constants $C > 0$ and $\hat{C} > 0$ such that

$$|\hat{u}|_{m,p} \leq C \, \|\boldsymbol{B}\|^m |\det B|^{-1/2}|u|_{m,p}\,, \tag{5.50}$$

and

$$|\hat{u}|_{m,p} \leq \hat{C} \, \|\boldsymbol{B}^{-1}\|^m |\det B|^{-1/2}|\hat{u}|_{m,p}\,. \tag{5.51}$$

Proof. We begin with an identity that follows from the definition of the seminorm $|\cdot|_{m,p}$,

$$|u|_{m,p}^p = \int_{\hat{\Omega}} \sum_{|\alpha|=m} |D^\alpha \hat{u}|^p d\hat{x}, \tag{5.52}$$

where we write the partial derivatives of a function as (see Appendix 2.3)

$$D^\alpha u = \frac{\partial^{|\alpha|} u}{\partial x_1^{\alpha_1} \ldots \partial x_d^{\alpha_d}}. \tag{5.53}$$

By the equivalence between finite dimensional norms we have the inequalities

$$c|D^m \hat{u}(\hat{\boldsymbol{x}})|_2 \leq \left(\sum_{|\alpha|=m} |D^\alpha \hat{u}(\hat{\boldsymbol{x}})|^p \right)^{1/p} \leq C|D^m \hat{u}(\hat{\boldsymbol{x}})|_2\,, \tag{5.54}$$

where $|\cdot|_2$ is the Euclidian norm applied to m-order tensors over $\mathbb{R}^d$ and $C > 0$, $c > 0$ are constants. These inequalities give

$$|\hat{u}|_{m,p}^p \leq C \int_{\hat{\Omega}} |D^m \hat{u}|_2^p d\hat{x}. \tag{5.55}$$

Changing the domain of integration to Ω in turn yields

$$|\hat{u}|_{m,p}^p \leq C \int_{\Omega} |\boldsymbol{B}^m D^m u|_2^p \det(\boldsymbol{B})dx, \tag{5.56}$$

which by the properties of matrix norms reduces to

$$|\hat{u}|_{m,p}^p \leq C \|\boldsymbol{B}\|^{m \cdot p} \det(\boldsymbol{B}) \int_\Omega |D^m u|_2^p dx \, , \tag{5.57}$$

and by the equivalence between finite dimensional norms to

$$|\hat{u}|_{m,p}^p \leq C \|\boldsymbol{B}\|^{m \cdot p} \det(\boldsymbol{B}) \int_\Omega \Big(\sum_{|\alpha|=m} |D^\alpha u|^p \Big) dx. \tag{5.58}$$

The sought inequality finally follows by raising both sides to $1/p$. The reverse inequality (5.60) follows likewise. □

The norm $\|\boldsymbol{B}\|$ in (5.50) and (5.51) is to cumbersome to work with in practice. Therefore, it needs to be replaced by more easily computed geometric features. Again, let $\eta = \boldsymbol{B}\hat{\boldsymbol{x}} + \boldsymbol{b}$ be the affine mapping which maps Ω to $\hat{\Omega}$. Then, the following bounds hold

$$\|\boldsymbol{B}\| \leq \frac{h}{\hat{\rho}} \tag{5.59}$$

and

$$\|\boldsymbol{B}^{-1}\| \leq \frac{\hat{h}}{\rho} \, . \tag{5.60}$$

Proof. We have

$$\|\boldsymbol{B}\| = \sup_{\hat{\boldsymbol{x}}} \frac{|\boldsymbol{B}\hat{\boldsymbol{x}}|}{|\hat{\boldsymbol{x}}|} = \sup_{|\hat{\boldsymbol{x}}|=1} |\boldsymbol{B}\hat{\boldsymbol{x}}| = \frac{1}{\hat{\rho}} = \sup_{|\hat{\boldsymbol{x}}|=\hat{\rho}} |\boldsymbol{B}\hat{\boldsymbol{x}}|. \tag{5.61}$$

Choose now two vectors $\hat{\boldsymbol{y}}, \hat{\boldsymbol{z}} \in \hat{\Omega}$ in such a way that $|\hat{\boldsymbol{y}} - \hat{\boldsymbol{z}}| = \hat{\rho}$. Let $\boldsymbol{y} = \eta(\hat{\boldsymbol{y}})$ and $\boldsymbol{z} = \eta(\hat{\boldsymbol{z}})$. Then $\boldsymbol{y}, \boldsymbol{z} \in \Omega$ and $\boldsymbol{y} - \boldsymbol{z} = \boldsymbol{B}(\hat{\boldsymbol{y}} - \hat{\boldsymbol{z}})$, $|\boldsymbol{y} - \boldsymbol{z}| \leq h$, and

$$\|\boldsymbol{B}\| = \frac{1}{\hat{\rho}} |\boldsymbol{B}(\hat{\boldsymbol{y}} - \hat{\boldsymbol{z}})| = \frac{1}{\hat{\rho}} |\boldsymbol{y} - \boldsymbol{z}| \leq \frac{h}{\hat{\rho}}. \tag{5.62}$$

Bound (5.60) is proven likewise. □

Now, let $u \in W^{k+1,p}(T)$, $k \geq 1$, $1 \leq p \leq \infty$ and let $u_h \in \mathcal{P}_p(T)$ be the polynomial of degree less or equal to k which interpolates u on the element T. Let $0 \leq m \leq k$. Then, there is a constant $C > 0$ such that

$$|u - u_h|_{m,p} \leq C \frac{h^{k+1}}{\rho^m} |u|_{k+1,p}. \tag{5.63}$$

Proof. Introduce the constant

$$\frac{1}{\hat{C}} = \inf \frac{|\hat{e}|_{k+1,p}}{|\hat{e}|_{m,p}} , \tag{5.64}$$

where the infimum is taken over all the error functions $\hat{e} \in W^{k+1,p}(\hat{T})$ which vanish identically on $\hat{T}$. Provided that $m \leq k$, the inequality $\hat{C} < \infty$ follows from general results pertaining to eigenvalue problems for self-adjoint operators over compact domains [87, 73]. Now let $\hat{e} = \hat{u} - \hat{u}_h$ be the actual local error function. From the definition of $\hat{C}$, it follows that

$$|\hat{e}|_{m,p} \leq \hat{C}|\hat{e}|_{k+1,p} . \tag{5.65}$$

Using (5.50), (5.51), (5.59) and (5.60) the equation (5.65) becomes

$$|e|_{m,p} \leq \hat{C}\frac{\hat{h}^m}{\hat{\rho}^{k+1}}\frac{h^{k+1}}{\rho^m}|e|_{k+1,p}. \tag{5.66}$$

Define $C = \hat{C}\hat{h}^m/\hat{\rho}^{k+1}$ and note, since $u_h \in \mathcal{P}_p(T)$,

$$|e|_{k+1,p} = |u - u_h|_{k+1,p} = |u|_{k+1,p} . \tag{5.67}$$

Inserting (5.67) into (5.66) finally gives (5.63). □

In terms of the aspect ratio, the bound (5.63) may be recast as

$$|u - u_h|_{m,p} \leq C\varsigma^m h^{k+1-m}|u|_{k+1,p} , \tag{5.68}$$

Please note the structure of the right-hand side in (5.68). The norm $|u|_{k+1,p}$ measures the variation of the function u over T, h measures the size of the element and ς its distortion. Consequently it follows that the **accuracy of the interpolation** is expected to increase with the order k of the interpolation and to decrease with element distortion, and that the polynomial interpolation may be expected to be more accurate for functions which vary slowly over T, as expected.

The local (element-wise) error bounds derived in the foregoing may be stringed together in order to obtain **global error bounds**. To do so we denote by T a element in the triangulation $\mathcal{T}$, by h_T its size, by ρ_T its in-radius and by ς_T its aspect ratio. We refer to the **global element size** of the triangulation

$$h = \max_{T \in \mathcal{T}} h_T \tag{5.69}$$

and to the **global aspect ratio**

$$\varsigma = \max_{T \in \mathcal{T}} \varsigma_T. \tag{5.70}$$

The **global interpolant** of order k, $k \geq 1$, relative to the triangulation $\mathcal{T}$ is the function u_h whose restriction $u_{hT} \equiv u_h(T)$ to an element $T \in \mathcal{T}$ is the polynomial of degree less or equal to k which interpolate u over T. Let $u \in W^{m,p}(\Omega)$. Then there are constants $C > 0$ such that

$$|u - u_h|_{m,p}^p \leq \sum_{T \in \mathcal{T}} \left(C \varsigma_T^m h_T^{k+1-m} |u_T|_{k+1,p} \right)^p , \tag{5.71}$$

$$|u - u_h|_{m,p} \leq \sum_{T \in \mathcal{T}} C \varsigma_T^m h_T^{k+1-m} |u_T|_{k+1,p} , \tag{5.72}$$

and,

$$|u - u_h|_{m,p} \leq C \varsigma^m h^{k+1-m} |u|_{k+1,p} . \tag{5.73}$$

Proof. From the definition of the Sobolev seminorms we have

$$|u - u_h|_{m,p}^p \leq \sum_{|\alpha|=m} \int_\Omega |D^\alpha (u - u_h)|^p \, dx = \sum_{|\alpha|=m} \sum_{T \in \mathcal{T}} \int_T |D^\alpha (u_T - u_{hT})|^p \, dx. \tag{5.74}$$

Now apply the local error bound (5.63) to each of the terms in the sum, which results in (5.71). Raising both sides of this inequality to the power $1/p$ and using the Hölder's inequality gives (5.72). Replacing h_T by h, and ς_T by ς, in (5.71) gives

$$|u - u_h|_{m,p}^p \leq \left(C \varsigma^m h^{k+1-m} \right)^p \sum_{T \in \mathcal{T}} |u_T|_{k+1,p}^p = \left(C \varsigma^m h^{k+1-m} |u|_{k+1,p} \right)^p . \tag{5.75}$$

Finally, (5.73) is obtained by raising both sides of this inequality to $1/p$. $\qquad \square$

The global bound (5.73) provides conditions under which the finite element method converges. Presume that the method is C^{m-1}-conforming, so that the global interpolants u_h belong to $W^{m,p}(\Omega)$. Now, let $\mathcal{T}_h$, be a sequence of triangulations of Ω parameterized by a global mesh size $h \to 0$. Suppose that the triangulations are constructed by a process of regular refinement, so that the aspect ratios ς_h are uniformly bounded. (There is a $\varsigma < \infty$ such that $\varsigma_h < \varsigma$ for all h). Then, given $u \in W^{k+1,p}(\Omega)$ the inequality (5.73) ensures that $u_h \to u$ as $h \to 0$. The convergence is of order $O(h^{k+1-m})$ in the $W^{m,p}(\Omega)$-norm. Thus, the exponent $k + 1 - m$ defines the global **rate of convergence**. Clearly, in order to have convergent interpolants we must have $k + 1 - m > 0$, or $k \geq m$. This condition sets a lower bound on the order of interpolation.

The potential energy of an elastic body given by functional Π in (4.16) and the classical displacement finite element method may be regarded as the result of effecting a constrained minimization of the potential energy Π among all finite element deformation mappings. The global accuracy of such approximation is determined a priori by the

rate of convergence. Statements about the local accuracy, i.e., magnitude and distribution of the error of an analysis, can be derived by a posteriori error estimation, see [47, 48, 74, 87, 353] and others for the fundamental approaches. The author contributed to the subject, e.g., in [76, 77, 78, 358, 357].

While methods of error estimation and finite element mesh adaption for linear problems are well understood, their extensibility to the finite deformation range and to non-linear material laws is very limited. However, error controlled mesh adaption in non-linear analysis can be achieved by reducing the general dynamic problem to (a sequence of) equivalent static problems by recourse to time discretization. Then, the solution of the incremental boundary value problem obeys a minimum principle — provided that the constitutive updates are formulated variationally. Such minimum principles can be taken as a basis for error estimation by measuring the error of projection to finite element spaces.

6. Finite Plasticity

In this chapter we extend the solids to irreversible, i.e., plastic materials. Irreversibility may be invoked by many effects like time- and temperature-dependent plastic deformations, microstructural changes, creep, cavitation, damage etc.. Moreover, large elastic-plastic deformations of a solid require a finite theory of plasticity. To restrict the extend of this treatise to a readable amount we present here only the fundamentals of the classical von Mises plasticity extended to the finite range. For this theory, commonly named J_2-theory of plasticity, the basic equations and the variational constitutive update algorithm for a finite element analysis is outlined.

6.1. General framework

Following the decomposition rule (1.22) of Section 1 we now presume a multiplicative decomposition of the deformation gradient $\boldsymbol{F}$ into an elastic part $\boldsymbol{F}^e$ and a plastic part $\boldsymbol{F}^p$, [187].

$$\boldsymbol{F} = \boldsymbol{F}^e \boldsymbol{F}^p. \tag{6.1}$$

The underlying assumption is that the elastic deformations are related to stresses whereas the plastic deformations are local, they induce no long range stress. This implies that the elastic and thermal responses of the solid are structure insensitive, i.e., invariant under the internal processes. The assumption corresponds to elastic and thermal expansion moduli independent of the plastic straining and holds for a wide class of engineering materials.

We now proceed with the governing equations of the **deformation theory of plasticity**. This theory fits naturally in the frame of constitutive equations outlined in Chapter 3 and requires an associated theory of plasticity, i.e., the flow rule and the direction of plastic flow are derived from the same inelastic potential. To this end the existence of a **free energy function** $A(\boldsymbol{F}, T, \boldsymbol{Q})$ is postulated, where T denotes the absolute temperature and $\boldsymbol{Q}$ is a set of internal variables characterizing, e.g., hardening or damaging processes.

Assume that the elastic as well as the thermal responses of the solid are independent of the internal processes and the plastic deformations are local. Then the free energy may be decomposed additively

$$A(\boldsymbol{F}, T, \boldsymbol{Q}) = W^e(\boldsymbol{F}^e, T) + W^p(\boldsymbol{F}^p, \boldsymbol{Q}, T), \qquad (6.2)$$

where W^e denotes the elastic strain energy density and W^p is the stored energy of plastic work. Owing to material-frame indifference, the elastic strain energy density can only depend on $\boldsymbol{F}^e$ through the elastic part of the right-Cauchy Green deformation tensor $\boldsymbol{C}$, see Section 3.2.2 equation (1.36),

$$\boldsymbol{C}^e = \boldsymbol{F}^{eT}\boldsymbol{F}^e = \boldsymbol{F}^{p-1T}\boldsymbol{C}\,\boldsymbol{F}^{p-1}. \qquad (6.3)$$

This leads to a free energy (6.2) of the form

$$A(\boldsymbol{F}, \boldsymbol{F}^p, T, \boldsymbol{q}) = W^e(\boldsymbol{C}^e, T) + W^p(T, \boldsymbol{Q}, \boldsymbol{F}^p). \qquad (6.4)$$

To specify the evolution of the internal variables $\boldsymbol{Q}$ suitable kinetic equations are required. Assuming that the rate of the internal processes described by $\dot{\boldsymbol{Q}}$ is determined solely by the local thermodynamic state the general form of the kinetic equations is simply

$$\dot{\boldsymbol{Q}} = f(\boldsymbol{F}^p, \dot{\boldsymbol{F}}^p, \boldsymbol{Q}). \qquad (6.5)$$

In addition the rate of plastic deformation $\dot{\boldsymbol{F}}^p$ is subjected to the kinematic restrictions imposed by the flow rule.

6.2. J2-flow theory of plasticity

The plastic behavior of the material is assumed to obey von Mises theory of plasticity, (cf. [58, 199, 141, 303, 306]), extended to the finite deformation range. In particular, the plastic deformation is volume preserving, i.e., det $\boldsymbol{F}^p = 1$. Thus, the rate of plastic deformation is deviatoric and the flow rule reads in general form

$$\dot{\boldsymbol{F}}^{dev,p}\boldsymbol{F}^{p-1} = \dot{\boldsymbol{Q}}\boldsymbol{N}(\boldsymbol{K}), \qquad (6.6)$$

where tensor $\boldsymbol{N}(\boldsymbol{K})$ defines the direction of plastic flow in dependence of additional kinematic parameter. These parameters result in von Mises theory from kinematic hardening because, in general, the plastic deformations are described by the difference between the total stress and the so-called backstress. In this text we restrict our attention to isotropic

hardening. Then, the hardening can be described by a single scalar internal variable and the **flow rule** is of the form

$$\dot{\boldsymbol{F}}^{dev,p}\boldsymbol{F}^{p-1} = \dot{\varepsilon}^p \boldsymbol{M} \tag{6.7}$$

where ε^p is the **effective plastic strain**. Within the context of J_2-flow theory of plasticity $\boldsymbol{M}$ may be any symmetric tensor satisfying the kinematic constraints

$$\mathrm{tr}\boldsymbol{M} = 0 \qquad \text{and} \qquad \boldsymbol{M} \cdot \boldsymbol{M} = \frac{3}{2}. \tag{6.8}$$

6.2.1. Elastic energy and stored plastic energy

Let us assume power-law hardening, i.e., the yield stress obeys the **hardening law**

$$\sigma_y = \sigma_{y0}\left(1 + \frac{\varepsilon^p}{\varepsilon_{y0}^p}\right)^{1/n}, \tag{6.9}$$

where $n \in [1, \infty)$ is the hardening exponent, $\sigma_{y0} = \sigma_{y0}(T)$ is the (temperature dependent) initial yield stress and ε_{y0}^p is a reference plastic strain. With $n = 1$ we prescribe linear isotropic hardening, whereas $n \to \infty$ enforces perfect plasticity, cf. Figure 6.1. The frequently used bilinear hardening law is described with (6.9) by simply replacing $\sigma_{y0}/\varepsilon_{y0}^p$ with a plastic tangent modulus E_{pl}. By the underlying von Mises theory the plastic work results from purely deviatoric responses, $W^p \equiv W^{p,\mathrm{dev}}$. Thence, the corresponding **stored energy** function per unit volume is

$$W^p(\varepsilon^p, T) = \frac{n\sigma_{y0}(T)\varepsilon_0^p}{n+1}\left(1 + \left(\frac{\varepsilon^p}{\varepsilon_{y0}^p}\right)\right)^{(n+1)/n}. \tag{6.10}$$

To include elastic deformations we follow the strategy outlined in Section 3. Assume that the **volumetric** and **deviatoric elastic** responses in (6.2) decouple, i.e.,

$$W^e(\boldsymbol{C}^e, T) = W^{e,\mathrm{vol}}(J^e, T) + W^{e,\mathrm{dev}}(\boldsymbol{C}^{e,\mathrm{dev}}, T), \tag{6.11}$$

where

$$J^e = \det(\boldsymbol{F}^e) \tag{6.12}$$

is the Jacobian of the elastic deformation and

$$\boldsymbol{C}^{e,\mathrm{dev}} = J^{e-2/3}\boldsymbol{C}^e \tag{6.13}$$

(a) hardening

(b) thermal softening ($n = 10$)
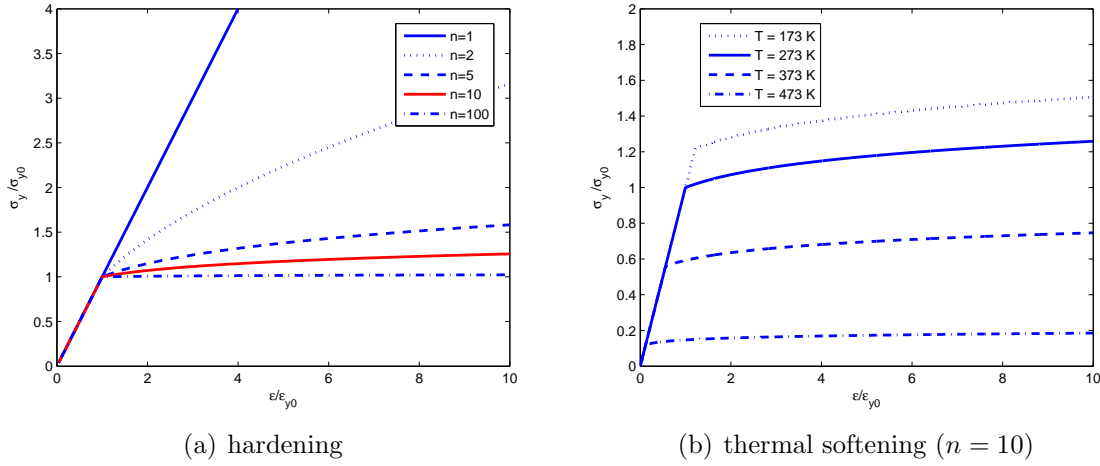
Figure 6.1.: Power law hardening for different hardening exponents n and thermal softening for $T_0 = 273 \ K$, $T_m = 500 \ K$, $l = 1$ and different temperatures T.

is the deviatoric elastic right Cauchy-Green deformation tensor. Then any constitutive relation of Section 3 may be employed. In calculations involving metals we specifically take W^e to be of the form

$$W^e(\boldsymbol{F}^e, T) = \frac{\kappa}{2} [\ln J^e - 3\alpha(T - T_0)]^2 + \frac{\mu}{4} \parallel \ln \boldsymbol{C}^{e,\text{dev}} \parallel^2 + \varrho_0 c_v T \left(1 - \ln \frac{T}{T_0} \right) \quad (6.14)$$

where $\kappa = \lambda + 2\mu/3$ is a reference bulk modulus, μ and λ are reference Lamé constants, α is the thermal expansion coefficient, T_0 is a reference absolute temperature, ϱ_0 is the mass density per unit undeformed volume, and c_v is the specific heat per unit mass at constant volume.

To relate the elastic strain and the effective von Mises stress σ from (6.2) we state the **thermodynamic force** conjugate to ε^p

$$Y = -\frac{\partial A}{\partial \varepsilon^p} = \sigma_e - \sigma_y, \quad (6.15)$$

where

$$\sigma_e = -\frac{\partial W^e}{\partial \varepsilon^p} = 2\frac{\partial W^e}{\partial \boldsymbol{C}^e} \cdot \boldsymbol{M} \quad (6.16)$$

is the effective Mises stress and

$$\sigma_y = \frac{\partial W^p}{\partial \varepsilon^p}(T, \varepsilon^p) \quad (6.17)$$

is the yield stress of the material.

84
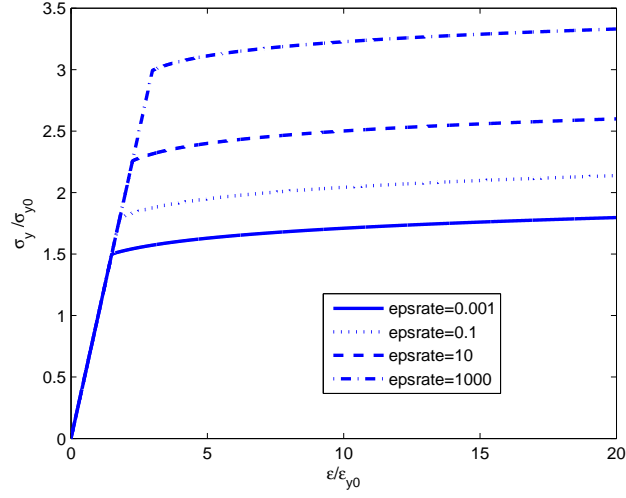
Figure 6.2.: Strain rate sensitivity for different relative strain rates $\dot{\varepsilon}^p/\dot{\varepsilon}^p_{y_0}$ and $m = 10$.

6.2.2. Thermal softening

Additionally, to account for the temperature sensitivity a **thermal-softening** law needs to be prescribed. For example, the yield stress may depend on the temperature as

$$\sigma_{y_0}(T) = \sigma_{T=T_0}\left(1 - \frac{T - T_0}{T_m - T_0}\right)^l , \tag{6.18}$$

where $\sigma_{T=T_0}$ is the yield stress at reference absolute temperature T_0, T_m is the melting temperature, and l is the thermal softening exponent, see Figure 6.1.

6.2.3. Rate sensitivity

In materials undergoing high speed deformations strain rate effects may play a significant role. With a view to ensuring a variational structure the rate sensitivity of the material is described here by a kinetic potential $\psi(Y)$ and a kinetic equation of the form

$$\dot{\varepsilon}^p = \frac{\partial \psi}{\partial Y}(Y) , \tag{6.19}$$

where Y denotes the conjugate thermodynamic driving force. Equation (6.19) can be expressed in inverse form as

$$Y = \frac{\partial \psi^*}{\partial \dot{\varepsilon}^p}(\dot{\varepsilon}^p) , \tag{6.20}$$

where the dual kinetic potential $\psi^*(\dot{\varepsilon}^p)$ follows from $\psi(Y)$ by a Legendre transformation.

$$\psi^*(\dot{\varepsilon}^p) = Y \cdot \dot{\varepsilon}^p - \psi(Y) \tag{6.21}$$

We assume a simple power-law rate-sensitivity. The corresponding dual kinetic potential is

$$\tilde{\psi}^* = \frac{m\sigma_y \dot{\varepsilon}^p_{y0}}{m+1} \left(\frac{\dot{\varepsilon}^p}{\dot{\varepsilon}^p_{y0}} \right)^{(m+1)/m}, \tag{6.22}$$

where m is the rate-sensitivity exponent and $\dot{\varepsilon}^p_0$ is a reference plastic strain rate. In Figure 6.2 some corresponding stress-strain relations are plotted for a hardening material with $n = 10$.

6.3. Constitutive update algorithm

For numerical solution we think of a process of incremental deformation where the solution is to be determined at times $t_0, \ldots, t_n, t_{n+1}, \ldots$. Let the state of the material be known at time t_n and let the deformation $\boldsymbol{F}_{n+1}$ and the temperature T_{n+1} at time t_{n+1} be given. The problem is now to determine the state of the material at time $t_{n+1} = t_n + \Delta t$ from this information. To this end we start discretizing the flow rule (6.7) in time. Using the exponential mapping technique introduced by Weber and Anand [356], see also [252, 216], the result reads

$$\boldsymbol{F}^p_{n+1} = \exp\left(\Delta\varepsilon^p \boldsymbol{M}\right) \boldsymbol{F}^p_n, \tag{6.23}$$

where $\Delta\varepsilon^p$ is the plastic strain increment and $\exp(\cdot)$ is the exponential mapping of square matrices, for computable algorithms see Appendix 2.3. Note that the discrete update (6.23) is consistent with its continuous counterpart (6.7)

$$\left[\frac{d}{d\epsilon} \exp\left(\epsilon(\Delta\varepsilon^p \boldsymbol{M})\right) \right]_{\epsilon=0^+} = \Delta\varepsilon^p \boldsymbol{M}. \tag{6.24}$$

Next we follow a strategy outlined in [257] and formulate an **incremental energy function**. Without loss of generality this function may be of the form

$$f_n(\boldsymbol{F}_{n+1}, T_{n+1}; \varepsilon^p_{n+1}, \boldsymbol{M}) = W^e(\boldsymbol{F}^e_{n+1}, T_{n+1})$$
$$+ W^p(\varepsilon^p_{n+1}, T_{n+1}) + \Delta t \psi^*(\Delta\varepsilon^p/\Delta t). \tag{6.25}$$

We now define an **effective work-of-deformation density** $W_n(\boldsymbol{F}_{n+1}, T_{n+1})$ by minimization of f_n with respect to the effective plastic strain ε^p_{n+1} and the direction of plastic flow $\boldsymbol{M}$, i.e.,

$$W_n(\boldsymbol{F}_{n+1}, T_{n+1}) = \min_{\varepsilon^p_{n+1}, \boldsymbol{M}} f_n(\boldsymbol{F}_{n+1}, T_{n+1}; \varepsilon^p_{n+1}, \boldsymbol{M}), \tag{6.26}$$

subjected to the constraints (6.8) and the plastic irreversibility constraint

$$\Delta\varepsilon^p = \varepsilon^p{}_{n+1} - \varepsilon^p{}_n \geq 0. \tag{6.27}$$

This effective work of deformation density $W_n(\boldsymbol{F}_{n+1})$ acts as a potential for the first Piola-Kirchhoff stress tensor $\boldsymbol{P}_{n+1}$ at time t_{n+1} (see Section 7.6.2 for a proof).

$$\boldsymbol{P}_{n+1} = \frac{\partial W_n}{\partial \boldsymbol{F}_{n+1}}(\boldsymbol{F}_{n+1}, T_{n+1}) \tag{6.28}$$

The consistent tangent moduli follow by linearization of (6.28) in the form

$$D\boldsymbol{P}_{n+1} = \frac{\partial^2 W_n}{\partial \boldsymbol{F}_{n+1}\partial \boldsymbol{F}_{n+1}}(\boldsymbol{F}_{n+1}, T_{n+1}). \tag{6.29}$$

6.3.1. Implementation based on logarithmic elastic strains

The **logarithmic elastic strain** is defined by equation (1.38), where a superscript e refers now to the elastic part of $\boldsymbol{\epsilon}$ and $\boldsymbol{C}$, respectively.

$$\boldsymbol{\epsilon}^e = \frac{1}{2}\ln(\boldsymbol{C}^e). \tag{6.30}$$

Moreover, the deviatoric part of the logarithmic elastic strain is abbreviated here by

$$\boldsymbol{e}^e \equiv \boldsymbol{\epsilon}^{e,\mathrm{dev}} = \boldsymbol{\epsilon}^e - \frac{1}{3}\boldsymbol{I}\,\mathrm{tr}\boldsymbol{\epsilon}^e. \tag{6.31}$$

With (6.13) and by the properties of the logarithmic mapping we have the identity

$$\boldsymbol{e}^e = \frac{1}{2}\ln(\boldsymbol{C}^{e,\mathrm{dev}}). \tag{6.32}$$

When the elastic strain-energy density of the material at time t_{n+1} is expressed in terms of logarithmic elastic strains and with an application of the discretized flow rule (6.23) the incremental energy function (6.25) can be written as

$$f_n = W^e\big(\ln\big(\exp(-\Delta\varepsilon^p\boldsymbol{M})\boldsymbol{C}^{e,\mathrm{trial}}\exp(-\Delta\varepsilon^p\boldsymbol{M})\big), T_{n+1}\big)$$
$$+ W^p(T_{n+1}, \varepsilon^p_{n+1}) + \Delta t\psi^*(\Delta\varepsilon^p/\Delta t). \tag{6.33}$$

Here we made use of a **trial elastic right Cauchy-Green deformation tensor**, which works like a **predictor** in the increment with frozen plastic deformation field $\boldsymbol{F}^p_n$,

$$\boldsymbol{C}^{e,\mathrm{trial}}_{n+1} = \boldsymbol{F}^{p-T}_n \boldsymbol{C}_{n+1} \boldsymbol{F}^{p-1}_n. \tag{6.34}$$

Presuming that the direction of the elastic tensor (6.34) corresponds with the direction of plastic flow $\boldsymbol{M}$, then

$$\boldsymbol{M}\boldsymbol{C}_{n+1}^{e,\text{trial}} = \boldsymbol{C}_{n+1}^{e,\text{trial}}\boldsymbol{M}, \tag{6.35}$$

and the following identity holds

$$\frac{1}{2}\ln\big(\exp(-\Delta\varepsilon^p\boldsymbol{M})\boldsymbol{C}_{n+1}^{e,\text{trial}}\exp(-\Delta\varepsilon^p\boldsymbol{M})\big) = \frac{1}{2}\ln(\boldsymbol{C}_{n+1}^{e,\text{trial}}) - \Delta\varepsilon^p\boldsymbol{M}. \tag{6.36}$$

Now, writing (6.36) with a elastic trial strain of the form (1.38)

$$\boldsymbol{\epsilon}_{n+1}^{\text{trial}} = \frac{1}{2}\ln(\boldsymbol{C}_{n+1}^{e,\text{trial}}), \tag{6.37}$$

we can express the incremental deformation energy (6.33) as

$$f_n = W^e(\boldsymbol{\epsilon}_{n+1}^{\text{trial}} - \Delta\varepsilon^p\boldsymbol{M}, T_{n+1}) + W^p(T_{n+1}, \varepsilon^p{}_{n+1}) + \Delta t\ \psi^*(\Delta\varepsilon^p/\Delta t) \tag{6.38}$$

Note that the incremental deformation energy function (6.38) is of the same form which arises from linearized kinematics. Consequently the constitutive updates are in complete analogy to small-strain updates, [252, 216].

6.3.2. Optimization with respect to ε^p and $\boldsymbol{M}$

The optimization of the incremental energy function (6.38) with respect to $\varepsilon^p{}_{n+1}$ and $\boldsymbol{M}$ subjected to the constraints (6.8) leads to the Euler-Lagrange equations:

$$\frac{\partial f_n}{\partial \varepsilon_{n+1}^p} = 0 \quad \Rightarrow \quad -\sigma_{v,n+1} + \sigma_y(\varepsilon^p{}_{n+1}) + \psi^{*\prime}\big(\frac{\Delta\varepsilon^p}{\Delta t}\big) = 0 \tag{6.39}$$

$$\frac{\partial f_n}{\partial \boldsymbol{M}} = 0 \quad \Rightarrow \quad -\boldsymbol{\sigma}_{n+1} + \lambda_1\boldsymbol{I} + \lambda_2\boldsymbol{M} = 0 \tag{6.40}$$

where $\psi^{*\prime} \equiv \partial\psi^*/\partial\varepsilon_{n+1}^p$ and

$$\boldsymbol{\sigma}_{n+1} = \frac{\partial W^e}{\partial \boldsymbol{\epsilon}_{n+1}^{e,\text{trial}}} \tag{6.41}$$

and λ_1 and λ_2 are Lagrange multipliers to be determined from constraints $(6.8)_1$ and $(6.8)_2$, respectively. This way the value of $\boldsymbol{M}$ is computed as

$$\boldsymbol{M} = \frac{3\boldsymbol{s}_{n+1}}{2|\boldsymbol{s}_{n+1}|}, \tag{6.42}$$

where we refer to the definition of the norm of a stress tensor in Appendix (1.28) and abbreviate the stress deviator by

$$s_{n+1} \equiv \sigma_{n+1}^{\text{dev}} = \sigma_{n+1} - \frac{1}{3}\text{tr}(\sigma_{n+1})I. \tag{6.43}$$

Equation (6.42) determines M implicitly in general. However, for the elastic strain-energy density (6.14), the stress deviator evaluates to

$$s_{n+1} = 2\mu e_{n+1}^e = s_{n+1}^{\text{trial}} - 2\mu\Delta\varepsilon^p M \tag{6.44}$$

where we apply a **trial stress deviator**

$$s_{n+1}^{\text{trial}} = 2\mu e_{n+1}^{e,\text{trial}}. \tag{6.45}$$

Inserting (6.42) into (6.44) gives

$$s_{n+1} = s_{n+1}^{\text{trial}} - 3\mu\Delta\varepsilon^p \frac{s_{n+1}}{|s_{n+1}|}, \tag{6.46}$$

which shows that s_{n+1} and s_{n+1}^{trial} are parallel. In particular, we verify that the commutativity condition (6.35) is indeed satisfied. Since the norm of M is fixed it follows that

$$M = \frac{3s_{n+1}^{\text{trial}}}{2|s_{n+1}^{\text{trial}}|}, \tag{6.47}$$

which now gives M explicitly in terms of the known data of the problem. Inserting (6.47) into (6.40) gives the equation

$$\frac{9}{2}\mu\Delta\varepsilon^p + \psi^{*\prime}(\Delta\varepsilon^p/\Delta t) = \sigma_{n+1}^{\text{trial}} - \sigma_y(\varepsilon_{n+1}^p), \tag{6.48}$$

which may be solved for the unknown $\varepsilon^p{}_{n+1}$ simply by iteration under the constraint imposed by (6.27).

6.3.3. Stresses and consistent tangent

Once $\varepsilon^p{}_{n+1}$ is determined, the **updated stresses** follow in the form

$$\sigma_{n+1} = p_{n+1}I + s_{n+1}, \tag{6.49}$$

with s_{n+1} given by (6.44) and the pressure p_{n+1} computed from the equation of state in terms of the **volumetric elastic strain** $\ln(J_{n+1}^e) = \text{tr}(\epsilon_{n+1}^e)$ as

$$p_{n+1} = \frac{\partial W^{e,\text{vol}}}{\partial\text{tr}(\epsilon_{n+1}^e)}(J_{n+1}^e, T_{n+1}). \tag{6.50}$$

Owing to the variational character of the update, the **stress-strain relations** satisfy the potential relations

$$\boldsymbol{\sigma}_{n+1} = \frac{\partial W_n}{\partial \boldsymbol{\epsilon}^e_{n+1}} \ , \tag{6.51}$$

where the incremental work-or-deformation density W_n is the optimal value of the incremental energy function (6.38), cf. equation (6.26). The **finite-kinematic relations** follow now simply from an application of the chain rule, with the result:

$$\boldsymbol{P}_{n+1} = \frac{\partial W_n}{\partial \boldsymbol{F}_{n+1}} = \frac{\partial W_n}{\partial \boldsymbol{\epsilon}^e_{n+1}} \cdot \frac{\partial \boldsymbol{\epsilon}^e_{n+1}}{\partial \boldsymbol{C}_{n+1}} \cdot \frac{\partial \boldsymbol{C}_{n+1}}{\partial \boldsymbol{F}_{n+1}} \ . \tag{6.52}$$

Differentiating this expression once more gives the consistent tangents in terms of the finite-kinematic relations $D\boldsymbol{P}_{n+1}$, equation (6.29). By a lengthy but straightforward calculation we get the linearization of (6.51) in the form

$$D\boldsymbol{\sigma}_{n+1} = \frac{\partial^2 W_n}{\partial \boldsymbol{\epsilon}^e_{n+1} \partial \boldsymbol{\epsilon}^e_{n+1}} = a\boldsymbol{I} + b\boldsymbol{M} \otimes \boldsymbol{M} \tag{6.53}$$

with coefficients a and b evaluated as follows:

$$a = \frac{1}{A} \qquad\qquad A = \frac{1}{2\mu} + \frac{3}{2}\frac{\Delta\varepsilon^p}{\sigma_{v,n+1}} \tag{6.54}$$

$$b = -\frac{B}{A^2 + \frac{3}{2}AB} \qquad\qquad B = \frac{1}{\sigma'_y(\varepsilon^p_{n+1}) + \psi^{*\prime\prime}/\Delta t} - \frac{\Delta\varepsilon^p}{\sigma_{v,n+1}} \tag{6.55}$$

The finite-kinematic relation follows by (6.52). In components equation (6.52) reads

$$\boldsymbol{P}_{iJ} = [\sigma_{AB} D\ln(\boldsymbol{C}^{e,\mathrm{trial}}_{n+1})_{ABCD}(\boldsymbol{F}^{p-1}_n)_{JC}(\boldsymbol{F}^{p-1}_n)_{KD}]F_{iK} \ , \tag{6.56}$$

where we have dropped the label $n+1$ for ease of reading. Differentiating this expression gives the **consistent tangent** in the form

$$DP_{iJkL} = \delta_{ik}\sigma_{AB}D\ln(\boldsymbol{C}^{e,\mathrm{trial}}_{n+1})_{ABCD}(\boldsymbol{F}^{p-1}_n)_{JC}(\boldsymbol{F}^{p-1}_n)_{LD}+$$
$$[D\sigma_{ABCD}D\ln(\boldsymbol{C}^{e,\mathrm{trial}}_{n+1})_{ABEF}(\boldsymbol{F}^{p-1}_n)_{JE}(\boldsymbol{F}^{p-1}_n)_{KF}D\ln(\boldsymbol{C}^{e,\mathrm{trial}}_{n+1})_{CDGH}(\boldsymbol{F}^{p-1}_n)_{LG}(\boldsymbol{F}^{p-1}_n)_{MH}$$
$$+ 2\sigma_{AB}D^2\ln(\boldsymbol{C}^{e,\mathrm{trial}}_{n+1})_{ABEFGH}(\boldsymbol{F}^{p-1}_n)_{JE}(\boldsymbol{F}^{p-1}_n)_{KF}(\boldsymbol{F}^{p-1}_n)_{LG}(\boldsymbol{F}^{p-1}_n)_{MH}]F_{iK}F_{kM} \ . \tag{6.57}$$

The tangent moduli are symmetric owing to the potential character of the incremental stress-strain relation, equation (6.51).

The computation of the exponential and logarithmic mappings and their derivatives, which is required for the evaluation of (6.23), (6.31), (6.56), (6.57), etc., may be accomplished by a variety of means such as, e. g., by a Taylor series expansion or through

a spectral decomposition of the argument, for a discussion see [256]. Algorithms for the computation of the exponential and logarithmic mapping and their first and second linearizations are summarized in the Appendix 2.3.

7. Porous Plasticity

In this chapter we develop a continuum theory to model solid materials with a certain porosity. The model, which allows for reversible and irreversible time-dependent deformations, enables us to link the mechanism of pore expansion and global softening of the material to parameters which describe the micromechanical mechanisms in general elastic and elasto-plastic solids.

The chapter is structured as follows: At first we describe the underlying model of a porous composite and in Section 7.1 we provide the basic equations of the underlying mesoscopic theory. The actual constitutive model of void growth in an elastic and a visco-plastic material is outlined in Section 7.3. Numerical results on void growth and void distribution are also provided there. Section 7.5 extends the void growth model to a variational constitutive model for porous elasto-plastic materials undergoing finite deformations. In analogy to the classical plasticity of Chapter 6 constitutive updates for time integration in numerical procedures are provided in the concluding Section 7.6.

7.1. Continua with a certain porosity

The majority of technical and natural materials contains a certain amount of arbitrarily distributed pores and cavities (voids). Here we have in mind in the first instance metals and its alloys. However, cavities are also observed in polymers, in ceramics and in certain bio-materials, like soft tissue of brain and inner organs. Typically the cavities are small compared to the size of the structure, and their distribution is defined by a characteristic function $f = f(x)$, $x \in \mathbb{R}^3$, representing the void volume at the position x in the material. The spatial average over the current volume of the body V defines the void volume fraction or porosity f_V

$$f_V = \frac{1}{V} \int_V f(x) \, dx. \tag{7.1}$$

In the materials under consideration here the initial porosity is small. For engineering metals it is initially in the range of $10^{-2} - 10^{-4}$ [343, 328], caused, e.g., by defects in

the crystal lattice or by (empty) inclusions along grain boundaries. By straining of the surrounding material the voids may grow but typically metals fail at a porosity of about $0.1 - 0.3$ [270, 95].

Similar porosity values are observed for the soft tissue of inner organs. Here a natural small porosity is observed, whereby many pores in a biological system are liquid filled (which, in turn, justifies the modelling of bio-tissue with the classical theory of porous media, see [109]). In opposite to metals bio-materials show a low resistance to hydrostatic tension: pores and cavities grow under straining until cell walls and capillaries rupture. But even at the state of traumatic injuries the volume fraction of pores is still moderate.

7.1.1. Spherical shell model of a porous composite
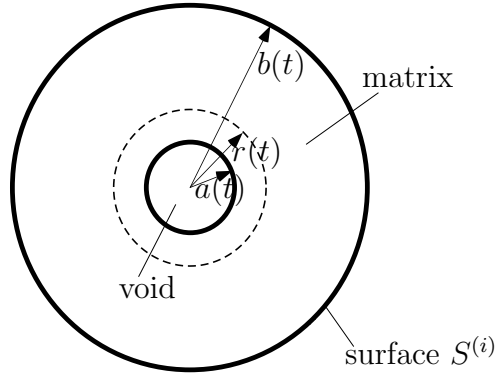
Figure 7.1.: Spherical shell model of a single void

In this text we analyze within the framework of a mesoscopic theory the growth of voids (i.e., cavities and pores) in a deforming body. For our analysis we imagine that each void i of a material is at every instance surrounded by a surface $S^{(i)}$ lying completely in the material (matrix), i.e., we exclude here the process of coalescence. The surface $S^{(i)}$ encloses a volume $V^{(i)}$ in such a way that for every void i holds

$$\frac{V^{(i)}}{V} = f_V{}^{(i)}. \tag{7.2}$$

Presuming a moderate porosity (up to $1/3$) such a subdivision of the material could be carried out and we assume that this has been done in such a way that the surfaces $S^{(i)}$ approach spheres as nearly as possible. Therefore, in the following any element containing a void will be called a **spherical shell**, see Figure 7.1.

The porous materials are now modeled as assemblages of isotropic spherical shells with a certain given initial void volume fraction and an initial size distribution. Note that the void volume of one spherical shell initially equals the void volume fraction of the whole composite whereas the size distribution of spherical shells may vary arbitrarily. During the process of deformation of the body the spherical shells may grow (in different ways) but retain their shapes whereas the matrix material follows classical material laws.
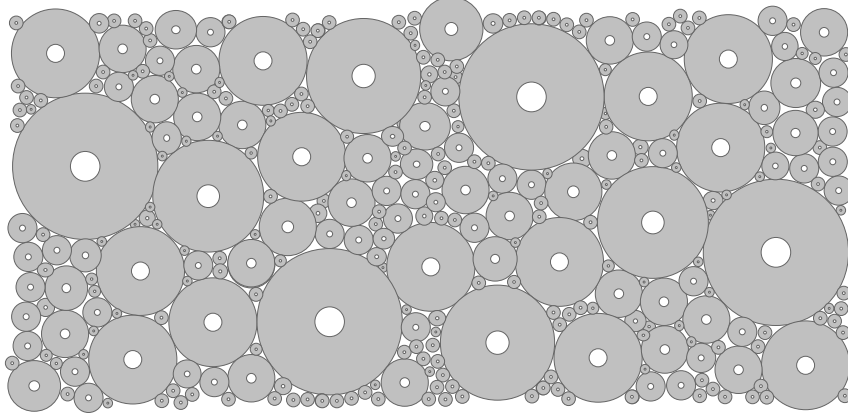
Figure 7.2.: Spherical shell model of porosity

Such materials may be "constructed" by filling a body with spherical shells which may be diminished to infinitesimal size, see Figure 7.2. As the remaining volume between the spheres can be made infinitesimally small by the filling process, the deformation energy density of the composite body will in the limit approach the sum of deformation energies densities stored in all spherical shells.

7.1.2. Kinematics of void growth

Let us consider a spherical shell with initial inner radius a_0 and outer radius b_0 and let it expand for some reason. The void will grow to a current radius $a \equiv a(t)$ and the outer shell expands to a current outer radius $b \equiv b(t)$. Consider now a material sphere surrounding the void and deforming with the body. The initial and current radii of that material sphere are denoted by $r_0 \in [a_0, b_0]$ and $r \equiv r(t) \in [a, b]$, respectively, see Figure 7.3. Presuming a volume preserving deformation, i.e.,

$$\frac{4\pi}{3}(r_0^3 - a_0^3) \quad = \quad \frac{4\pi}{3}(r^3 - a^3),$$

(7.3)

the deformation mapping $r = \varphi(r_0)$ is uniquely determined by

$$r = \left(r_0^3 - a_0^3 + a^3\right)^{1/3}. \tag{7.4}$$

As a consequence, the current outer radius of a shell of incompressible material surrounding a void is given by

$$b = \left(b_0^3 - a_0^3 + a^3\right)^{1/3}. \tag{7.5}$$

Writing the volume constraint (7.3) equivalently as,

$$\frac{d}{dt}\frac{4\pi}{3}(r^3 - a^3) = 0\,, \tag{7.6}$$

defines the velocity field over the current configuration. In particular, the radial component of the spatial velocity is

$$v_r = \frac{dr}{dt} = \frac{a^2}{r^2}\dot{a}, \tag{7.7}$$

where the rate of change of void radius a, $\dot{a} = \frac{da}{dt}$, is the **velocity of void expansion**. The corresponding full velocity field is

$$\boldsymbol{v} = \frac{v_r}{r}\boldsymbol{x} = \frac{a^2\dot{a}}{r^3}\boldsymbol{x}, \tag{7.8}$$

$\boldsymbol{x}$ being the spatial position vector relative to the center of the void.
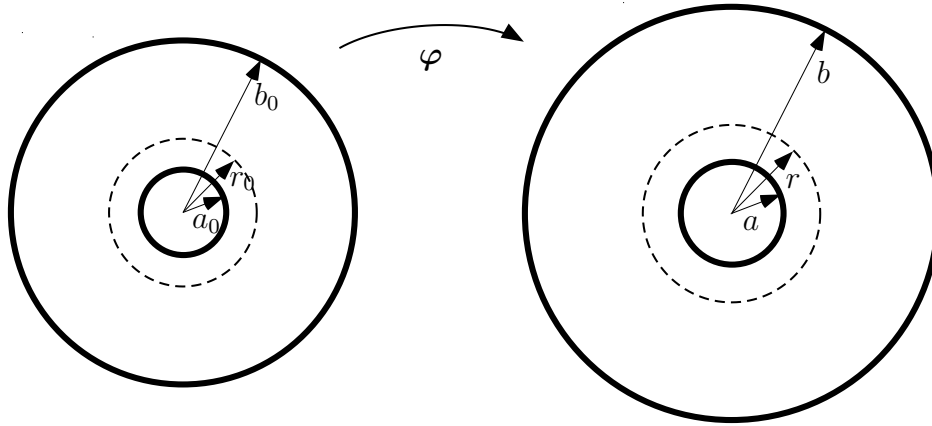
Figure 7.3.: Spherical shell model of void growth

For any point located on the material sphere surrounding the void we write the deformation gradient as

$$\boldsymbol{F} = \frac{r}{r_0}\boldsymbol{I}. \tag{7.9}$$

and the corresponding spatial velocity gradient (1.45) is

$$\boldsymbol{l} = \frac{a^2\dot{a}}{r^3}\left(\boldsymbol{I} - 3\boldsymbol{e}_r \otimes \boldsymbol{e}_r\right) \tag{7.10}$$

where $\boldsymbol{e}_r$ is the unit radial vector. It follows from (7.10) that $\boldsymbol{l}$ is symmetric and coincides with the rate of deformation tensor (1.47); the spin tensor (1.48) vanishes.

7.1.3. Effective elastic moduli

The proposed model of porosity is basically an inhomogeneous material, precisely, a composite with (empty) inclusions. A common way to homogenize, i.e., to approximate the effective properties of a general composite, is Hill's [151] self consistent method. In this method the equations of elasticity are solved for an inclusion embedded into a medium of unknown effective moduli. The effective bulk modulus κ^* and the effective shear modulus μ^* are then derived, cf. [79, 222, 223, 335]. However, more consistent to our approach is the so-called composite sphere model which was analytically treated by Hashin [145, 146] and others [82, 83, 84, 336].

In [145, 146] a linear elastic analysis on one spherical shell was carried out to determine effective moduli. If the external boundary b of the spherical shell is subjected to purely radial displacement $u_r(r = b) = \bar{\epsilon}\,b$, the radial stress on the boundary is

$$\sigma_r(r = b) = 3\kappa^*\,\bar{\epsilon} \tag{7.11}$$

where the effective bulk modulus κ^* is a function of the ratio a/b (and, if general second material inclusions are considered as in [145], also of core and shell elastic moduli). On the other hand, if a homogenous isotropic body with bulk modulus κ^* is subjected to isotropic strain $\bar{\epsilon}\,\delta_{ij}$, the displacement and the traction on any internal surface with radius r are purely radial. The stresses $\sigma_r(r = b)$ are precisely those given in the foregoing equation (7.11), cf. [146].

In general such an approach yields only upper and lower bounds for the effective moduli. Only for the effective bulk modulus both bounds coincide, i.e., to an external observer the composite sphere behaves just like a homogeneous sphere of radius b with bulk modulus κ^*.

It follows that such a radially symmetric spherical shell can be replaced by the composite sphere without perturbing the homogeneous isotropic state of stress and strain in the body. Therefore, such a replacement can be performed again and again with composite spheres of different size as long as the spheres all have the same κ^* (which is the case if in all composite spheres the ratios a/b and the constitutive properties are the same). If the body is filled with composite spheres which diminish to infinitesimal size, then (as the remaining volume goes to zero) the effective bulk modulus of this composite material converges to κ^*. For a composite as an assemblage of spherical voids enclosed in isotropic concentric spherical matrices the effective bulk modulus κ^* is [188, 146]

$$\kappa^* = \kappa\left(1 - f_V \frac{3\kappa + 4\mu}{3\kappa + 4\mu/f_V}\right). \tag{7.12}$$

Effective moduli for small concentrations of voids may be found by linearizing general bounds for bulk and shear modulus. The effective bulk modulus (7.12) is easily linearized by neglecting the f_V-term in the denominator of (7.12). This approach is identical to the so-called dilute model, i.e., a spherical inclusion embedded in an infinite solid matrix with elastic constants κ and μ or E and ν, respectively,

$$\kappa^* = \kappa\left(1 - f_V \frac{3(1 - \nu)}{2(1 - 2\nu)}\right). \tag{7.13}$$

For the shear modulus the bounds derived in [145] may analogously be simplified and are then found to be the same as in the dilute case

$$\mu^* = \mu\left(1 - f_V \frac{15(1 - \nu)}{7 - 5\nu}\right). \tag{7.14}$$

7.2. A mesoscopic theory of void growth

A general mesoscopic concept was introduced by Muschik and his co-workers [236, 237, 238, 267, 350] to model microstructural effects within a continuum mechanical framework. The basic idea of this theory is to extend the classical space-time domain $\{\boldsymbol{x}, t\}$ of continuums mechanics by a set of mesoscopic variables $\boldsymbol{m} = \{m^{(1)}, \ldots, m^{(k)}\}$ of arbitrary tensorial order. These additional parameters, the mesoscopic variables, extend the configuration domain to a so-called mesoscopic space $\{\boldsymbol{x}, t, \boldsymbol{m}\}$, on which the fields appearing in the classical balances equations are defined. Furthermore, an additional function describes the distribution of the mesoscopic variables at time and position. This mesoscopic distribution function has no analog in the macroscopic description, in this way a statistical element enters the theory. In this section we provide the basic equations of the mesoscopic framework.

7.2.1. The mesoscopic concept

The balances for mass, momentum and energy are material independent and defined on the space-time domain $(\boldsymbol{x}, t) \in \mathbb{R}^3 \times \mathbb{R}$. For their solution constitutive relations are required (i.e., for $\boldsymbol{\sigma}$ or $\boldsymbol{q}$), which result in field equations for a specific material. Conventionally, the domain of the constitutive equations is called the state space, in which the elements are also defined on space-time. If more fields are introduced (e.g., internal variables), additional balances or evolution equations are stated which need to be satisfied by these fields.

The mesoscopic concept is different and in some sense easier. Instead of space-time an extended configuration space is introduced. This configuration space is called a mesoscopic space on which now the usual fields, such as mass density ϱ, material velocity $\boldsymbol{v}$, internal energy density e etc., have to be redefined. Consecutively the balances of mass, momentum and energy need now to be formulated on the mesoscopic space.

Following the approach of Muschik et al. [236] we introduce a manifold $\mathcal{M}$ called mesoscopic manifold, which is spanned by the set of mesoscopic variables $\boldsymbol{m}$. Then the mesoscopic space is defined by

$$(\boldsymbol{m}, \boldsymbol{x}, t) \ \in \ \mathcal{M} \times \mathbb{R}^3 \times \mathbb{R} \tag{7.15}$$

In the materials of interest the particles of a volume element do not have the same value of a mesoscopic variable (e.g., in our porous model we have spherical shells with different void radii). Thus a statistical element needs to be introduced which accounts for the different values of the mesoscopic variables $\boldsymbol{m}$ at each time t and position $\boldsymbol{x}$ — this is the so-called **mesoscopic distribution function** $\tilde{f}(\boldsymbol{m}, \boldsymbol{x}, t)$. Because this function has no analog in the macroscopic description, a mesoscopic theory handles more information than a purely macroscopic one.

The physical meaning of the mesoscopic distribution function $\tilde{f}(\boldsymbol{m}, \boldsymbol{x}, t)$ follows from the definition of a continuum: in the volume element associated with $(\boldsymbol{x}, t)$ the value of the mesoscopic variables $\boldsymbol{m}$ has the fraction $\tilde{f}$ of all particles in the volume element. Consequently, let $\tilde{N}_V(\boldsymbol{m}, \boldsymbol{x}, t)$ be the number of particles at $(\boldsymbol{x}, t)$ with a certain value of $\boldsymbol{m}$ whereas $N_V(\boldsymbol{x}, t)$ is the total number of particles within the volume element $\boldsymbol{x}$ at time t. Then we define

$$\tilde{f}(\boldsymbol{m}, \boldsymbol{x}, t) := \frac{\tilde{N}_V(\boldsymbol{m}, \boldsymbol{x}, t)}{N_V(\boldsymbol{x}, t)} \ . \tag{7.16}$$

The mesoscopic distribution function is always normalized

$$1 = \int_{\mathcal{M}} \tilde{f}(\boldsymbol{m}, \boldsymbol{x}, t) \, d\boldsymbol{m} = \frac{1}{N_V(\boldsymbol{x}, t)} \int_{\mathcal{M}} \tilde{N}_V(\boldsymbol{m}, \boldsymbol{x}, t) \, d\boldsymbol{m} \ . \tag{7.17}$$

In case of the porous material model under consideration here the mesoscopic variables are only the (scalar) void radii[1] $a(t)$ for the different spherical shells in a representative volume element at position $\boldsymbol{x}$. For this reason let us consider a spherical shell ensemble characterized by a mesoscopic void number density $\tilde{N}_V(a, t)$, representing the number of shells with the void radius a in the volume element at time t. We shall suppose that all voids have a nucleation size a_0, so that the function $\tilde{N}_V(\cdot, t)$ is defined over the interval $[a_0, \infty)$. Then, the total number of voids per unit undeformed volume is

$$N_V(t) = \int_{a_0}^{\infty} \tilde{N}_V(a, t) da. \tag{7.18}$$

With the mesoscopic distribution function (7.16) the fields of mass density, momentum, total energy etc. can be defined on the mesoscopic space. For distinguishing these fields from the macroscopic ones and to omit the arguments $\boldsymbol{m}, \boldsymbol{x}, t$ in the remaining of the text, we add a tilde to symbol, i.e,

$$\tilde{\varrho} \equiv \tilde{\varrho}(\boldsymbol{m}, \boldsymbol{x}, t) \qquad \tilde{\boldsymbol{v}} \equiv \tilde{\boldsymbol{v}}(\boldsymbol{m}, \boldsymbol{x}, t) \qquad \tilde{e} \equiv \tilde{e}(\boldsymbol{m}, \boldsymbol{x}, t) \quad \text{and so on.} \tag{7.19}$$

In particular, the mesoscopic mass density is defined by using the mesoscopic distribution function (7.16) as

$$\tilde{\varrho} = \tilde{f} \varrho(\boldsymbol{x}, t) = \frac{\tilde{N}_V(\boldsymbol{m}, \boldsymbol{x}, t)}{N_V(\boldsymbol{x}, t)} \varrho(\boldsymbol{x}, t). \tag{7.20}$$

The mesoscopic mass density $\tilde{\varrho}$ describes the mass density of all particles in a volume element for which the value of the mesoscopic variable is $\boldsymbol{m}$. In our case this is the mass density per volume of all spherical shells containing a void with radius a. Moreover, the macroscopic mass density $\varrho(\boldsymbol{x}, t)$ can be recovered from equation (7.20) by integration over the mesoscopic space (what basically corresponds to a sum over all spherical shells)

$$\varrho(\boldsymbol{x}, t) = \int_{\mathcal{M}} \tilde{\varrho}(\boldsymbol{m}, \boldsymbol{x}, t) \, d\boldsymbol{m}. \tag{7.21}$$

Other fields defined on the mesoscopic space are the mesoscopic material velocity $\tilde{\boldsymbol{v}}$ of the particles belonging to the mesoscopic variable $\boldsymbol{m}$ at time t in a volume element around $\boldsymbol{x}$, the mesoscopic stress tensor $\tilde{\boldsymbol{\sigma}}$, the mesoscopic heat flux density $\tilde{\boldsymbol{q}}$ etc.. The balance equations belonging to these mesoscopic fields are discussed in the next section.

---

[1]The exclusive use of the scalar mesoscopic variable a presumes, that the different radii a and b of the spherical shells are not independent. This assumption will be justified in Section 7.3. A more general case can be formulated introducing the independent mesoscopic variables $\boldsymbol{m} = \{a(t), b(t)\}$.

7.2.2. Mesoscopic balance equations

From a mathematical point of view, the mesoscopic balance equations differ from the macroscopic ones only in their domain which is enlarged by the mesoscopic variables, i.e., the domain of integration is now $\Omega \times \mathcal{M}$. Therefore derivatives with respect to these variables appear in the balances. Considering the outward flux of quantity Ψ per unit volume we have now $\tilde{\boldsymbol{J}}^\psi = \tilde{\boldsymbol{J}}^{\psi,\Omega} \cup \tilde{\boldsymbol{J}}^{\psi,\mathcal{M}}$, the fluxes through the surface in position space and on the manifold $\mathcal{M}$, respectively. Analogously the gradient splits

$$
\boldsymbol{\nabla} \cdot \tilde{\boldsymbol{J}}^\psi(\boldsymbol{m},\boldsymbol{x},t) \;\Bigg\langle\;
\begin{array}{c}
\boldsymbol{\nabla}_x \cdot \tilde{\boldsymbol{J}}^{\psi,\Omega}(\boldsymbol{m},\boldsymbol{x},t) \\[2em]
\boldsymbol{\nabla}_m \cdot \tilde{\boldsymbol{J}}^{\psi,\mathcal{M}}(\boldsymbol{m},\boldsymbol{x},t).
\end{array}
\tag{7.22}
$$

Similar to equation (2.46) we can now state a generic global equation for the balanced field Ψ, (see [238] for more details of the derivation).

$$
\frac{d}{dt} \int_\Omega \int_\mathcal{M} \tilde{\varrho}(\boldsymbol{m},\boldsymbol{x},t)\tilde{\psi}(\boldsymbol{m},\boldsymbol{x},t)\,d\boldsymbol{m}\,dV =
$$
$$
- \int_\Omega \int_\mathcal{M} \left(\boldsymbol{\nabla}_x \cdot \tilde{\boldsymbol{J}}^{\psi,\Omega}(\boldsymbol{m},\boldsymbol{x},t) + \boldsymbol{\nabla}_m \cdot \tilde{\boldsymbol{J}}^{\psi,\mathcal{M}}(\boldsymbol{m},\boldsymbol{x},t) \right)\,d\boldsymbol{m}\,dV +
$$
$$
+ \int_\Omega \int_\mathcal{M} \left(\tilde{\Pi}^\psi(\boldsymbol{m},\boldsymbol{x},t) + \tilde{\Sigma}^\psi(\boldsymbol{m},\boldsymbol{x},t) \right)\,d\boldsymbol{m}\,dV \tag{7.23}
$$

The total change of quantity $\tilde{\rho}\tilde{\psi}$ is the sum of the production, the supply and the total flux over the boundary and it is attributed to both, the spatial and the mesoscopic part of the space of definition. The physical interpretation of the balanced quantity is determined by the meaning of the set of mesoscopic variables $\boldsymbol{m}$. Consequently, a physical explanation of a global mesoscopic balance equation can be given only if the set of mesoscopic variables is specified.

From the global mesoscopic balance equation (7.23) the local form can be derived,

$$
\frac{\partial}{\partial t} \tilde{\rho}(\boldsymbol{m},\boldsymbol{x},t)\tilde{\psi}(\boldsymbol{m},\boldsymbol{x},t) + \boldsymbol{\nabla}_x \cdot \left[\tilde{\boldsymbol{v}}\,\tilde{\rho}(\boldsymbol{m},\boldsymbol{x},t)\tilde{\psi}(\boldsymbol{m},\boldsymbol{x},t) - \tilde{\boldsymbol{J}}_{\mathrm{cond}}^{\psi,\Omega}(\boldsymbol{m},\boldsymbol{x},t) \right] +
$$
$$
+ \boldsymbol{\nabla}_m \cdot \left[\tilde{\boldsymbol{u}}\,\tilde{\rho}(\boldsymbol{m},\boldsymbol{x},t)\tilde{\psi}(\boldsymbol{m},\boldsymbol{x},t) - \tilde{\boldsymbol{J}}_{\mathrm{cond}}^{\psi,\mathcal{M}}(\boldsymbol{m},\boldsymbol{x},t) \right] = (\tilde{\Pi}^{\tilde{\psi}} + \tilde{\Sigma}^{\tilde{\psi}})(\boldsymbol{m},\boldsymbol{x},t) \tag{7.24}
$$

where $\tilde{\boldsymbol{J}}_{\mathrm{cond}}^{\psi,\Omega}$ and $\tilde{\boldsymbol{J}}_{\mathrm{cond}}^{\psi,\mathcal{M}}$ are the *conductive* parts of the fluxes. The analogue to the material velocity is the velocity of mesoscopic change $\tilde{\boldsymbol{u}} \equiv \tilde{\boldsymbol{u}}(\boldsymbol{m},\boldsymbol{x},t)$ which is defined

as follows. Let t and $(t + \Delta t)$ be two instances of one particle at $\boldsymbol{x}$ with $\Delta t \to 0$ then follows the mapping

$$(\boldsymbol{m}, \boldsymbol{x}, t) \longmapsto (\boldsymbol{m} + \tilde{\boldsymbol{u}}\Delta t \; , \; \boldsymbol{x} + \tilde{\boldsymbol{v}}\Delta t \; , \; t + \Delta t), \tag{7.25}$$

where $\tilde{\boldsymbol{v}}$ is the mesoscopic material velocity (with respect to $\boldsymbol{x}$). In more detail the special mesoscopic balance equations are:

- *mesoscopic mass balance*

$$\frac{\partial \tilde{\varrho}}{\partial t} + \boldsymbol{\nabla}_x \cdot (\tilde{\varrho}\tilde{\boldsymbol{v}}) + \boldsymbol{\nabla}_m \cdot (\tilde{\varrho}\tilde{\boldsymbol{u}}) = 0 \tag{7.26}$$

- *balance of mesoscopic linear momentum $\tilde{\boldsymbol{l}}$*

$$\tilde{\boldsymbol{l}} \;\; := \;\; \tilde{\varrho}\tilde{\boldsymbol{v}} \;\; , \tag{7.27}$$

$$\frac{\partial \tilde{\boldsymbol{l}}}{\partial t} \;\; + \;\; \boldsymbol{\nabla}_x \cdot \left(\tilde{\boldsymbol{v}}\tilde{\boldsymbol{l}} - \tilde{\boldsymbol{\sigma}}^T \right) + \boldsymbol{\nabla}_m \cdot \left(\tilde{\boldsymbol{u}}\tilde{\boldsymbol{l}} - \boldsymbol{\varsigma}^T \right) = \tilde{\varrho}\tilde{\boldsymbol{a}} \tag{7.28}$$

Here is $\boldsymbol{\varsigma}$ an analog to the stress tensor, the non-convective momentum flux with respect to the mesoscopic variables $\boldsymbol{m}$.

- *balance of mesoscopic angular momentum $\tilde{\boldsymbol{g}}$*

$$\tilde{\boldsymbol{g}} \;\; := \;\; \boldsymbol{x} \times \tilde{\varrho}\tilde{\boldsymbol{v}} \;\; , \tag{7.29}$$

$$\frac{\partial \tilde{\boldsymbol{g}}}{\partial t} \;\; + \;\; \boldsymbol{\nabla}_x \cdot \left[\tilde{\boldsymbol{v}}\tilde{\boldsymbol{s}} - \tilde{\varrho}\left(\boldsymbol{x} \times \tilde{\boldsymbol{\sigma}}\right)^T - \tilde{\boldsymbol{\zeta}}^T \right] +$$
$$\;\; + \;\; \boldsymbol{\nabla}_m \cdot \left[\boldsymbol{u}\tilde{\boldsymbol{s}} - \tilde{\varrho}\left(\boldsymbol{x} \times \boldsymbol{\varsigma}\right)^T - \tilde{\boldsymbol{\eta}}^T \right] = \tilde{\varrho}(\boldsymbol{x} \times \tilde{\boldsymbol{a}}) + \varrho\boldsymbol{g} \tag{7.30}$$

The symbols $\tilde{\boldsymbol{\zeta}}$, $\tilde{\boldsymbol{\eta}}$ and $\boldsymbol{g}$ stand for couple stress tensor, the couple stress tensor on the manifold $\mathcal{M}$ and for the sum of all external specific angular momentums.

- *balance of total energy $\tilde{e}$*

$$\tilde{e} \;\; := \;\; \frac{1}{2}\tilde{\boldsymbol{v}}^2 + \tilde{u} \;\; , \tag{7.31}$$

$$\frac{\partial \tilde{\varrho}\tilde{e}}{\partial t} \;\; + \;\; \boldsymbol{\nabla}_x \cdot \left(\tilde{\boldsymbol{v}}\tilde{\varrho}\tilde{e} - \tilde{\boldsymbol{\sigma}}^T \cdot \tilde{\boldsymbol{v}} + \tilde{\boldsymbol{q}} \right) + \boldsymbol{\nabla}_m \cdot \left(\tilde{\boldsymbol{u}}\tilde{\varrho}\tilde{e} - \boldsymbol{\varsigma}^T \cdot \tilde{\boldsymbol{v}} + \tilde{\boldsymbol{\varpi}} \right) =$$
$$\;\; = \;\; \tilde{\varrho}\tilde{\boldsymbol{a}} \cdot \tilde{\boldsymbol{v}} + \tilde{\varrho}\tilde{r} \tag{7.32}$$

Here $\tilde{u}$ is the mesoscopic specific internal energy and $\tilde{r}$ is a possible mesoscopic absorption (supply). Furthermore the mesoscopic heat flux density is $\tilde{\boldsymbol{q}}$ and $\tilde{\boldsymbol{\varpi}}$ is the mesoscopic heat flux density on $\mathcal{M}$.

- *balance of internal energy $\tilde{u}$*

$$\frac{\partial \tilde{\varrho}\tilde{u}}{\partial t} \;+\; \boldsymbol{\nabla}_x \cdot (\tilde{\boldsymbol{v}}\tilde{\varrho}\tilde{u} + \tilde{\boldsymbol{q}}) + \boldsymbol{\nabla}_m \cdot (\tilde{\boldsymbol{u}}\tilde{\varrho}\tilde{u} + \tilde{\boldsymbol{\varpi}}) =$$
$$= \tilde{\varrho}\tilde{r} + \tilde{\boldsymbol{\sigma}}^T \cdot \boldsymbol{\nabla}_x \tilde{\boldsymbol{v}} + \boldsymbol{\varsigma}^T \cdot \boldsymbol{\nabla}_m \tilde{\boldsymbol{v}} \tag{7.33}$$

Note that the *mesoscopic balance of entropy* is of no special interest. In general the mesoscopic entropy production is not definite and, therefore, the second law of thermodynamics has to be formulated as usual by the macroscopic balance of entropy.

The mesoscopic concept does not introduce any new balance for the additional fields because these are included in the mesoscopic space. However, the new mesoscopic distribution function $\tilde{f}(\boldsymbol{m}, \boldsymbol{x}, t)$ and the velocity of mesoscopic change $\tilde{\boldsymbol{u}}$, require additional equations. The mesoscopic distribution function has a generic balance of its own, see below. A general equation for the velocity of mesoscopic change $\tilde{\boldsymbol{u}}$ cannot be stated, the specific form of this balance depends on the microstructure of the material. Examples are given in [238, 266] for liquid crystals and in [268, 351] for Griffith cracks in linear elastic material. In our case of a porous composite the velocity of mesoscopic change is simply the velocity of change of void radius a defined in equation (7.7) as void expansion velocity $\dot{a}$.

By definition (7.16) the mesoscopic distribution function satisfies a balance equation of it own. Starting with the mesoscopic mass balance (7.26) and using the relation (7.20) a straightforward calculation gives [38]

$$\frac{\partial}{\partial t}\left[\tilde{f}\,\varrho(\boldsymbol{x},t)\right] \;+\; \boldsymbol{\nabla}_x \cdot \left[\varrho(\boldsymbol{x},t)\,\tilde{f}\,\tilde{\boldsymbol{v}}\right] + \boldsymbol{\nabla}_m \cdot \left[\varrho(\boldsymbol{x},t)\,\tilde{f}\,\tilde{\boldsymbol{u}}\right] = 0. \tag{7.34}$$

Equation (7.34) is a function of the macroscopic mass density $\varrho(\boldsymbol{x},t)$. Inserting (7.20) shows that (7.34) is highly non-linear. Taking into account the macroscopic mass balance results in the

- *balance of the mesoscopic distribution function*

$$\frac{\partial \tilde{f}}{\partial t} + \boldsymbol{\nabla}_x \cdot (\tilde{f}\,\tilde{\boldsymbol{v}}) + \boldsymbol{\nabla}_m \cdot (\tilde{f}\,\tilde{\boldsymbol{u}}) = -\frac{\tilde{f}}{\varrho}\left[\frac{\partial \varrho}{\partial t} + \tilde{\boldsymbol{v}} \cdot \boldsymbol{\nabla}_x \varrho\right]. \tag{7.35}$$

where $\varrho \equiv \varrho(\boldsymbol{x},t)$. With the help of a mesoscopic differential operator $\mathcal{D}[\cdot] := \frac{\partial}{\partial t}[\cdot] + \tilde{\boldsymbol{v}} \cdot \boldsymbol{\nabla}_x[\cdot]$ and with the relation $\frac{\mathcal{D}\rho}{\rho} = \mathcal{D}(\ln \rho)$ the balance equation (7.35) can be written as

$$\frac{\partial \tilde{f}}{\partial t} + \boldsymbol{\nabla}_x \cdot \left[\tilde{f}\,\tilde{\boldsymbol{v}}\right] + \boldsymbol{\nabla}_m \cdot \left[\tilde{f}\,\tilde{\boldsymbol{u}}\right] + \tilde{f}\,\mathcal{D}[\ln \varrho(\boldsymbol{x},t)] = 0\,. \tag{7.36}$$

Note that the macroscopic mass density $\varrho(\boldsymbol{x}, t)$ influences the mesoscopic distribution function $\tilde{f}$. This macroscopic influence on mesoscopic quantities is sometimes denoted as a "mean field" theory [238].

The macroscopic balances can be recovered from the mesoscopic ones by replacing the mesoscopic space by space-time $(\boldsymbol{x}, t)$. This is clear from equation (7.21) in the special case of the mass density and can be extended to the general case. To this end we need to relate all macroscopic quantities by their mesoscopic background,

$$\boldsymbol{v}(\boldsymbol{x}, t) := \int_{\mathcal{M}} \tilde{f} \, \tilde{\boldsymbol{v}} \, d\boldsymbol{m} \,, \qquad e(\boldsymbol{x}, t) := \int_{\mathcal{M}} \tilde{f} \, \tilde{e} \, d\boldsymbol{m} \,, \qquad \text{etc.} \tag{7.37}$$

Without a formal axiomatic setting we illustrate the procedure by Figure 7.4.
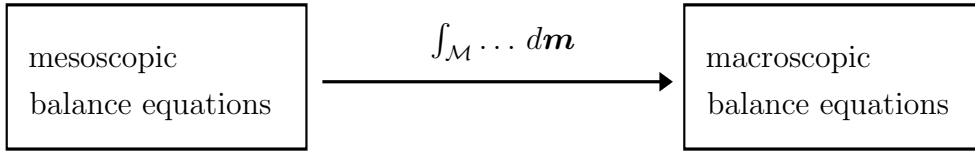
Figure 7.4.: Relation between mesoscopic and macroscopic balances

7.2.3. Balance of the mesoscopic distribution function for a porous composite

When modelling a material as an ensemble of spherical shells (Figure 7.2) the crucial variables for the mesoscopic description are the mesoscopic void number density $\tilde{N}_V$ or its normalized counterpart $\tilde{f} = \tilde{N}_V / N_V$, see equation (7.16). Following the strategy of the foregoing paragraph the balance equation for $\tilde{N}_V$ is found to be

$$\frac{\partial \tilde{N}_V}{\partial t} + \boldsymbol{\nabla}_x \cdot (\tilde{N}_V \tilde{\boldsymbol{v}}) + \frac{\partial}{\partial a}(\tilde{N}_V \dot{a}) = \tilde{\Pi}^{\tilde{N}_V}. \tag{7.38}$$

Equation (7.38) states that the temporal change of the number of voids with radius a per volume is attributed to the (in and out) flux of voids of radius a. The right hand side $\tilde{\Pi}^{\tilde{N}_V} \equiv \tilde{\Pi}^{\tilde{N}_V}(a, t)$ represents a source term and will be specified shortly. In case of a constant void number we get a conservation equation, i.e., $\tilde{\Pi}^{\tilde{N}_V} = 0$. Furthermore, the mesoscopic translational velocity $\tilde{\boldsymbol{v}}(a, t)$ does not depend on the radius a, i.e., it is the same for all shells and voids. It can be identified with the macroscopic velocity

of the continuum element, $\tilde{\boldsymbol{v}}(a, \boldsymbol{x}, t) = \boldsymbol{v}(\boldsymbol{x}, t)$, because in the solid materials under consideration here the voids cannot move independently with respect to the surrounding material.

In order to specify the balance equation for the mesoscopic void distribution $\tilde{f}$ we multiply equation (7.38) with $\frac{1}{N_V}$. With (7.16) and a straightforward calculation one can find

$$\frac{\partial \tilde{f}}{\partial t} + \boldsymbol{\nabla}_x \cdot (\tilde{f} \boldsymbol{v}) + \frac{\partial}{\partial a}(\tilde{f} \dot{a}) = \tilde{\Pi}^{\tilde{N}_V} + \frac{\tilde{f}}{N_V}\left(\frac{\partial N_V}{\partial t} + \boldsymbol{v} \cdot \boldsymbol{\nabla}_x N_V\right). \tag{7.39}$$

The right hand side of equation (7.39) represents the production of voids in two different ways:

1. The mesoscopic void number production $\tilde{\Pi}^{\tilde{N}_V}$ accounts for sources or sinks of voids with a specific radius a, namely the change of $\tilde{N}_V(a, t)$ caused by production.

2. The expression in brackets stands for the temporal change of the macroscopic void number in a volume element observable by a co-moving observer

$$\left(\frac{\partial N_V}{\partial t} + \boldsymbol{v} \cdot \boldsymbol{\nabla}_x N_V\right) = \frac{dN_V}{dt} \equiv \dot{N}_V. \tag{7.40}$$

   Note that the influence of the macroscopic void number density N_V on distribution function $\tilde{f}$ represents the mean field effect.

Let us define the macroscopic void number production by

$$\Pi^{N_V} := \dot{N}_V \qquad \text{with} \qquad \Pi^{N_V} = \int_{a_0}^{\infty} \tilde{\Pi}^{\tilde{N}_V}\, da\ . \tag{7.41}$$

Consequently, equation (7.39) has two parts of production: the mesoscopic and the macroscopic void number production. In summary the following compact form of the mesoscopic distribution function is obtained

$$\frac{\partial \tilde{f}}{\partial t} + \boldsymbol{\nabla}_x \cdot (\tilde{f} \boldsymbol{v}) + \frac{\partial}{\partial a}(\tilde{f} \dot{a}) = \frac{\tilde{f}}{N_V}\Pi^{N_V} + \tilde{\Pi}^{\tilde{N}_V}. \tag{7.42}$$

Obviously equation (7.42) and (7.35) have the same structure, except for the mesoscopic production term $\tilde{\Pi}^{\tilde{N}_V}$, which is zero in equation (7.35) because of mass conservation. (In the special case of no void production both equations are identical.) However, Π^{N_V} and $\tilde{\Pi}^{\tilde{N}_V}$ are not independent. This is evident from equation (7.41)$_2$, where Π^{N_V} can be interpreted as the sum over all void productions $\tilde{\Pi}^{\tilde{N}_V}$ with specific radius a.

By comparison of equation (7.42) and (7.35) we find

$$\frac{\dot{\rho}}{\rho} = \frac{\dot{N_V}}{N_V} + \frac{\tilde{\Pi}^{\tilde{N}_V}}{\tilde{f}} = \frac{\Pi^{N_V}}{N_V} + \frac{\tilde{\Pi}^{\tilde{N}_V}}{\tilde{f}} \ . \tag{7.43}$$

If an initial mesoscopic void number density $\tilde{N}_V(a, t = 0)$ is known the quantities $N_V(t = 0)$ and $\tilde{f}(a, t = 0)$ can be calculated. Together with an ansatz for the mesoscopic void number production $\tilde{\Pi}^{\tilde{N}_V}(a, t)$ the values for Π^{N_V} and $N_V(t) = N_V(t = 0) + t\,\Pi^{N_V}$ can be determined. Additionally, if a constitutive law for void expansion velocity $\dot{a}$ exists a (numerical) solution of equation (7.42) is possible.

7.3. Dynamic growth of voids under remote hydrostatic pressure and tension

In the preceding section we have established the theoretical frame for a mesoscopic theory of void growth in a continuum. By means of balance equation (7.42) the evolution of voids in a general material is predictable. For application to the specific materials we envision here, the constitutive equations for the void velocities within the void ensemble, $\dot{a}(\boldsymbol{x}, t)$, remain to be specified.

In this section we establish in a fully variational approach a set of constitutive relations for void growth. To this end, energy contributions of an expanding (or shrinking) void ensemble will be derived as functions of the void radii a, b, its distribution and time derivatives as well as of the temperature, the initial geometry and the material parameter. In particular we shall see that for an incompressible matrix material the state space $\mathcal{Z}$, i.e., the domain of the constitutive equations, reduces to

$$\mathcal{Z} = \{T, a, \epsilon, \dot{\epsilon}\} \quad \Rightarrow \quad \dot{a} = \dot{a}(\mathcal{Z}), \tag{7.44}$$

where T is the absolute temperature and ϵ is an effective strain within the spherical shell (to be specified later) and $\dot{\epsilon}$ describes its temporal development. Following the ideas of classical continuum thermodynamics [339] we expect the energetic terms to compete among themselves and the optimal internal process is that which minimizes the overall energy function. The insistence on energy minimization in statics (presuming the existence of a stable equilibrium configuration, cf., equation (4.17)) will be generalized to the dynamic process of void growth by recourse to Hamilton's variational principle of stationary action (4.39).

7.3.1. Constitutive model

With a view to ensuring a variational structure, we postulate the existence of a deformation energy density function

$$A = A(\dot{a}) \tag{7.45}$$

where all dependencies other than of $\dot{a}$ are understood in the sense of the state space (7.44). Additionally we require the time-dependent material equations to derive from a total dual kinetic potential $\Psi^*(\dot{a})$ following the strategy of [257, 282]. The external power P put into a composite of volume V is a function of the remotely applied pressure history $p(t)$:

$$P(\dot{a}) = \frac{d}{dt}\left[p(t)\,V(a,t)\right]. \tag{7.46}$$

Now an action integral $\mathcal{I}(\dot{a})$ can be formulated as the sum of all contributions of the rate of energy $\dot{A}$, of potential Ψ^* and of external power P. Hamilton's principle simply requires stationarity of the action integral

$$\delta\mathcal{I}(\dot{a}) = 0, \tag{7.47}$$

or, equivalently,

$$\frac{\delta}{\delta\dot{a}}\left[\dot{A} + \Psi^* - P\right] = 0. \tag{7.48}$$

Let us now specify the constitutive equations for, first, an elastic, and second, a viscoplastic material. Exploiting the spherical symmetry of the model we can derive from the kinematics outlined in Section 7.1.2 the principle stresses and strains within one shell. Correspondingly, the velocity over the current configuration (7.7) defines the strain rate as

$$\dot{\varepsilon}(r,t) = \frac{\partial\dot{r}}{\partial r} = \frac{2a^2(t)}{r^3(t)}\dot{a}(t). \tag{7.49}$$

Note that with the deformation mapping (7.4) equation (7.49) as well as all subsequent equations depending on the current radius r can be expressed in terms of the current void radius a and the initial geometry.

Elastic energy

The elastic response of the material may be described by a general Ogden material, cf. Section 3.4, which will here be simplified to a Neo-Hookean Material with an energy density of the form

$$\frac{\mu^*(a)}{2}\left(\lambda_1^2 + \lambda_2^2 + \lambda_3^2 - 3\right), \tag{7.50}$$

where $\lambda_{1,2,3}$ are the principle elastic stretches in tangential and radial directions, respectively, and $\mu^*(a)$ is the effective shear modulus (7.14). For a single spherical shell it evaluates to

$$\mu^*(a) = \mu_0\Big(1 - \frac{a^3(15\kappa_0 + 20\mu_0)}{b^3(9\kappa_0 + 4\mu_0)}\Big) \tag{7.51}$$

with κ_0 and μ_0 denoting the bulk and shear modulus of the virgin material with initial void volume fraction f_{V0}, respectively. By the geometry of the spherical shell and by incompressibility of the matrix material we find

$$\lambda \equiv \lambda_1 = \lambda_2 = \frac{r}{r_0} \quad \text{und} \quad \lambda_3 = \frac{1}{\lambda^2} = \frac{r_0^2}{r^2}. \tag{7.52}$$

The total elastic energy of one spherical shell follows by integration over the volume as

$$\tilde{W}^e(a, T) = \int_a^b \frac{\mu^*(a)}{2}\Big(2\big(\frac{r}{r_0}\big)^2 + \big(\frac{r_0}{r}\big)^4 - 3\Big)4\pi r^2\,dr \tag{7.53}$$

$$= 2\mu^*(a)\Big(a_0^3 - b_0^3 - \frac{a_0}{a}(2a^3 - a_0^3) + \frac{b_0}{b}(2b^3 - b_0^3)\Big). \tag{7.54}$$

Consider now an ensemble of spherical shells characterized by the mesoscopic distribution function (7.16) of Section 7.2.1. The total elastic energy stored by the void ensemble is the first moment of the elastic energy stored by all individual spherical shells. Consequently, the elastic work of deformation for the void ensemble is

$$W^e = \int_0^\infty \tilde{f}\,\tilde{W}^e(a, T)\,da, \tag{7.55}$$

where we dropped on the left hand side the arguments for convenience.

Note that in (7.51) and (7.54) radius b can be expressed as a function of a by volume constraint (7.6). To ensure constraint (7.6) we presume volumetric incompressibility of the material surrounding the void. This assumption is, of course, made to ease the derivation of a constitutive model but it is also justified by the particular materials under consideration. Materials with a significant elastic range are, e.g., bio-materials and rubbery polymers, both are (almost) incompressible. On the other hand, metals deform elasto-plastically where the plastic deformation is volume preserving and the compressible elastic range is small, its influence on void growth may easily be neglected.

Stored plastic work

To analyze the void growth in a time-dependent plastic material we follow a strategy adopted from [254] and neglect the elastic expansion of the void ensemble. All void

growth is attributed to plasticity. (Note that elasticity of the voided material may easily be added, see [365].) Thus the absolute value of strain rate (7.49) defines the rate of the effective von Mises strain, $\dot{\varepsilon}^p \equiv |\dot{\varepsilon}(r,t)|$. Presuming a monotonic void growth, equation (7.49) can be integrated to give

$$\varepsilon^p = \left| -\frac{2}{3}\ln\left(1 + \frac{a^3 - a_0^3}{r^3 - (a^3 - a_0^3)}\right)\right| = \frac{2}{3}\ln\left(1 + \frac{a^3 - a_0^3}{r_0^3}\right). \tag{7.56}$$

Let us consider classical von Mises plasticity with power law hardening, i.e., the yield stress obeys a hardening law of the form (6.9). Furthermore, we assume thermal-softening of the power-law form (6.18). The stored plastic energy density follows from the rate of plastic straining by

$$\int_0^t \sigma_y \dot{\varepsilon}^p \, d\bar{t} = \int_0^{\varepsilon^p} \sigma_y d\bar{\varepsilon}^p. \tag{7.57}$$

By volume integration the stored plastic energy of one spherical shell can be computed,

$$\tilde{W}^p(a,b,T) = \int_a^b \frac{n\sigma_{y0}(T)\varepsilon_{y0}^p}{n+1}\left(\left(1 + \frac{\varepsilon^p}{\varepsilon_{y0}^p}\right)^{\frac{n+1}{n}} - 1\right)4\pi r^2 dr. \tag{7.58}$$

Evaluating (7.58) with (7.56) gives

$$\tilde{W}^p(a,b,T) = \frac{n\sigma_{y0}\varepsilon_{y0}^p}{n+1}\frac{4\pi a^3}{3}g(a,b;n), \tag{7.59}$$

where, with substitution $x := r^3/a^3$,

$$g(a,b;n) = \int_0^{b^3/a^3}\left(1 + \frac{2}{3\varepsilon_{y0}^p}\ln\frac{x}{x-1+a_0^3/a^3}\right)^{\frac{n+1}{n}} dx. \tag{7.60}$$

Note that because of the plastic incompressibility of the matrix material the dependence of $\tilde{W}^p$ on shell radius b can be eliminated by relation (7.5). We obtain

$$\tilde{W}^p(a,T) = \frac{n\sigma_{y0}\varepsilon_{y0}^p}{n+1}\frac{4\pi a_0^3}{3}g(a;n), \tag{7.61}$$

$$g(a;n) = \int_0^{b_0^3/a_0^3}\left(1 + \frac{2}{3\varepsilon_{y0}^p}\ln\left(1 + \frac{1}{x}\left(\frac{a^3}{a_0^3} - 1\right)\right)\right)^{\frac{n+1}{n}} dx. \tag{7.62}$$

It is worth mentioning that an analytical integration of (7.60/7.62) is possible only in the special case $n \to \infty$.

Assume now that the void radius history $a(t)$ grows monotonically from a_0 to a_1, then decreases monotonically from a_1 to a_2, and so on. Then the integration of (7.49) with respect to the time gives

$$\varepsilon^p(r_0, t) = \frac{2}{3} \ln\left(\frac{a_1{}^3 + r_0^3 - a_0^3}{r_0^3}\right) + \frac{2}{3} \ln\left(\frac{a_1{}^3 + r_0^3 - a_0^3}{a_2{}^3 + r_0^3 - a_0^3}\right) + \frac{2}{3} \ln\left(\frac{a_3{}^3 + r_0^3 - a_0^3}{a_2{}^3 + r_0^3 - a_0^3}\right) + \cdots$$

Grouping terms corresponding to increasing and decreasing intervals yields

$$\varepsilon^p(r_0, t) = \frac{2}{3} \ln\left(\frac{q(t)^3 + r_0^3 - a_0^3}{r_0^3}\right) + \frac{2}{3} \ln\left(\frac{a^3(t) + r_0^3 - a_0^3}{q^3(t) + r_0^3 - a_0^3}\right), \tag{7.63}$$

or, summarized,

$$\varepsilon^p(r_0, t) = \frac{2}{3} \ln\left(\frac{\left(a^3(t) + r_0^3 - a_0^3\right)^2}{r_0^3(t)\left(q^3(t) + r_0^3 - a_0^3\right)}\right). \tag{7.64}$$

Here

$$q(t) = \max_{0 \leq \tau \leq t} a(\tau) \tag{7.65}$$

defines the maximum attained void size. Evidently, it holds

$$\dot{q}(t) = \begin{cases} \dot{a}(t) & \text{if } a(t) = q(t) \text{ and } \dot{a}(t) > 0 \\ 0 & \text{otherwise} . \end{cases} \tag{7.66}$$

In particular, $q(t)$ is a monotonically increasing function for every history of $a(t)$. The stored plastic work in the spherical shell surrounding the void is then

$$\tilde{W}^p(a, q, T) = \int_{a_0}^{b_0} \frac{n\sigma_{y0}(T)\varepsilon_{y0}^p}{n+1}\left[\left(1 + \frac{1}{\varepsilon_{y0}^p}\frac{2}{3}\ln\frac{(q^3 + r_0^3 - a_0^3)}{r_0^3(a^3 + r_0^3 - a_0^3)}\right)^{\frac{n+1}{n}} - 1\right]4\pi r_0^2 dr. \tag{7.67}$$

The stored energy functions (7.58-7.67) are attributed to the growth of one void of radius $a(t)$. For an ensemble of spherical shells characterized by the mesoscopic distribution function (7.16) the plastic work is given by

$$W^p = \int_0^\infty \tilde{f}\, \tilde{W}^p(a, T)\, da. \tag{7.68}$$

Kinetic energy

In an analogous manner the kinetic energy of an expanding void ensemble can be determined. With velocity (7.7) and energy (2.23) the kinetic energy of an expanding (or collapsing) spherical shell is computed to be

$$
\begin{aligned}
\tilde{K}(a, \dot{a}) &= \int_a^b \frac{1}{2} \varrho_0\, v_r^2\, 4\pi r^2 dr \\
&= 2\pi \varrho\, a^4 \left(\frac{1}{a} - \frac{1}{b}\right) \dot{a}^2,
\end{aligned}
\tag{7.69}
$$

where ϱ_0 is the initial mass density of the matrix material. In the dilute limit, the total kinetic energy attributed to the growth of the void ensemble is the "weighted sum" of the kinetic energies due to the expansion of each individual void,

$$
K = \int_0^\infty \tilde{f}\, \tilde{K}(\dot{a}, a)\, da,
\tag{7.70}
$$

where $\dot{a} \equiv \dot{a}(a)$ is understood to be the expansion velocity of the void with current radius a.

Surface energy

The surface energy of one void with radius $a(t)$ is

$$
\tilde{S}(a) = 4\pi a^2 \gamma
\tag{7.71}
$$

where γ is the surface energy per unit undeformed area [N/m]. The surface energy of the void ensemble is

$$
S = \int_0^\infty \tilde{f}\, \tilde{S}(a)\, da.
\tag{7.72}
$$

Rate sensitivity

Assuming a linear rate sensitivity (cf. Section 6.2.3) we define a dual kinetic potential for one spherical shell as

$$
\begin{aligned}
\tilde{\Psi}^*(\dot{a}, a) &= \int_a^b \frac{\sigma_0(T)}{2\dot{\varepsilon}_{y0}^p}\left(\frac{2a^2|\dot{a}|}{r^3}\right)^2 4\pi r^2 dr \\
&= \frac{\sigma_0(T)}{\dot{\varepsilon}_{y0}^p}\int_{a_0}^{b_0}\left(\frac{a^2|\dot{a}|}{a^3 + r_0^3 - a_0^3}\right)^2 8\pi r_0^2 dr_0 \\
&= \frac{2\sigma_0(T)}{\dot{\varepsilon}_{y0}^p}\frac{4\pi a^3}{3}|\frac{\dot{a}}{a}|^2\left(1 - \frac{a^3}{a^3 + b_0^3 - a_0^3}\right)
\end{aligned}
\tag{7.73}
$$

where $\dot{\varepsilon}_{y0}^p$ is the reference strain rate.

Vacancy diffusion

Consider a small void, possibly just a few atomic spacing in diameter, surrounded by a supersaturated vacancy concentration c_b generated, e.g., by unbalanced diffusion or by plastic deformation [252]. To render the problem analytically tractable, we idealize the defect to be spherical with characteristic radius a, the diffusion constants to be isotropic, and we assume that a steady state vacancy concentration profile is maintained all times, i.e., $\partial c_{\text{vac}}/\partial t \ll \partial J_{\text{vac}}/\partial x$, where J_{vac} is the vacancy flux. This eliminates the time dependence of the solution and confers spherical symmetry to the problem. With b being the (large) radius of the basin of attraction around the void, cf., Figure 7.5, and $b/a \to \infty$, the diffusion equation for volume concentration c reduces to the following boundary value problem in spherical coordinates:

$$
\frac{\partial}{\partial r}\left(r^2 \frac{\partial c}{\partial r}\right) = 0 ,
\tag{7.74}
$$

subject to the boundary conditions

$$
c(r = b) = c_b ,
\tag{7.75}
$$

$$
c(r = a) = c_a = c_0 e^{d/a}.
\tag{7.76}
$$

Here the equilibrium vacancy concentration near a free surface is given by

$$
c_0 = e^{-E_v/kT}
\tag{7.77}
$$

and the concentration c_a at the void surface follows as above with $d = \frac{2\gamma V_V}{kT}$. In these expressions γ is the surface tension, V_V the atomic volume, k the Bolzmann constant

and E_v is the free-energy gain/loss resulting from adding a vacancy into the system. The solution of (7.74)-(7.76) is elementary, namely

$$c(r) = c_b - (c_b - c_a)\frac{a}{r} \ . \tag{7.78}$$

For void growth to take place there must be a net flux of vacancies into the void, which requires $c_b > c_a$. This in turn requires

$$c_b > c_0 \exp\left(\frac{2\gamma V_V}{a_0 kT}\right). \tag{7.79}$$

For very small values of a_0 or c_b this inequality is not satisfied and voids fail to grow. However, the value of radius a_0 which equals relation (7.79) at a given value of c_b marks the inception of void growth, i.e., a critical nucleation size.
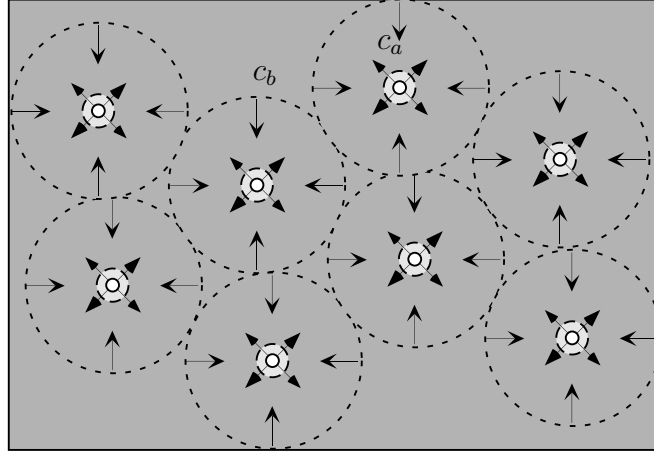
Figure 7.5.: Model of vacancy diffusion.

Furthermore, the flux J is defined to be the change of volume per unit area and time, viz.

$$J(r) = -\frac{1}{4\pi a^2}\frac{d}{dt}\left(\frac{4}{3}\pi a^3\right) = -\dot{a}(r) \ . \tag{7.80}$$

Applying additionally Fick's law $J(r) = -D\frac{\partial c}{\partial r}$ to equation (7.80) yields for voids of radius a by means of equation (7.78):

$$\dot{a}(a) = \frac{D}{a}\left(c_b - c_0 e^{d/a}\right) \ , \tag{7.81}$$

where D is the vacancy diffusion coefficient. As the void grows, c_a decreases according to equation (7.76) which amplifies the concentration gradient towards the void and, thus, accelerates the void growth. The rate of void growth may be computed by means of equation (7.81).

Following the strategy of Wagner [354] but allowing for an additional source term $s(t)$ the background vacancy concentration c_b can be subjected to a "void volume balance" of the form:

$$
\dot{c}(t) = s(t) - \int_0^\infty \tilde{f}\,\dot{a}(a)\,4\pi a^2\,\mathrm{d}a
$$

$$
= s(t) - \int_0^\infty \tilde{f}\,D\big(c_b - c_0 e^{d/a}\big)4\pi a\,\mathrm{d}a\,,
\tag{7.82}
$$

where, again, $\tilde{f}$ is the void size distribution function. The source term $s(t)$ in equation (7.82) represents a *vacancy production rate* which may be caused, e.g., by plastic deformation.

In addition we ask for an energetic formulation of the above vacancy diffusion problem. In particular, we look for a diffusion rate potential $\Phi(\dot{a}, a)$, for which the variational form:

$$
\frac{\delta\Phi(\dot{a}, a)}{\delta\dot{a}} = 0
\tag{7.83}
$$

holds. For that reason we multiply equation (7.81) with a characteristic factor E_v/D. A subsequent integration w.r.t. $\dot{a}$ finally results in

$$
\Phi = \frac{E_v\dot{a}^2}{2D} - \frac{E_v\dot{a}}{a}\big(c_b - c_0 e^{d/a}\big).
\tag{7.84}
$$

External work

Finally, the external power put into one spherical shell by an applied (positive or negative) pressure $p(t)$ is

$$
\tilde{P}(\dot{a}, a) = \frac{d}{dt}\Big(p(t)\,\frac{4\pi}{3}b^3\Big) = p(t)\,4\pi a^2\dot{a}.
\tag{7.85}
$$

If, as outlined in [254], the pressure p derives from a potential through a relation of the type

$$
p = \frac{\partial}{\partial a}\hat{\tilde{W}}^{ex}\big(V(a)\big)
\tag{7.86}
$$

where $V(a)$ is the void volume change, then equation (7.85) can be integrated to give the external work applied on a spherical shell

$$\tilde{W}^{ex}(a) = \hat{\tilde{W}}^{ex}\big(\frac{4\pi}{3}(a^3 - a_0^3)\big). \tag{7.87}$$

The total external work of the remote pressure applied to the composite follows with similar arguments as above,

$$W^{ex} = \int_0^\infty \tilde{f}\,\tilde{W}^{ex}(a)\,da. \tag{7.88}$$

Governing differential equation

With the aim to establish Hamilton's principle (7.48) we summarize the energetic terms and derive the free energy rate

$$\dot{A} = \int_0^\infty \tilde{f}\,\Big(\frac{\partial\tilde{W}^e}{\partial a} + \frac{\partial\tilde{W}^p}{\partial a} + \frac{\partial\tilde{S}}{\partial a} \underbrace{- \frac{\partial\tilde{K}}{\partial a} + \frac{d}{dt}\frac{\partial\tilde{K}}{\partial\dot{a}}}_{\text{inertia}}\Big)\dot{a}\,da. \tag{7.89}$$

where we have accounted for the work of d'Alembert inertia forces in accelerated processes. The external power applied to a spherical shell composite evaluates simply to

$$P = \int_0^\infty \tilde{f}\,\frac{\partial\tilde{W}^{ex}}{\partial a}\,\dot{a}\,da, \tag{7.90}$$

whereas the total dual kinetic potential including the diffusion potential is

$$\Psi^* = \int_0^\infty \tilde{f}\,\Big(\psi^*(\dot{a}, a) + \frac{E_v\dot{a}^2}{2D} - \frac{E_v\dot{a}}{a}\big(c_b - c_0 e^{d/a}\big)\Big)\,da. \tag{7.91}$$

The equation of motion of the voids of size a now follows from the variational form (7.48) as

$$-\frac{\partial W^{ex}}{\partial a} + \frac{\partial W^e}{\partial a} + \frac{\partial W^p}{\partial a} + \frac{\partial S}{\partial a} + \frac{\partial\psi^*}{\partial\dot{a}}$$
$$-\frac{\partial K}{\partial a} + \frac{d}{dt}\frac{\partial K}{\partial\dot{a}} + \frac{E_v\dot{a}}{D} - \frac{E_v}{a}\big(c_b - c_0 e^{d/a}\big) = 0. \tag{7.92}$$

Equation (7.92) can now be solved (numerically) to provide a constitutive law for $\dot{a}$ required to determine the mesoscopic distribution function (7.16). Once $\dot{a}$ is known to be the resulting velocity of the voids of size a, then equation (7.38) governs the evolution of the mesoscopic distribution function (7.16).

114
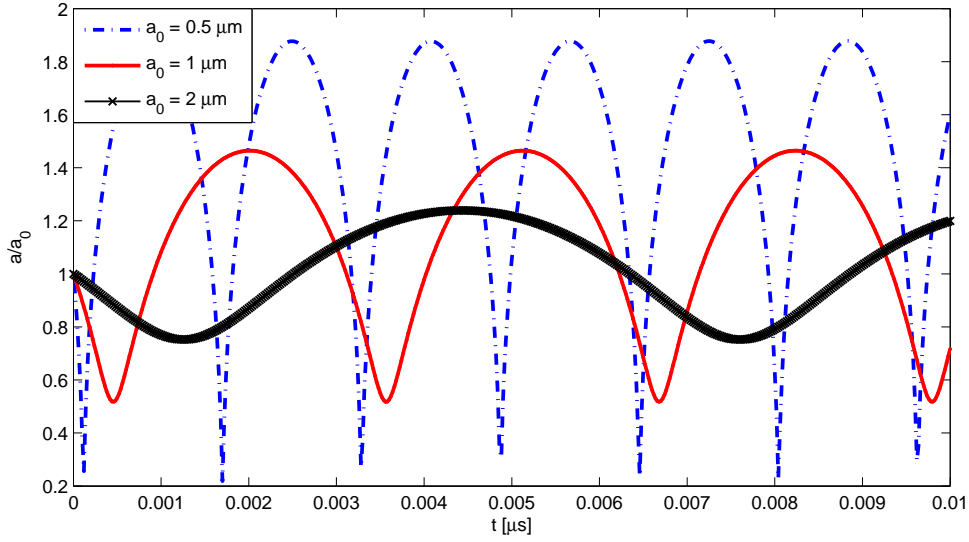
Figure 7.6.: Void growth in an elastic medium induced by a pressure impulse.

7.3.2. Analysis of an ensemble of voids of equal size in an elastic material

In an attempt to illustrate the capability of the constitutive model derived in the preceding section we start here with the special case of a void ensemble with an average radius of size $\bar{a}$, i.e., the mesoscopic distribution function $\tilde{f}$ has the form of a Dirac impulse at a_0 and retains this shape for the expanding voids of radius $\bar{a} \geq a_0$.

At first we study void expansion in an elastic material, as, e.g., the growth of pores in a soft tissue. Then, equation (7.92) simplifies to

$$\frac{\partial W^e}{\partial a} - \frac{\partial K}{\partial a} + \frac{d}{dt}\frac{\partial K}{\partial \dot{a}} = \frac{\partial W^{ex}}{\partial a} \tag{7.93}$$

We subject an elastic specimen to a sudden pressure impulse with magnitude of 1000 GPa within $10^{-6}\mu$s. The pores in the elastic material with material data of $\mu = 1000$ MPa and $\varrho = 1000$ kg/m^3 are assumed to be initially of size $a_0 = 1\mu$m. Since the matrix material in the porous composite is presumed to be incompressible all change of volume is a consequence of pore expansion or shrinkage. Therefore, the pressure impulse forces the pores to close, i.e., $\bar{a} \to 0$. After the impulse has passed, the voids expand again. However, by elasticity and inertia the attained maximal void radius $\bar{a}_{max}$ is much bigger than the initial radius a_0, the voids oscillate. This process is similar to the effect of

cavitation observed in fluids which are subjected to (high intensity) pressure waves [123, 155, 313].

Because in our simplified ansatz (7.93) there is no dissipation, the process of opening and closure of pores goes on periodically. It is interesting to note, that the ratio of $\bar{a}_{max}/a_0$ gets bigger the smaller the initial void is whereas the duration of one cycle raises with the initial void radius, see Figure 7.6.

7.3.3. Analysis of an ensemble of voids of equal size in a visco-plastic material

In the following we study void growth under different loading regimes for a typical metal with material data of Table 7.3.1. Additional temperature and rate effects are not considered. Moreover, for ease of reading we write $a \equiv \bar{a}$.

E [GPa]	ν	ϱ [kg m^{-3}]	σ_{y0} [MPa]	$\varepsilon^p{}_{y0}$	n	γ [N/m]
69	0.33	2700	80	0.0012	10	5

Table 7.3.1. Material parameter representative of aluminum.

Quasistatic void growth

In case of a slow loading regime we do not have inertia effects and the material can considered to be time-independent. Then, equation (7.92) reduces to the first three terms. Assuming a constant remotely applied tension $\bar{p}$ equation (7.92) evaluates to

$$4\pi\bar{p}a^2 = \frac{n\sigma_{y0}\varepsilon^p_{y0}}{n+1}\frac{4\pi a_0{}^3}{3}\, g'(a;n) + 8\pi\gamma a, \tag{7.94}$$

where $g'(a;n)$ denotes the derivative of integral (7.62) w.r.t. radius a. Solving the plastic energy term of (7.94) for the special case of ideal plasticity, i.e., $n \to \infty$, and dividing the expression by $4\pi a^2$ results in

$$\bar{p} = \frac{2\sigma_{y0}}{3}\big(\ln(a^3 - a_0^3 + b_0^3) - \ln(a^3)\big) + \frac{2\gamma}{a}. \tag{7.95}$$

Expression (7.95) defines an algebraic relation between applied pressure and void radius a. Note that we neglect in our constitutive model a certain elastic range of void expansion and, therefore, equation (7.95) is actually an inequality determining a critical applied

tension necessary to induce any void to growth plastically. This corresponds to the concept of critical cavitation pressure as discussed, e.g., in [116, 254, 365]. Only if the applied tension exceeds a cavitation pressure p_y void expansion happens.

$$\bar{p} \geq p_y \quad = \quad \frac{2\sigma_{y0}}{3} \ln\left(1 + \frac{b_0^3 - a_0^3}{a^3}\right) \;+\; \frac{2\gamma}{a} \tag{7.96}$$

The cavitation pressure depends on the material parameter and on the initial and current void volume fraction. For ideal plastic material relation (7.96) defines a high initial cavitation pressure which decreases immediately after the voids start to grow, see Figure 7.7. In general, for a hardening material the slope is smaller, the cavitation pressure reduces slowly with rising void size.
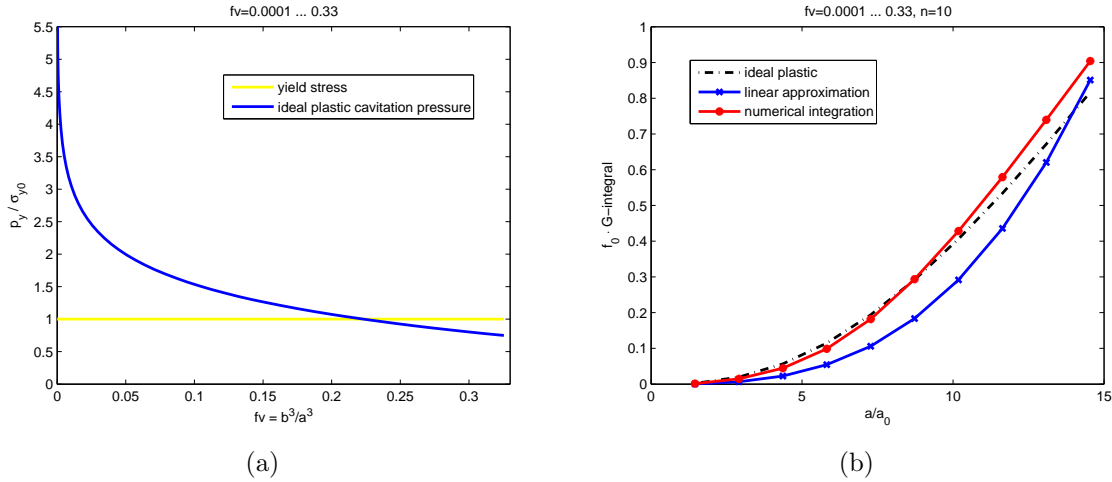
Figure 7.7.: Quasistatic regime a) ideal plastic cavitation pressure depending on void volume fraction f_V, b) solution and approximation of equation (7.60) divided by $(1.5\varepsilon_{y0}^p)^{-1-1/n}$

For a hardening material ($n \in \mathbb{N}$) an analytical expression for p_y cannot be obtained because the derivative of integral (7.60/7.62) w.r.t. a cannot be solved analytically. If a repeated numerical solution for every value of a appears to be too cumbersome, we suggest a simple approximation of (7.62) in the form

$$g(a; n) \approx h_n \left(\frac{2}{3\varepsilon_{y0}^p}\right)^{\frac{n+1}{n}} \left(\frac{a^3}{a_0^3} - 1\right), \tag{7.97}$$

where h_n is a constant depending on hardening exponent n. This constant needs to be fitted to the values of integral (7.60), once numerically evaluated over a range of realistic

(initial and final) void volume fractions, see Figure 7.7. We proceed here with

$$h_n = 2.21 \quad \text{for} \quad n = 10. \tag{7.98}$$

Note that approximation (7.97) may also provide a way to fit the critical cavitation pressure to values known from experiments, if available.

Assuming from now on a hypercritical tension $\bar{p}$ let us discuss void growth due to the equations (7.94–7.96). The yield stress of a material, usually in the range of some MPa, weights the first term in these equations much stronger than the surface energy per unit surface, for material data see Table 7.3.1. This effect is compensated by the $1/a$ term for very small void sizes, e.g., a void of vacancy size up to maximal 100-times of it (approx. 0.5 nm – 50 nm). Only in this regime the surface energy contributes significantly to void growth. For bigger voids the second term in equations (7.95, 7.96) is negligible.

Summarizing these considerations we define the quasistatic initial cavitation pressure for void expansion in an ideal plastic material by

$$p_{y0} = \frac{2\sigma_{y0}}{3} \ln\left(\frac{1}{f_{V0}}\right) \tag{7.99}$$

and in a hardening material by

$$p_{y0} = \frac{(n+1)\sigma_{y0}}{n} \frac{4\pi}{3} a_0^3 \, \varepsilon_{y0}^p \, g'(a;n) \approx \frac{(n+1)\sigma_{y0}}{n} \, \varepsilon_{y0}^p \, h_n, \tag{7.100}$$

respectively.

Dynamic void growth

In a next step we extend the above relations to dynamic loading regimes with a pressure of the form (7.86). If inertia affects the process of void growth but the material law is rate independent a solution of (7.92) is equivalent to a simple conservation of energy approach

$$W^{ex} = W^p + S + K. \tag{7.101}$$

Inserting (7.59), (7.69), (7.71), (7.87) and (7.100) equation (7.101) becomes

$$4\pi\bar{p}(a^3 - a_0^3) = \frac{4\pi}{3} p_{y0}(a^3 - a_0^3) + 4\pi\gamma a^2 + 2\pi\varrho_0 \, a^4\left(\frac{1}{a} - \frac{1}{b}\right)\dot{a}^2. \tag{7.102}$$

Evaluating this ODE gives

$$\dot{a} = \sqrt{\frac{2}{3\varrho_0}} \left(\bar{p} - p_{y0} - p_\gamma\right)^{\frac{1}{2}} \left(\frac{1 - \frac{a_0^3}{a^3}}{1 - \frac{a}{(a^3 + b_0^3 - a_0^3)^{1/3}}}\right)^{\frac{1}{2}}, \tag{7.103}$$

where $p_\gamma = 3\gamma a^2/(a^3 - a_0^3)$ is the term resulting from surface energy contributions which has significance only at the beginning of the void grows process when $a \approx a_0$. By presumption the pressure difference $\Delta p \equiv \bar{p} - p_{y0} - p_\gamma > 0$ and thus the second term of (7.103) is positive. Moreover, it is clear from equation (7.103) as well as from the underlying physics that the velocity of void expansion reduces for high density materials, whereas a small ϱ_0 allows the voids to grow faster. Equation (7.103) is displayed in Figure 7.8 for $\varrho_0 = 2/3$, $\Delta p = 1$ and some realistic initial void sizes. Note that even through the applied tension $\bar{p}$ is constant the void expansion velocity increases unbounded with rising void size.
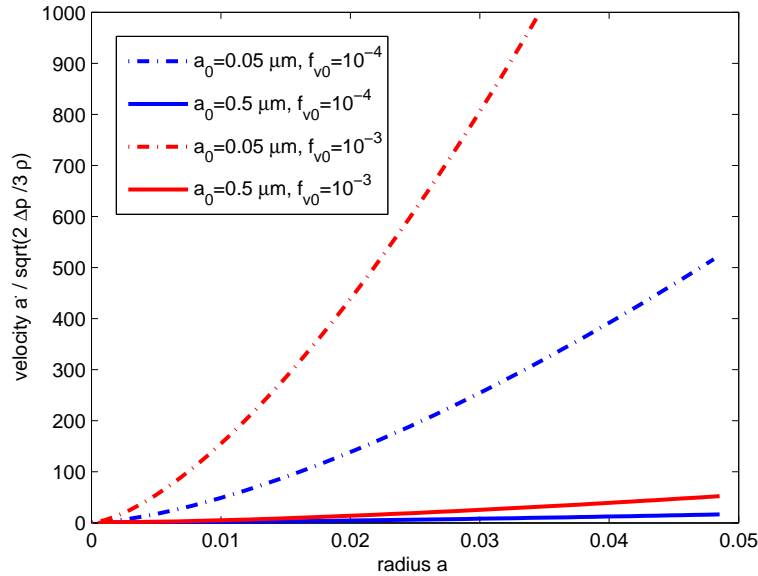
Figure 7.8.: Velocity of void expansion as a function of radius a for different initial data.

Some particular cases deserve special attention:

I: $b_0 \to \infty$. This case equals a void of radius a_0 in an infinite matrix. Equation (7.103) becomes

$$\dot{a} = \sqrt{\frac{2}{3\varrho_0}} \left(\bar{p} - p_{y0}\right)^{\frac{1}{2}} \left(1 - \frac{a_0^3}{a^3}\right)^{\frac{1}{2}}, \tag{7.104}$$

119

with the third term $\in [0, 1)$. In this case (and only in this case!) the void expansion velocity is bounded.

II: $b_0 \to \infty, a_0 \to 0$. For a very small void in an infinite matrix the void expansion velocity is constant, without surface energy contributions it has the value

$$\dot{a} = \sqrt{\frac{2}{3\varrho_0}} \left(\bar{p} - p_{y0}\right)^{\frac{1}{2}}. \tag{7.105}$$

III: $a_0 \to 0$. Here we have a very small void in a spherical shell model. Evaluation of equation (7.103) gives

$$\dot{a} = \sqrt{\frac{2}{3\varrho_0}} \left(\bar{p} - p_{y0}\right)^{\frac{1}{2}} \left(1 - (1 + \frac{b_0^3}{a^3})^{-\frac{1}{3}}\right)^{-\frac{1}{2}}, \tag{7.106}$$

where we have no solution for $a < b_0$ and a void velocity $\dot{a} \to \infty$ for $a > b_0$. The latter corresponds to the effect of unbounded rising void velocity $\dot{a} \to \infty$ visible in Figure 7.8.

Full Model

Finally, the motion of the voids in a general visco-plastic material shall be analyzed. Evaluating equation (7.92) for the void acceleration $\ddot{a}$ gives

$$\ddot{a} = -\left[\frac{\partial W^p}{\partial a} + 8\pi\gamma a + \frac{\partial \psi^*}{\partial \dot{a}} + \frac{\partial^2 K}{\partial \dot{a} \partial a} - \frac{\partial K}{\partial a} \right.$$
$$\left. - \frac{\partial W^{ex}}{\partial a}\right] \bigg/ 4\pi\varrho_0 a^4 \left(a^{-1} - (a^3 - b_0^3 + a_0^3)^{-1/3}\right), \tag{7.107}$$

which will be solved for a material with data of Table 7.3.1 by recourse to a Runge-Kutta scheme with a time step ensuring convergence, [311, 392]. The cavitation pressure p_y is computed numerically (no approximation).

Applying rapidly a constant remote tension of 1 GPa we compute the results displayed in Figure 7.9. A population of voids with initial radius of $a_0 = 25\mu$m expands and, despite of the hardening material, we observe a raise of void radius, of void velocity *and* of void acceleration up to the theoretical limit of $f_V = 1$. Note that this "self-accelerating" void expansion is equivalent to a *macroscopic softening* of the composite shell material.

In general, the dynamic void expansion is faster the smaller the initial voids are. The surface energy retards void growth in the first stages, superposed by a significant effect
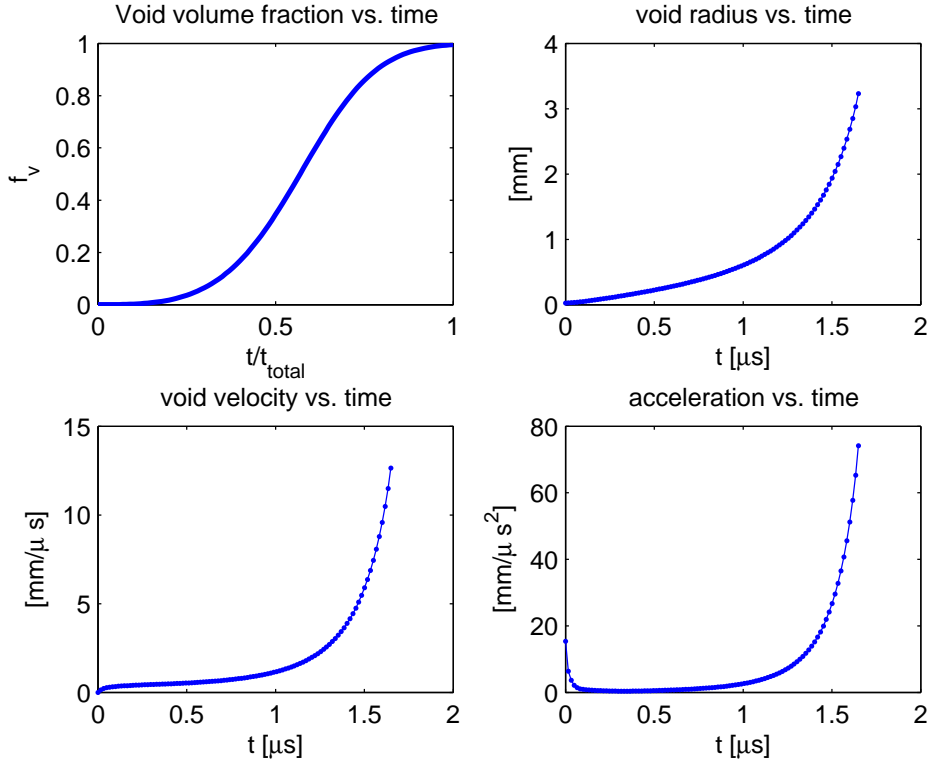
Figure 7.9.: Void growth of a mean sized void under constant remote tension.

of inertia. The initial void volume fraction (here $f_{V0} = 10^{-4}$) is of small influence, but generally the void growth accelerates with higher values of f_{V0}.

In a next computation we apply to the material a sinusoidal pressure impulse with an amplitude of 10 GPa within a time interval of $t_{load} = 10^{-3}\mu$s. A void ensemble with $a_0 = 0.1\mu$m expands to $a = 1.57\mu$m at $t = t_{load}$. The corresponding void volume fraction is $f_V = 0.28$. A smaller initial void size increases the void expansion, in particular holds

$$\dot{a}(t) \propto \frac{\sqrt{p}}{a_0} \quad \text{for } t \in [0, t_{load}]. \tag{7.108}$$

The void expansion is here clearly dominated by inertia effects. This is nicely illustrated by Figure 7.10 where we see that the voids continue to grow after the load impulse has passed, i.e., for $\bar{p} = 0$, $t > t_{load}$. For $a_0 = 0.1\mu$m the final void volume goes to $f_v \to 1$. Starting with a bigger void of $a_0 = 1\mu$m the void velocity and size increase is smaller, $a(t = t_{load}) = 1.76\mu$m, and the void growth converges to a final void size of $a = 4.03\mu$m.

121
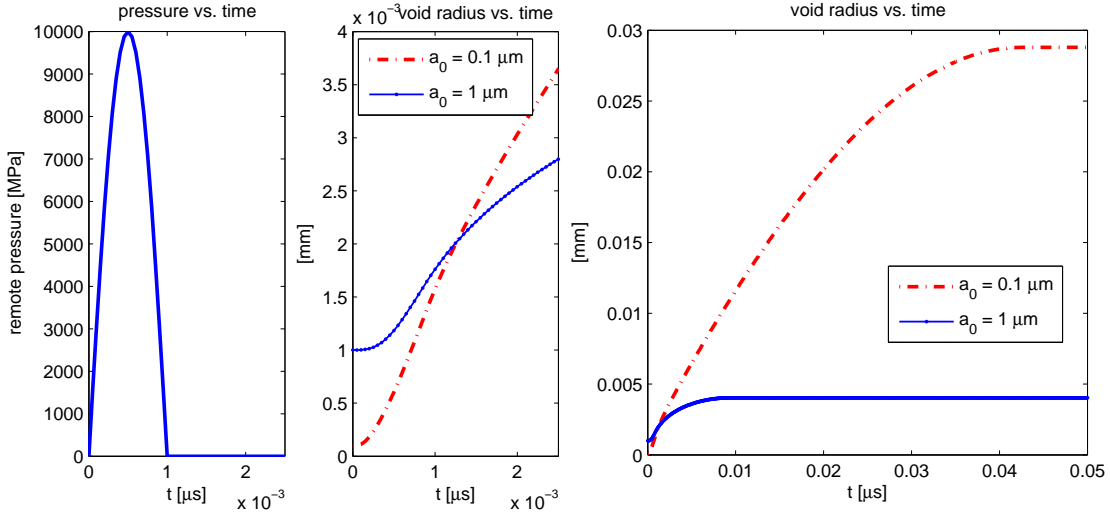
Figure 7.10.: Inertia dominated void growth due to a tension impulse for two different radii, short term and long term response.

This regime of inertia dominated void growth is particulary important for impact and spallation problems, see, e.g. [128, 213, 312, 367].

Note that, if the duration of the load impulse decreases to t_{load}/α a pressure amplitude of αp_{max} is required to compute approximately the same final void size.
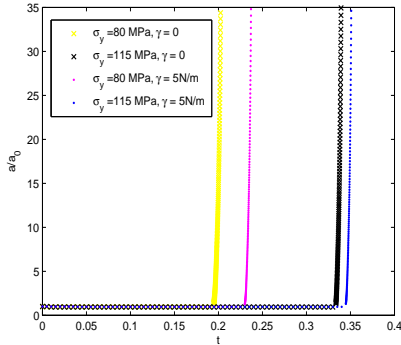
Figure 7.11.: Static void growth.

This strategy does not work the other way round. If the period of loading increases the inertial effects start to vanish. To illustrate that, we apply a reduced sinusoidal impulse of $p_{max} = 1$GPa within a period of 1μs. As long as the applied pressure is below the cavitation pressure p_y — which is now dominated by plasticity — voids do not expand, $a = a_0$. If the applied pressure exceeds p_y the voids grow unbounded, $a \rightarrow \infty$, see Figure 7.11 for a rough illustration. This corresponds to the situation analyzed in Section 7.3.3. Because this regime is dominated by plasticity we choose to raise the initial yield stress in Figure 7.11, an effect which may be induced, e.g., by a rate-sensitivity of the material. The point where the applied pressure exceeds the cavitation pressure, and, thus, where the voids grow unbounded, shifts from $t = 0.23\mu$s for $\sigma_y = 80$MPa to $t = 0.42\mu$s for $\sigma_y = 115$MPa. If, additionally, the material shows rate

122

effects which further increase σ_y no plastic void growth would happen. The influence of the surface energy contributions in this regime is also visible in Figure 7.11.

In this section we analyzed void expansion within a simple visco-plastic material. Note that additional energy or power contributions attributed to void growth can be derived in a manner completely analogous to the one outlined here.

7.3.4. Analysis of void distribution

After studying the growth of equally sized voids we proceed considering the interaction in an ensemble of voids. Point of departure is the balance of the mesoscopic distribution function written in compact form (7.42). For our (numerical) analysis we consider a body such that the mesoscopic void velocity is $\boldsymbol{v} = 0$. Moreover, in our first approach we neglect the production of voids, i.e., the right hand side of (7.42) equals zero. Thus, equations (7.42) simplifies to a balance equation of the form

$$\frac{\partial \tilde{f}}{\partial t} + \frac{\partial}{\partial a}\left(\tilde{f}\dot{a}\right) = 0. \tag{7.109}$$

With (7.16) the void volume fraction in a porous composite is given by

$$f_V = \frac{4\pi}{3} \int_0^\infty \tilde{f} \, a^3 \, da. \tag{7.110}$$

We assume that the initial number of voids in a material is given by a Gaussian distribution around a mean initial radius $\bar{a}_0$

$$C_0 \exp\left(-\frac{1}{2\epsilon_0^2}\left(\frac{a_0}{\bar{a}_0} - 1\right)^2\right) \tag{7.111}$$

where C_0 is a normalization factor, ϵ_0 denotes the deviation (the "width" of distribution) and index $_0$ refers to the initial configuration. By integration of the mesoscopic void number $\tilde{N}_V(a,t)$ over the range of definition $(0,\infty)$ the initial number of particles N_{V0} is obtained, see equation (7.18). Introducing an integration variable $x = (a - \bar{a}_0)/(\sqrt{2}\epsilon_0\bar{a}_0)$ we get

$$\int\limits_0^\infty \tilde{N}_V(a, t = 0) \, da = \sqrt{2}\epsilon_0\bar{a}_0 C_0 \int\limits_{-1/\sqrt{2}\epsilon_0}^\infty \mathrm{e}^{-x^2} dx \approx \sqrt{2\pi}\epsilon_0\bar{a}_0 C_0 = N_{V0} \tag{7.112}$$

to determine C_0 where the approximation refers to small values of ϵ_0. Consequently, with

$$C_0 = \frac{N_{V0}}{\sqrt{2\pi}\epsilon_0 \bar{a}_0} \tag{7.113}$$

and condition (7.17) the initial distribution function reads

$$\tilde{f}(a, t = 0) = \frac{C_0}{N_{V0}} \exp\left(-\frac{1}{2\epsilon_0^2}\left(\frac{a_0}{\bar{a}_0} - 1\right)^2\right). \tag{7.114}$$
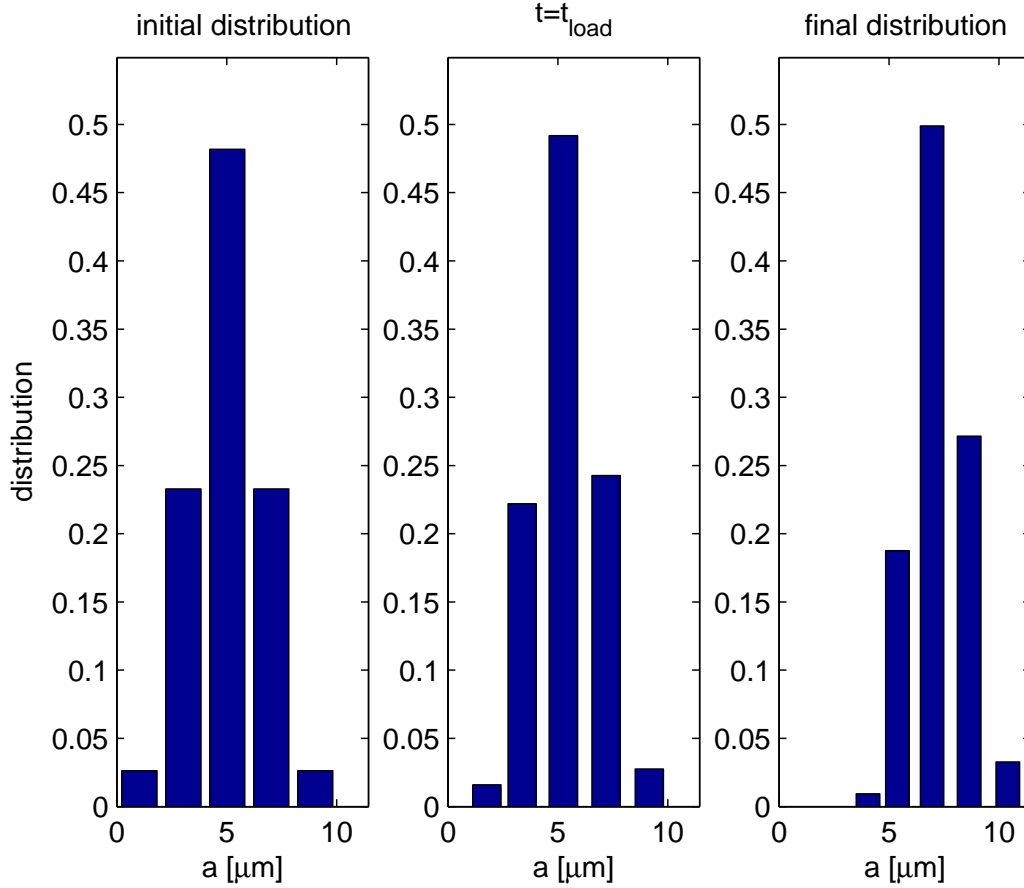
Figure 7.12.: Initial, intermediate and final distribution in a void ensemble of 5 sizes.

The problem of interest is now to investigate how does this distribution change in time. Exemplarily we analyze ensembles of voids with maximal initial void radii of $a_0 = 10\mu$m subjected to the sinusoidal loading impulse of Figure 7.10, $p_{max} = 10$ GPa.

We start by discretizing the mesoscopic distribution function for the void radius a

$$\tilde{f}(a,t) = \lim_{\Delta a \to 0} \frac{\tilde{f}^{(i)}(a, a + \Delta a, t)}{\Delta a}, \tag{7.115}$$

where $\tilde{f}^{(i)}(a, a+\Delta a, t)$ is the distribution of voids with radii $a \in [a, a+\Delta a]$. Consequently, the number of voids per unit volume is

$$N_V = \int_0^\infty N_V \tilde{f}(a,t) da \approx N_V \sum_{i=1}^n \tilde{f}^{(i)} a^{(i)}. \tag{7.116}$$

At time t the number of voids growing into $[a, a + \Delta a]$ equals the product of the distribution function $\tilde{f}$ and the evolution of the radius $\dot{a}$, see equation (7.109).
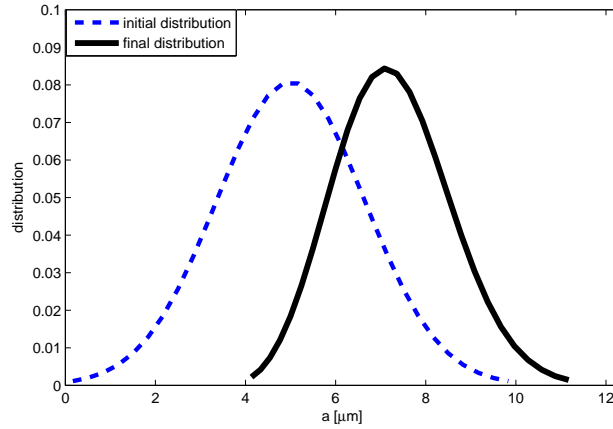
Figure 7.13.: Dynamic change of void distribution computed with an ensemble of 30 different voids.

At first we study an ensemble of 5 types of voids with initial void volume fraction $f_{V0} = 10^{-4}$ ad $a_0^{(1)} = 1\mu$m, $a_0^{(2)} = 3\mu$m, $a_0^{(3)} = 5\mu$m, $a_0^{(4)} = 7\mu$m, $a_0^{(5)} = 9\mu$m. The parameters of the distribution function (7.114) are $\bar{a}_0 = 5\mu$m, $\epsilon_0 = 1/3$, $C_0 = N_{V0}/(0.942\sqrt{(\pi)}\bar{a}_0\,\epsilon_0)$, see Figure 7.12. All voids grow when subjected to the loading impulse. From the analysis of Section 7.3.3 we know that voids with small initial size are less inert and grow faster than their bigger companions. Consequently, the change of distribution function $\tilde{f}$ is not symmetric. The set of small voids reduces whereas the numbers of bigger void sizes grow. This observation is in agreement with other theories of multi-phase materials (as, e.g., Ostwald ripening [277], the LSW-theory for liquid droplets in a gas [354] and grain coarsening theories of Cahn and Hillard [66]) where the bigger inclusions grow on cost of the smaller ones, an effect which is often called the "survival of the fattest".

(a) load impulse of 10 GPa

(b) load impulse of 20 GPa
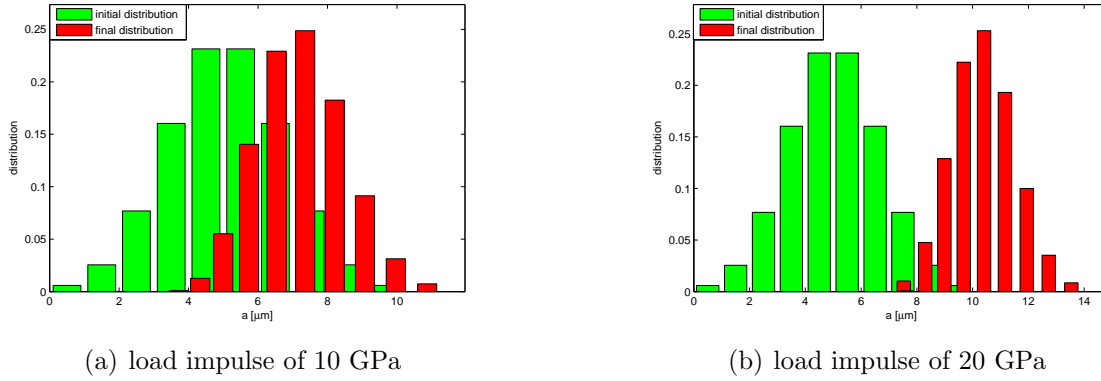
Figure 7.14.: Initial and final distribution for an ensemble of 10 voids after two different pressure impulses.

As a consequence of the inertial effects the void distribution keeps changing after the actual loading time is over. Therefore, in Figure 7.12 the initial distribution, the distribution at the end of the impulse $t = t_{load}$ and the final distribution are displayed.[2] For a quasi continuous distribution (computed with 30 different void sizes) the initial and final distribution is plotted in Figure 7.13.

Finally, two different loading impulses are applied to a void ensemble. Assuming an initial standard distribution of 10 void sizes with a maximum initial void size of 10μm the initial and final distribution functions are displayed in Figure 7.14. Clearly, the mean radius increases with higher applied load and, again, the deviation from the mean radius gets smaller. Note that initially very small voids tend to grow rapidly to $a \to b$, see Section 7.3.3. By equation (7.109) the set of such spherical shells basically vanishes, $\tilde{f}(a^{(1)}, t > t_{load}) \approx 10^{-5}$ for $a_0^{(1)} = 0.05\mu$m, and, therefore is not visible in Figure 7.14 b. The resulting void distribution groups around the mean radius $\bar{a}(t)$. This is in clear contrast to the quasistatic case where the distribution function broadens, Figure 7.15.

It is obvious from all these figures that the effect of inertia yields a smaller variety of void sizes: The "width" of distribution function $\tilde{f}$ gets smaller. This effect may explain some of the difference between static and dynamic fracture of ductile metals. Whereas in static experiments we usually observe a cup-cone like fracture with large plastic straining and small and big (coalesced) voids, the fracture surface is more or less plain but dimpled in dynamic experiments. Voids of similar sizes grew here and set up sheets of voids resulting in fragmentation surfaces (e.g., spallation planes, see Figure 7.16, and Figure 9.2, 9.3),

---

[2]Note that the width of the bars in Figure 7.12 and 7.14 has no meaning.
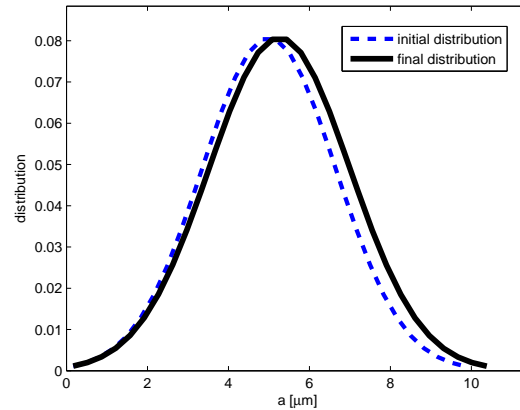
Figure 7.15.: Change of void distribution computed with an ensemble of 30 different voids in a quasistatic loading regime.

for experimental studies see among many others [29, 128, 280, 325].

7.4. Thermodynamic frame for a general porous plastic material

In this section we present a variational constitutive model for porous plastic materials under static and dynamic loading conditions. The constitutive framework used here is
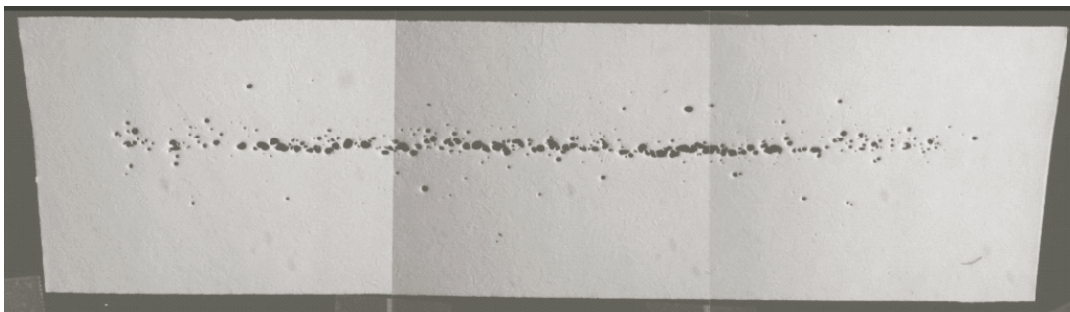

Figure 7.16.: Voids in a dynamically loaded copper disk (used in a gas-gun experiment of [29]).

based on a multiplicative decomposition of the deformation gradient into an elastic part and an inelastic part, and on a conventional internal-variable formulation of continuum thermodynamics, cf. [198, 257]. Using a simplified porosity model we link the mechanism of plastic expansion and global softening of the material to parameters that describe the micromechanical mechanisms of void growth. Note that more elaborate models may easily be integrated in the presented general framework.

We start by providing a simple framework for integrating a conventional model of deviatoric plasticity, such as J_2-flow theory of Chapter 6, to an equation of state representing the effective macroscopic behavior of an ensemble of voids with mean radius $\bar{a}$.

Consider a representative sample of material of undeformed volume V_0 and deformed volume $V = JV_0$. The local volume fraction of voids (7.1) in the undeformed configuration is

$$f_{V0} = N_V \frac{4\pi \bar{a}_0^3}{3}, \tag{7.117}$$

where N_V is the void density. We simplify the void ensemble to a number of N_V spherical voids with mean radius $\bar{a}$ per unit undeformed volume of the body, i.e., the mesoscopic distribution function degenerates to a dirac-impulse and will be dropped in the subsequent equations.

In addition, the volume of undeformed matrix material is $(1 - f_{V0})V_0$. By $\bar{a}$ we denote the mean void radius in the intermediate, or plastically deformed, configuration. By assuming a spherical shell model with a plastically-incompressible matrix, and neglecting the elastic volume change of the voids, we have

$$J^p = 1 - f_{V0} + N_V \frac{4\pi \bar{a}^3}{3}, \tag{7.118}$$

$$f_V = \frac{f_{V0} + J^p - 1}{J^p}. \tag{7.119}$$

This relation places the mean void radius $\bar{a}$ and the Jacobian of the deformation J^p in one-to-one correspondence. In all subsequent expressions we conventionally take J^p to be the primary independent variable and regard $\bar{a}$, and its functions, as functions of J^p through equation (7.118).

7.4.1. Variational constitutive relations

The thermo-mechanical response of the solids considered in this work is characterized by a free-energy density per unit undeformed volume of the form

$$A = A(\boldsymbol{F}, \boldsymbol{F}^p, \epsilon^p, \theta^p, T), \tag{7.120}$$

where $\boldsymbol{F}$ is the deformation gradient, $\boldsymbol{F}^p$ is the plastic part of the deformation gradient, $\epsilon^p \geq 0$ is an effective deviatoric plastic strain, $\theta^p \geq 0$ is an effective volumetric plastic strain, T is the absolute temperature, and

$$\boldsymbol{F}^e = \boldsymbol{F}\boldsymbol{F}^{p-1} \tag{7.121}$$

is the elastic part of the deformation gradient, cf. equation (6.1).

The plastic deformation rate is assumed to obey the flow rule

$$\dot{\boldsymbol{F}}^p \boldsymbol{F}^{p-1} = \dot{\epsilon}^p \boldsymbol{M} + \dot{\theta}^p \boldsymbol{N}, \tag{7.122}$$

where $\dot{\epsilon}^p$ and $\dot{\theta}^p$ are subject to irreversibility constraints

$$\dot{\epsilon}^p \geq 0, \tag{7.123}$$
$$\dot{\theta}^p \geq 0, \tag{7.124}$$

and the tensors $\boldsymbol{M}$ and $\boldsymbol{N}$ determine the direction of the deviatoric and volumetric plastic deformation rates, respectively. The deviatoric plasticity tensor $\boldsymbol{M}$ is assumed to satisfy

$$\mathrm{tr}\boldsymbol{M} = 0, \quad \boldsymbol{M} \cdot \boldsymbol{M} = \frac{3}{2}, \tag{7.125}$$

and the volumetric plasticity tensor $\boldsymbol{N}$ is

$$\boldsymbol{N} = \pm\frac{1}{3}\boldsymbol{I}, \tag{7.126}$$

with the plus sign in $\boldsymbol{N}$ corresponding to void expansion, and the minus sign to void collapse. The tensors $\boldsymbol{M}$ and $\boldsymbol{N}$ are otherwise unknown and are to be determined as part of the solution. The constraints (7.125–7.126) may be regarded as defining the assumed kinematics of plastic deformation. As we shall see, the direction of plastic deformation, as determined by $\boldsymbol{M}$ and $\boldsymbol{N}$, follows from the variational structure of the constitutive update in a manner which generalizes the principle of maximum dissipation [140, 257].

Imagine now for a moment a purely volumetric deformation of the body, i.e., the deformation gradient is of the spherical form $\boldsymbol{F} = J^{1/3}\boldsymbol{I}$. Then the flow rule (7.122) reduces to

$$\frac{d}{dt}\ln J^p \, \boldsymbol{I} \;=\; \dot{\vartheta}^p \, \boldsymbol{N}$$

which is evaluated to

$$\frac{d}{dt}\ln(J^p)^{1/3} \;=\; \mathrm{tr}\boldsymbol{N}\dot{\vartheta}^p = \pm\dot{\vartheta}^p, \tag{7.127}$$

where the plus sign corresponds to void expansion and the minus sign to void collapse. From (7.127) we find

$$\dot{\vartheta}^p = \left| \frac{d}{dt} \ln J^p \right| \tag{7.128}$$

and

$$\vartheta^p(t) = \vartheta^p(0) + \int_0^t \dot{\vartheta}^p(\xi)\, d\xi, \tag{7.129}$$

i.e., the variable ϑ^p is a measure of the *accumulated* volumetric plastic deformation. Evidently, ϑ^p and $\ln J^p$ coincide for monotonic expansion up to a constant. In this case we state

$$\vartheta^p = \ln J^p \tag{7.130}$$

and the logarithmic plastic volumetric expansion ϑ^p can be expressed as a simple function of radius $\bar{a}(t)$

$$\vartheta^p \equiv \vartheta^p(\bar{a}(t)) = \ln\Big(1 + \frac{4\pi}{3} N(\bar{a}^3(t) - a_0^3)\Big). \tag{7.131}$$

The distinction between the two variables J^p and ϑ^p becomes important for arbitrary loading combining alternating phases of void expansion and collapse. The simple one-to-one relations (7.130)-(7.131) do not hold in that case.

The first Piola-Kirchhoff stress tensor $\boldsymbol{P}$ follows from Coleman's relations as

$$\boldsymbol{P} = \frac{\partial A}{\partial \boldsymbol{F}}, \tag{7.132}$$

while the thermodynamic force Y conjugate to the internal variable ϵ^p is

$$Y = -\frac{\partial A}{\partial \boldsymbol{F}^p} \cdot \frac{\partial \boldsymbol{F}^p}{\partial \epsilon^p} - \frac{\partial A}{\partial \epsilon^p} = \sigma_e - \sigma_y, \tag{7.133}$$

where

$$\sigma_e = \boldsymbol{\Sigma} \cdot \boldsymbol{M}, \qquad \sigma_y = \frac{\partial A}{\partial \epsilon^p}, \tag{7.134}$$

are the effective deviatoric stress and the deviatoric flow stress, respectively. In (7.134) we made use of a tensor Σ which is defined as

$$\boldsymbol{\Sigma} = -\frac{\partial A}{\partial \boldsymbol{F}^p} \boldsymbol{F}^{pT}. \tag{7.135}$$

Likewise, the thermodynamic force Z conjugate to the internal variable θ^p takes the form

$$Z = -\frac{\partial A}{\partial \boldsymbol{F}^p} \cdot \frac{\partial \boldsymbol{F}^p}{\partial \theta^p} - \frac{\partial A}{\partial \theta^p} = p - p_y, \tag{7.136}$$

130

where

$$p = \mathbf{\Sigma} \cdot \mathbf{N}, \qquad p_y = \frac{\partial A}{\partial \theta^p}, \tag{7.137}$$

are the effective pressure and the flow pressure, respectively.

Appropriate rate equations for the internal variables ϵ^p and θ^p must be specified to formulate a complete set of constitutive relations. With a view to ensuring a variational structure, we postulate the existence of a dual kinetic potential $\psi^*(\dot{\epsilon}^p, \dot{\theta}^p, \mathbf{F}^p, T)$ such that

$$Y = \frac{\partial \psi^*}{\partial \dot{\epsilon}^p}, \tag{7.138}$$

$$Z = \frac{\partial \psi^*}{\partial \dot{\theta}^p}. \tag{7.139}$$

7.4.2. Variational formulation of the dynamic problem

Consider a body occupying a region $B \subset \mathbb{R}^3$ and undergoing a deformation described by a mapping $\boldsymbol{\varphi} : B \times [t_1, t_2] \to \mathbb{R}^3$. Suppose that the boundary ∂B is the disjoint union of a displacement boundary $\partial_1 B$ and a traction boundary $\partial_2 B$. Let $\rho_0 : B \times [t_1, t_2] \to \mathbb{R}$ denote the referential mass density per unit undeformed volume, $\mathbf{B} : B \times [t_1, t_2] \to \mathbb{R}^3$ the applied body-force field, $\bar{\boldsymbol{\varphi}} : \partial_1 B \times [t_1, t_2] \to \mathbb{R}^3$ the prescribed boundary displacements, $\bar{\mathbf{T}} : \partial_2 B \times [t_1, t_2] \to \mathbb{R}^3$ the applied tractions. For definiteness, we assume that the kinetic energy of the body is of the form

$$K = \int_B \frac{1}{2} \rho_0 \, |\dot{\boldsymbol{\varphi}}|^2 dV + \int_B L(\dot{\mathbf{F}}^p, \mathbf{F}^p) \, dV, \tag{7.140}$$

where the first term represents the macroscopic inertia and the second term the microinertia related to plastic deformation. The first variation of K is

$$\delta \int_{t_1}^{t_2} K \, dt = -\int_{t_1}^{t_2} \int_B \rho_0 \ddot{\boldsymbol{\varphi}} \cdot \delta \boldsymbol{\varphi} \, dV \, dt \tag{7.141}$$

$$+ \int_{t_1}^{t_2} \int_B \left(\frac{\partial L}{\partial \mathbf{F}^p} - \frac{d}{dt} \frac{\partial L}{\partial \dot{\mathbf{F}}^p} \right) \cdot \delta \mathbf{F}^p dV \, dt,$$

for all admissible variations $\delta \boldsymbol{\varphi}$ and $\delta \mathbf{F}^p$. The term in parenthesis may be regarded as an additional stress acting on $\mathbf{F}^p$, arising from microinertia. In addition, for every

131

$t \in [t_1, t_2]$ we introduce the power functional

$$\Phi[\dot{\boldsymbol{\varphi}}, \dot{\epsilon}^p, \dot{\theta}^p, \boldsymbol{M}, \boldsymbol{N}] = \int_B \left[\dot{A} + \psi^* - \left(\frac{\partial L}{\partial \boldsymbol{F}^p} - \frac{d}{dt} \frac{\partial L}{\partial \dot{\boldsymbol{F}}^p} \right) \cdot \dot{\boldsymbol{F}}^p \right] dV \qquad (7.142)$$
$$- \int_B \rho_0 (\boldsymbol{B} - \ddot{\boldsymbol{\varphi}}) \cdot \dot{\boldsymbol{\varphi}} \, dV - \int_{\partial_2 B} \bar{\boldsymbol{T}} \cdot \dot{\boldsymbol{\varphi}} \, dS.$$

where $\boldsymbol{F}^p$, ϵ^p, θ^p, $\boldsymbol{M}$ and $\boldsymbol{N}$ are now regarded as fields over B, and $\dot{\boldsymbol{F}}^p$ is determined by $\dot{\epsilon}^p$, $\dot{\theta}^p$, $\boldsymbol{M}$ and $\boldsymbol{N}$ through the flow rule (7.122). Using the identities (7.132), (7.133) and (7.136) and the flow rule (7.122), (7.142) may be rewritten as

$$\Phi[\dot{\boldsymbol{\varphi}}, \dot{\epsilon}^p, \dot{\theta}^p, \boldsymbol{M}, \boldsymbol{N}] = \int_B (\boldsymbol{P} \cdot \text{Grad}\dot{\boldsymbol{\varphi}} - Y \dot{\epsilon}^p - Z \dot{\theta}^p + \psi^*) \, dV \qquad (7.143)$$
$$- \int_B \rho_0 (\boldsymbol{B} - \ddot{\boldsymbol{\varphi}}) \cdot \dot{\boldsymbol{\varphi}} \, dV - \int_{\partial_2 B} \bar{\boldsymbol{T}} \cdot \dot{\boldsymbol{\varphi}} \, dS,$$

where $\boldsymbol{F} = \text{Grad}\boldsymbol{\varphi}$ has been introduced (cf. Chapter 1), and with

$$\boldsymbol{\Sigma} = -\frac{\partial A}{\partial \boldsymbol{F}^p} \boldsymbol{F}^{pT} + \left(\frac{\partial L}{\partial \boldsymbol{F}^p} - \frac{d}{dt} \frac{\partial L}{\partial \dot{\boldsymbol{F}}^p} \right) \boldsymbol{F}^{pT} \qquad (7.144)$$

in place of (7.135). For every $t \in [t_1, t_2]$, the rates $\dot{\boldsymbol{\varphi}}$, $\dot{\epsilon}^p$, $\dot{\theta}^p$, and the directions of plastic flow $\boldsymbol{M}$ and $\boldsymbol{N}$, follow jointly from the minimization problem

$$\Phi^{\text{eff}}[\dot{\boldsymbol{\varphi}}] = \inf_{\dot{\epsilon}^p, \dot{\theta}^p, \boldsymbol{M}, \boldsymbol{N}} \Phi[\dot{\boldsymbol{\varphi}}, \dot{\epsilon}^p, \dot{\theta}^p, \boldsymbol{M}, \boldsymbol{N}], \qquad (7.145)$$

subject to the constraints (7.123), (7.125), (7.126).

Problem (7.145) additionally defines the reduced power functional $\Phi^{\text{eff}}[\dot{\boldsymbol{\varphi}}]$. The material velocity field $\dot{\boldsymbol{\varphi}}$ finally follows from the minimization problem

$$\inf_{\dot{\boldsymbol{\varphi}}} \Phi^{\text{eff}}[\dot{\boldsymbol{\varphi}}], \quad \dot{\boldsymbol{\varphi}} = \dot{\bar{\boldsymbol{\varphi}}} \text{ on } \partial_2 B. \qquad (7.146)$$

Since the extended functional $\Phi[\dot{\boldsymbol{\varphi}}, \dot{\epsilon}^p, \dot{\theta}^p, \boldsymbol{M}, \boldsymbol{N}]$ does not depend on spatial derivatives of the fields, the minimization (7.145) may be effected locally, with the result

$$\Phi^{\text{eff}}[\dot{\boldsymbol{\varphi}}] = \int_B [\phi(\text{Grad}\dot{\boldsymbol{\varphi}}) - \rho_0 (\boldsymbol{B} - \ddot{\boldsymbol{\varphi}}) \cdot \dot{\boldsymbol{\varphi}}] \, dV - \int_{\partial_2 B} \bar{\boldsymbol{T}} \cdot \dot{\boldsymbol{\varphi}} \, dS, \qquad (7.147)$$

where

$$\phi(\dot{\boldsymbol{F}}) = \inf_{\dot{\epsilon}^p, \dot{\theta}^p, \boldsymbol{M}, \boldsymbol{N}} f(\dot{\boldsymbol{F}}, \dot{\epsilon}^p, \dot{\theta}^p, \boldsymbol{M}, \boldsymbol{N}), \qquad (7.148)$$

subject to the constraints (7.123), (7.125), (7.126), and

$$f(\dot{\boldsymbol{F}}, \dot{\epsilon}^p, \dot{\theta}^p, \boldsymbol{M}, \boldsymbol{N}) = \boldsymbol{P} \cdot \dot{\boldsymbol{F}} - Y \dot{\epsilon}^p - Z \dot{\theta}^p + \psi^*, \tag{7.149}$$

is a power density per unit undeformed volume. Evidently, by the construction of the power functional the kinetic relations (7.139) are Euler-Lagrange equations of the minimum problem (7.148). The additional Euler-Lagrange equations with respect to $\boldsymbol{M}$ and $\boldsymbol{N}$ are

$$\boldsymbol{\Sigma} - \lambda_1 \boldsymbol{I} - \lambda_2 \boldsymbol{M} = \boldsymbol{0}, \tag{7.150}$$
$$\mathrm{tr}(\boldsymbol{\Sigma}) - \lambda_3 \mathrm{tr}(\boldsymbol{N}) = 0, \tag{7.151}$$

where λ_1, λ_2 and λ_3 are Lagrange multipliers arising from the constraints (7.125), (7.126). Using these constraints, equations. (7.151) and (7.151) can be solved for $\boldsymbol{M}$ and $\boldsymbol{N}$, with the result

$$\boldsymbol{M} = \frac{3\mathrm{dev}(\boldsymbol{\Sigma})}{2\sigma_e}, \tag{7.152}$$

$$\boldsymbol{N} = \frac{1}{3}\mathrm{sgn}\big(\mathrm{tr}(\boldsymbol{\Sigma})\big)\boldsymbol{I}, \tag{7.153}$$

where

$$\sigma_e = \|\boldsymbol{\sigma}\| \equiv \sqrt{(3/2)\mathrm{dev}(\boldsymbol{\Sigma}) \cdot \mathrm{dev}(\boldsymbol{\Sigma})} \tag{7.154}$$

is the von Mises effective stress. Using (7.153) and (7.153) in (7.122) we obtain

$$\dot{\boldsymbol{F}}^p \boldsymbol{F}^{p-1} = \dot{\epsilon}^p \frac{3\mathrm{dev}(\boldsymbol{\Sigma})}{2\sigma} + \frac{1}{3}\dot{\theta}^p \mathrm{sgn}\big(\mathrm{tr}(\boldsymbol{\Sigma})\big)\boldsymbol{I}, \tag{7.155}$$

which is an **extension of the Prandtl-Reuss flow rule into the compressible range**.

The power density function $\phi(\dot{\boldsymbol{F}})$ has the fundamental property [257]

$$\boldsymbol{P} = \frac{\partial \phi}{\partial \dot{\boldsymbol{F}}}(\dot{\boldsymbol{F}}), \tag{7.156}$$

and, consequently, the Euler-Lagrange equations corresponding to the minimization problem (7.146) are the equations of motion

$$\begin{aligned}
\mathrm{Div}\boldsymbol{P} + \rho_0 \boldsymbol{B} &= \rho_0 \ddot{\boldsymbol{\varphi}} \quad \text{in } B, \\
\boldsymbol{P} \cdot \bar{\boldsymbol{N}} &= \bar{\boldsymbol{T}} \quad \text{on } \partial_2 B,
\end{aligned} \tag{7.157}$$

where in the latter expression $\bar{\boldsymbol{N}}$ is the unit normal to ∂B.

7.5. A model of volumetric plasticity

Here we specify the preceding general framework for the case of a porous plastic material. In particular, energy contributions arising from elasticity, plasticity, temperature and time-dependent effects are treated in a rigorous variational setting.

7.5.1. Elastic strain-energy density

To this end assume that the free-energy density (7.120) has the additive structure

$$A(\boldsymbol{F}, \boldsymbol{F}^p, \epsilon^p, \theta^p, T) = W^e(\boldsymbol{F}^e, T) + W^p(\epsilon^p, \theta^p, T), \tag{7.158}$$

where $W^e(\boldsymbol{F}^e, T)$ and $W^p(\epsilon^p, \theta^p, T)$ are the elastic and stored energy densities per unit undeformed volume, respectively. Then σ_c and p_c reduce to

$$\sigma_y(\epsilon^p, \theta^p, T) = \frac{\partial W^p}{\partial \epsilon^p}(\epsilon^p, \theta^p, T), \tag{7.159}$$

$$p_y(\epsilon^p, \theta^p, T) = \frac{\partial W^p}{\partial \theta^p}(\epsilon^p, \theta^p, T). \tag{7.160}$$

Due to material-frame indifference, W^e can only depend on $\boldsymbol{F}^e$ through the corresponding elastic right-Cauchy Green deformation tensor

$$\boldsymbol{C}^e = \boldsymbol{F}^{eT}\boldsymbol{F}^e = \boldsymbol{F}^{p-T}\boldsymbol{C}\,\boldsymbol{F}^{p-1}. \tag{7.161}$$

Furthermore, the elastic strain-energy density may alternatively be expressed in terms of the logarithmic elastic strain (6.30) whereupon W^e takes the form

$$W^e = W^e(\boldsymbol{\epsilon}^e, T). \tag{7.162}$$

We denote by $\boldsymbol{\sigma}$ the stress conjugate to $\boldsymbol{\epsilon}^e$, namely,

$$\boldsymbol{\sigma} = \frac{\partial W^e}{\partial \boldsymbol{\epsilon}^e}(\boldsymbol{\epsilon}^e, T). \tag{7.163}$$

In order to obtain a simple form of $W^e(\boldsymbol{C}^e, T)$ we consider a representative neighborhood in the plastically-deformed or 'intermediate' configuration of the material. We attribute the volumetric part of $\boldsymbol{F}^p$ to void growth, with J^p related to the current void size through (7.118), and assume that the plastic deformation of the matrix leaves the elastic properties of the matrix unchanged. This assumption is appropriate for metals,

whose elastic properties are ostensibly insensitive to isochoric plastic deformation. The plastically deformed configuration can thus be regarded as a two-phase composite consisting of an elastic matrix and a distribution of voids. A simple form of the resulting elastic energy is given by (6.14) and repeated here in terms of the logarithmic strains

$$W^e(\boldsymbol{\epsilon}^e, T) = W^{e,\mathrm{vol}}(\theta^e, T) + W^{e,\mathrm{dev}}(\boldsymbol{\epsilon}^e, T), \tag{7.164}$$

$$W^{e,\mathrm{vol}}(\theta^e, T) = \frac{\kappa}{2}\left[\theta^e - \alpha(T - T_0)\right]^2 + \rho_0 c_v T\left(1 - \ln\frac{T}{T_0}\right), \tag{7.165}$$

$$W^{e,\mathrm{dev}}(\boldsymbol{\epsilon}^e, T) = \mu \parallel \mathrm{dev}(\boldsymbol{\epsilon}^e) \parallel^2, \tag{7.166}$$

where $\theta^e = \ln J^e$, κ is the bulk modulus, μ is the shear modulus, α is the thermal expansion coefficient, T_0 is a reference absolute temperature, and c_v is the specific heat per unit mass at constant volume.

7.5.2. Stored energy

A simple stored energy function can be formulated by assuming an additive decomposition into deviatoric and volumetric components. The deviatoric part of the stored energy function can be modeled simply by a conventional power-law of hardening, equation (6.9). The volumetric part of the stored energy function is attributed directly to void growth. In the dilute limit, the total energy stored by the void ensemble is the sum of the energy stored by each individual void. The stored energy for a spherical void in a power-law hardening material, which equals the plastic work of deformation attendant to the expansion of the void, has been determined in Section 7.3. These considerations applied to a spherical shell model with average radius $\bar{a}$ lead to the stored energy function

$$W^p(\epsilon^p, \theta^p, T) = W^{p,\mathrm{vol}}(\theta^p, T) + W^{p,\mathrm{dev}}(\epsilon^p, T), \tag{7.167}$$

$$W^{p,\mathrm{vol}}(\theta^p, T) = \frac{n\sigma_0(T)\epsilon_0^p}{n+1} N_V \frac{4\pi\bar{a}^3}{3} g(\theta^p, n), \tag{7.168}$$

$$W^{p,\mathrm{dev}}(\epsilon^p, T) = \frac{n\sigma_0(T)\epsilon_0^p}{n+1}\left(1 + \frac{\epsilon^p}{\epsilon_0^p}\right)^{\frac{n+1}{n}}, \tag{7.169}$$

where

$$g(\theta^p, n) = \int_1^{\frac{1}{f_V}}\left(1 + \frac{2}{3\epsilon_0^p}\ln\frac{x}{x - 1 + \frac{f_{V0}}{f_{V0}+\exp\theta^p-1}}\right)^{\frac{n+1}{n}} dx. \tag{7.170}$$

In these expressions, n is the hardening exponent, $\sigma_0(T)$ is the yield stress, and ϵ_0^p is a reference deviatoric plastic strain. The yield stress is assumed to depend on temperature by relation (6.18), see Figure 6.1. For a discussion of the expressions for the stored energy function see Section 7.3.

7.5.3. Rate sensitivity

We consider two types of rate effects: rate sensitivity in the plastic deformation and microinertia due to expanding voids. The deviatoric rate sensitivity may be modeled simply by means of a conventional power-law of hardening. In the dilute limit, the volumetric component of ψ^* is the sum of all contributions from the individual voids. Based on these considerations, the analysis of Section 7.3, and the same approach as in the previous section, we have

$$\psi^*(\dot{\epsilon}^p, \dot{\theta}^p, J^p, T) = \psi^{*,\mathrm{vol}}(\dot{\theta}^p, J^p, T) + \psi^{*,\mathrm{dev}}(\dot{\epsilon}^p, T), \tag{7.171}$$

$$\psi^{*,\mathrm{vol}}(\dot{\theta}^p, J^p, T) = \frac{m^2\sigma_0(T)\dot{\epsilon}_0^p}{m+1} N_V \frac{4\pi\bar{a}^3}{3}(1 - f_V^{\frac{1}{m}}) \left| \frac{2\dot{\bar{a}}}{\dot{\epsilon}_0^p \bar{a}} \right|^{\frac{m+1}{m}}, \tag{7.172}$$

$$\psi^{*,\mathrm{dev}}(\dot{\epsilon}^p, T) = \frac{m\sigma_0(T)\dot{\epsilon}_0^p}{m+1} \left(\frac{\dot{\epsilon}^p}{\dot{\epsilon}_0^p} \right)^{\frac{m+1}{m}}. \tag{7.173}$$

In these expressions, m is the rate sensitivity exponent, $\dot{\epsilon}_0^p$ is a reference plastic strain rate, and $\bar{a}$ is regarded as a function of J^p through (7.118). In addition, by virtue of (7.118), the dependence of ψ^* on $|\dot{\bar{a}}/\bar{a}|$ induces a dependence on $|(d/dt)\ln J^p|$, or, in view of (7.128), on $\dot{\theta}^p$.

7.5.4. Microinertia

The microinertia attendant to dynamic void growth can be regarded as dissipated energy. In the dilute limit, the total kinetic energy attendant to the growth of the void ensemble is the sum of the kinetic energies due to the expansion of each individual void. For spherical voids in an incompressible material this *microkinetic energy* can be computed readily in terms of the void radius (e.g.,[254]), with the result

$$L(\bar{a}, \dot{\bar{a}}) = \frac{3}{2}\varrho_v(\bar{a})\dot{\bar{a}}^2 \tag{7.174}$$

where

$$\varrho_v(\bar{a}) = N_V \varrho_0 \frac{4\pi\bar{a}^3}{3}. \tag{7.175}$$

For simplicity we have neglected a factor of $(1 - f_V^{\frac{1}{3}})$. In contrast to the approach of Section 7.3 we denote now the microkinetic energy with L to distinguish it from the overall kinetic energy K of the body (7.140).

Note that (7.174) describes a collection of noninteracting shell-like particles, each with variable effective mass

$$m(\bar{a}) = 4\pi\rho_0\bar{a}^3. \tag{7.176}$$

The kinetic energy L may as well be written as a function of the variables $(J^p, \dot{\bar{a}})$ using relation (7.118).

7.6. Constitutive updates

Next we address the time integration of the constitutive equations. We therefore envision an incremental solution procedure with time intervals $[t_n, t_{n+1}]$. Assume that the state of the material, $\boldsymbol{F}_n^p$, ε_n^p, ϑ_n^p, $\dot{\vartheta}_n^p$ and $\ddot{\vartheta}_n^p$, is known at time t_n, and let the deformation gradient $\boldsymbol{F}_{n+1}$ and the temperature T_{n+1} at time t_{n+1} be given. The problem is then to determine the state of material, $\boldsymbol{F}_{n+1}^p$, ε_{n+1}^p, ϑ_{n+1}^p, $\dot{\vartheta}_{n+1}^p$ and $\ddot{\vartheta}_{n+1}^p$, at time t_{n+1}, as well as the directions $\boldsymbol{M}, \boldsymbol{N}$ of the incremental plastic deformation. Also of interest is the value of the Piola-Kirchhoff stress $\boldsymbol{P}_{n+1}$ and the tangent moduli $D\boldsymbol{P}_{n+1}$.

7.6.1. Variational time-discretization of microinertia

A somewhat nonstandard feature of the present model is the consideration of microinertia, which renders the equations of motion for the growth of the voids of second order in time. In order to formulate updates possessing a variational structure, the time-discretization of the equations of motion must itself possess an incremental variational structure. Radovitzky and Ortiz [276] have shown that Newmark's algorithm, when applied to systems with quadratic inertia and constant mass, leads to a minimum problem for the incremental displacements. Unfortunately, the microkinetic energy L, equation (7.174), is not in the class of kinetic energies contemplated in [276].

However, L can be reduced to the canonical case by a change of variables, and a variational time-discretization scheme then follows as in [276]. In order to see this, begin with (7.174) and write the action integral as

$$\mathcal{I}[\bar{a}] = \int_{t_1}^{t_2} \left[\frac{3}{2}\varrho_v\big(\bar{a}(t)\big)\dot{\bar{a}}^2(t) - A\big(\bar{a}(t), t\big) \right] dt \tag{7.177}$$

where all dependencies of A on variables other than $\bar{a}$ are regarded as introducing an explicit dependence of A on time. Consider now a change of variables of the form[3]

$$\bar{a} = F(b) \tag{7.178}$$

whereupon (7.174) becomes

$$L(b, \dot{b}) = \frac{3}{2}\rho_v(F(b))F'^2(b)\dot{b}^2. \tag{7.179}$$

Inserting this change of variables in (7.177) gives

$$\mathcal{I}[b] = \int_{t_1}^{t_2} \left[\frac{3}{2}\varrho_v\big(F(b(t))\big)F'^2(b(t))\dot{b}^2(t) - A\big(F(b(t)), t\big) \right] dt \tag{7.180}$$

In order to obtain an equivalent system with constant mass, we must choose $F(b)$ such that

$$\rho_v(F(b))F'^2(b) = \rho_{v0} \equiv \rho_0 N \frac{4\pi \bar{a}_0^3}{3}. \tag{7.181}$$

This ordinary differential equation is separable and, therefore, it can be solved explicitly, with the result

$$L(b, \dot{b}) = \frac{3}{2}\rho_{v0}\dot{b}^2, \tag{7.182}$$

$$b = \int_0^{\bar{a}} \sqrt{\frac{\varrho_v(r)}{\varrho_{v0}}} dr = \frac{2}{5}\frac{\bar{a}^{5/2}}{\bar{a}_0^{3/2}} \tag{7.183}$$

which corresponds to a system of noninteracting particles with constant mass, as desired.

The Newmark update for b is now equivalent to the minimization of the function

$$f_n(b_{n+1}) = \frac{3\varrho_{v0}}{2} \frac{(b_{n+1} - b_{n+1}^{\mathrm{pre}})^2}{\beta \triangle t^2} + A(b_{n+1}, t_{n+1}) \tag{7.184}$$

where the Newmark predictor is given by

$$b_{n+1}^{\mathrm{pre}} = b_n + \triangle t \dot{b}_n + \left(\frac{1}{2} - \beta \right) \triangle t^2 \ddot{b}_n$$

and the derivates $\dot{b}$ and $\ddot{b}$ are updated according to the rules

$$\dot{b}_{n+1} = \dot{b}_n + \triangle t[(1 - \gamma)\ddot{b}_n + \gamma \ddot{b}_{n+1}] \tag{7.185a}$$

$$\ddot{b}_{n+1} = -\frac{1}{3\varrho_{v0}} \frac{\partial A}{\partial b_{n+1}} \tag{7.185b}$$

In the equations above, $\beta \in (0, 1/2)$ and $\gamma \in [0, 1]$ are Newmark's parameters, cf. Section 5.1.

---

[3]Note that in this section b is an auxiliary variable which has nothing in common with the spherical shell radius of Section 7.1; $F(b)$ simply denotes any function of b.

7.6.2. Variational updates

The strategy for the remaining of the model is similar to the one outlined in Chapter 6. We start by discretizing the flow rule in time

$$\boldsymbol{F}^p_{n+1} = \exp\left(\Delta\varepsilon^p \boldsymbol{M} + \Delta\vartheta^p \boldsymbol{N}\right) \boldsymbol{F}^p_n. \tag{7.186}$$

Clearly, the update (7.186) is consistent with the flow rule (7.122) by virtue of the identity

$$\left\{\frac{d}{dt}\exp\left[t\left(\dot{\varepsilon}^p\boldsymbol{M} + \dot{\vartheta}^p\boldsymbol{N}\right)\right]\right\}_{t=0^+} = \dot{\varepsilon}^p\boldsymbol{M} + \dot{\vartheta}^p\boldsymbol{N} \tag{7.187}$$

We update the remaining internal state variables, ε^p_{n+1} and ϑ^p_{n+1}, and simultaneously determine the incremental direction of plastic flow, $\boldsymbol{M}$ and $\boldsymbol{N}$, for the time step by recourse to a variational formulation. To this end, let us introduce an incremental objective function of the form

$$f_n(\boldsymbol{F}_{n+1}, T_{n+1}, \varepsilon^p_{n+1}, \vartheta^p_{n+1}, \boldsymbol{M}, \boldsymbol{N}) = W^e(\boldsymbol{C}^e_{n+1}, T_{n+1}) + W^p(T_{n+1}, \varepsilon^p_{n+1}, \vartheta^p_{n+1})$$
$$+ \Delta t\, \psi^*\left(\frac{\triangle\varepsilon^p}{\triangle t}, \frac{\triangle\vartheta^p}{\triangle t}, T_{n+1}, J^p_{n+1}\right) \tag{7.188}$$

where $\Delta t = t_{n+1} - t_n$, $\Delta\varepsilon^p, \Delta\vartheta^p$ analogously. For convenience we dropped here the microinertia term of equation (7.184). This may easily be added, regarding b_{n+1} as a function of ϑ^p_{n+1} through (7.183) and (7.127), (7.128), see also Chapter 9 of the application part.

In the sense of a variational formulation we now define an effective work of deformation density $W_n(\boldsymbol{F}_{n+1}, T)$ by minimizing f_n with respect to the internal variables and the direction of plastic flow

$$W_n = \min_{\varepsilon^p_{n+1}, \vartheta^p_{n+1}, \boldsymbol{M}, \boldsymbol{N}} f_n \tag{7.189}$$

subjected to the constraints (7.125) and (7.126), which define the kinematics of plastic deformation, and the irreversibly constraints

$$\triangle\varepsilon^p \geq 0 \tag{7.190a}$$
$$\triangle\vartheta^p \geq 0. \tag{7.190b}$$

Evidently the effective work of deformation density (7.189) returns the updated values of the internal variables and the direction of plastic flow over the time step. Moreover,

$W_n(\boldsymbol{F}_{n+1})$ acts as a potential for the first Piola-Kirchhoff stress tensor $\boldsymbol{P}_{n+1}$ at time t_{n+1}. In order to prove this property, suppose that the deformation gradient $\boldsymbol{F}_{n+1}$ is perturbed to $\boldsymbol{F}_{n+1} + \delta\boldsymbol{F}_{n+1}$. The corresponding variation of the effective work of deformation density (7.189) reads

$$\delta W_n = \frac{\partial W^e}{\partial \boldsymbol{F}_{n+1}}\delta\boldsymbol{F}_{n+1} + \frac{\partial W_n}{\partial \varepsilon^p_{n+1}}\delta\varepsilon^p_{n+1} + \frac{\partial W_n}{\partial \vartheta^p_{n+1}}\delta\vartheta^p_{n+1} + \frac{\partial W_n}{\partial \boldsymbol{M}}\delta\boldsymbol{M} + \frac{\partial W_n}{\partial \boldsymbol{N}}\delta\boldsymbol{N}, \quad (7.191)$$

but the last three terms in this identity vanish due to stationarity. In addition, we have

$$\boldsymbol{P}_{n+1} = \frac{\partial W^e}{\partial \boldsymbol{F}_{n+1}} \tag{7.192}$$

and (7.191) reduces to

$$\delta W_n = \boldsymbol{P}_{n+1}\,\delta\boldsymbol{F}_{n+1}. \tag{7.193}$$

Since $\delta\boldsymbol{F}_{n+1}$ is arbitrary this implies

$$\boldsymbol{P}_{n+1} = \frac{\partial W_n}{\partial \boldsymbol{F}_{n+1}}. \tag{7.194}$$

Consequently W_n acts as a potential for first Piola-Kirchhoff stresses $\boldsymbol{P}_{n+1}$ and the constitutive update possesses an incremental potential structure. The tangent modulus corresponding to the variational updates follow by linearization of (7.194).

$$D\boldsymbol{P}_{n+1} = \frac{\partial^2 W_n}{\partial \boldsymbol{F}_{n+1}\partial \boldsymbol{F}_{n+1}} \tag{7.195}$$

The relations (7.194) and (7.195) correspond to the ones given in Chapter 6 for finite plasticity. For details we refer to the equations (6.53)–(6.57).

7.6.3. Implementation based on logarithmic elastic strains

Without loss of generality, the elastic energy density may be recast in the form

$$W^e(\boldsymbol{F}, T) = W^e(\boldsymbol{\epsilon}^e, T) \tag{7.196}$$

where $\boldsymbol{\epsilon}^e$ is the logarithmic elastic strain (6.30). Furthermore let (6.34) be the trial or predictor elastic right Cauchy-Green deformation tensor obtained by assuming no incremental plastic deformation, and suppose that the commutation relation (6.35) holds between $\boldsymbol{C}^{e,\text{trial}}_{n+1}$ and the direction of plastic flow $\boldsymbol{M}$ for the same step. Then, by the properties of the exponential mapping, we have

$$\boldsymbol{\epsilon}^e_{n+1} = \boldsymbol{\epsilon}^{e,\text{trial}}_{n+1} - \triangle\varepsilon^p\boldsymbol{M} - \triangle\vartheta^p\boldsymbol{N} \tag{7.197}$$

where (6.37) is the trial or predictor value of the logarithmic elastic strain. Using these identities, (7.188) becomes

$$f_n(\boldsymbol{F}_{n+1}, T_{n+1}, \varepsilon^p_{n+1}, \vartheta^p_{n+1}, \boldsymbol{M}, \boldsymbol{N}) = W^e(\boldsymbol{\epsilon}^{e,\text{trial}}_{n+1} - \triangle\varepsilon^p \boldsymbol{M} - \triangle\vartheta^p \boldsymbol{N}, T_{n+1}) +$$
$$W^p(T_{n+1}, \varepsilon^p_{n+1}, \vartheta^p_{n+1}) + \Delta t\, \psi^*\left(\frac{\triangle\varepsilon^p}{\Delta t}, \frac{\triangle\vartheta^p}{\Delta t}, T_{n+1}\right). \tag{7.198}$$

This function now has an additive structure in terms of elastic and plastic deformations which is entirely analogous to that of small-strain plasticity. In particular, in simple cases, such as that of an elastic strain-energy density W^e quadratic in $\boldsymbol{\epsilon}^e$, the minimization of f_n with respect to ε^p_{n+1}, ϑ^p_{n+1}, $\boldsymbol{M}$ and $\boldsymbol{N}$ can be carried out explicitly.

The underlying commutation condition (6.35) ensures that the additive decomposition (7.197) is *exactly* consistent with the multiplicative decomposition (7.121). The requirement that (6.35) holds places restrictions on the form of the elastic strain-energy density W^e, which are satisfied, e.g., by the isotropic function (7.164). Alternatively, as pointed out by Miehe [218], equation (7.197) can directly be taken as a point of departure for the formulation of a finite-deformation plasticity theory, regardless of the form of W^e. However, in this case the resulting theory is not consistent with the multiplicative decomposition (7.121) in general.

7.6.4. Optimization with respect to ε^p, ϑ^p, $\boldsymbol{M}$, $\boldsymbol{N}$

The optimization of the incremental energy function (7.198) with respect to the internal variables and the directions of plastic flow leads to the Euler-Lagrange equations.

Let us first consider the kinematic of plastic flow. The tensor $\boldsymbol{M}$ which determines the direction of plastic strain rate follows from

$$\frac{\partial f_n}{\partial \boldsymbol{M}} = 0 \quad \Rightarrow \quad -\boldsymbol{\sigma}_{n+1} + \lambda_1 \boldsymbol{I} + \lambda_2 \boldsymbol{M} = 0 \tag{7.199}$$

where λ_1, λ_2 are Lagrange multipliers to be determined from the constraints (6.8). From Chapter 6 the solution is known to be

$$\boldsymbol{M} = \frac{3\boldsymbol{s}_{n+1}}{2|\boldsymbol{s}_{n+1}|} \equiv \frac{\boldsymbol{s}_{n+1}}{\|\boldsymbol{s}_{n+1}\|} = \frac{\operatorname{dev} \boldsymbol{\epsilon}^e_{n+1}}{\|\boldsymbol{\epsilon}^e_{n+1}\|}. \tag{7.200}$$

The direction of plastic dilatation is

$$\frac{\partial f_n}{\partial \boldsymbol{N}} = 0 \quad \Rightarrow \quad -p_{n+1} + \lambda_3 \operatorname{tr}(\boldsymbol{N}) = 0 \tag{7.201}$$

which resolves simply to

$$\boldsymbol{N} = \frac{p_{n+1}}{3|p_{n+1}|}\,\boldsymbol{I}. \tag{7.202}$$

Once the optimal direction of plastic flow rate is fixed, the optimization of the incremental deformation energy with respect to the incremental plastic strain rate follows

$$\frac{\partial f_n}{\partial \varepsilon^p{}_{n+1}} = 0 \quad\Rightarrow\quad -\frac{\partial W^{e,\mathrm{dev}}}{\partial \varepsilon^p{}_{n+1}} = \frac{\partial\big(W^{p,\mathrm{dev}} + \Delta t\,\psi^{*,\mathrm{dev}}\big)}{\partial \varepsilon^p{}_{n+1}}. \tag{7.203}$$

The plastic strain depends only on the deviatoric part of the energy and thus the solution of (7.203) corresponds to the solution of (6.39)

$$\|\boldsymbol{s}^{\mathrm{trial}}_{n+1}\| - 3\mu\Delta\varepsilon^p{}_{n+1} \;=\; \sigma_y(T_{n+1}, \varepsilon^p{}_{n+1}) + \psi^{*,\mathrm{dev}\prime}\Big(\frac{\Delta\varepsilon^p}{\Delta t}\Big) \tag{7.204}$$

and for later reference we abbriviate

$$F_1(\varepsilon^p{}_{n+1}) := \sigma_y + \psi^{*,\mathrm{dev}\prime} - \|\boldsymbol{s}_{n+1}\|. \tag{7.205}$$

The optimization of the incremental energy of deformation function (7.198) with respect to the incremental volumetric plastic dilatation reads

$$\frac{\partial f_n}{\partial \vartheta^p{}_{n+1}} = 0 \quad\Rightarrow\quad -\frac{\partial W^{e,\mathrm{vol}}}{\partial \vartheta^p{}_{n+1}} = \frac{\partial\big(W^{p,\mathrm{vol}} + \Delta t\,\psi^{*,\mathrm{vol}}\big)}{\partial \vartheta^p{}_{n+1}}. \tag{7.206}$$

The volumetric part of the stress tensor is the pressure

$$p_{n+1} \equiv \mathrm{tr}\boldsymbol{\sigma}_{n+1} = \kappa\,\mathrm{tr}\boldsymbol{\epsilon}^e_{n+1} \tag{7.207}$$

and, analogous to (6.45), we define a volumetric trial stress

$$p^{\mathrm{trial}}_{n+1} = \kappa\,\mathrm{tr}\boldsymbol{\epsilon}^{\mathrm{trial}}_{n+1}. \tag{7.208}$$

Then, the pressure (7.207) evaluates to

$$p_{n+1} = \kappa(\mathrm{tr}\boldsymbol{\epsilon}^{\mathrm{trial}}_{n+1} - \Delta\vartheta^p) = p^{\mathrm{trial}}_{n+1} - \kappa\Delta\vartheta^p. \tag{7.209}$$

The right hand side of $(7.206)_2$ represents a yield pressure p_y thenceforward plastic expansion occurs. Applying the chain rule we obtain

$$
\begin{aligned}
\frac{\partial\big(W^{p,\mathrm{vol}} + \Delta t\,\psi^{*,\mathrm{vol}}\big)}{\partial \vartheta^p{}_{n+1}} &= \frac{\partial\big(W^{p,\mathrm{vol}} + \Delta t\,\psi^{*,\mathrm{vol}}\big)}{\partial \bar{a}_{n+1}} \cdot \frac{\partial \bar{a}_{n+1}}{\partial \vartheta^p{}_{n+1}} \\
&= \frac{n\sigma_{y_0}(T_{n+1})\varepsilon^p_{y_0}}{n+1}\Big[g(\bar{a}_{n+1}, n) + \frac{1}{3}\frac{\partial g(\bar{a}_{n+1}, n)}{\partial \bar{a}_{n+1}}\bar{a}_{n+1}\Big] + \psi^{*,\mathrm{vol}\prime},
\end{aligned} \tag{7.210}
$$

where we write

$$g(\bar{a}_{n+1}, n) = \int_0^{1/f_V} \left(\ln \frac{x}{x - 1 + a_0^3/\bar{a}_{n+1}^3}\right)^{\frac{n+1}{n}} dx \qquad (7.211)$$

For simplicity we formulate (7.210) and (7.211) here with help of the unknown void radius $\bar{a}_{n+1}$, but the equations may as well be expressed by $\vartheta^p{}_{n+1}$ only. Now we write

$$F_2(\vartheta^p{}_{n+1}) := p_y - p_{n+1}. \qquad (7.212)$$

The equations (7.205) and (7.212) can be solved for the unknown $\varepsilon^p{}_{n+1}$ and $\vartheta^p{}_{n+1}$ by recourse to a Newton-Raphson iteration under the plastic irreversibility constraints imposed by (7.190). In order to set up this iteration (7.205) and (7.212) must be linearized.

$$dF_1 = \left(3\mu + H_{\varepsilon\varepsilon}\right) d\varepsilon^p{}_{n+1} \qquad (7.213)$$
$$dF_2 = \left(\kappa + H_{\vartheta\vartheta}\right) d\vartheta^p{}_{n+1} \qquad (7.214)$$

where we use the hardening moduli $H_{\varepsilon\varepsilon}$, $H_{\vartheta\vartheta}$

$$H_{\varepsilon\varepsilon} = \frac{\partial^2 \left(\tilde{W}^{p,\mathrm{dev}} + \Delta t\, \psi^*\right)}{\partial \varepsilon^p{}_{n+1} \partial \varepsilon^p{}_{n+1}} = \frac{\sigma_{y0}(T_{n+1})}{n\varepsilon_{y0}^p}\left(1 + \frac{\varepsilon^p{}_{n+1}}{\varepsilon_{y0}^p}\right)^{1/n-1} + \frac{\psi^{*,\mathrm{dev}''}}{\Delta t} \qquad (7.215)$$

$$H_{\vartheta\vartheta} = \frac{\partial^2 W^{p,vol}}{\partial \vartheta^p{}_{n+1} \partial \vartheta^p{}_{n+1}} = \frac{n\sigma_{y0}(T_{n+1})\varepsilon_{y0}^p}{n+1}\left[g(\bar{a}_{n+1}, n) + \frac{1}{3}\frac{\partial g(\bar{a}_{n+1}, n)}{\partial \bar{a}_{n+1}}\bar{a}_{n+1}\right] \qquad (7.216)$$

$$+ \left[\frac{4}{3}\frac{\partial g(\bar{a}_{n+1}, n)}{\partial \bar{a}_{n+1}} + \frac{1}{3}\frac{\partial^2 g(\bar{a}_{n+1}, n)}{\partial \bar{a}_{n+1}^2}\bar{a}_{n+1}\right]\frac{1}{4\pi N_v \bar{a}_{n+1}^2} + \frac{\psi^{*,vol''}}{\Delta t}$$

7.6.5. Stress and consistent tangent

Once $\varepsilon^p{}_{n+1}$ and $\vartheta^p{}_{n+1}$ are determined, the updated stresses follow as

$$\boldsymbol{\sigma}_{n+1} = p_{n+1}\boldsymbol{I} + \boldsymbol{s}_{n+1} \qquad (7.217)$$
$$= \kappa\left(\mathrm{tr}\boldsymbol{\epsilon}_{n+1}^{\mathrm{trial}} - \Delta\vartheta^p\right)\boldsymbol{I} + 2\mu\left(\mathrm{dev}\,\boldsymbol{\epsilon}_{n+1}^{\mathrm{trial}} - \Delta\varepsilon^p\boldsymbol{M}\right) \qquad (7.218)$$

As noted earlier, owing to the variational character of the update, the stress-strain relations satisfy the potential relations

$$\boldsymbol{\sigma}_{n+1} = \frac{\partial W_n}{\partial \boldsymbol{\epsilon}_{n+1}^e} \qquad (7.219)$$

where the incremental work of deformation density W_n is the optimal value of f_n, cf. (7.188).

Finally we address the computation of the tangent modulus, i.e., the linearization of (7.219).

$$D\boldsymbol{\sigma}_{n+1} = \frac{\partial^2 W_n}{\partial \boldsymbol{\epsilon}^e_{n+1} \partial \boldsymbol{\epsilon}^e_{n+1}} \tag{7.220}$$

To this end, we imagine perturbing the logarithmic strain $\boldsymbol{\epsilon}_{n+1}$ by an infinitesimal amount $d\boldsymbol{\epsilon}$. The problem is to compute the attendant infinitesimal variation in the conjugate stress $d\boldsymbol{\sigma}$. With a straitforward calculation we get

$$D\boldsymbol{\sigma}_{n+1} = \frac{1}{C} \overset{<4>}{I}_{\text{vol}} + \frac{1}{A} \overset{<4>}{I}_{\text{dev}} - \frac{B}{A^2 + \frac{3}{2}AB} \boldsymbol{M} \otimes \boldsymbol{M} \tag{7.221}$$

where $\overset{<4>}{I}$ is the unity tensor corresponding to the volumetric and deviatoric part of the tangent, $\boldsymbol{M}$ is given by (6.42) and

$$A = \frac{1}{2\mu} + \frac{3}{2} \frac{\Delta \varepsilon^p}{\|\boldsymbol{s}_{n+1}\|}, \qquad B = \frac{1}{H_{\varepsilon\varepsilon}} - \frac{\Delta \varepsilon^p}{\|\boldsymbol{s}_{n+1}\|} \qquad C = \frac{1}{K} + \frac{1}{J^p_n H_{\vartheta\vartheta}}. \tag{7.222}$$

The finite-kinematic relation follows by an application of (7.194) and (7.195). In components the results are stated in Chapter 6, equations (6.56) and (6.57).

Evidently, the evaluation of the Piola-Kirchhoff stress $\boldsymbol{P}$ and the tangent moduli $D\boldsymbol{P}$ requires the first and second linearizations, $D\ln(\cdot)$ and $D^2\ln(\cdot)$, respectively, of the logarithmic mapping. Thus, the simplicity of the additive elastic-plastic decomposition (7.197), and the analogy to small-strain updates that it affords, is not entirely without penalty. However, the transformations in (6.56) and (6.57) arising from the use of the logarithmic mapping are material-independent and, therefore, can be implemented once for all materials.

The variational update presented here is a time-discretized version of the variational statement of the constitutive relations. We have seen that the minimization of an incremental energy function, which combines the free energy of the solid including elastic, plastic and inertia terms and the conjugate inelastic potential for the rate equations, returns the updated values of the internal variables and the direction of plastic flow over the time step. We also have shown that the obtained minimum of this incremental energy function acts as a potential for the stress-strain relations. The consistent tangent moduli are consequently symmetric.

8. Damage, Fatigue and Failure

At first glance it seems obvious that a material undergoing deformations will be damaged at a certain point. But as easy as this is to imagine, it is tricky to define damage or failure of a material neighborhood from the mechanical point of view. Generally spoken damage represents surface discontinuities in form of decohesion and (micro)cracks as well as volume discontinuities in form of pores and cavities. Obviously, damage is characterized by irreversibility and dissipation. The actual criteria to define damage are as different as the underlying micro-mechanical mechanisms. Damage may be indicated by accumulated plastic strain in ductile materials (see Chapter 6 and 10), by a critical volume fraction of pores (see Chapter 7 and 9), by fatigue (see Chapter 10 and 11) by temperature, by time in viscoplastic materials, by aging and so on.

Continuum mechanical theories of damage go back to Kachanow [171], who first introduced a **damage variable** d with $d \in [0, 1]$. The limit case $d = 0$ defines the material to be free of any damage (this is actually an undefined state, usually it is set to be the state from which on the history of loading is known). On the opposite, $d = 1$ corresponds to a fully damaged material which has completely lost its load carrying capacity. The description of the temporal evolution of d is subject of damage mechanics and material theory, see [177, 208, 189] and many other.

8.1. Models of damaged materials

Figure 8.1 illustrates the meaning of the damage variable d in the special case of a damaged elastic material compared with an elastic-plastic material. We assume the same (bilinear) loading path for both models. In case of an elastic-plastic material the unloading path is parallel to the initial elastic loading with the same slope E; the unloaded structure is not strain-free because of the remaining plastic strain ε^p. In case of a damaged elastic material no permanent strains remain after unloading, but the slope of the unloading/reloading path reduces. By means of the damage parameter d the degradation of stiffness is captured.
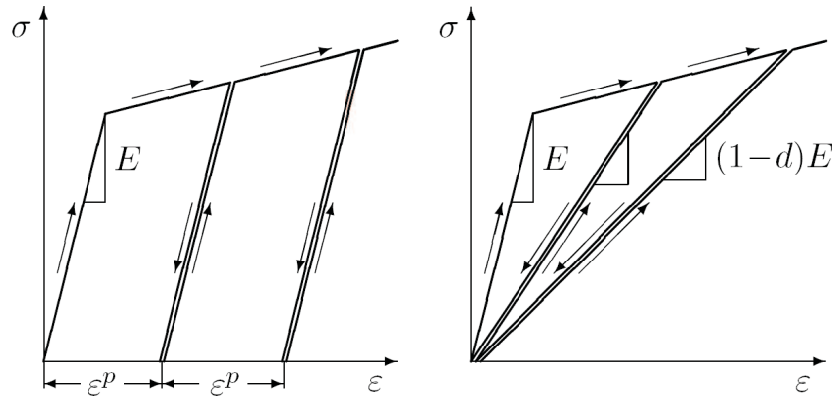
Figure 8.1.: Stress-strain relations in uniaxial tension for an elasto-plastic and an elasto-damaged material.

Not displayed is the case of plastic but damaged material where we observe at a certain strain (ductility) a reduction of the maximal bearable stress in the material. This effect is known as strain softening. In a uniaxial tension test this corresponds to the onset of necking of the specimen, i.e., to a localization of the deformation.

Here we proceed with a short overview about (some) different types of damage. Details of the underlying models follow in the subsequent sections of this chapter.

8.1.1. Brittle damage

Let us consider first brittle, non-linear elastic materials. Processes of damage in brittle materials have been subject of extensive research and have been modeled by a variety of means (see, e.g., [40, 51, 44, 178]). Most established models are empirical and are based on special solutions from linear elasticity, on internal variable formalisms or related modelling schemes. At this point we want to emphasize the essential distinction between the concepts of brittle damage and brittle fracture. Damage is commonly understood to be a *distributed* processes which is described by constitutive laws relating stress to strain. On the other hand fracture is *localized* to surfaces and is described, e. g., by local stress intensities or by cohesive laws relating local tractions to opening displacements.

This distinction implies that the processes of fracture in brittle solids requires tension. The underlying theory is governed by fracture mechanics (see below). Distributed brittle damage is a compression dominated phenomenon which only occurs when sufficient confinement is present. Brittle damage may arise in a number of situations of interest,

146

e.g., in geological formations, in confined structural ceramics and in crushed concrete. The objectives of brittle damage theories are to compute the effective or macroscopic behavior of the material from its elastic and fracture properties, and (if possible) to describe the microstructures underlying the macroscopic behavior, see [251, 261] and others.

8.1.2. Fracture and fragmentation

The onset of macroscopic cracks is indicated by damage. Fracture mechanics, i.e., the theory of cracking phenomena then is employed to predict the evolution of the cracks up to a complete failure of the structure. The fundamental concepts of fracture mechanics have been developed in the context of small deformations, [51, 50, 116, 189]. Well established theories are here the traditional K- and J-based crack-growth initiation and propagation criteria, however, their application to situations involving finite deformations or large-scale yielding encounters enormous difficulties. Even in cases which conform to the assumptions of small-scale fracture mechanics, considerable uncertainties remain as regards the proper choice of criteria that account for such phenomena as high loading rates, crack kinking and branching and other complicating circumstances.
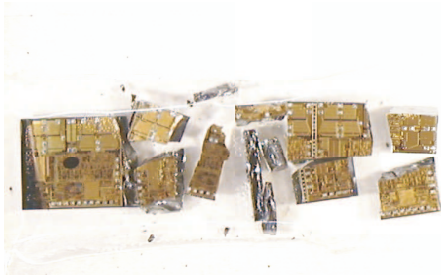
Figure 8.2.: Silicon chip, fragmented in a 4-point bending test.

An alternative approach was pioneered by Dugdale [108], Barenblatt [18], Rice [281] and others. Here fracture is regarded to be a phenomenon in which separation takes place across an extended crack tip — the cohesive zone — and is resisted by cohesive tractions. An appealing feature of this approach is that it does not presuppose a particular type of constitutive response in the material, in the extent of crack growth, or in the size of the plastic zone. In addition, the shape and location of the successive crack fronts is not predetermined. This concept was revived by Needleman [241, 380, 381] and Ortiz and Pandolfi [71, 255, 265, 290] for numerical computations of damaged structures undergoing large deformations. This finite element technique is meanwhile well established for the computation of brittle fracture and fragmentation, see, e.g., the impressive agreement to experiments reported in [262, 289, 383, 384]. However, for ductile materials the definition of cohesive laws is somewhat questionable, [263, 302, 301].
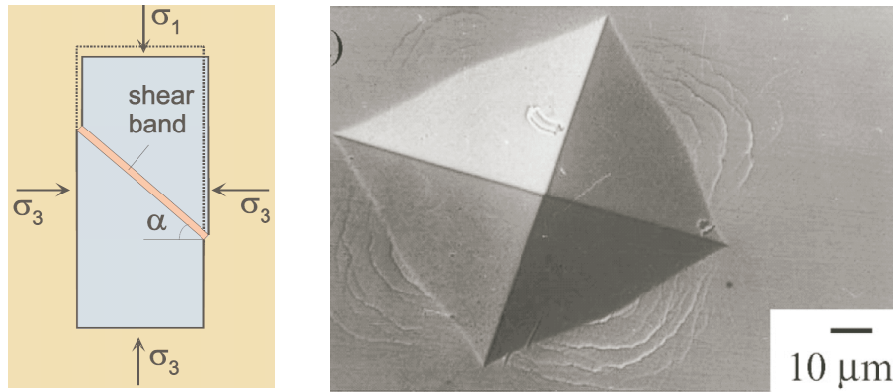
Figure 8.3.: Schematics of shear band formation in uniaxial tension and shear bands initiated by a Vickers indentation experiment [164]

8.1.3. Shear banding

A phenomena that frequently accompanies inelastic deformation is the formation of localized bands of intense straining. Such localization is known in ductile metals as shear banding but similar localized bands are also observed in concrete, in rocks, in ceramics and even in snow.

The formation of shear bands occurs particulary in metals subjected to high strain rates. The narrow bands of high (adiabatic) straining with typical widths in the order of $1 - 100\mu m$ [169], result from temperature rise and localization of deformation. The high local shear strains can reach values of up to 100 and ultra-high local shear strain rates, often in excess of $10^6 s^{-1}$, see [286, 333]. Typical are also local temperature rises of several hundred degrees [132, 205] and high propagation speeds, sometimes of more than 1000m/s [132, 207, 389]. Moreover, cracks and voids grow and coalesce along shear bands [22, 136, 207, 389]. Shearbands are also observed in over-consolidated soil, concrete or ceramics, where not only shear but also a certain dilatancy plays a role. Also, the effect of spallation observed in ductile metals under shock loading leads to local sheets of voids with similarity to shear banding, see Figure 7.16.

The modelling and computation of of strain localization has been subject of research for years. Early approaches to the problem were done, e.g., by stationary wave solutions [242] and by local bifurcation analysis of a homogeneous solution. At the band the solution evolves a discontinuous deformation gradient [253] (termed weak discontinuity in [305]), requiring discontinous deformation modes embedded into special finite elements [190, 191]. Rate-independent plasticity models do not possess an intrinsic characteristic

length scale, therefore, less standard approaches have been developed in conjunction with the weak discontinuity assumption to allow continuation of the solution beyond the point of bifurcation. An alternative idea for the analysis of strain localization in elasto-plastic solids involves the assumption of a discontinuous displacement field, (termed strong discontinuity in [305]). Within the context of finite element analysis, non-standard ansatz functions are necessary to compute such discontinuous fields, see e.g., [30, 166, 214, 310]. The mathematical challenge imposed by the presence of strongly discontinuous fields within a body has meanwhile itself become a subject of extensive research, cf. the work of Babuška [10] and many followers.

However, few numerical simulations are able to capture the physical process of dynamic shear band propagation. One of the challenges here is to reproduce the shear band propagation speed observed in experiments [132, 389]. One successful finite element simulation of dynamic shear band advance and speed is reported by Zhou et al. [388], but the attempt to resolve shearbands with a fixed mesh can not cope with the possible severe mesh distortion due to finite plastic deformation in shear bands. Mesh adaption is applied in [225]. In recent literature mesh-free Galerkin methods are employed [169, 193], [194] for the simulation of shear band propagation. The experimentally observed failure mode transition and the thermo-mechanical instability inside the shear band could be replicated in [194], the predicted shear band propagation speed, however, is different than the one observed experimentally. In [388] as well as in [193, 194] a fluid-type constitutive law for the damaged material inside a shear band was applied. (These ad hoc models assume that the band behaves as a Newtonian or non-Newtonian fluid, correspondingly.) This approach is somewhat artificial considering the fact that shear bands do have the constitutive law like the surrounding bulk material. A very recent technique of Yang et al. [382] describes the discontinuity of the deformation gradient across the shear band and embed it into a three-dimensional shear band finite element. This strategy is similar to one introduced by Ortiz and Pandolfi for the location of brittle fracture [255]. Therefore, we will follow this approach here stating the underlying theory in Section 8.3.

8.1.4. Fatigue

Fatigue roughly summarizes the effect of damage progressing over a long period of time. The microscopic reasons of fatigue may be very different, however, the macroscopic approach is commonly a simple empirical one. Typically, the fatigue failure of a material is estimated using a heuristic Coffin-Manson relationship (cf., e.g., [288]). For engineering metals it is of the form [27]

$$\frac{\Delta\varepsilon}{2} = \frac{\sigma_f}{E}(2N_f)^b + \varepsilon_f(2N_f)^c, \tag{8.1}$$

where $(2N_f)$ is the number of strain reversals (cycles), E is Young's modulus, σ_f is the tensile strength, and ε_f is the related ductility. The exponents b, c are empirical constants, commonly ranging from -0.5 to -0.7 for metals.

Generally, fatigue of metals is characterized by elastic and plastic strain components. Elastic deformations play a role mainly during low-strain/high-cycle testing. Therefore, the region of elastic deformation is also considered as the dynamic region. In that case, the first term of equation (8.1) dominates and fatigue performance is mainly a function of the tensile strength. Conversely, during a high-strain/low-cycle testing the dominant component is not the stress but the plastic deformation. The second term of (8.1) dominates and fatigue is a mainly function of ductility.

A microscopic reason for fatigue of metal alloys is presented in the next section.

8.1.5. Phase decomposition

The question of fatigue by aging raises especially for alloys of metals and other multi-phase materials. In particular, the temporal development of the material's microstructure is of importance. To illustrate the effect of aging, Figure 8.4 shows experimental evidence for phase decomposition in an eutectic Ag-Cu alloy. The two stable phases of Ag_6Cu_{94} are denoted as α-phase (Ag-rich) and β-phase (Cu-rich). Initially the α- and β-phase are homogenously distributed in small grains; note that one square in Figure 8.4 has a side length of 50μm. With a heat treatment at 970 K the process of aging is accelerated and we observe a phase decomposition and subsequent phase growth resulting in a significant grain coarsening.

The increasing trend for miniaturization which, for example, occurs in microelectronics, makes grain sizes of several microns a significant problem for the strength of the material. For example, in modern chip-scale packages the solder joints which connect different layers of the packages may be less than 50μm in diameter. Along grain boundaries easily form micro-cracks and voids, resulting in a reduced lifetime of the solder joints and consequently the whole structure. Therefore, the investigation of the changing microstructure of alloys (as well as the resulting macroscopic properties) are subjects of increasing interest. We will present the mechanical theory to describe such processes in the next section.
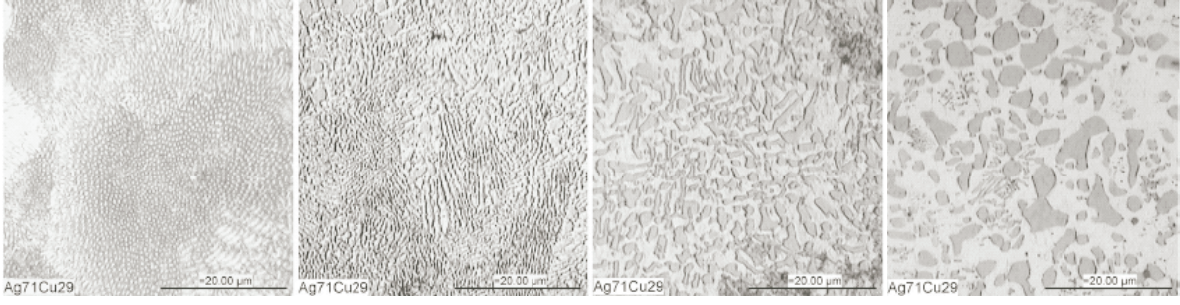
Figure 8.4.: Microstructural changes in eutectic Ag-Cu at 970 K (dark/light areas denote β/α-phases). From left to right: after solidification, 2h, 20h, 40h.

8.2. Localization of damage

Phase decomposition, void growth and brittle damage are microstructural phenomena which damage the structure and may cause the whole structure to fail. Such structural failure bases on local phenomena, e.g., macroscopic cracks or void sheets. Therefore, in this Section the variational framework to account for such localized failure is presented.

To generalize the conventional virtual work expression to a body containing a discontinuous surface, we make use of the relations derived in Chapter 1.3 and 2.8. Consider a body occupying an initial placement $B_0 \subset R^3$, Figure 8.5, which undergoes a motion described by a deformation mapping $\boldsymbol{\varphi} : B_0 \times [0, T] \to R^3$. The body contains a discontinuous surface S (corresponding to surface Λ in Chapter 2.8). This surface may be a crack, a shear band or a similar local effect within the body. We will refer to it as *discontinuous local surface* or for short *band* and proceed establishing the basic kinematics in the material frame.

A local material reference frame is chosen such that the $\{X_1, X_2\}$-plane is tangent to the local surface S_0 and the direction X_3 is normal to it. Motivated by the decomposition of the deformation gradient 1.22–(1.35) we represent the deformation gradient within the local surface in the form

$$\boldsymbol{F} = \boldsymbol{F}^{\parallel}\boldsymbol{F}^{\perp}, \tag{8.2}$$

where $\boldsymbol{F}^{\parallel}$ is the in-plane part and $\boldsymbol{F}^{\perp}$ is the out-of-plane part of the deformation gradient. The in-plane part of the deformation gradient satisfies the identity (1.34), $\boldsymbol{F}^{\parallel}\boldsymbol{N} = \boldsymbol{N}$, where $\boldsymbol{N}$ is the unit normal to the band in the undeformed placement. The transverse deformation follows as

$$\boldsymbol{F}^{\perp} = \boldsymbol{I} + \frac{[\![\boldsymbol{\varphi}]\!]}{h} \otimes \boldsymbol{N} \,, \tag{8.3}$$
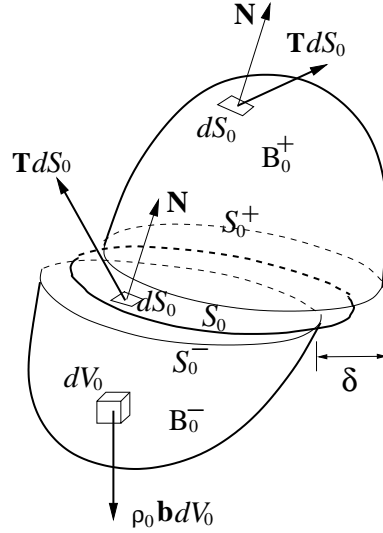
Figure 8.5.: Discontinuous local surface in a three-dimensional body.

where h is the thickness of the band. In the following $\delta \equiv [\![\boldsymbol{\varphi}]\!]$ denotes the displacement jump across the local discontinuous surface. Consequently, the total deformation gradient may also be expressed as

$$\boldsymbol{F} = \boldsymbol{F}^{\|} + \frac{\boldsymbol{\delta}}{h} \otimes \boldsymbol{N}. \tag{8.4}$$

With a view to establish a variational structure we introduce an **incremental work of deformation per unit area** of the band as

$$\phi_n(\boldsymbol{F}, \delta, h) = hW_n(\boldsymbol{F}), \tag{8.5}$$

where W_n is the incremental work of deformation per unit volume of the band. The thermodynamic force conjugate to thickness h evaluates to

$$\frac{\partial \phi_n}{\partial h} = W_n - \frac{\partial W_n}{\partial \boldsymbol{F}^{\perp}} \cdot \frac{\partial \boldsymbol{F}^{\perp}}{\partial h} = W_n - \frac{\partial W_n}{\partial \boldsymbol{F}^{\perp}} \cdot \frac{\boldsymbol{\delta}}{h} \equiv 0. \tag{8.6}$$

This expression is simply the normal component of the jump in the Eshelby energy-momentum tensor across the band. It is set to zero by assuming that the band is in configurational equilibrium at all times. Actually, this defines a scalar equation in the unknown thickness h.

The transverse stresses per unit length of a band $\boldsymbol{P}^{\perp}$ derive from the first Piola-Kirchhoff stress tensor $\boldsymbol{P}$ and are related to the tractions, whereas the membrane stresses per unit

length of a band $\boldsymbol{P}^{\parallel}$ are conjugate to $\boldsymbol{F}^{\parallel}$ and evaluate by

$$\boldsymbol{P}^{\parallel} = \frac{\partial \phi_n}{\partial \boldsymbol{F}^{\parallel}} = h \frac{\partial W_n}{\partial \boldsymbol{F}^{\parallel}} = h \left(\boldsymbol{P} - \boldsymbol{T} \otimes \boldsymbol{N} \right) . \tag{8.7}$$

Here $\boldsymbol{T}$ is the local surface traction conjugate to $\boldsymbol{\delta}$ which results from

$$\boldsymbol{T} = \frac{\partial \phi_n}{\partial \boldsymbol{\delta}} = \frac{\partial W_n}{\partial \boldsymbol{F}^{\perp}} = \boldsymbol{P} \boldsymbol{N}. \tag{8.8}$$

It is worth noting that the membrane forces (8.11) are of order h and, therefore, may be neglected in a first approximation for very thin bands.

The **deformation power identity of a discontinuous local surface** with constant thickness h can be evaluated as (cf. Equation (2.28))

$$\begin{aligned} P^D &= \int_{S_0} h\, \boldsymbol{P} \cdot \dot{\boldsymbol{F}}\, dS_0 \\ &= \int_{S_0} h\, \boldsymbol{P} \cdot \left[\dot{\boldsymbol{F}}^{\parallel} \boldsymbol{F}^{\perp} + \boldsymbol{F}^{\parallel} \dot{\boldsymbol{F}}^{\perp} \right] dS_0 \\ &= \int_{S_0} h \left[\boldsymbol{P} \boldsymbol{F}^{\perp T} \cdot \dot{\boldsymbol{F}}^{\parallel} + \boldsymbol{F}^{\parallel \top} \boldsymbol{P} \cdot \dot{\boldsymbol{F}}^{\perp} \right] dS_0 \end{aligned} \tag{8.9}$$

or, equivalently,

$$\begin{aligned} P^D &= \int_{S_0} h\, \boldsymbol{P} \cdot \dot{\boldsymbol{F}}\, dS_0 \\ &= \int_{S_0} \left[h \boldsymbol{P} \cdot \dot{\boldsymbol{F}}^{\parallel} + \boldsymbol{P} \cdot \left(\dot{\boldsymbol{\delta}} \otimes \boldsymbol{N} \right) \right] dS_0. \end{aligned} \tag{8.10}$$

For the stresses per unit length of a band follows

$$\boldsymbol{P}^{\parallel} = \boldsymbol{P} \boldsymbol{F}^{\perp \top} , \tag{8.11}$$

$$\boldsymbol{P}^{\perp} = \boldsymbol{F}^{\parallel \top} \boldsymbol{P} , \qquad \boldsymbol{T} = \boldsymbol{P}^{\perp} \boldsymbol{N} , \tag{8.12}$$

and, with (8.7) and (8.8),

$$P^D = \int_{S_0} \left(\boldsymbol{P}^{\parallel} \cdot \dot{\boldsymbol{F}}^{\parallel} + \boldsymbol{T} \cdot [\![\dot{\boldsymbol{\varphi}}]\!] \right) dS_0. \tag{8.13}$$

From the balance of linear momentum (2.15) follows the total deformation power of a body containing a discontinuous local surface

$$P^D = \sum_{\pm} \int_{B_0^{\pm}} \boldsymbol{P} \cdot \dot{\boldsymbol{F}}\, dV_0 + \int_{S_0} \left(\boldsymbol{P}^{\parallel} \cdot \dot{\boldsymbol{F}}^{\parallel} + \boldsymbol{T} \cdot [\![\dot{\boldsymbol{\varphi}}]\!] \right) dS_0. \tag{8.14}$$

This expression generalizes the conventional deformation power identity (2.28) to a body containing a discontinuous local surface. It is evident from equation (8.14) that the presence of a discontinuous local surface results in the addition of a new term to the deformation power identity.

In a cohesive zone model fracture is assumed to happen along an extended crack tip and is resisted by tractions, Figure (8.6) depicts the type of irreversible relation envisioned here. In principle, a cohesive law defines a relation between crack opening displacements $\boldsymbol{\delta}$ and tractions on the crack flanks $\boldsymbol{t}$. By recourse to Coleman and Noll's method (e.g. [93, 339]) it is possible to show that a cohesive law takes the general form

$$\boldsymbol{t} = \frac{\partial \phi}{\partial \boldsymbol{\delta}}. \tag{8.15}$$

Therefore, an appropriate choice of internal variable is the maximum attained effective opening displacement δ_{max}. Loading of the cohesive surface is then characterized by the conditions $\delta = \delta_{max}$ and $\dot{\delta} \geq 0$. (By definition a cohesive surface undergoes unloading when it does not undergo loading.) We assume the existence of a loading envelope, i.e., a relation between (effective) traction t and (effective) displacement δ under conditions of loading. A simple and convenient relation is the universal binding law proposed by Smith and Ferrante [287], Figure 8.6,

$$t = e\sigma_c \frac{\delta}{\delta_c} \exp(-\frac{\delta}{\delta_c}) \qquad \text{if } \delta = \delta_{max} \text{ and } \dot{\delta} \geq 0 \tag{8.16}$$

where $e = 2.71828\ldots$ is the e-number, σ_c is the maximum cohesive normal traction and δ_c is a characteristic opening displacement. The corresponding potential is

$$\phi = e\sigma_c \delta_c \left(1 - \left(1 + \frac{\delta}{\delta_c}\right) \exp(-\frac{\delta}{\delta_c})\right). \tag{8.17}$$

The irreversibility of the process manifests itself upon unloading, with law (8.16) unloading to the origin gives

$$t = \frac{t_{max}}{\delta_{max}} \delta \qquad \delta < \delta_{max} \text{ or } \dot{\delta} < 0, \tag{8.18}$$

and, consequently,

$$\dot{\delta} = \begin{cases} \dot{\delta} & \text{if } \delta = \delta_{max} \text{ and } \dot{\delta} \geq 0 \\ 0 & \text{otherwise} \end{cases} \tag{8.19}$$

defines the kinetic equations for the evolution of the internal variable in the present model. Figure 8.6 also displays a simplified cohesive law with linear loading envelope.
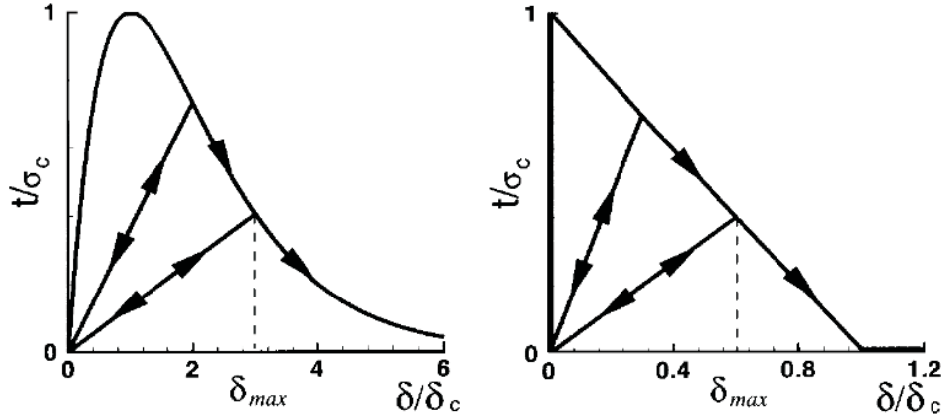
Figure 8.6.: Cohesive laws expressed in terms of an effective opening displacement δ and traction t; left: loading envelope of the Smith-Ferrante type with loading–unloading rule; right: linearly decreasing loading envelop with loading–unloading rule

In elastic materials an application of the J–integral concept of Rice [281] establishes a link between the critical energy release rate G_c for crack propagation and the cohesive law, see reference [255]. Imagine the cohesive surface S_0 to have a local orthonormal reference coordinate system such that basis vector $\boldsymbol{e}_1$ points in the direction of propagation of the crack front, $\boldsymbol{e}_2$ is aligned with the crack front direction and $\boldsymbol{e}_3$ coincides with the unit normal $\boldsymbol{N}$. Choose a contour Γ for the evaluation of the J–integral which surrounds the cohesive zone and we evaluate

$$G_c = \int_\Gamma \boldsymbol{t} \cdot \boldsymbol{\delta}_{,1} \, d\,x_1 \,. \tag{8.20}$$

In terms of the scalar effective opening δ and the corresponding effective traction we can write

$$G_c = \int_0^R t \, \delta_{,1} \, d\,x_1 \,, \tag{8.21}$$

where R is the cohesive zone length. A change of variables gives

$$G_c = \int_0^\infty t \, d\delta \equiv \phi_\infty \,. \tag{8.22}$$

For our particular case of Smith-Ferrante potential (8.16) equation (8.22) evaluates to

$$G_c = e \, \sigma_c \, \delta_c \,, \tag{8.23}$$

which relates σ_c and δ_c to the fracture energy G_c. Now we can define a damage variable

$$d = \frac{\phi(\delta_{max})}{G_c} \, , \tag{8.24}$$

which, clearly, ranges from 0 to 1. These limits correspond to an intact and a fully opened cohesive surface, respectively. Furthermore, it follows from (8.19) as well as from the irreversibility of damage that

$$\dot{d} \geq 0. \tag{8.25}$$

8.3. Numerical computation of local damage
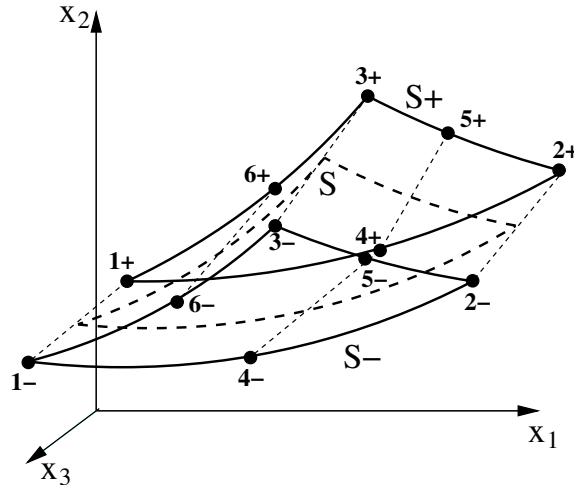
Figure 8.7.: Geometry of shear band element. The surface S^- and S^+ coincide in the reference placement of the solid.

The particularly appealing aspect of the introduced localization model is that it fits naturally within the conventional framework of finite element analysis. The deformation power (8.14) is distinct to the classical formulation only by an additional jump term for the localized surfaces. Depending on the constitutive relation employed within these jumps, the effective incremental potential for a material with cracks (following special cohesive laws, see Section 8.1) or a material with shear bands (with the constitutive properties of the bulk material) can be derived. Here, we outline the procedure of how to embed the discontinuous local surface into finite elements, leading to the formulation of *cohesive elements* [255] or *shear band elements* [382].
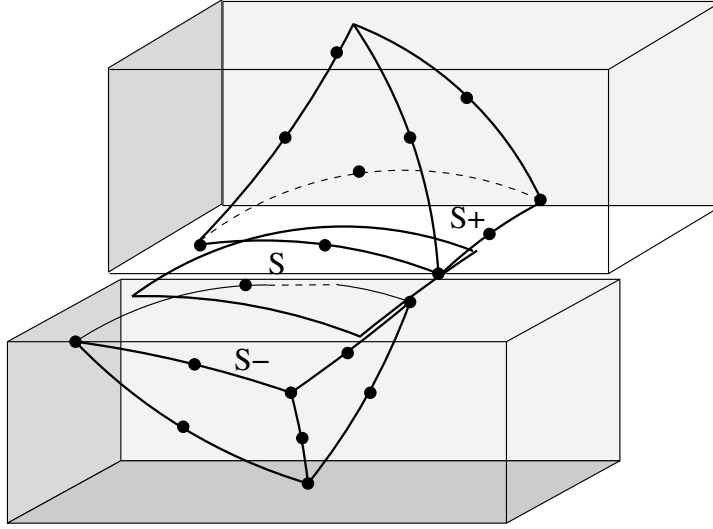
Figure 8.8.: Assembly of one 12-node triangular shear band element and two 10-node tetrahedral elements.

The class of elements considered here consists of two surface elements which coincide in space in the reference placement of the solid, Figure 8.7. Each of the surface elements has n nodes. The total number of nodes for the localization band element is, therefore, $2n$. The particular triangular geometry depicted in Figure 8.7 is compatible with three-dimensional tetrahedral elements, see Figure 8.8 and Chapter 5.2. The compatibility of such band elements with other bulk elements is straightforward.

The standard shape functions for each of the constituent surface elements are denoted by $N_a(s_1, s_2), a = 1, \ldots, n$, where (s_1, s_2) are the natural coordinates of each of the surface elements in some convenient standard setting. We designate one of the surface elements as S^- and the other as S^+, however, all geometrical operations such as the computation of the normal are carried out on the *mid-surface* S of the element. The surface coordinates are defined parametrically as

$$\boldsymbol{x}(\boldsymbol{s}) = \sum_{a=1}^{n} \bar{\boldsymbol{x}}_a N_a(\boldsymbol{s}), \tag{8.26}$$

where the mean coordinates are

$$\bar{\boldsymbol{x}}_a = \frac{1}{2}\left(\boldsymbol{x}_a^+ + \boldsymbol{x}_a^-\right), \tag{8.27}$$

and $\boldsymbol{x}_a^{\pm}, a = 1, \ldots, n$ are the coordinates of the nodes in the undeformed setting of the element. Additionally, the natural coordinates (s_1, s_2) define a convenient system of

curvilinear coordinates for the mid-surface of the element. The corresponding tangent basis vectors are

$$\boldsymbol{A}_\alpha\left(\boldsymbol{s}\right) = \boldsymbol{x}_{,\alpha}\left(\boldsymbol{s}\right) = \sum_{a=1}^{n} \bar{\boldsymbol{x}}_a N_{a,\alpha}\left(\boldsymbol{s}\right), \tag{8.28}$$

where $\alpha = 1, 2$. The unit normal to S is

$$\boldsymbol{N} = \frac{\boldsymbol{A}_1 \times \boldsymbol{A}_2}{\left|\boldsymbol{A}_1 \times \boldsymbol{A}_2\right|}, \tag{8.29}$$

which, by definition, points from S^- to S^+.

The displacement-jump vector in the deformed placement is obtained by

$$\boldsymbol{\delta}\left(\boldsymbol{s}\right) = \sum_{a=1}^{n} [\![\boldsymbol{x}_a]\!] N_a\left(\boldsymbol{s}\right), \tag{8.30}$$

where

$$[\![\boldsymbol{x}_a]\!] = \boldsymbol{x}_a^+ - \boldsymbol{x}_a^-. \tag{8.31}$$

Evidently, $\boldsymbol{\delta}$ remains invariant under superposed rigid translations of the element.

For one localization element, the potential energy is computed from equation (8.5) to be

$$\Pi_n = \int_{S_0} \phi_n \, dS_0 = \int_{S_0} h W_n(\boldsymbol{F}) \, dS_0. \tag{8.32}$$

The nodal forces now follow as

$$f_{ia}^\pm = \frac{\partial \Pi_n}{\partial x_{ia}^\pm} = \int_{S_0} \left(\frac{\partial \phi_n}{\partial h} \frac{\partial h}{\partial x_{ia}^\pm} + h \frac{\partial W_n}{\partial x_{ia}^\pm} \right) dS_0. \tag{8.33}$$

For the case of a shear band element, we follow the assumption that the shear band thickness remains constant, as observed in experiments [132]. Introducing equation (8.6) gives

$$f_{ia}^\pm = \int_{S_0} h \frac{\partial W_n}{\partial F_{mL}} \frac{\partial F_{mL}}{\partial x_{ia}^\pm} \, dS_0 = \int_{S_0} h P_{mL} \frac{\partial F_{mL}}{\partial x_{ia}^\pm} \, dS_0. \tag{8.34}$$

The calculation of the first Piola-Kirchhoff stresses $\boldsymbol{P}$ is straightforward by using, e.g., a finite plasticity stress update as outlined in Chapter 6 and 7. In case of a cohesive zone model the nodal forces follow from a cohesive law.

The term $\partial F_{mL}/\partial x_{ia}^\pm$ can be calculated conveniently by introducing a local coordinate system on the mid-surface. Given an arbitrary vector $\boldsymbol{b}$ such that $\boldsymbol{b} \times \boldsymbol{N} \neq \boldsymbol{0}$, this local coordinate system can be defined by

$$\hat{\boldsymbol{X}}_1 = \frac{\boldsymbol{b} \times \boldsymbol{N}}{\left|\boldsymbol{b} \times \boldsymbol{N}\right|}, \quad \hat{\boldsymbol{X}}_2 = \frac{\boldsymbol{N} \times \hat{\boldsymbol{X}}_1}{\left|\boldsymbol{N} \times \hat{\boldsymbol{X}}_1\right|}, \tag{8.35}$$

which gives a transformation matrix $\boldsymbol{Q} = [\hat{\boldsymbol{X}}_1 \ \hat{\boldsymbol{X}}_2 \ \boldsymbol{N}]$. Thus,

$$\boldsymbol{F}^{\parallel} = \boldsymbol{Q}\hat{\boldsymbol{F}}^{\parallel}\boldsymbol{Q}^T, \quad \frac{\partial \boldsymbol{F}^{\parallel}}{\partial \boldsymbol{x}} = (\boldsymbol{Q}\frac{\partial \hat{\boldsymbol{F}}^{\parallel}}{\partial \hat{\boldsymbol{x}}}\boldsymbol{Q}^T)\boldsymbol{Q}^T. \tag{8.36}$$

The deformation gradient as given by equation (8.4) can be written as

$$F_{mL} = F_{mL}^{\parallel} + \frac{\delta_m}{h}N_L, \tag{8.37}$$

It follows that

$$\frac{\partial F_{mL}}{\partial x_{ia}^{\pm}} = \frac{\partial F_{mL}^{\parallel}}{\partial x_{ia}^{\pm}} + \frac{1}{h}N_L\frac{\partial \delta_m}{\partial x_{ia}^{\pm}}, \tag{8.38}$$

with

$$\frac{\partial}{\partial x_{ia}^{\pm}} = \frac{\partial \bar{x}_{lc}}{\partial x_{ia}^{\pm}}\frac{\partial}{\partial \bar{x}_{lc}} = \frac{1}{2}\frac{\partial}{\partial \bar{x}_{ia}}, \tag{8.39}$$

and, in the local coordinate system

$$\left[\hat{F}_{mL}^{\parallel}\right] = \left[\begin{array}{ccc} & & 0 \\ \sum\limits_{b=1}^{n} \bar{x}_{mb}\hat{N}_{b,\beta} & 0 \\ & & 1 \end{array}\right], \tag{8.40}$$

where $\hat{N}_{b,\beta}$ $(b = 1, \ldots, n; \beta = 1, 2)$ are the derivatives of the local shape functions with respect to the material frame. Finally, we obtain

$$\left[\frac{\partial \hat{F}_{mL}^{\parallel}}{\partial \hat{x}_{ia}^{\pm}}\right] = \left[\begin{array}{ccc} & & 0 \\ \frac{1}{2}\delta_{mi}\hat{N}_{a,\beta} & 0 \\ & & 0 \end{array}\right] \tag{8.41}$$

where δ_{mi} is the Kronecker delta. From equation (8.30), we have

$$\frac{\partial \delta_m}{\partial x_{ia}^{\pm}} = \pm\delta_{mi}N_a. \tag{8.42}$$

Thus, the nodal forces can be obtained analytically by substituting (8.38), (8.40), (8.41) and (8.42) into (8.34). As usual in finite elements, the integration over the surface may conveniently be approximated by using a numerical quadrature rule. Moreover, we can see from (8.38) that for very thin bands, the membrane forces may be neglected, which leads to

$$f_{ia}^{\pm} = \pm\int_{S_0} P_{mL}N_L\delta_{mi}N_a \, dS_0 = \pm\int_{S_0} T_iN_a \, dS_0. \tag{8.43}$$

159

It is worth noting that this expression is used in cohesive elements for force recovery, whereas in shear bands the tractions are obtained naturally from the first Piola-Kirchhoff stress.

Summarizing we emphasize that the dual work-conjugate relations between stress and deformation measure (8.14) hold for general bodies with discontinuous local surfaces. These can be brittle or ductile cohesive zones as well as shear bands. As in conventional solids, the first Piola-Kirchhoff stress tensor $\boldsymbol{P}$ does work on the total deformation gradients $\boldsymbol{F}$ over the bulk of the body. In case of a shear band the tractions $\boldsymbol{T}$ are a natural outcome of the first Piola-Kirchhoff stress tensors, which in turn are completely determined by the deformation gradient once a (bulk) constitutive relationship is specified. No other constitutive relationships are needed. If the discontinuous local surface is modeled as a cohesive zone the tractions $\boldsymbol{T}$ do work on the displacement jumps $[\![\boldsymbol{\varphi}]\!]$ or opening displacements over the cohesive zone; their relation is prescribed by a cohesive law.

8.4. Simulations of phase decompositions and grain coarsening

The specific structure of phase decomposition and ex-solution follows from an interplay of different physical effects. In a typical aging metal alloy these are:

Fickean diffusion: Classical diffusion is induced by a local difference in concentration of the constituents. The flux of concentration $\boldsymbol{j}$ [mol s/m^2] is generated by the concentration gradient ∇c weighted with the diffusion coefficient D. The evolution of concentration follows by Fick's law

$$\dot{c} = -\operatorname{div}\boldsymbol{j} \qquad (8.44)$$
$$= \operatorname{div} D\nabla c. \qquad (8.45)$$

In equilibrium Fickean diffusion would result in a reduction of the differences in concentration and, finally, in a uniformly distributed concentration (downhill diffusion). However, this result is a contradiction to many experimental observations. More general — non-equilibrium — theories of diffusion introduce a chemical potential μ of the mixture [231]. Then, the diffusion (8.45) is driven by a local difference in the chemical potential $\mu \equiv \mu^A - \mu^B$, instead.

$$\dot{c} = \operatorname{div} M\nabla\mu \qquad (8.46)$$

Here M is a phenomenological determined diffusion mobility coefficient.

Surface tension: A description of a non-local phase separation, i.e., a specific morphology of ex-solution, requires the concept of gradient energies (known as Landau-Ginzburg functionals). In physical terms this means, that differences in surface energy generate morphological evolution and define number and size of the islands of different phases.

Thermo-mechanical straining: Mechanical stresses and strains — caused by temperature difference or by mechanical loading — superpose the natural aging effects of an alloy and may induce a specific morphology like, e.g., a specific orientation or lamella-like shapes of the phases.

In the following we want to analyze and model these physical effects in more detail, starting with some classical relations of the thermodynamics of mixtures. Here we restrict ourselves to binary alloys and mixtures. Then, for the mass concentrations c^A and c^B holds $c^B = 1 - c^A$ and we define

$$c = c^B \quad \text{and} \quad (1 - c) = c^A. \tag{8.47}$$

Starting from the first and second law of thermodynamics (2.37–2.39) and from the definition of **Gibbs free energy**, equation 2.45, we can derive for its temporal development the inequality

$$\dot{G} \leq S\dot{T} + V\dot{p}. \tag{8.48}$$

In other words, the Gibbs free energy G attains a minimum in mechanical and thermodynamical equilibrium with $\dot{T} = 0$ and $\dot{p} = 0$. In the following we will consider sequences of such (quasistatic) solutions.

In a binary alloy with constant pressure and prescribed temperature the total Gibbs free energy is a function of contributions of both constituents. Figure 8.9 illustrates the typical form of $G(c^A, c^B, T) \equiv G(c, T)$ during a phase transition from liquid to solid. At temperatures higher than the melting point of both constituents the free energy is a simple convex function of concentration within the admissible region $0 \leq c \leq 1$. For an ideal mixture (nearly the case in a fluid) the **configurational Gibbs free energy density** can be derived by means of the thermal equation of state $p = RT/V$ (R denotes the gas constant and V the volume) summed for all mols of constituent A and B referred to the unit initial volume, and, by the additivity of pressure (Dalton's law). Simple thermodynamical considerations (cf. [41]) lead for a binary mixture to[1]

$$G^{ideal} = cG^A(T, p) + (1 - c)G^B(T, p) + RT\big(c\ln(c) + (1 - c)\ln(1 - c)\big), \tag{8.49}$$

---

[1]In a minor misuse of notation we denote form now on with the letter G the Gibbs free energy per unit initial volume.
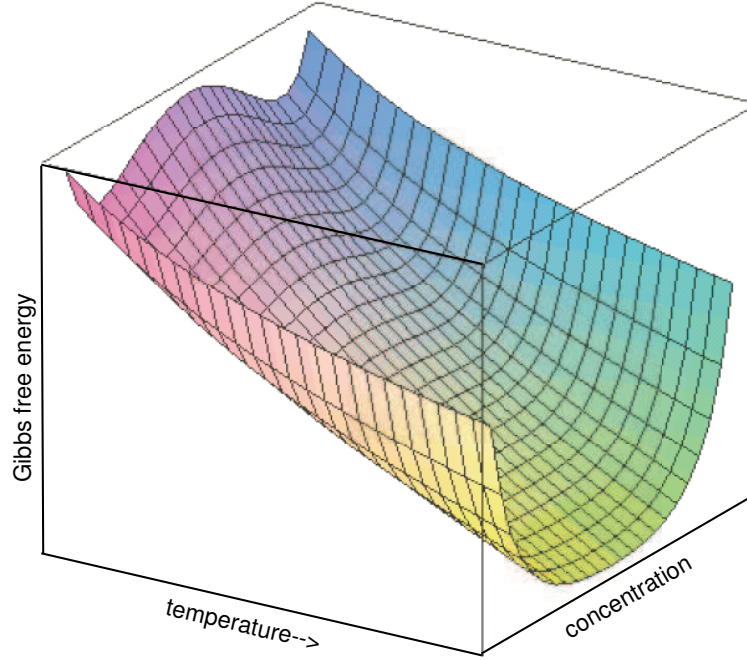
Figure 8.9.: Gibbs free energy as a function of temperature and concentration for liquid to solid phase transition.

where G^A and G^B denote the configurational Gibbs free energy density of the constituents which can be found in tables for most pure substances.

With decreasing temperature the magnitude of G raises, and at beginning solidification the shape of G starts to change — resulting in a function which has two internal minima in the solid state. For this non-ideal state of a mixtures accounts an **excess energy density**, which is a general function of higher order terms of c and added to equation (8.49). Data for the excess energy can also be found in tables for many materials. Moreover, there exists several different functions to account for that non-ideal energy contribution. Among others, the so-called Margules ansatz is frequently used (cf. [41])

$$G^{ex} = c(1-c)\Big(c\,\chi^A(T,p) + (1-c)\,\chi^B(T,p)\Big), \tag{8.50}$$

where χ^A, χ^B are empirical parametric functions depending on pressure and temperature. In another approach, the Redlich-Kister ansatz, the empirical contributions are developed in series resulting in an ansatz of the form

$$G^{ex} = c(1-c)\Big(\mathtt{A} + \mathtt{B}(c^A - c^B) + \mathtt{C}(c^A - c^B)^2 + \dots\Big), \tag{8.51}$$

with $A, B, C, \ldots$ to be determined. The excess energy density is essentially responsible for the actual shape of the configurational free energy density , in particular, for being a **double well potential** in a solid binary mixture.

This non-convex shape of the free energy function reflects the phenomena that there exists a region of concentration where two phases are stable, a so-called miscibility gap. The center of this region is the unstable **spinodal** region, here holds $\partial^2 G / \partial y^2 < 0$, see also Figure 8.10. The two points where $\partial^2 G / \partial c^2 = 0$, are called the spinodal points ($\bullet$ in Figure 8.10), they mark the change of curvature of function G. The two minima of the Gibbs free energy function are external to the spinodal region. The two **binodal** points ($*$ in Figure 8.10) are defined by a common tangent known as Maxwell-tangent construction, with condition

$$\left.\frac{\partial G}{\partial c}\right|_\alpha = \left.\frac{\partial G}{\partial c}\right|_\beta = \frac{G(c_\beta) - G(c_\alpha)}{c_\beta - c_\alpha}. \tag{8.52}$$

The corresponding characteristic concentrations c_α and c_β are the equilibrium concentrations of phase α (rich in constituent A) and phase β (rich in constituent B). A mixture of concentration c with $c_\alpha \leq c \leq c_\beta$ will separate into two phases of either of the two binodal compositions c_α and c_β.
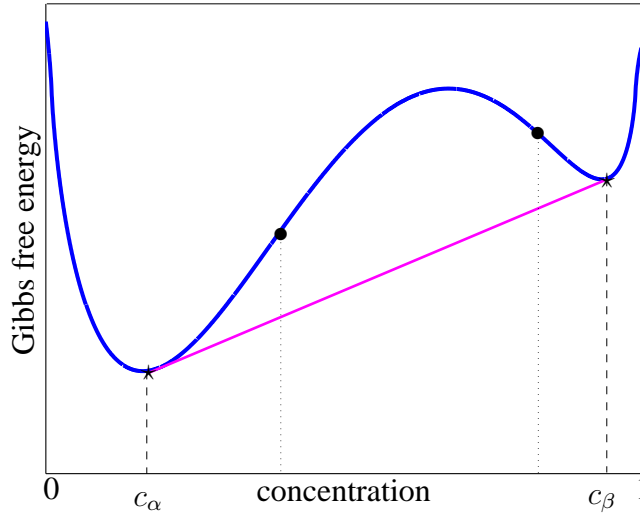
Figure 8.10.: Gibbs free energy functional in a solid binary mixture.

In the process of phase separation the material moves against concentration gradients (uphill diffusion). The local driving force for such diffusion processes is the chemical

potential, which controls the optimization of the Gibbs free energy density with respect to the concentration, i.e., $\mu = \partial G/\partial c$. Then, the diffusion equation (8.46) gets the form

$$\dot{c} = \operatorname{div} M \nabla \frac{\partial G}{\partial c} .$$

However, phase separation (and subsequent grain coarsening) are non-local diffusion processes where the actual phase morphology is determined by the "neighbors" of the material point under consideration. To account for such neighboring effects additional surface (or interfacial) energy contributions need to be added to the Gibbs free energy density (8.49-8.51). Following Cahn and Hilliard [67, 66] we assume an surface energy contribution of the form,

$$G^{surf} = \frac{1}{2} \gamma l_c^2 \left(\nabla c \right)^2 , \tag{8.53}$$

where γl_c^2 is the surface tension multiplied with some material depended critical length l_c. Surface energy contributions in a mixture are related to the gradient of concentration, ∇c. Consequently the optimization of the Gibbs free energy functional requires a variational approach[2]. In the context of gradient functionals the first variation reads $\delta(\cdot) = \partial \cdot/\partial c - \operatorname{div}(\partial \cdot/\partial(\nabla c))$. Accordingly, the chemical potential follows as

$$\mu = \frac{\partial G}{\partial c} - \operatorname{div}\left(\frac{\partial G}{\partial(\nabla c)}\right) = \frac{\partial G^{conf}}{\partial c} - \operatorname{div}\left(\gamma l_c^2 \nabla c\right). \tag{8.56}$$

Inserting (8.56) in the diffusion equation (8.46) results in a fourth order differential equation in terms of the concentration,

$$
\begin{aligned}
\dot{c} &= \operatorname{div}\left[\boldsymbol{M}\nabla\mu\right] \\
&= \operatorname{div}\left[\boldsymbol{M}\nabla\left(\frac{\partial G^{conf}}{\partial c} - \operatorname{div}(\gamma l_c^2 \nabla c)\right)\right] \\
&= \operatorname{div}\left[\boldsymbol{M}\left(\frac{\partial^2 G^{conf}}{\partial c^2}\nabla c - \nabla\left(\operatorname{div}(\gamma l_c^2 \nabla c)\right)\right)\right]
\end{aligned}
\tag{8.57}
$$

---

[2]Presuming necessary continuity and differentiability the optimum of the (one-dimensional) functional

$$\mathcal{I} = \int_{x_0}^{x_1} f\left(x, y, y^{'}, y^{''}, \ldots, y^{(n)}\right)dx \tag{8.54}$$

with appropriate boundary condition $y(x_0) = y_0$, $y^{'}(x_0) = y_0^{'}$, ..., $y^{(n)}(x_1) = y_1^{(n)}$ is the solution of the Euler-Lagrange equation

$$f_{,y} - \frac{d}{dx}f_{,y'} + \frac{d^2}{dx^2}f_{,y''} - + \ldots (-1)^n \frac{d^{(n)}}{dx^{(n)}}f_{,y^{(n)}}. \tag{8.55}$$

The extension to more dimensions is straightforward, cf. [53].

where the materials mobility coefficients $\boldsymbol{M}$ are written in tensorial form. This is motivated by the experimental observation of anisotropic phase separation textures; this effect can be modeled e.g., by anisotropic mobility coefficients.

The classical Cahn–Hilliard equation (8.58) governs the process of initial ex-solution, where phase separation is controlled by the configurational free energy, as well as later-stage domain coarsening driven by the reduction of the surface free energy [67, 68, 65, 69]. This coarsening is equivalent to the well known Ostwald ripening where the domain size grows proportional to the third root of time as derived by Lifshitz, Slyozov and Wagner [195, 354]. Grain ripening (attributed to an early work of Ostwald [258]) involves solid-state grain boundary migration driven by locally high surface energies which, in turn, depend on the difference in concentration gradients.

A particular important influence on the phase separation and grain coarsening process is the stress and strain state induced by mechanical (or thermal) loading. Therefore, our starting point to investigate spinodal decomposition and phase growth in binary mixtures will be an extended diffusion equation, whereby an additional term accounts for local thermo-mechanical stresses,

$$\dot{c} = \text{div}\left[\boldsymbol{M}\left(\frac{\partial G^{conf}}{\partial c}\nabla c - \nabla\big(\text{div}(\gamma l_c^2 \, \nabla c)\big) - \frac{\partial}{\partial c}\big(\frac{1}{2}\boldsymbol{\sigma}\cdot\boldsymbol{\epsilon}\big)\right)\right] \tag{8.58}$$

Here $\boldsymbol{\epsilon}$ denotes the (linear) strain and $\boldsymbol{\sigma}$ the corresponding stress tensor. The latter may depend on the concentration via the stiffness tetrad.

Starting from the fundamental investigations of Cahn and Hilliard, [67, 69] several extensions and additions followed. Dreyer et al. [104, 105, 107] recently developed an extended diffusion equation strictly basing on the principles of Rational Thermodynamics. In particular, the theory accounts for concentration and strain depended material coefficients. Written in components the resulting equation of [107] reads

$$\begin{aligned}
\frac{\partial c}{\partial t} &= \frac{\partial}{\partial x_i}\Big[M_{ij}\frac{\partial}{\partial x_j}\Big(\frac{\partial G(\epsilon_{kl}, c, T)}{\partial c} - 2A_{kl}\frac{\partial^2 c}{\partial x_k \partial x_l} - \frac{\partial A_{kl}}{\partial c}\frac{\partial c}{\partial x_k}\frac{\partial c}{\partial x_l} \\
&\quad -2\frac{\partial A_{kl}}{\partial \epsilon_{mn}}\frac{\partial c}{\partial x_k}\frac{\partial \epsilon_{mn}}{\partial x_l} - \frac{\partial^2 a_{kl}}{\partial \epsilon_{op}\partial \epsilon_{mn}}\frac{\partial \epsilon_{op}}{\partial x_k}\frac{\partial \epsilon_{mn}}{\partial x_l} - \frac{\partial a_{kl}}{\partial \epsilon_{mn}}\frac{\partial^2 \epsilon_{mn}}{\partial x_k \partial x_l}\Big).\Big]
\end{aligned} \tag{8.59}$$

The material coefficients $M_{ij}(c, T)$, $A_{ij}(\epsilon_{kl}, c)$ and $a_{ij}(\epsilon_{kl}, c)$ are the mobility and the higher gradient coefficients. These material parameters can be obtained either from literature or from calculations based on atomic interaction models, see [42, 43].

A one-dimensional numerical solution of Equation (8.59) is illustrated for the strain-free case in Figure 8.11 (i.e., all terms of ϵ are dropped and, moreover, the coefficients
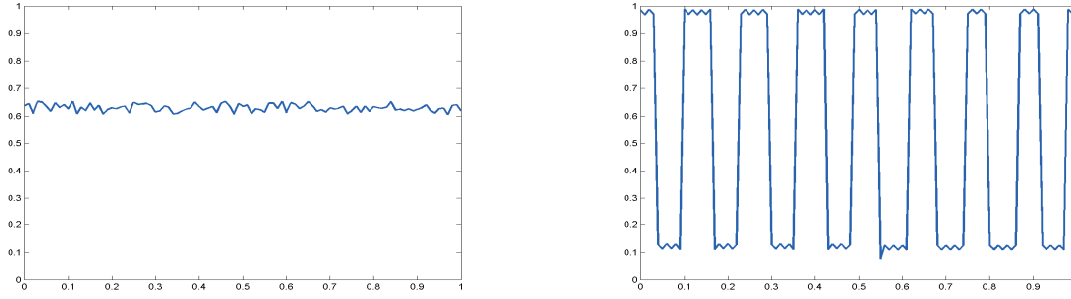
Figure 8.11.: FE-Simulation of spinodal decomposition and phase growth in an Sn-Pb alloy: an initially eutectic solution with randomly distributed deviations in concentration (left) decomposes to regions of α and β-phases within several minutes (right, after 8 minutes).

A_{ij} are assumed to be constant). Using the data of [348, 349] for an eutectic SnPb alloy, a discretization with 100 linear finite elements is carried out for spatial, and a fully implicit scheme for time discretization. The length of the probe is 10μm, the temperature of simulation is 423 K (eutectic Sn-Pb has a melting temperature of 453K). Initially, the eutectic solution has little randomly distributed deviations in concentration. After few minutes the alloy decomposes into islands of α-phases (Pb-rich) and β-phases (Sn-rich). Further coarsening, i.e., a reduced number of islands, will be observed within hours.

Part II.

Applications

9. Dynamic Failure and Fragmentation in Ductile Metal Structures

In Chapter 7 a variational finite-deformation framework for irreversible volumetric expansion in a plastically deforming material was developed. The specific model presented here exploits the void growth ideas for the finite element simulation of ductile damage in metals under dynamic loading conditions. The spacial and temporal discretizations of the structures follow the concepts of Section 5.2 and 5.1, respectively. The constitutive relations are discretized in time by means of the variational update outlined in Section 7.6.

The resulting engineering model and constitutive updates provide a fully variational alternative to Gurson-like models. In particular, the present variational update decouples finite volumetric and deviatoric deformations, is exactly material-frame indifferent under finite rotations, and results in symmetric tangent moduli.

The predictive capabilities of the model are demonstrated by the finite simulation of the Taylor impact test and the forced expansion and fragmentation of U-6%Nb rings. Comparisons of the localisation of void growth, the velocity histories and number of ring fragments show that the results of the calculations are in very good agreement with experimental observations.

9.1. Void growth in metals

The failure of ductile metals is based on the process of nucleation, growth and finally coalescence of voids. The ratio of the total volume of all voids to the volume of the body is defined as the void volume fraction f_V, see equation (7.1) of Chapter 7. Through plastic straining of the surrounding material the voids may grow and change shape. From experiments we know that the voids start to coalesce and finally ductile failure occurs when the porosity in the material reaches about $0.1 - 0.3$ [22, 270, 95]. This may still be observed on the fracture surface of ductile materials which is typically dimpled.

First micromechanical studies on void growth go back to the 60th [210, 283]. McClintock [210] analyzed the expansion of a single cylindrical vacancy subjected to remote tensile and hydrostatic strain fields and pointed out that the fracture ductility decreases rapidly with rising hydrostatic tension. This observation agrees with several experiments [202, 203, 331]. Rice and Tracey [283] found that the size and the shape of a void in a plastic material is determined by the superposition of volumetric and (minor) shape-changing components that amplify the distortion imposed by the remote strain field.

The classical yield condition for porous ductile materials was developed by Gurson [137] who, like most subsequent authors, exploits the idea that the physical process of damage in ductile media may be described by the structural behavior of simple representative volume elements. The characteristic volume element of Gurson is a conglomerate of voids in a rigid perfectly-plastic matrix. The voids are assumed to be randomly distributed so that the macroscopic response is isotropic. Averaged solutions on the microlevel have been used to estimate upper bounds for the macroscopic stress field. For a spherical unit cell including a spherical void the plastic potential as a function of the porosity f_V, the mean normal stress (hydrostatic tension and pressure) p and the effective von Mises stress σ reads

$$\Psi(f_V, p, \sigma_e) = \left(\frac{\sigma_e}{\sigma_y}\right)^2 + 2q_1\, f_V\, \cosh\left(\frac{q_2 p}{2\sigma_y}\right) - \left(1 + (q_1\, f_V)^2\right), \tag{9.1}$$

where σ_y is the macroscopic yield strength. The weight coefficients q_1, q_2 equal one in the original work [137]. The plastic potential (9.1) defines with $\Psi(f_V, p, \sigma_e) = 0$ a macroscopic yield condition. Moreover, the void volume fraction f_V is considered to be the internal variable characterizing damage and final failure occurs in the limit $f_V \to 1$.

It soon became apparent that Gurson criterion in its original form leads not only to an unrealistic failure limit, it also overestimates the dilatational component of the strain [6, 341, 342]. Therefore numerous experimentally and numerically based modifications followed, see [343] for an review on this subject. Essentially the modifications introduced adjustable weights and functional dependencies for the void volume fraction f_V, fitting them to more realistic values [346, 133, 309], considering void nucleation and coalescence [52, 85, 308], as well as incorporating a more complex bulk material behavior [25, 184, 122, 334, 347, 142]. Tvergaard and Needleman [346] introduced a bilinear function which accounts for an accelerated damage of voids due to the effect of coalescence after reaching an empirical critical void volume fraction. This so called Gurson-Tvergaard-Needleman model became the conventional criterion for ductile fracture problems. One reason for its success is that the set of adjustable parameters can be fitted to any particular numerically or experimentally analyzed material behavior.

However, accurate failure strains for rate and temperature dependent materials with

randomly distributed voids can not be obtained this way. Because the porosity is characterized by a single parameter f the model can not account for different distributions, sizes or shapes of voids, that means a population of small voids and one void having equal volume would be treated equally. In addition there is no intrinsic ability to predict void coalescence.

An alternative way to model the macroscopic properties of a porous plastic metal is to understand it as a two phase composite, i.e. a bulk material with (empty) inclusions [185]. By homogenization techniques upper and lower bounds for the effective properties of an equivalent homogenized medium can be derived, cf. [79]. Herewith the solutions are not only more rigorous, this technique also allows to consider additional damage parameters, as e.g., in [119], the void aspect-ratio and the void distribution (randomly distributed voids may weaken the material much more than a uniformly distributed porosity [202, 26, 250]). However, dynamical effects on the growth of voids are not regarded. Newer developments [385, 269, 224] combine

Figure 9.1.: Surface in brittle fracture.

both approaches and replace the empirical parameter in Gurson's criterion by micromechanically motivated relations, as e.g., a plastic limit load model for the intervoid matrix proposed by Thomason [329, 328].
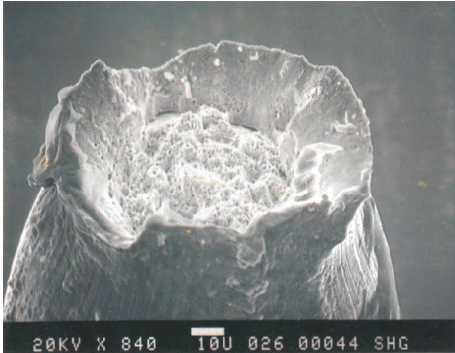
Figure 9.2.: Typical surface in static ductile fracture [1].

One relevant result in the understanding of void growth is the concept of critical cavitation pressure. When the hydrostatic tension is sufficiently high, the voids inside a material grow unboundedly even through the remote stresses and strains are kept fixed. The existence of such an instability was recognized by Ball for nonlinear elastic solids [13] and later determined for quasistatic elasto-plastic solids by Huang et al., [156, 344]. The unstable cavitation can be thought of as a process in which the elastic energy of the remote field drives the plastic expansion of voids. Only for undercritical hydrostatic tension the voids undergo a bounded growth, eventually attaining stationary configurations. The initial shape of the void has a minor effect on the critical cavitation pressure [345].

170

Whereas the ductile failure mechanism under static conditions are extensively studied, the dynamical effects on void expansion have been relatively disregarded. In an early theoretical work Carroll and Holt (1972) [72] analyzed the collapse of a sphere in an ideal plastic material and concluded that effect of elastic compressibility on the solution is negligible. In a similar manner Johnson [167] studied plastic void expansion under shock load. Nemat-Nasser and Hori [153, 243] reason that the global response of the material is different in compression and tension and significantly affected by the loading rate. The analysis of Cortes [96, 97] shows important effects of rate sensitivity but does not account for inertia.
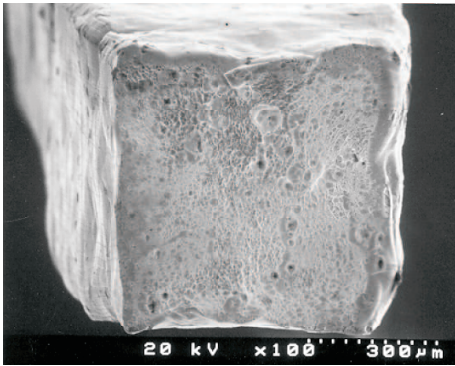
Figure 9.3.: Typical surface in dynamic ductile fracture [249].

At very high strain rates ($> 10^6 s^{-1}$) the typical void growth turns out to be very different to the quasistatic case. In general extremely high stress levels, especially very high hydrostatic tensions, are developed and the inertial stresses are not longer negligible. Many experimental results are reported investigating the effect of impact loading on the failure of metals, see e. g. [21, 101, 227, 316, 326]. Upon impact compressive stress waves travel through the body which by reflection and superposition may induced high tension and the material will fail dynamically. This process, known as spallation, has been studied extensively, cf. [16, 28, 124, 312, 391]. The spall strength of the material, which is determined by impact-spallation experiments, may be understood as critical tensile strength under shock load conditions [270].

Ortiz and Molinari analyzed in [254] the dynamic expansion of a single spherical void in an infinite rigid plastic medium under the action of remote hydrostatic tension. They pointed out that if the void radius increases the initial radius by at least one order of magnitude the void growth is dominated by micro-inertia effects, whereas the effect of rate dependence of the material and the plastic dissipative effects play a secondary role. Under the regime of rapidly applied, supercritical hydrostatic tension the void radius growth unboundedly as a linear function of time. Tong and Ravichandran [334] and Thomason [330] draw similar conclusions, they also emphasize the strong stabilizing effect of microinertia on the void growth process which consequently delays coalescence of the voids. Molinari and Mercier [224] found that high accelerations sustained by the material particles in the vicinity of voids result in significant inertia effects particularly

for materials with low strain-rate sensitivity.

Here we apply a variational formulation for a rapidly loaded porous plastic material. The compelling aspect of variational formulations is that they provide the theoretical background for error controlled finite elements methods. Fe-mesh adaption is extensively studied and well understood for linear problems, see e.g. [353, 48], but it is hardly developed in the context of strongly nonlinear and dynamic problems. If the constitutive updates follow from a minimum principle like presented here, this can be taken as a basis for error estimation and finite element mesh adaption [276]. As outlined in Chapter 7 a relatively simple void growth model describes plastic expansion and global softening of the material with parameters of the mesomechanical model; avoiding altogether the need of macroscopic failure criteria.

9.2. Constitutive relations

Here the application of the general framework of Chapter 7 to the case of porous metal plasticity is illustrated. We specifically focus on conditions such as arise in shocked metals, involving high pressures, high strain rates and non-negligible microinertia.

Motivated by the evolution of void distribution in rapidly loaded materials (Chapter 7.3.4) we proceed describing the porous metal by an ensemble of voids with a mean radius $\bar{a}(t)$. The initial local volume fraction of voids in the undeformed placement is

$$f_{V0} = N_V \frac{4\pi \bar{a}_0^3}{3}, \tag{9.2}$$

where N_V is void density, i.e., the number of spherical voids per unit undeformed volume of the body, and $\bar{a}_0$ is the initial mean void radius in the representative volume. As introduced in Chapter 7.4 the void radius is in one-to-one correspondence to the plastic Jacobian

$$J^p = 1 - f_{V0} + N_V \frac{4\pi \bar{a}^3}{3}, \tag{9.3}$$

and the current void volume fraction is

$$f_V = \frac{f_{V0} + J^p - 1}{J^p}. \tag{9.4}$$

Let the free-energy density (7.120) have an additive structure (7.158),

$$A(\boldsymbol{F}, \boldsymbol{F}^p, \epsilon^p, \theta^p, T) = W^e(\boldsymbol{F}^e, T) + W^p(\epsilon^p, \theta^p, T),$$

where $W^e(\boldsymbol{F}^e, T)$ and $W^p(\epsilon^p, \theta^p, T)$ are the elastic and stored energy densities per unit undeformed volume, respectively. These energy contributions are defined by equations (7.167) – (7.164) of Chapter 7. Additionally, power contributions follow from rate sensitivity and microinertia, equations (7.171) – (7.174).

The plastic deformation rate is assumed to obey the flow rule (7.122) which we repeat here for convenience

$$\dot{\boldsymbol{F}}^p \boldsymbol{F}^{p-1} = \dot{\varepsilon}^p \boldsymbol{M} + \dot{\vartheta}^p \boldsymbol{N},$$

where the rate of the effective deviatoric plastic strain $\dot{\varepsilon}^p$ and the rate of the effective volumetric plastic strain $\dot{\vartheta}^p$ are subject to the irreversibility constraints

$$\dot{\varepsilon}^p \geq 0 \tag{9.5a}$$

$$\dot{\vartheta}^p \geq 0 \tag{9.5b}$$

and the tensors $\boldsymbol{M}$ and $\boldsymbol{N}$ set the direction of the deviatoric and volumetric plastic deformation rates, respectively.

In finite element analysis an incremental solution procedure with time intervals $[t_n, t_{n+1}]$ is used for the time integration of the constitutive equations. Assume that the state of the material, $\boldsymbol{F}_n^p$, ϵ_n^p, θ_n^p, $\dot{\theta}_n^p$ and $\ddot{\theta}_n^p$, is known at time t_n, and let the deformation gradient $\boldsymbol{F}_{n+1}$ and the temperature T_{n+1} at time t_{n+1} be given. The problem is then to determine the current state of material, $\boldsymbol{F}_{n+1}^p$, ϵ_{n+1}^p, θ_{n+1}^p, $\dot{\theta}_{n+1}^p$ and $\ddot{\theta}_{n+1}^p$, as well as the directions $\boldsymbol{M}, \boldsymbol{N}$ of the incremental plastic deformation, the value of the Piola-Kirchhoff stress $\boldsymbol{P}_{n+1}$ and the tangent moduli $D\boldsymbol{P}_{n+1}$. The general way of solution is outlined in Section 7.6. Here we shortly summarize the results and put special emphasis on the additional contributions arising from microinertia.

The differential equations of motion for the growth of the voids are second order in time due to microinertia. In order to formulate updates possessing a variational structure, the time-discretization of the equations of motion must itself possess an incremental variational structure. Newmark's algorithm, when applied to systems with quadratic inertia and constant mass such as (7.174), leads to a minimum problem for the incremental displacements. Thus, we introduce the Newmark predictor

$$b_{n+1}^{\text{pre}} = b_n + \triangle t \dot{b}_n + \left(\frac{1}{2} - \beta\right) \triangle t^2 \ddot{b}_n, \tag{9.6}$$

where $\beta \in (0, 1/2)$. Note that b is here the auxiliary variable defined by solution of equation (7.182),

$$b = \frac{2}{5} \frac{\bar{a}^{5/2}}{\bar{a}_0^{3/2}}. \tag{9.7}$$

We may now introduce the incremental objective function

$$f_n(\boldsymbol{F}_{n+1}, \epsilon^p_{n+1}, \theta^p_{n+1}, T_{n+1}, \boldsymbol{M}, \boldsymbol{N}) = W^e(\boldsymbol{\epsilon}^e_{n+1}, T_{n+1}) + W^p(\epsilon^p_{n+1}, \theta^p_{n+1}, T_{n+1})$$
$$+ \triangle t\, \psi^*_{n+1} + \beta\triangle t^2 B_{n+1}, \quad (9.8)$$

with $\triangle t = t_{n+1} - t_n$, and

$$\psi^*_{n+1} = \psi^*\left(\frac{\triangle\epsilon^p}{\triangle t}, \frac{\triangle\theta^p}{\triangle t}, J^p_{n+1}, T_{n+1}\right), \quad (9.9)$$

$$B_{n+1} = \frac{3\rho_{v0}}{2}\left(\frac{b_{n+1} - b^{\text{pre}}_{n+1}}{\beta\triangle t^2}\right)^2, \quad (9.10)$$

where $\triangle\epsilon^p = \epsilon^p_{n+1} - \epsilon^p_n$, $\triangle\theta^p = \theta^p_{n+1} - \theta^p_n$, and b_{n+1} is to be regarded as a function of J^p_{n+1} through (9.7) and (9.3).

Thus the update may be expressed in variational form as

$$W_n(\boldsymbol{F}_{n+1}, T_{n+1}) = \min_{\epsilon^p_{n+1}, \theta^p_{n+1}, \boldsymbol{M}, \boldsymbol{N}} f_n(\boldsymbol{F}_{n+1}, T_{n+1}, \epsilon^p_{n+1}, \theta^p_{n+1}, \boldsymbol{M}, \boldsymbol{N}), \quad (9.11)$$

subject to the kinematic constraints of plastic deformation and to the plastic irreversibly constraints

$$\triangle\epsilon^p \geq 0, \quad (9.12)$$
$$\triangle\theta^p \geq 0.$$

Equation (9.11) also defines the effective incremental strain-energy density $W_n(\boldsymbol{F}_{n+1}, T_{n+1})$ as the minimum of f_n. Finally, the Newmark correctors

$$\dot{b}_{n+1} = \dot{b}_n + \triangle t[(1 - \gamma)\ddot{b}_n + \gamma\ddot{b}_{n+1}], \quad (9.13)$$

$$\ddot{b}_{n+1} = \frac{b_{n+1} - b^{\text{pre}}_{n+1}}{\beta\triangle t^2}, \quad (9.14)$$

where $\gamma \in [0, 1]$, complete the update.

The effective work of deformation density (9.11) returns the updated values of the internal variables and the direction of plastic flow over the time step. Moreover, $W_n(\boldsymbol{F}_{n+1})$ acts as a potential for the first Piola-Kirchhoff stress tensor $\boldsymbol{P}_{n+1}$ at time t_{n+1} as shown in Section 7.6.

Minimization of f_n with respect to $\boldsymbol{M}$ and $\boldsymbol{N}$ gives after some algebraic manipulation,

$$\boldsymbol{M} = \frac{3\boldsymbol{s}^{\text{pre}}_{n+1}}{2\sigma^{\text{pre}}_{n+1}}, \quad (9.15)$$

$$\boldsymbol{N} = \frac{1}{3}\text{sgn}(p^{\text{pre}}_{n+1})\boldsymbol{I}, \quad (9.16)$$

where

$$
\begin{aligned}
\boldsymbol{s}_{n+1}^{\mathrm{pre}} &= 2\mu\mathrm{dev}(\boldsymbol{\epsilon}_{n+1}^{e,\mathrm{pre}}), \\
\sigma_{n+1}^{\mathrm{pre}} &= \sqrt{(3/2)\boldsymbol{s}_{n+1}^{\mathrm{pre}} \cdot \boldsymbol{s}_{n+1}^{\mathrm{pre}}}, \\
p_{n+1}^{\mathrm{pre}} &= \kappa\left[\,\mathrm{tr}(\boldsymbol{\epsilon}_{n+1}^{e,\mathrm{pre}}) - \alpha(T_{n+1} - T_0)\,\right],
\end{aligned}
\tag{9.17}
$$

can be computed explicitly from the initial data for the time step. Thus, the effective Mises stress and the magnitude of the pressure are found to be the thermodynamic forces driving $\dot{\epsilon}^p$ and $\dot{\theta}^p$, respectively.

Minimization with respect to ϵ_{n+1}^p and θ_{n+1}^p gives

$$
\begin{aligned}
\triangle\epsilon^p &= \epsilon_{n+1}^p - \epsilon_n^p = 0, \\
\triangle\theta^p &= \theta_{n+1}^p - \theta_n^p = 0,
\end{aligned}
\tag{9.18}
$$

if

$$
\begin{aligned}
\sigma_{n+1}^{\mathrm{pre}} &\leq \sigma_y(\epsilon_n^p, \theta_n^p, T_{n+1}), \\
p_{n+1}^{\mathrm{pre}} &\leq p_y(\epsilon_n^p, \theta_n^p, T_{n+1}),
\end{aligned}
\tag{9.19}
$$

or, otherwise,

$$
\begin{aligned}
\sigma_{n+1}^{\mathrm{pre}} - 3\mu\triangle\epsilon^p &= \sigma_{y,n+1} + \frac{\partial}{\partial\epsilon_{n+1}^p}\left[\triangle t\,\psi_{n+1}^* + \beta\triangle t^2 B_{n+1}\right], \\
p_{n+1}^{\mathrm{pre}} - \kappa\triangle\theta^p &= p_{y,n+1} + \frac{\partial}{\partial\theta_{n+1}^p}\left[\triangle t\,\psi_{n+1}^* + \beta\triangle t^2 B_{n+1}\right].
\end{aligned}
\tag{9.20}
$$

Note that these results in part differ from the constitutive updates in Chapter 7.6 by additional terms due to microinertia.

9.3. Examples of predicted material behavior

An area of application where microinertia is potentially important is the propagation of shocks in metals. The deformations of interest in this case are of uniaxial strain, and the corresponding deformation gradients are of the form $\boldsymbol{F} = \mathrm{diag}\{\lambda, 1, 1\}$, cf. Chapter 1, for some uniaxial stretch ratio λ. This type of deformation combines volumetric and deviatoric deformations, and thus illustrates many of the features of the model presented in the foregoing. Unless otherwise indicated, the material parameters used in all examples are as in Table 9.1.

E [GPa]	ν	$\sigma_0(T_0)$ [MPa]	ϵ_0^p	n	$\bar{a}_0$ [μm]	ρ_0 [kg m^{-3}]
165	0.15	600	0.01	10	100	17300

N [m^{-3}]	$\dot{\epsilon}_0^p$	m	T_0 [K]	T_m [K]	l	α [K^{-1}]
10^{10}	0.001	10	293	1400	0.75	42×10^{-6}

Table 9.1.: Material parameters used in the examples of Section 9.3

For the simple case of uniaxial strain, the elastic deformation is of the form

$$\boldsymbol{F}^e = \mathrm{diag}\{\lambda^e, \lambda_T^e, , \lambda_T^e\}, \qquad (9.21)$$

where λ^e and λ_T^e are the longitudinal and transverse stretch ratios, respectively, and the plastic deformation is of the form

$$\boldsymbol{F}^p = \mathrm{diag}\{\lambda^p, \lambda_T^p, , \lambda_T^p\}, \qquad (9.22)$$

where λ^p and λ_T^p are the longitudinal and transverse stretch ratios, respectively.

9.3.1. Yield phenomena
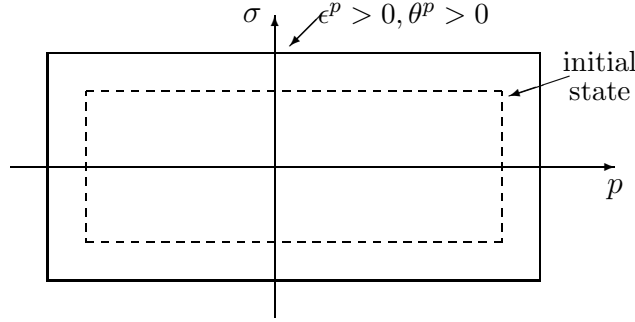
Figure 9.4.: Yield locus in the pressure-Mises stress plane.

The elastic domain at initial state $\boldsymbol{F}^p = \boldsymbol{I}$, $\epsilon^p = 0$, $\theta^p = 0$ and a second state $\boldsymbol{F}^p \neq \boldsymbol{I}$, $\epsilon^p > 0$, $\theta^p > 0$ are shown in Fig. 9.4 on the (p, σ)-plane. The deviatoric and volumetric parts of the yield surface intersect discontinuously, resulting in a corner. This is in contrast to models such as Gurson's and extensions thereof [137, 346], in which the yield surface is smooth.

During deformation the voids may further expand or collapse under the action of positive and negative pressures, respectively. Note that the processes of void expansion and collapse are predicted to be asymmetric, with the magnitude of the critical pressure for void collapse being smaller than the critical pressure for void expansion. Once the voids are collapsed the plastic response of the material becomes insensitive to negative pressure.

9.3.2. Hardening
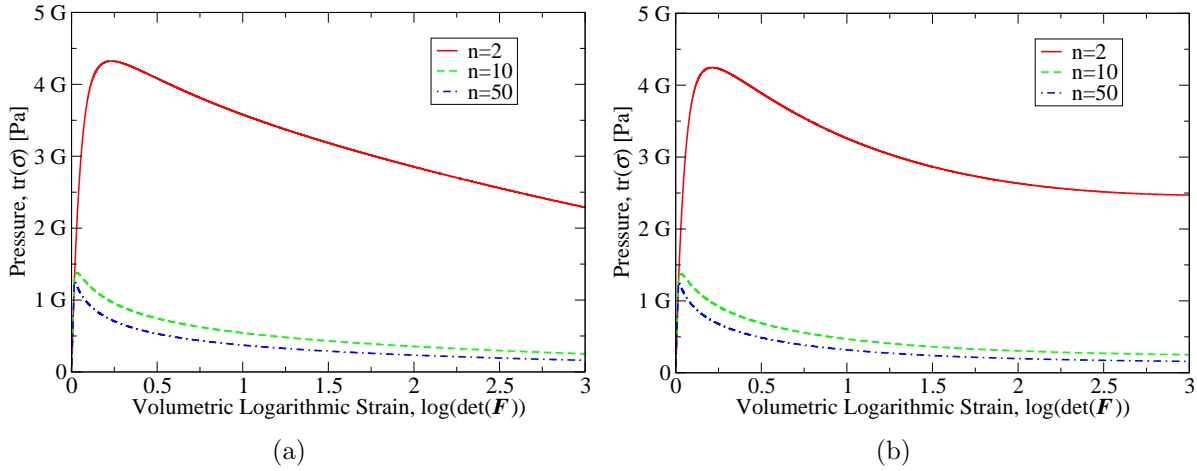
Figure 9.5.: Quasistatic monotonic response for three different hardening exponents. a) Matrix pressure in hydrostatic loading. b) Volumetric component of the stress tensor in uniaxial strain.

The volumetric response predicted by the model is of primary interest in applications. In order to exhibit this response, we begin by applying a monotonically increasing, quasistatic, pure volumetric deformation to the material. Fig. 9.5a shows the dependence of the matrix pressure $\mathrm{tr}\boldsymbol{\sigma}$ on the logarithmic volumetric strain θ^p for three values of the hardening exponent n. As may be seen from this plot, the behavior of the material is ostensibly linear elastic prior to the attainment of the critical pressure. At this point the material yields and starts deforming plastically involving strain softening, i.e., $p \to 0$ as $\theta^p \to \infty$.

The behavior at large volumetric strains in a uniaxial strain state is displayed in Fig. 9.5b in terms of the volumetric component of the stress tensor $\mathrm{tr}\boldsymbol{\sigma}$. Here the interaction of

volumetric strain softening and deviatoric strain hardening leads to an approximately constant value of the pressure as the strain increases.

9.3.3. Microinertia
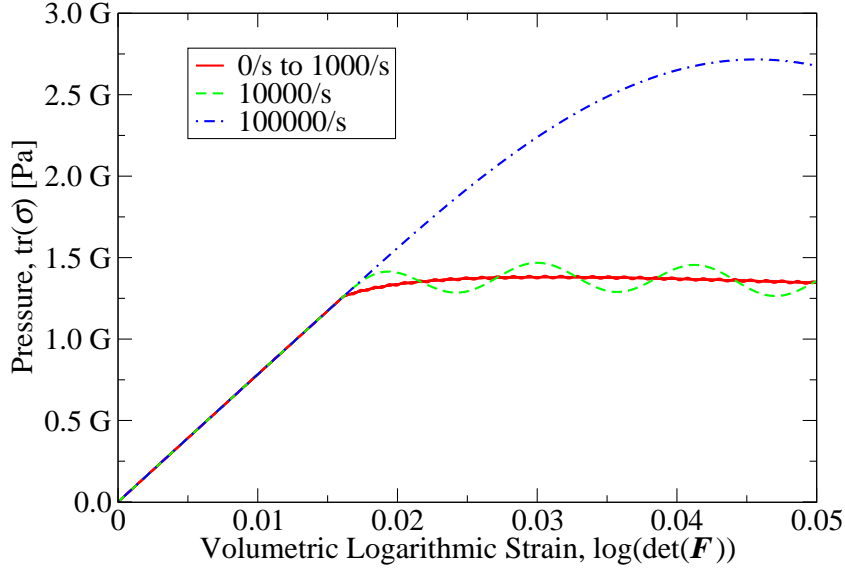
Figure 9.6.: Effect of microinertia on the volumetric stress-strain relation.

At high rates of deformation void growth may significantly be retarded by microinertia [254, 213, 186, 224]. Microinertia may be expected to be significant when $\dot{\theta}$ becomes comparable to $c/\bar{a}$, where c is the elastic sound speed. In order to exhibit this behavior, we artificially turn off rate sensitivity, and subject the material to a constant rate of volumetric expansion. The resulting volumetric stress-strain curve is shown in Fig. 9.6. As may be seen from the figure, the volumetric stress-strain behavior is ostensibly indistinguishable from the quasistatic behavior for small rates of deformation. For rates comparable the threshold $c/\bar{a} = 3.7 \times 10^7 \mathrm{s}^{-1}$, the stress-strain curve depends sensitively on the rate of deformation and effects a smooth transition from strain softening to initially elastic curves as the strain rate increases. As the expansion continues, the pressure exhibits oscillations with amplitude and wave length proportional to the volumetric strain rate.
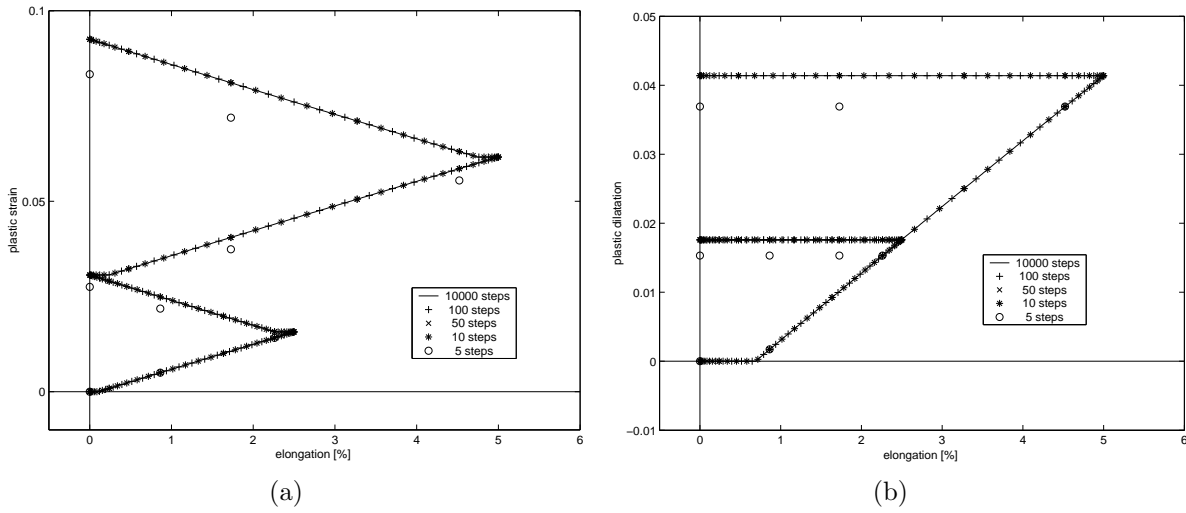
Figure 9.7.: Volumetric plastic expansion and reference plastic strain corresponding to uniaxial elongation with varying number of time steps per cycle.

9.3.4. Convergence analysis

In the following we demonstrate the characteristic behavior of the material with a uniaxial example and analyze the convergence of the variational update within a finite element computation. Unfortunately it is not possible to access the solution properties of a general finite-deformation constitutive update by analytical means. Owing to the fact, that the strain energy density of a finitely deforming solid must be non-convex (to ensure material frame indifference, cf. [86, 206]), the conventional tools of convex analysis are not applicable in this case. For that reason we show here the convergence of the proposed variational method by way of direct numerical testing.

We consider a $100 \times 10 \times 10$mm bar subjected to cyclic tension in axial direction. In contrast to common uniaxial tension tests, we enforce an uniaxial strain state, i.e. the bar can not deform transversal to its longest axis. In that way a significant volumetric expansion is caused. This model corresponds to an uniaxial loading test for highly constrained clamped wires as performed by Ashby et al. in [8]. It is known from these experiments that the material fails allready at about $1/3$ of the failure strain in uniaxial tension tests. Therefore we apply here a relatively small maximal extension of 5%.

The uniaxial loading is simulated using a simple 2d-finite element mesh of 10 composite triangles, Chapter 5. A plane strain state as well as appropriate boundary conditions

179
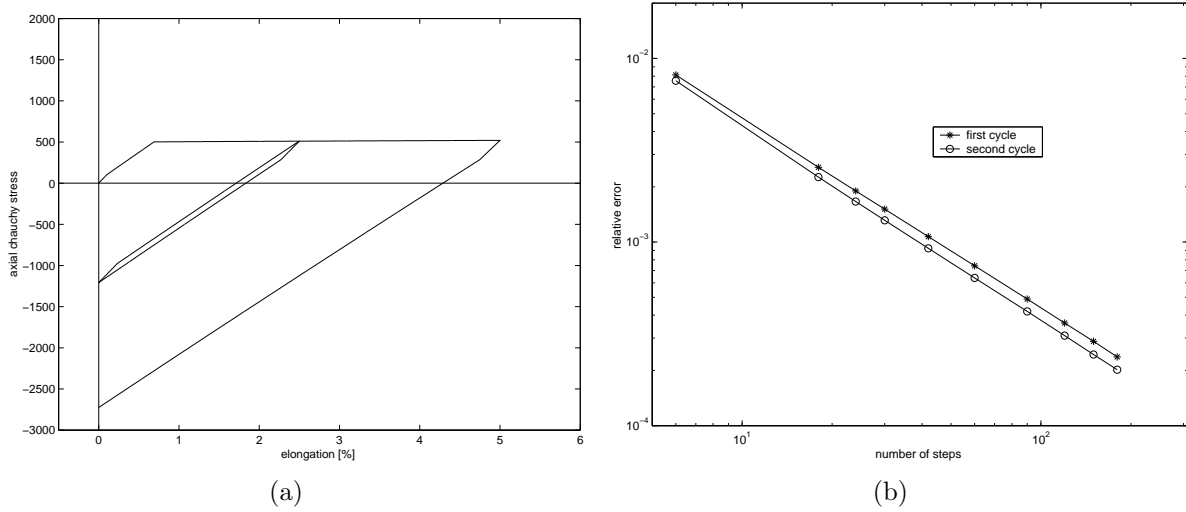
Figure 9.8.: Axial Cauchy stress within two load cycles and error of the stresses at maximal elongation vs. the number of time steps.

are prescribed. A sinusoidal tension-relaxation test with rising amplitudes of 2.5 and 5 % is applied within a time period of $10s$ per cycle. Voids start growing at a critical tension and collapse due to compression. Once the void volume fraction has reached its initial value (here: $f_{V0} = 4e - 6$, $a_0 = 1\mu$m), the pressure is unbounded. The deviatoric plastic strain is accumulative, i.e., it may grow in tension and compression.

The convergence of the numerical solution with decreasing time step is illustrated in Figure 9.7. Displayed are the computed plastic volumetric expansion and the equivalent plastic strain. For visibility we enforce here $\boldsymbol{N} > 0$. Thus only tension causes plastic volumetric expansion, whereas plastic strain accumulates in tension as well as in compression. The reference solution is obtained by an extremely fine time discretization of 10000 steps per cycle and is ostensibly indistinguishable from the exact solution. The strong convergence of the numerical solution and the excellent accuracy obtained with relatively large time steps is evident from the plots.

Figure 9.8 shows the axial Cauchy stress within two cycles and the error measured at maximal elongation in both cycles. The computed rate of convergence is linear. It is noteworthy that the error appears to be very insensitive to variations in the material parameter.

9.3.5. Taylor bar

A common experiment to determine deformation in ductile metals is the Taylor impact test. In this test a cylinder of metal is impacted against a rigid flat surface. Typically this experiment results in a flared end of the cylinder at the impact surface, with decreased bulging towards the free end. Consequently internal ductile damage is expected. Because of the bulging (which is a volumetric expansion) a nucleation and expansion of voids is observed in experiments, see Figure 9.9.
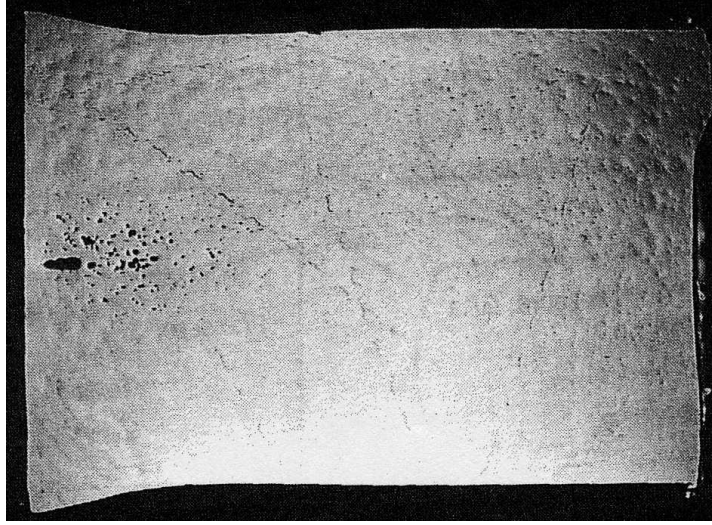
Figure 9.9.: Void formation in a Taylor impact specimen loaded with an initial velocity of $v = 300$ m/s, cited from [127].

E [GPa]	ν	$\sigma_0(T_0)$ [MPa]	ϵ_0^p	n	a_0 [μm]	ρ_0 [kg m^{-3}]
69	0.33	1000	0.01	10	100	2700
N [m^{-3}]	$\dot{\epsilon}_0^p$	m	T_0 [K]	T_m [K]	l	α [K^{-1}]
10^9	0.01	100	293	700	1	42×10^{-6}

Table 9.2.: Material parameters for 1100 aluminum.

Referring to experimental results provided in [127], we analyze a Taylor impact specimen with diameter $d = 12.5$ mm made of 1100 aluminum with material data of Table 9.2, see
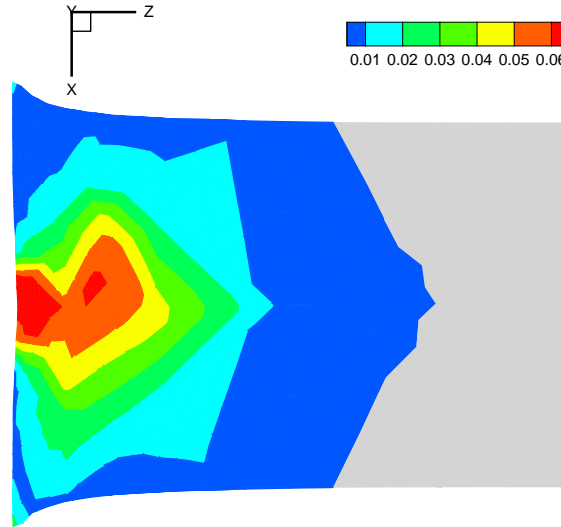
Figure 9.10.: Volumetric plastic expansion ϑ^p in the Taylor impact specimen loaded with an initial velocity of $v = 300$ m/s at time 3 μs.

also [359, 360]. The impact is presumed to be normal to the initial surface at a relative velocity $v = 300$ m/s, contact boundary conditions are applied on the impact interface. This way no penetration of the rigid target is allowed, but lifting is possible. The impact causes a compressive shock wave propagating through the cylinder; tensile stresses are observed to form along the axis as a result of interacting release waves emanating from the lateral free surfaces of the cylinder. This tension induces plastic void cavitation.

For the numerical analysis an explicit Newmark-time discretization algorithm is employed, with the stable time step estimated from the Courant condition based on the elastic modulus. The spacial finite element model consists of composite 10-node tetrahedral elements with piecewise linear shape functions (cf. Chapter 5). The meshes are generated automatically by a commercial mesh generator [307]. Note that the triangulations are somewhat irregular and show no rotational symmetry.

Figure 9.9 shows the midsurface of a Taylor impact specimen from [127]. The photo illustrates the void formation near the impact interface caused by a relative impact velocity of $v = 300$ m/s. Figure 9.10 displays the computed volumetric plastic expansion in the midsurface of our finite element model. We observe in our computation the largest plastic volumetric expansion along the axis near the impact interface. This localization matches very well the experimental results.

182

(a) $v = 300$ m/s (b) $v = 500$ m/s
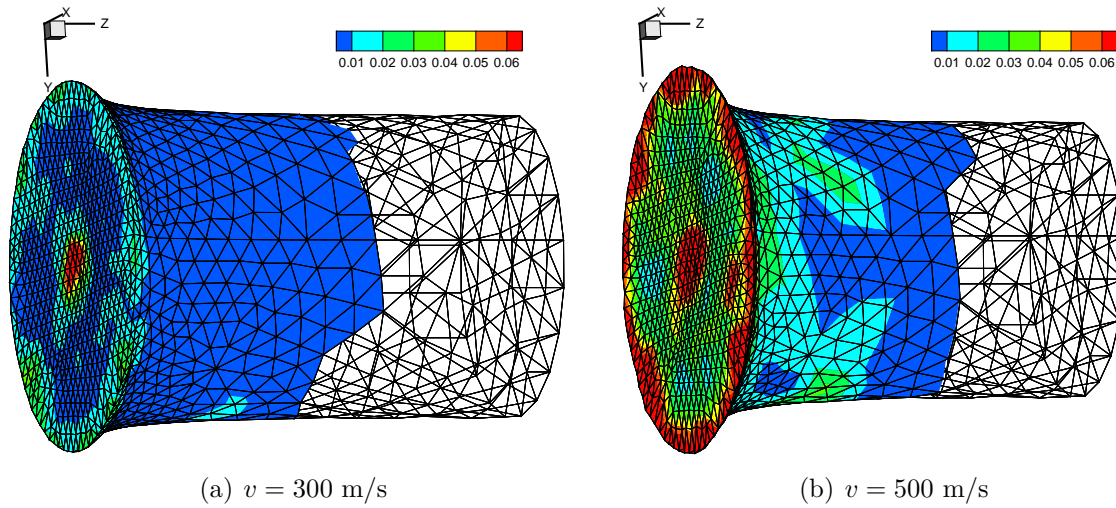
Figure 9.11.: Plastic volumetric expansion in Taylor impact specimen at time $3\mu s$

In Figure 9.11 the distribution of plastic volumetric expansion is plotted at the outer surface of the deformed cylinder. The values of the plastic variable ϑ^p are much smaller here. But if the impact velocity increases, we observe high plastic volumetric expansion also at the boundary, indicating a shattering fringe of the impact surface.

9.4. Fragmentation of an expanding ring

An example of the versatility of the porous plasticity model developed here is the simulation of the forced expansion and ductile fracture and fragmentation of U-6%Nb rings. An outward radial force is applied to the rings by a driver ring, which in turn interacts with a solenoid. When current is applied to the solenoid, a magnetic force is induced in the driver ring creating a uniform radial body force. The U-6%Nb rings are thus forced to expand and eventually fracture dynamically [24]. Such magnetic loading has distinct advantages such as the fact that the motion of the sample results from continuous body forces instead of shock loading and the ability to control loading rates through the driving-current pulse.

The U-6%Nb rings have an inner diameter of 34.37mm, an outer diameter of 35.89mm, and thickness of 0.76mm. An arrestor ledge in the experimental device prevents the driver ring to expand beyond a diameter of 40.0mm, but the U-6%Nb rings are allowed to
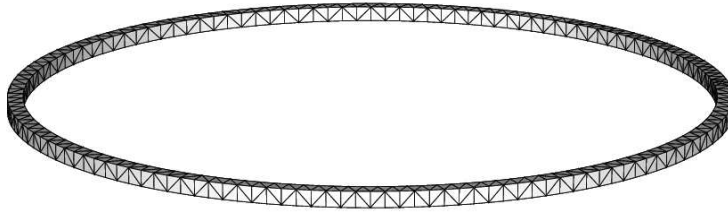
Figure 9.12.: Finite element mesh for U-6%Nb rings: 2634 nodes, 882 elements.

expand driven by their kinetic energy, until they eventually fracture and fragment. The initial velocity history applied to the U-6%Nb rings varies according to three different accelerating voltages of 5.0kV, 6.0kV, and 7.5kV [24]. Figure 9.13 shows the resulting ring fragmentation at 7.5kV.

The U-6%Nb alloy is modeled by using the porous plasticity model developed here in conjunction with the strain localization model developed in Section 8.3, which is specially well-suited for the simulation of nucleation and propagation of ductile fracture. The coarsest finite element mesh used in our simulations is shown in Figure 9.12. The finite element model is three dimensional and consists of composite ten-noded tetrahedra. The initial number of nodes is 2634 and the initial number of tetrahedral elements is 882. The calculations are fully lagrangian. The nucleation and propagation of fracture is simulated by adaptively inserting surface-like strain localization elements between bulk elements when $\epsilon^p \geq 0.4$ at the interface. This value is representative of the critical plastic strain for metal ring fragmentation at high strain rates observed in experiments [129]. The material parameters used in the calculation are as shown in Table 9.3.
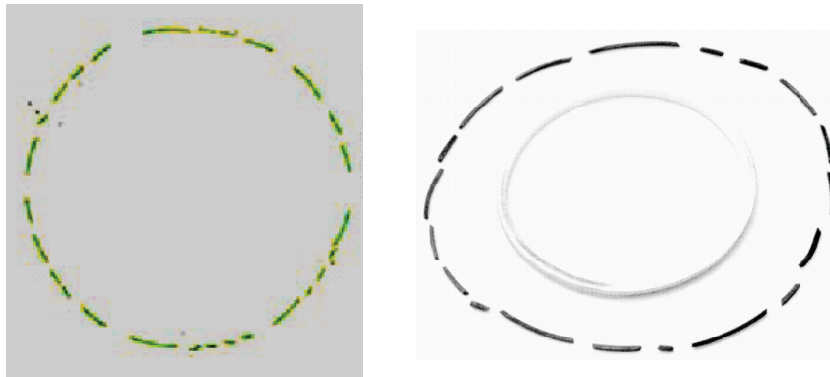
Figure 9.13.: Fragmentation pattern, numerical vs. experimental result [24].

The fragmentation of a body due to impulsive loads is a complex phenomenon in which stress waves, the effect of high strain rates on material properties and the statistics of fracture nucleation and growth interact strongly. Grady and Benson [129] observed in experimental tests on (aluminum and copper) rings subjected to electromagnetic loading that fracture was preceded by the nucleation and growth of numerous necks resulting in the formation of multiple fragments. The fragment sizes exhibit a characteristic distribution. Moreover, they observed that the number of necks and fragments is an increasing function of the expansion speed indicating that inertia and strain rate effects play a significant role.

E [GPa]	ν	$\sigma_0(T_0)$ [MPa]	ϵ_0^p	n	a_0 [μm]	ρ_0 [kg m^{-3}]
165	0.15	600	0.01	10	100	17300

N [m^{-3}]	$\dot{\epsilon}_0^p$	m	T_0 [K]	T_m [K]	l	α [K^{-1}]
10^{10}	0.001	500	293	1400	0.75	42×10^{-6}

Table 9.3.: Material parameters for U-6%Nb alloy.
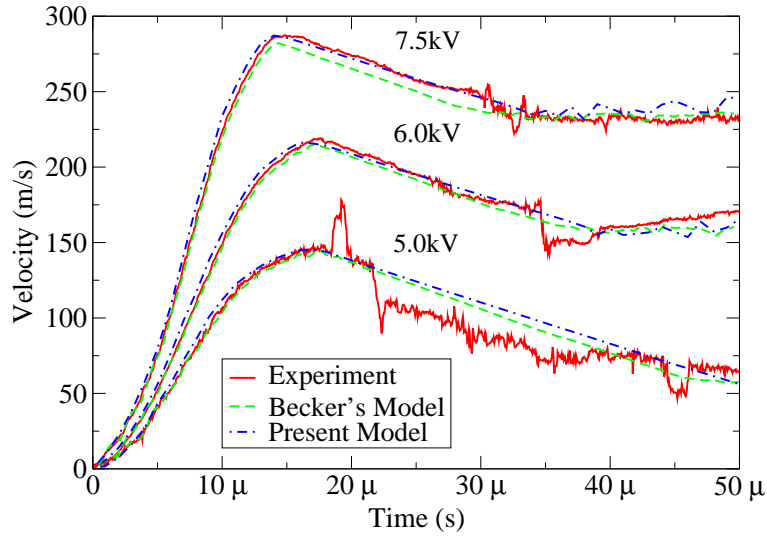
Figure 9.14.: Velocity history for U-6%Nb rings. Experimental data taken from Becker [24].

Figure 9.14 shows the calculated and experimental velocity histories reported by Becker [24], as well as the velocity histories obtained in our simulations. The radial velocity of

all the nodes on the inner radius is initially prescribed to match the radial velocity of the driver ring, as measured by experiments [24], up to the peak velocity for each curve in Figure 9.14. The figure shows that after release there is a noticeable decrease in velocity which can be attributed to kinetic energy being converted to plastic deformation. The region in which the curves become irregular and constant on average is where fracture has occurred. We see from Figure 9.14 that our calculations capture very well the region of plastic flow and the initiation of fracture and fragmentation as measured by experiments. The closeness of our calculations to those of Becker [24] is also remarkable, considering that the mesh used in our calculation is much coarser (882 vs. 15000 elements).
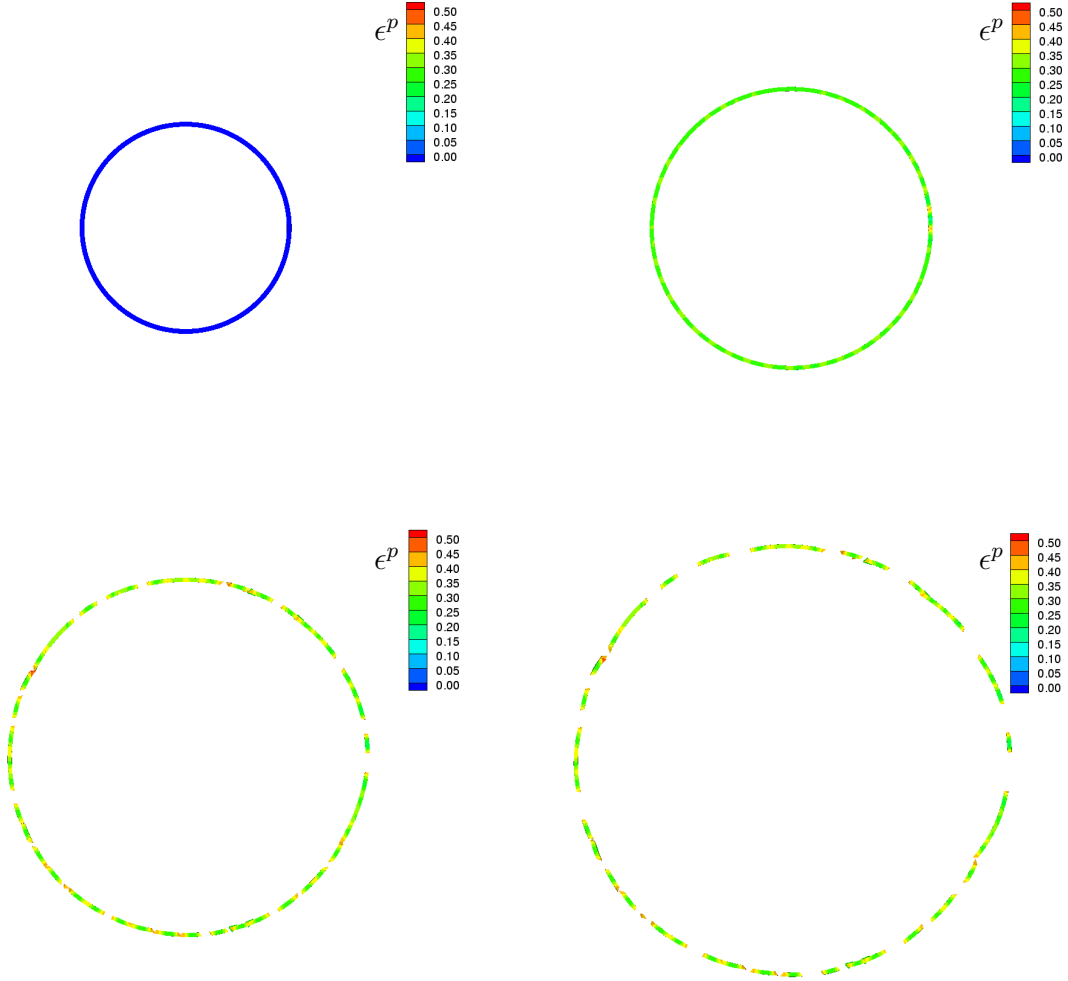
Figure 9.15.: Dynamic fracture and fragmentation of U-6%Nb rings. Configurations at $0\mu s$, $30\mu s$, $60\mu s$ and $90\mu s$.

A sequence of frames of the fracture and fragmentation of the U-6%Nb rings for the case of an applied voltage of 7.5kV is shown in Figure 9.15. The elapsed time between frames is $30\mu s$, and the color bar indicates the value of the plastic strain. For this particular voltage, the time when fracture starts to occur is approximately $30\mu s$ [24]. The figure clearly shows the expansion of the ring and the process of fracture and fragmentation that begins around $30\mu s$. The number of major fragments obtained in the simulation is 26, compared to 19 fragments as observed in experiments [24].

It is worth to emphasize that the material is assumed to undergo strain hardening at all times, and that the temperature rise in the bulk material is modest. Therefore, the necking instability is essentially geometrical in nature, with competition between the necks, some of which thrive while other arrest. The arrested necks result from the arrival of relief waves emitted by the most active necks. These relief waves cause the driving force for the extension of the weak necks to drop, with the result that the necks eventually arrest. Since it takes time for waves to travel around the ring, the failure mode is sensitive to the expansion speed. Note that the many competing unstable modes renders the solution of the perfect system massively non-unique. As is common in bifurcation problems, the particular choice of solution depends sensitively on initial imperfections such as effectively introduced by the mesh. Correspondingly, this imperfection sensitivity explains the variability in the experimental measurements. In this challenging setting, the numerical simulations have proven highly predictive, with no significant mesh dependence. For example, the very fine mesh of 32000 elements (not shown here) which needs to run on a 32 processor parallel machine leads to very similar fragmentation patterns [228].

The framework presented in here puts forth a workable set of constitutive functions to be modeled or identified, namely, the elastic energy density, the stored energy function, the dual rate-sensitivity potential and the microinertia density. For actual materials, this identification can be achieved, e.g., by analyzing a periodic distribution of voids in a single crystal.

10. Damage Assessment of Microelectronic Components in Printed Circuit Boards under Thermal Cycling
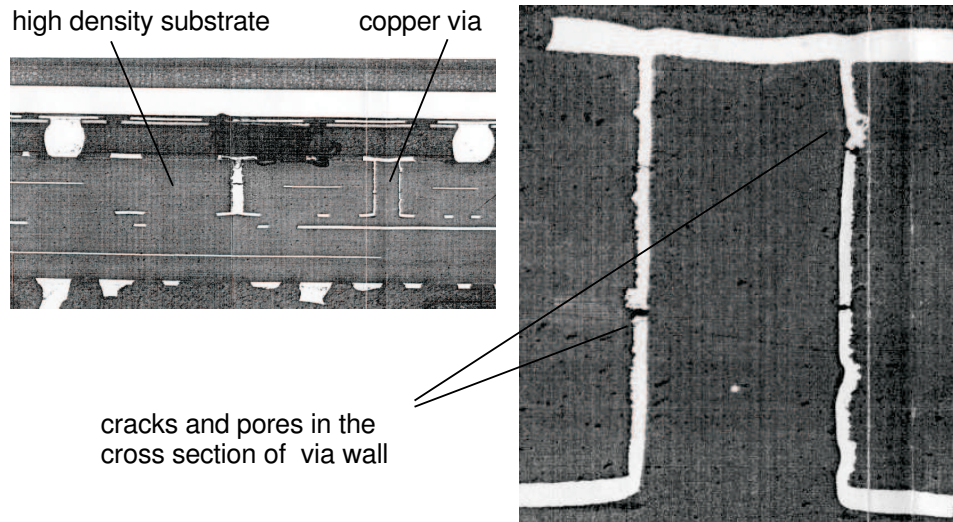
Figure 10.1.: Cross section of a microchip

The stress and strain state of the metal components in microelectronic circuit boards essentially determines the life expectation of the whole chip unit. Therefore, the thermal fatigue of the plated-through copper vias and fatigue and aging the solder joints are subjects of great interest for the chip producing industry. Failure of these connectors due to thermo-mechanical stresses remains a subject of concern, particularly when exposed to high operating temperatures as, e.g., associated with automotive applications. To illustrate the typical components of a printed circuit board an experimental picture from [3] is shown in Figure 10.1, a schematic view provides Figure 10.2.
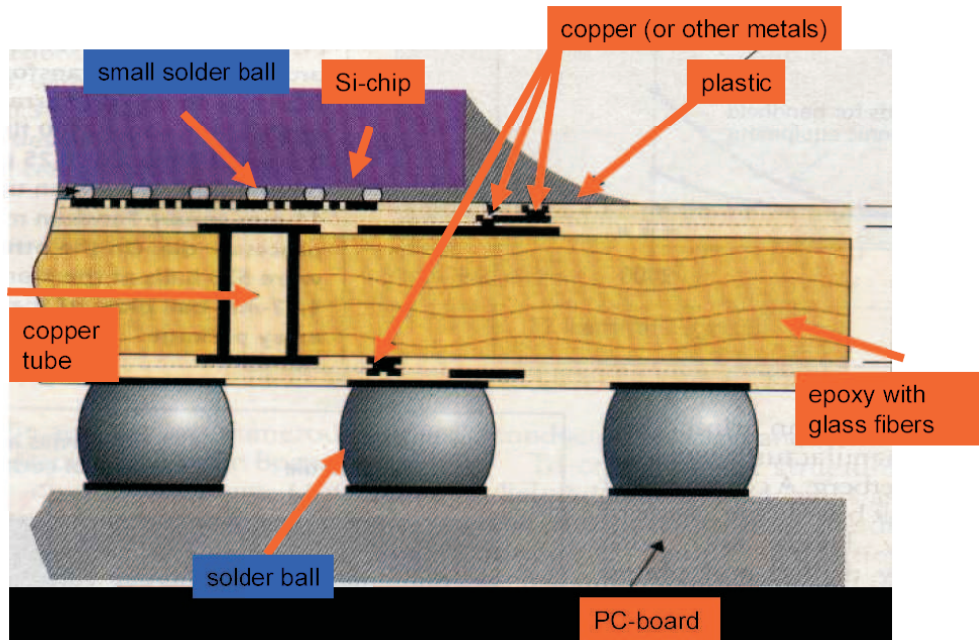
Figure 10.2.: Schematic view of a microchip

In this Chapter we analyze in detail the performance of different types of copper vias in different positions on a printed circuit board. To this end a two-scale finite element analysis under the loading conditions of thermal cycling is employed. A new material model basing on the concepts outlined in Chapter 6 and Chapter 7 is applied for the electrolytically deposited copper. This material model accounts for large elastic and plastic deformations and, additionally, for the growth of pores.

To estimate the long term response, i.e., the fatigue performance, it is common practice to extrapolate the plastic straining computed within few steps of thermal cycling by means of a Coffin-Manson-Equation. We critical examine this strategy here and point out, that a certain number of about 20 cycling steps is necessary to obtain meaningful extrapolations, cf. [366]. Furthermore, an extrapolation of the computed porosity up to critical values (known from ductile fracture) allows similar conclusions.

The presented strategy can serve as a predictive tool for the stress state of plated through holes and vias and can reduce the need of repetitive experimental failure tests. Prerequisite for reliable predictions of any finite element analysis are material parameter of sufficient accuracy. This, in turn, requires experimental measurements on these microscopic small parts. This problem arises for the electrolytically deposited copper (where

we rely on the material data provided by [103]) but is nowadays especially significant for the alloys of the solder bumps. Environmental awareness motivates the replacement of traditional plumbiferous solder joints in microelectronic devices by new lead-free alloys. A strategy of how to obtain information about the unknown material will be sketched in the final section of this chapter on the example of SnAg solder.

10.1. Thermally stressed plated-through vias in printed circuit boards

Plated-through holes and vias form conductive paths between the different copper layers of circuit boards, see Figure 10.3. Failure of these connectors due to thermomechanical stresses is an established cause of failure of circuit boards. Therefore, life expectation of plated through vias is of great interest for the microelectronic industry.

Vias are commonly made of (electrolytically deposited) copper whereas the surrounding material is typical a non-isotropic resin, e.g., the glass fibre reinforced resin FR4 (flame-retardant 4 material substrate), [233]. To ensure the required life expectation of circuit units standardized thermal cycle tests are performed. Due to the different thermal expansion coefficients of the copper and the anisotropic board the copper vias are highly stressed and strained. This leads to an accumulation of permanent irreversible strains associated with cracks and pores which eventually result in the electro-mechanical destruction of the connector.

COPPER VIA

(a) HDI components, cf. [3]   (b) schematics of plated-through via and microvia
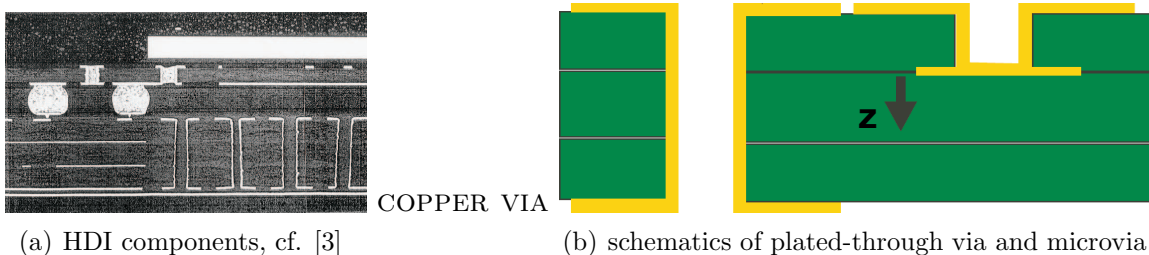
Figure 10.3.: Board and SMT components in the cross section of a microchip

In this paper we will present a numerical study of such copper vias subjected to thermal cycling between -40^oC and $+150^oC$ (automotive standard, see Figure 10.4). After introducing a general technique of how to analyze the stress state in small chip components we focus on a new material model accounting for both, plastic straining and the growth of pores and voids within the copper via. We estimate the damage for vias with different

fillings and in different positions in an FR4 board onto which a flip chip component has been mounted (FCOB = Flip Chip On Board) and we suggest a technique for improved life time estimation.

10.2. Finite-element modelling of the circuit board and the plated-through vias

High Density Interconnect (HDI) technology is an advanced packaging technology enabling more and more functions to be utilized in a smaller area for, e.g., the next generation of small portable electronic communication devices. HDI technology is based on various types of build up methods for the manufacture of multi-layer Printed-Circuit boards (PC boards). Figure 10.3 illustrates the principle setup of a PC board with plated-through holes, vias and microvias, where the main physical difference between the first two is the diameter of the hole. A plated-through-hole is usually made to have a wire or a lead of a component soldered into it. After plating the inner diameter of the hole is sized such as to receive a wire with sufficient clearance. A via is a special kind of plated through holes that is not intended to contain a wire but simply to provide a conductive path from one copper layer to another. Thus, its hole diameter is usually much smaller. A microvia is an even smaller connection to attach solder balls to the copper layer structure on the PC board (right hand side of Figure 10.3b). Microvias can be studied in a manner completely analogous to the one presented here for vias.

Note that the issue of filling the plated-through vias with solder or epoxy and, if possible, to increase its life expectation as opposed to leaving it unfilled has been open to
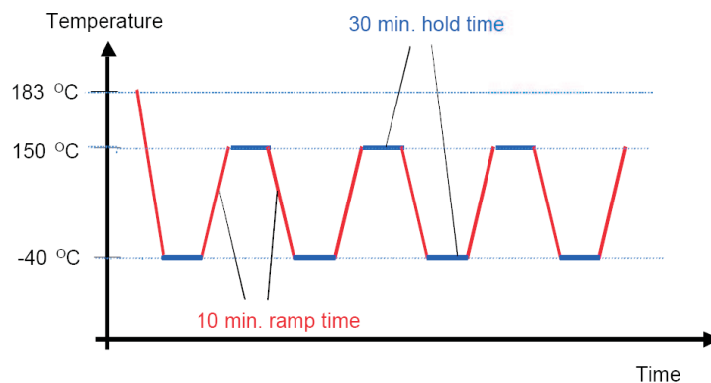
Figure 10.4.: Temperature cycling between -40^oC and 150^oC

chip
base line: 6 x6 mm
thickness: 0.53 mm

underfill
thickness: 0.13 mm

solder stop mask
thickness: 0.03 mm

FR4-board
thickness: 1.5 mm
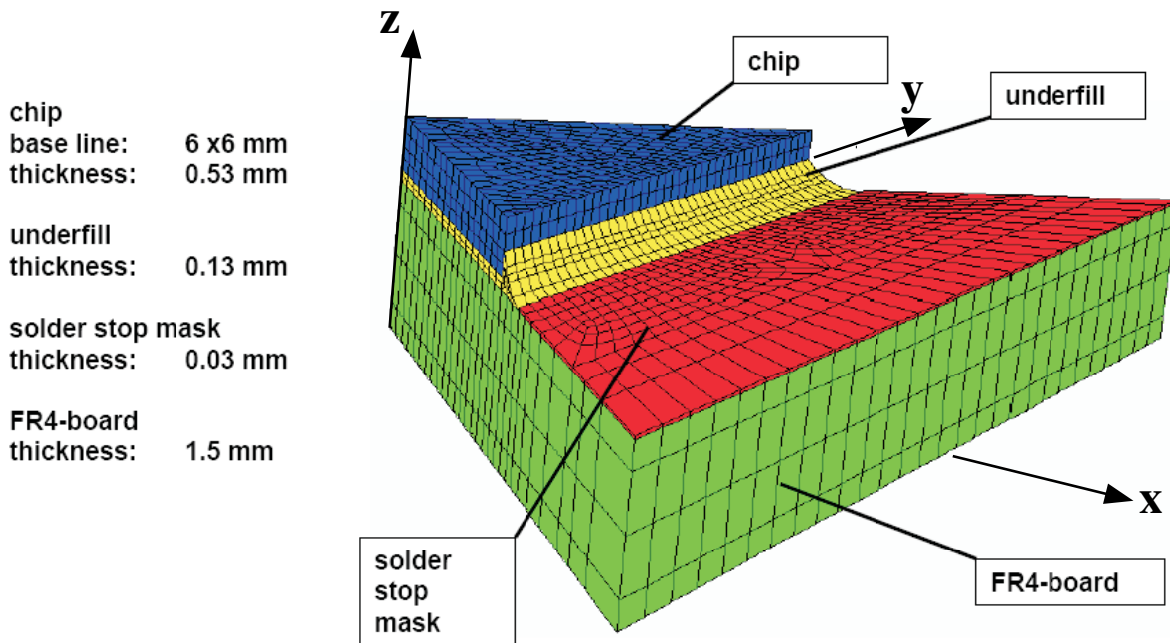
Figure 10.5.: Finite-element model of a FCOB circuit unit.

considerable debate, see, e.g., [17].

Compared to a PC board and the microelectronic components mounted thereon the plated-through vias and microvias are much smaller. If modeled directly this would lead to a finite-element mesh with an unnecessarily high amount of degrees of freedom. For that reason we make use of a submodelling technique. This is a two-step procedure during which a global model is created first. In the presented case the global model consists of the chip (more precisely: the FCOB unit) and of the PC board, for dimensions see Figure 10.5. Note that delicate substructures, such as the vias, are not included. Moreover, by symmetry the finite-element mesh is reduced to one quarter of chip and board. A finite-element analysis is then performed with this model, i.e., temperature cycles between $-40^{o}C$ and $150^{o}C$ are imposed (233/423 K), see Figure 10.4, where the first step describes the cooling down from the melting temperature of SnPb solder of $183^{o}C$. From the global structure the locally resulting stresses, strains, and deformations are calculated.

In a second step finite-element submodels of the structures of interest, namely the plated-through vias, are created in a way that the geometry of the real objects is reflected in a sufficiently accurate manner. The deformations at selected positions that result from the finite-element calculation of the global model are now extrapolated and imposed onto the
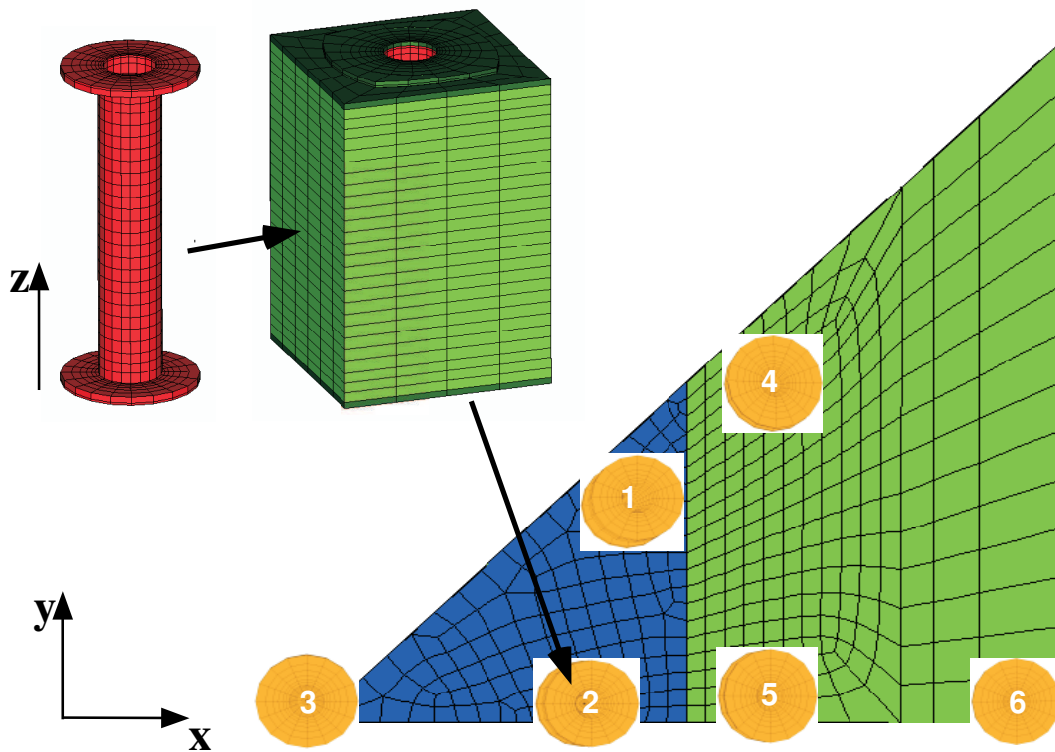
Figure 10.6.: Positions of the vias within the global structure

periphery of the local models. Thus, the mechanical response within the substructures can be calculated. Clearly, it is desirable that during the Finite-Element Analysis (FEA) the stresses and strains are as accurately calculated as possible. Therefore, special attention must be paid to the generation of the submodel meshes so that all regions of interest, in the present case the copper, are sufficiently far away from the boundary of the submodel.

The global model essentially consist of a chip mounted upon a PC board. The board is made of FR4, a special resin with high glass-transition temperature and with orthotropic material properties $E_x = E_y = 14218$ MPa and $E_z = 7109$ MPa at 223K and $E_x = E_y = 11225$ MPa and $E_z = 5613$ MPa at 423 K. More detailed data for the material can be found in [233]. In order to avoid the aforementioned numerical inaccuracy problems in context with the submodels, i.e., in order not to use submodels that show copper structures upon their surfaces a quarter of the whole structure was modeled. Symmetry conditions were imposed along the *diagonal* surfaces. Moreover, it was made sure that the front surface of the compound consisting of solder stop mask and PC-board did not tilt but rather moved in a straight manner in order to mimic the embodiment of the

via	1	2	3	4	5	6
x	1.5	0.0	0.0	2.91	0.0	0.0
y	2.5	2.35	1.0	4.0	4.0	4.8

Table 10.1.: Positions of the vias

package within the whole assembly.

A submodel for the straight-through via is shown in Figure 10.6. Note that the copper part is also completely surrounded by underfill, solder stop mask and PC board material. The submodels were positioned at various points of the board, see Table 10.1. For reasons of conciseness only one eighth of the whole structure is shown in Figure 10.6 with the out-of plane direction being the $z-$axis. However, all submodels, also those along the horizontal line, i.e., the $y-$axis, are completely embedded in the global model.

The dimensions of the plated-through vias are as follows: width of the basal plane of the whole submodel 1.0 mm, wall thickness of the copper cylinder 0.022 mm, inner diameter 0.256 mm, outer diameter 0.65 mm, height of the submodel 1.5 mm. At the upper and the lower surface the copper via is covered by a thin layer of solder stop mask with material parameters from $E = 6000$ MPa, $\nu = 0.34$ at $T = 218$ K down to $E = 1000$ MPa, $\nu = 0.42$ at $T = 423$ K and a thermal expansion coefficient of $\alpha = 6$ 1/K. The copper structure is surrounded by the orthotropic FR4 resin (cf. Figure 10.6).
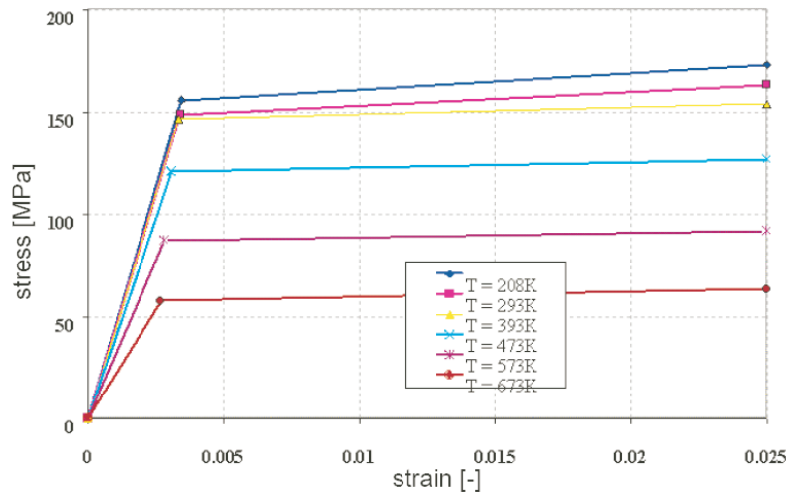
Figure 10.7.: Stress-strain curves for electrodeposited copper provided by [103].

During the manufacturing of plated-through vias and other electrical connectors in

high-density-substrates the copper is electrolytically deposited, hence, the mechanical properties may differ significantly from those of bulk copper. Stress-strain curves for electrolytically deposited copper are provided in the literature with data depending on temperature. The presented finite-element simulations make use of the material data shown in Figure 10.7. These stress-strain diagrams were published by DiTomaso [103], obtained from data provided by IBM electronics division at Endicott, NY, based upon in-house testing of electrodeposited copper. The corresponding thermal expansion coefficient is $\alpha = 17.6$ 1/K. At all the temperatures shown in Figure 10.7 an initial yield stress can clearly be distinguished at the end of an elastic branch. This is then followed by hardening up to strains of $\varepsilon = 0.025$. By experience the region of hardening is frequently extrapolated toward higher strains without experimental verification. Presuming that the stress-strain curves from Figure 10.7 are realistic even at larger strains we apply these data to describe hardening of the yield stress by a power law of the form

$$\sigma_y = \sigma_{y_0}\big(1 + \frac{\varepsilon^p}{\varepsilon_{y_0}^p}\big)^{1/n},\tag{10.1}$$

where $n = 25$ is the hardening exponent and σ_{y_0}, $\varepsilon_{y_0}^p$, are the (temperature dependent) initial yield stress and reference plastic strain, respectively.

The material data of [103] describe a very soft material behavior, with an elastic modulus in the range of 40000 MPa and an initial yield stress of 150 MPa and lower, see Figure 10.7. Different but only qualitative observations are reported in [149] and [245] stating that electrodeposited copper has a higher tensile strength than bulk copper. Read et al. [278] observe in electrodeposited copper films material properties of the same range as typical bulk copper, i.e., $E \approx 120$ GPa and initial yield stresses of ≈ 250 MPa, whereas Lu et al. [183] measure initial yield stresses from of 250-500 MPa up to 1000 MPa depending on the microstructure of the electrodeposited copper. Atomic-scale numerical simulations of nano-crystalline copper in [296] even yield, depending on temperature and grain size, to initial yield stresses of $0.8 - 1.5$ GPa. Furthermore, in [260] the influence of processing conditions on the properties of copper interconnects is investigated, with the result that, e.g., the porosity of the copper reduces while the hardness increases with increasing processing pressure. Unfortunately, none of the other sources provide such detailed information about the temperature dependency of the material data of electrolytically deposited copper as [103].

In Figure 10.8 the von Mises stress in the deformed board after cooling to a minimum temperature is shown, with the red and grey colored regions referring to the maxima (of $150\ldots460$ MPa) and blue marking the nearly unstressed regions. The warpage of the global structure is magnified by a factor of 50. It can clearly be seen that the highest deformation is along the diagonal surfaces, whereas in the vicinity of via position 4 the highest stresses occur. Depending on the position within the board the warpage will
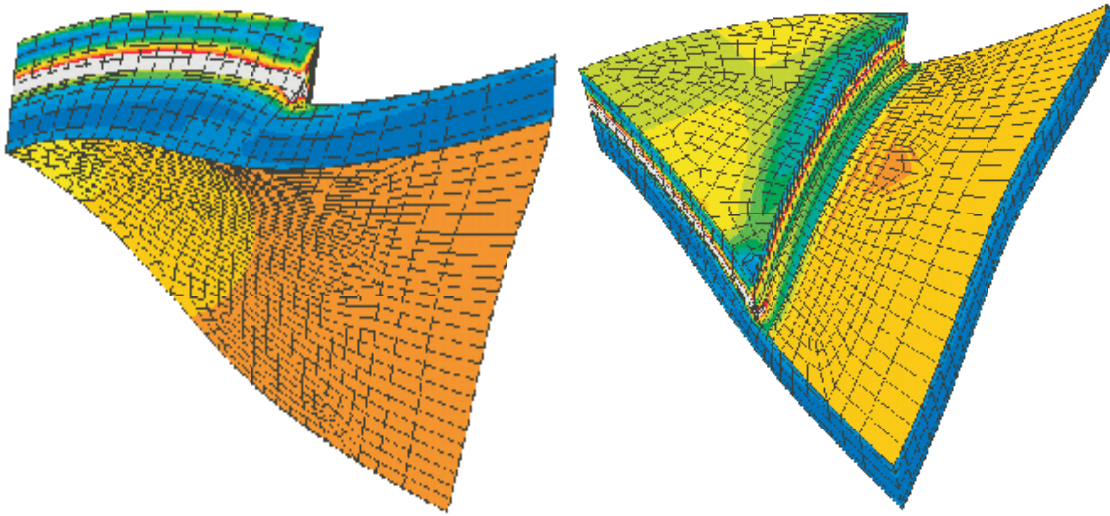
Figure 10.8.: Von Mises stress in the deformed PC board model

directly influence the deformations of the submodels. Anticipated from the global model in the via positions 1, 2, 4 and 5 shearing deformation appears to be dominant whereas in positions 3 and 6 the via will essentially be stretched.

10.3. Material model for the electrolytically deposited copper

Cavities or voids in metals may be defects in the crystal lattice, along grain boundaries or simply vacancies arising during manufacturing, [189, 275]. Typically the size of these cavities is small compared to the size of the structure. Their amount is measured by pore volume fraction or porosity (see Chapter 7)

$$f_V = \frac{\text{volume of pores}}{\text{total volume}}. \tag{10.2}$$

In metals the initial porosity is typically in the range of 10^{-2} to 10^{-4}. By the technique of electrolytically depositing copper the initial porosity is expected to be higher (cf. [246]), but exact data are not available. To account for both damaging mechanisms, shear induced plastic straining and growing porosity in the copper material, we describe the material with the constitutive model of Chapter 7 which combines classical von Mises plasticity with plastic volumetric expansion as induced by the growth of pores. In the

following we shortly summarize the essential ingredients employed here and repeat some basic equations for readability.

The thermo-mechanical response of the material is characterized by a free-energy density per unit reference volume $A = A(T, \boldsymbol{F}, \boldsymbol{F}^p, \varepsilon^p, \vartheta^p)$, where T is the absolute temperature, $\boldsymbol{F}$ denotes the deformation gradient whereas $\boldsymbol{F}^p$ and $\boldsymbol{F}^e$ denote the plastic and elastic part of the deformation gradient, respectively, which are related multiplicatively, equation (6.1). Moreover, the internal variable ε^p describes the effective plastic straining, whereas ϑ^p measures the effective volumetric plastic expansion.

Note that we account in this material model for the full kinematics of large deformations. By the use of logarithmic and exponential mappings the subsequent equations can in part be written in the more familiar terms of strain tensor $\boldsymbol{\epsilon}$ with elastic and plastic components $\boldsymbol{\epsilon}^e$ and $\boldsymbol{\epsilon}^p$, respectively. To this end we remember the definition

$$\boldsymbol{\epsilon} = \frac{1}{2}\ln(\boldsymbol{F}^\top \boldsymbol{F}) \tag{10.3}$$

and

$$\boldsymbol{\epsilon}^e = \frac{1}{2}\ln(\boldsymbol{F}^{e\top}\boldsymbol{F}^e) \quad \text{and} \quad \boldsymbol{\epsilon}^p = \frac{1}{2}\ln(\boldsymbol{F}^{p\top}\boldsymbol{F}^p) \tag{10.4}$$

to obtain with (6.1) the additive decomposition

$$\boldsymbol{\epsilon} = \boldsymbol{\epsilon}^e + \boldsymbol{\epsilon}^p. \tag{10.5}$$

In general the material response is time-dependent. Here the speed of loading is slow (in the range of several minutes) and therefore strain rate effects are of minor influence. On the other hand, creep effects might play a role. The proper criterium to apply in that case is the so-called homologous temperature, i.e., the current temperature divided by the melting temperature of the material (in K). Creep shall dominate at homologous temperatures above 0.5. However, with a melting temperature of about 1300 K copper has a homologous temperature ≤ 0.3 for the temperature range of interest in this chapter. Therefore, for the calculation of the irreversible deformation in copper creep will be neglected and we proceed to establish a time-independent material model.

We assume that the free-energy density has the additive structure

$$A(\boldsymbol{F}, \boldsymbol{F}^p, \varepsilon^p, \vartheta^p, T) = W^e(\boldsymbol{F}^e, T) + W^p(\varepsilon^p, \vartheta^p, T), \tag{10.6}$$

where $W^e(\boldsymbol{F}^e, T)$ and $W^p(\varepsilon^p, \vartheta^p, T)$ are the elastic and stored plastic (i.e., dissipated) energy densities per unit undeformed volume, respectively. The elastic strain-energy density may alternatively be expressed in terms of the logarithmic elastic strains (10.3),

$$W^e \equiv W^e(\boldsymbol{\epsilon}^e, T) = W^{e,\mathrm{vol}}(\mathrm{tr}\boldsymbol{\epsilon}^e, T) + W^{e,\mathrm{dev}}(\mathrm{dev}(\boldsymbol{\epsilon}), T), \tag{10.7}$$

where we split the energy density into a volumetric component and a shear deformation controlled deviatoric component. The corresponding deviatoric part of the strains results from the decomposition

$$\operatorname{dev} \boldsymbol{\epsilon} = \boldsymbol{\epsilon} - \frac{1}{3} \boldsymbol{I} \operatorname{tr}\boldsymbol{\epsilon} \quad \text{with} \quad \operatorname{tr}\boldsymbol{\epsilon} = \epsilon_{11} + \epsilon_{22} + \epsilon_{33}. \tag{10.8}$$

Then, with bulk modulus κ, shear modulus μ, mass density ϱ_0 and specific heat per unit mass c_v the elastic energy density reads

$$W^e = \frac{\kappa}{2}\big(\operatorname{tr}\boldsymbol{\epsilon}^e - 3\alpha(T - T_0)\big)^2 + \varrho_0 c_v T\big(1 - \ln\frac{T}{T_0}\big) + \frac{2}{3}\mu\,|\operatorname{dev}\boldsymbol{\epsilon}^e|^2. \tag{10.9}$$

Following the classical thermo-mechanical approach of Chapter 6.1 and 7.4 the stresses can be computed from the derivative of the energy density with respect to the conjugate deformation variable. In particular, the von Mises (or effective deviatoric) stress σ_e is determined by the relation

$$\sigma_e = -\frac{\partial W^e}{\partial \varepsilon^p}(\boldsymbol{\epsilon}^e, T) \tag{10.10}$$

whereas the pressure is recovered as

$$p = -\frac{\partial W^e}{\partial \vartheta^p}(\boldsymbol{\epsilon}^e, T). \tag{10.11}$$

The dependence of the elastic energy density W^e on the plastic variables ε^p and ϑ^p is a consequence of the (prior solution unknown) decomposition (10.5).

The rate of plastic deformation is assumed to obey the flow rule (7.122)

$$\dot{\boldsymbol{F}}^p \boldsymbol{F}^{p-1} = \dot{\varepsilon}^p \boldsymbol{M} + \dot{\vartheta}^p \boldsymbol{N},$$

where the tensors $\boldsymbol{M}$ and $\boldsymbol{N}$ set the direction of the deviatoric and volumetric plastic deformation rates, respectively. The tensor $\boldsymbol{M}$ is assumed to be trace-free and normed, i.e., $\operatorname{tr}\boldsymbol{M} = 0$ and $|\boldsymbol{M}|^2 = \frac{3}{2}$ whereas the tensor $\boldsymbol{N}$ is allowed to take one of two values, $\boldsymbol{N} = \pm\frac{1}{3}\boldsymbol{I}$ with the plus sign corresponding to plastic volumetric expansion (pore growth), and the minus sign to plastic compression (pore collapse). The tensors $\boldsymbol{M}$ and $\boldsymbol{N}$ are otherwise unknown and are to be determined as part of the solution. The constraints may be regarded as defining the assumed kinematics of plastic deformation. The rates of the internal variables $\dot{\varepsilon}^p$ and $\dot{\vartheta}^p$ describe plasticity due to deviatoric straining and volumetric expansion. They are subject to the irreversibility constraints

$$\dot{\varepsilon}^p \geq 0 \quad \text{and} \quad \dot{\vartheta}^p \geq 0. \tag{10.12}$$

The stored plastic energy density W^p is also additively split into volumetric and deviatoric components. The deviatoric part of W^p is constructed to prescribe power-law hardening of the yield stress σ_y according to equation (10.1). This gives

$$W^{p,\text{dev}} \equiv W^{p,\text{dev}}(\varepsilon^p, T) = \frac{n\sigma_y(T)\varepsilon^p_{y0}}{n+1}\left(1 + \frac{\varepsilon^p}{\varepsilon^p_{y0}}\right)^{\frac{n+1}{n}}. \tag{10.13}$$

The volumetric component $W^{p,\text{vol}} = W^{p,\text{vol}}(\vartheta^p, T)$ will be specified in detailed below. Then, the deviatoric yield stress reduces to

$$\sigma_y = \frac{\partial W^p}{\partial \varepsilon^p}(T, \varepsilon^p, \vartheta^p), \tag{10.14}$$

and, likewise, the critical cavitation pressure is

$$p_y = \frac{\partial W^p}{\partial \vartheta^p}(T, \varepsilon^p, \vartheta^p). \tag{10.15}$$

Summarizing the thermo-mechanical framework we define the thermodynamic force Y conjugate to the internal variable ε^p as

$$Y = -\frac{\partial A}{\partial \varepsilon^p} = \sigma_e - \sigma_y, \tag{10.16}$$

where the effective deviatoric stress and the yield stress are given by (10.10) and (10.14), respectively. With pressure (10.11) and (10.15) the thermodynamic force Z conjugate to the internal variable ϑ^p takes the form

$$Z = -\frac{\partial A}{\partial \vartheta^p} = p - p_y. \tag{10.17}$$

Up to here the components of the free-energy density function coincide with established theories of elasto-plasticity extended to the finite range. The goal of the remaining paragraph is to relate the continuum measures of volumetric deformation to the materials porosity. For further analysis we assume a spherical shell model, i.e., the material is modeled as a conglomerate of (initially very small) spherical pores each surrounded by a sphere of matrix material, Figure 7.2. In that way the properties of the porous ensemble can be inferred from the behavior of a single pore.

Consider a representative volume of material of undeformed volume V_0 and deformed volume V related by $V = JV_0$, where

$$J \equiv \det \boldsymbol{F} = \det(\boldsymbol{F}^e \boldsymbol{F}^p) = J^e J^p \tag{10.18}$$

is the local Jacobian of the deformation and J^e and J^p are the corresponding elastic and plastic parts. We recall that J^p is the ratio of the volumes of infinitesimal material neighborhoods in the plastically-deformed setting and the reference setting. In standard theory of plasticity the solid is not assumed to expand (or compress) plastically, i.e., $J^p \equiv 1$. Alternatively we formulate here with (10.18)

$$J^p = \frac{V}{J^e V_0} \tag{10.19}$$

to explicitly allow for plastic volumetric expansion of the material.

Let now $\tilde{N}_V(a,t)$ be a given mesoscopic void number density of pores with radius $a(t)$, [363, 362]. Then, the number of spherical voids per unit undeformed volume of the body is

$$N_V(t) = \int_0^\infty \tilde{N}_V(a,t)\,d\,a. \tag{10.20}$$

By

$$\bar{a} \equiv \bar{a}(t) = \frac{1}{N_V(t)} \int_0^\infty \tilde{N}_V(a,t)\,a(t)\,d\,a \tag{10.21}$$

we define the current mean void radius. The local volume fraction of pores (10.2) in the deformed configuration is then simply given by

$$f(t) = N_V(t)\frac{V_0}{V(t)}\frac{4\pi\bar{a}(t)^3}{3}. \tag{10.22}$$

Neglecting the elastic volume change of the voids we can write for the plastic Jacobian (10.19) of a body with N_V voids per volume

$$J^p = 1 - f_0 + N_V\frac{4\pi\bar{a}^3}{3}. \tag{10.23}$$

This relation place the mean void radius $\bar{a}$ and J^p in one-to-one correspondence.

From the plastic incompressibility of the matrix material and the kinematics of void growth outlined in Chapter 7.1 we derive the rate of the effective von Mises strain

$$\dot{\varepsilon}^p(r,t) = |\frac{\partial \dot{r}}{\partial r}| = \frac{2\bar{a}^2(t)}{r^3(t)}|\dot{\bar{a}}(t)| \tag{10.24}$$

with current radius $r = (r_0^3 - a_0^3 + \bar{a}^3)^{1/3}$. Presuming a monotonic void growth time integration of (10.24) gives the plastic strain

$$\varepsilon^p = \frac{2}{3}\ln\left(1 + \frac{\bar{a}^3 - a_0^3}{r_0^3}\right). \tag{10.25}$$

The stored energy for a spherical void in a power-law hardening material equals the plastic work of deformation attendant to the expansion of the void. In the dilute limit, the total energy stored by the void ensemble is the sum of the energy stored by each individual void. These considerations applied to a spherical shell model lead by direct calculation to the stored energy of volumetric plastic work

$$W^{p,\text{vol}}(\bar{a}, T) \;=\; N_V \int_a^b \frac{n\sigma_0(T)\varepsilon_{y0}^p}{n+1} \left(1 + \frac{\varepsilon^p}{\varepsilon_{y0}^p}\right)^{\frac{n+1}{n}} 4\pi r^2 \, d\,r. \tag{10.26}$$

As discussed in Chapter 7.4 the variable ϑ^p is a measure of the *accumulated* volumetric plastic deformation and ϑ^p coincides with $\ln J^p$ for monotonic expansion, equations (7.130, 7.131). Then, the stored energy of volumetric plastic work can be formulated as

$$W^{p,\text{vol}}(\vartheta^p, T) = \frac{n\sigma_0(T)\varepsilon_{y0}^p}{n+1} N \frac{4\pi\bar{a}^3}{3} g(\vartheta^p, n), \tag{10.27}$$

with function (7.170) of Chapter 7.3 reformulated as

$$g(\vartheta^p, n) = \int_1^{\frac{1}{f}} \left(1 + \frac{2}{3\varepsilon_{y0}^p} \ln \frac{x}{x - 1 + \frac{f_0}{f_0 + \exp\vartheta^p - 1}}\right)^{\frac{n+1}{n}} d\,x. \tag{10.28}$$

Note that these relations hold for arbitrary plastic deformation of the matrix material, $\boldsymbol{F}^p$ and $\boldsymbol{\epsilon}^p$, respectively. In an analogous manner additional energy contributions , e.g., the kinetic energy of the body attributed to void expansion, can be computed, see Chapter 7.3 or [365].

For an arbitrary loading combining alternating phases of pore expansion and collapse the distinction between the two variables J^p and ϑ^p becomes important. For instance, imagine now that the pore radius history $\bar{a}(t)$ grows monotonically from a_0 to a_1, then decreases monotonically from a_1 to a_2 etc., see equations (7.63–7.66), and we define $q(t)$ of equation (7.66) to be the maximum attained pore size. In particular, $q(t)$ is a monotonically increasing function for every history of $\bar{a}(t)$. For integration of the accumulated plastic strain from (10.24) and for the formulation of the stored energy function (10.27) now function $q(t)$ needs to be employed.

Note that for an arbitrary history of the plastic volumetric expansion the value of $\vartheta^p(t)$ rises even when the pores shrink. That means by constraint (10.12) the internal variable $\vartheta^p(t)$ basically measures the ups and downs of pore growth and, therefore, can not anymore be compared to the monotonic loading. The information about current pore size is in general solely in $J^p(t)$ via relation (10.23). The corresponding physical constraint is now

$$J^p \geq 1, \tag{10.29}$$

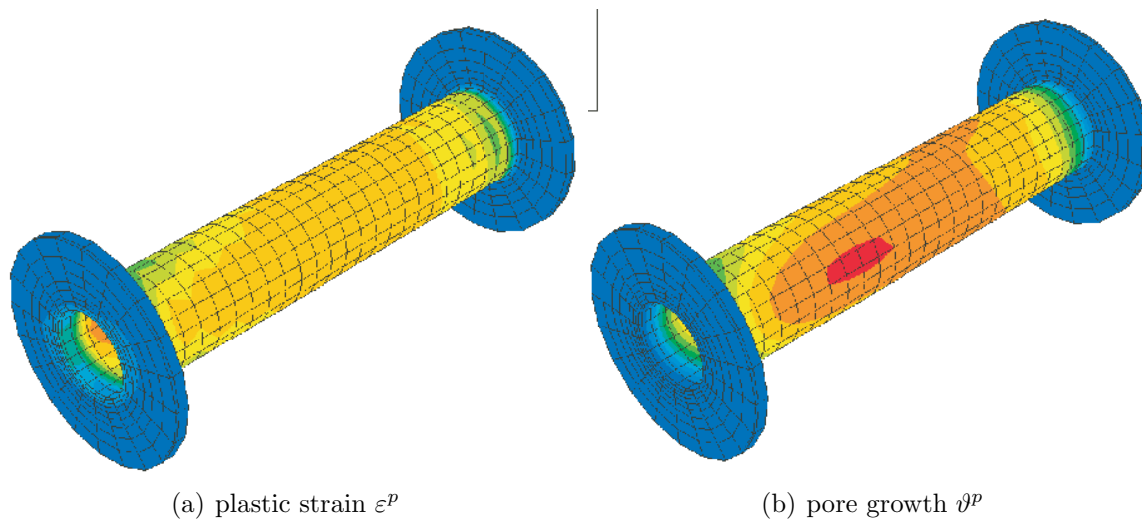i.e., the pores are not allowed to be smaller than the initial pore size with $J^p = 1$.

(a) plastic strain ε^p (b) pore growth ϑ^p

Figure 10.9.: Distribution of accumulated plastic strain and porosity (as indicated by ε^p and ϑ^p) in an unfilled via at position 4 after 5 temperature steps (maxima: red, minima: blue)

10.4. Comparison of numerical results after five temperature steps

The presented material model was employed to study the response of the plated-through vias during thermal cycling. It is common practise to simulate only a few steps of the temperature cycling test and extrapolate the results until fatigue failure is anticipated. Following the traditional approach of, e.g., [2, 3, 17, 233, 378], we apply a temperature history as follows: 456 K—233 K—423 K—233 K—423 K—233 K, where 456 K refers to the melting temperature of eutectic SnPb which was assumed to be the stress free state of reference. Note that we apply two forms of loading on the via submodel, the temperature dependent material behavior and the deformation resulting from the global model. Moreover, in order to account for the maximal possible growth of pores within the copper material the irreversibility constraint (7.190) is applied. Physically speaking this means that we allow the voids to open but not to close irreversibly.

Three (limit) cases are considered.

1. **unfilled**: The plated-through vias are empty copper vias embedded in the board as described in Section 10.2.

2. **soft filled**: The copper vias are filled with solder stop mask with material data as

(a) plastic strain ε^p (b) pore growth ϑ^p
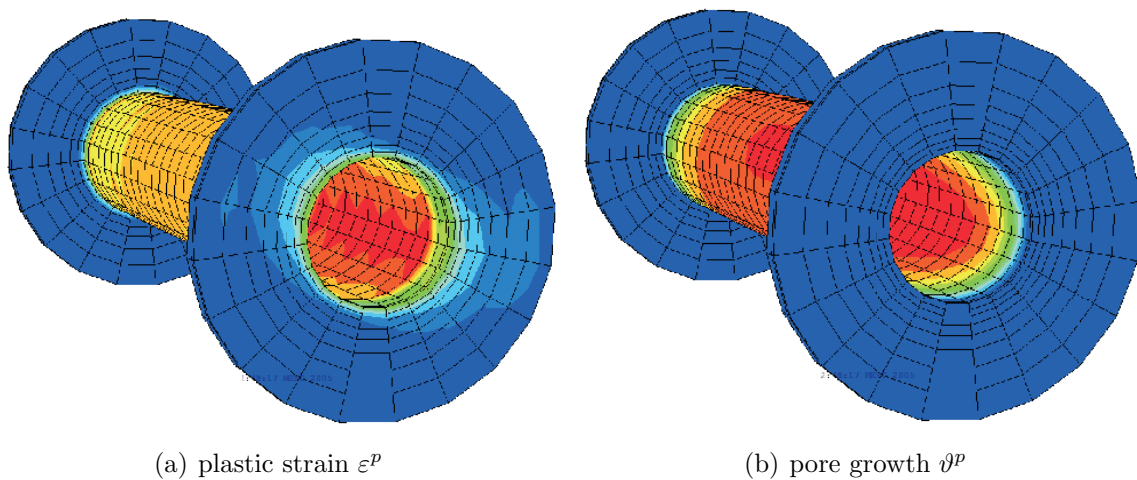
Figure 10.10.: Distribution of accumulated plastic strain and porosity in a soft-filled via at position 4 after 5 temperature steps (maxima: red, minima: blue)

outlined in Section 10.2.

3. **hard filled**: The vias are filled with a material harder than copper. We choose here the material parameter of mild steel.

All via positions are analyzed with these three fillings.

Summarizing the results after the temperature changes have been applied we observe that in the cases of no filling and soft filling the vias are — to a different extend — strained mostly in the middle of the copper cylinder. The typical strain distribution is displayed for an unfilled and a soft-filled via of position 4 in Figure 10.9 and Figure 10.10, respectively. In the unfilled via the values of both, plastic strain and volumetric plastic dilatation, i.e., maximal porosity, are smaller than in the filled via. Depending on the position of the unfilled via the maxima of plastic strain and of plastic dilatation occur in the outer region (position 1, 2, 4, 5) as well as in the inner regions (position 3, 6) of the thin copper cylinder, whereas in case of a soft filling the maximum values are all found on the inner side. In that context the wall thickness of the copper cylinder may be of considerable influence and needs to be further investigated.

For hard fillings the location of the maximum straining shifts — as one may expect — away from the copper tube to the attached upper and lower layers, see Figure 10.11. Note that because our FEA does not consider debonding of the copper material from the filling the straining that was computed here is not necessarily realistic. The values may differ in particular in case of a loose fitting of a stiff filler, e.g., a wire. This may

203

(a) plastic strain ε^p (b) pore growth ϑ^p
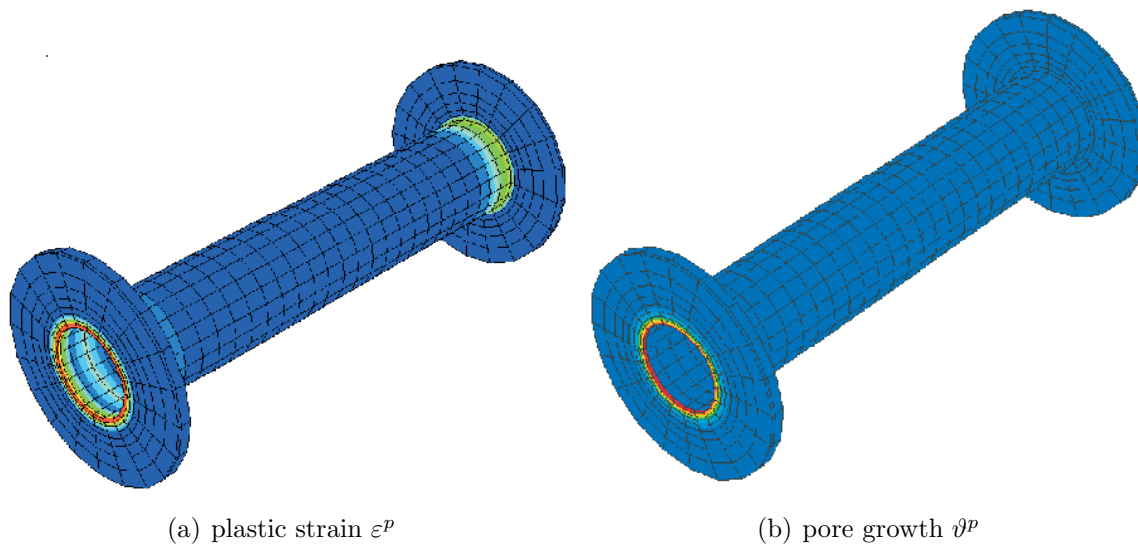
Figure 10.11.: Typical distribution of accumulated plastic strain and porosity in a hard-
filled via (maxima: red, minima: blue)

also prevent bending of the copper tube but it allows for pressure and tension, the main
mechanisms that cause pores to grow.

In Table 10.2 the results are given in detail. Because FEA of the vias at position 1 and
4, and, 2 and 5, respectively, leads to very similar results, we list here only the latter.
Moreover, for clarity all values are referred to an average strain and an average dilatation
with value 0.03.

Note that we compare maximum values and that the position of the maxima may differ.
In particular we emphasize that in case of a hard filling the maximum value is on the
upper boundaries of the via, see Figure 10.11. Nonetheless we can summarize as follows:

- The filling of the vias with solder stop mask does not necessarily improve the
  mechanical properties of the structure. After five temperature changes the unfilled
  vias show lower plastic strain and lower porosity.

- A hard filling supports the via, i.e, it prevents bending. The maximum of straining
  is shifted from the center to the boundary of the structure instead.

- The via at position 3 (in the middle of the chip) as well as the via at position 4 (on
  the diagonal) are the most strained ones, and, moreover, show different regimes
  of loading (stretching, bending). We therefore proceed analyzing only these two
  positions.

via position		relative strain maximum	relative dilation maximum
3		0.8588	0.2905
4	no	0.9123	0.4183
5	filling	0.8012	0.2859
6		0.8478	0.3095
3		1.1223	0.7630
4	solder stop	1.2328	0.8547
5	mask filled	1.0567	0.7880
6		1.1088	0.7507
3		1.1687	0.6353
4	hard	1.1757	0.6380
5	filling	1.0737	0.6637
6		1.1128	0.6340

Table 10.2.: Maxima of plastic strain and pore growth in the different via positions after 5 temperature steps.

The diagrams in Figure 10.12 allow to gain an overview of the development of maximum plastic strain and plastic dilatation in time for the soft-filled vias located at positions 3–6. The response in all positions of the via is similar. The initial cooling 456K–233K causes a formidable plastic strain but no plastic dilatation. The reason for that may be a pressure dominated stress state; because of the different thermal expansion coefficients the copper is bent but under pressure. On the opposite, rising temperature causes tension and voids to grow but — at least in the first steps observed here — no plastic straining. The process repeats with smaller amplitude.

The vias along the diagonals are the most severely strained, all other vias show approximately the same level of strain. In all cases the finite element with the highest absolute value in strain also shows the highest increments in strain after 5 steps. The analog holds for the plastic dilatation, but the locations of maxima do not coincide.

A similar behavior was observed for the (not displayed) unfilled vias, but here the rising temperature also causes a (comparative small) growth in plastic strain. Cases where in unfilled vias the element with the highest plastic strain shows saturation already after first cooling, as reported in [3], were not found here. However, in case of the hard-filled vias the temporal development shows these saturation after the first step of cooling for both, plastic strain and pore growth.

(a) plastic strain   (b) pore growth
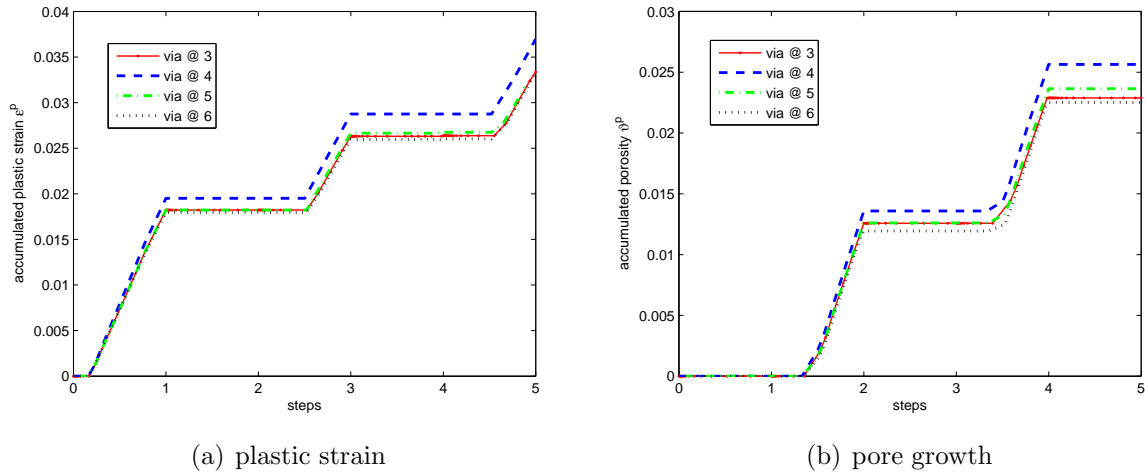
Figure 10.12.: Temporal development of the maxima of plastic strain and pore growth in the soft-filled via.

10.5. Long term response

In experiments the number of temperature cycles that a circuit board can tolerate is generally considered to be a measure of the circuit copper's resistance to fatigue damage. It depends in a large part on an inverse relationship with strain amplitude $\Delta\varepsilon$ within one cycle. The fatigue failure of a metal, as here the electrodeposited copper, is commonly estimated using a Coffin-Manson relationship of the form (8.1).

Fatigue of copper is characterized by elastic and plastic strain components. During a high-strain/low-cycle testing as considered here the dominant component is the plastic deformation. Elastic deformations play a role mainly during low-strain/high-cycle testing, therefore, the region of elastic deformation is also considered as the dynamic region. In that case the first term of equation (8.1) dominates and fatigue performance is mainly a function of the tensile strength.

Conversely, in the high-strain/low-cycle regime, the second term of (8.1) dominates and fatigue is a function of ductility. The account in terms of stress is less useful and the first term in equation (8.1) does not apply. The strain amplitude within one cycle is replaced by the plastic strain increment to give

$$\frac{\Delta\varepsilon^p}{2} = \varepsilon_f(2N_f)^c, \tag{10.30}$$

where $(2N_f)$ is the number of strain reversals (cycles) and ε_f is the related ductility.

(a) plastic strain

(b) volumetric plastic dilatation
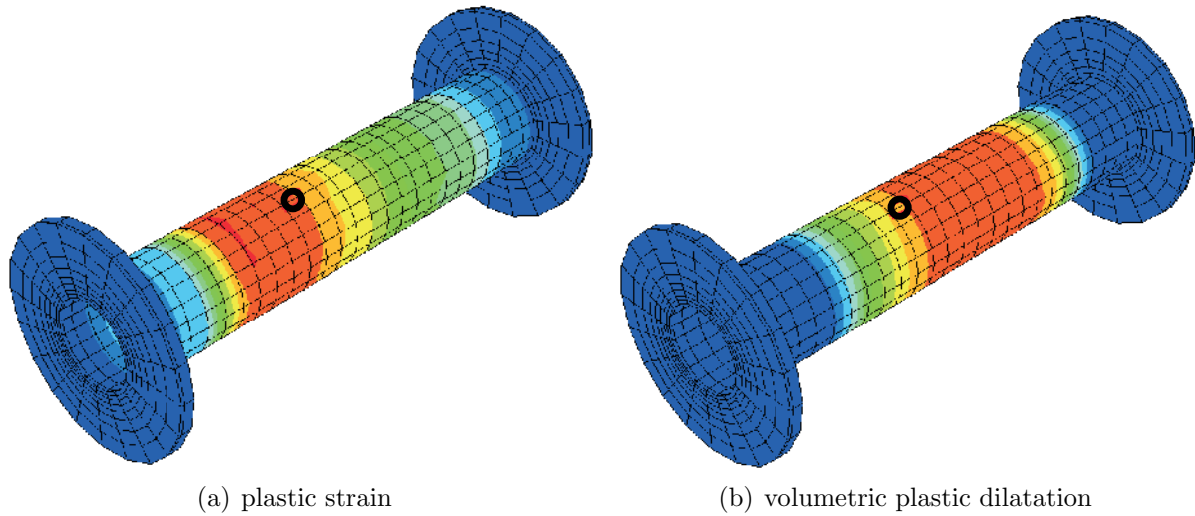
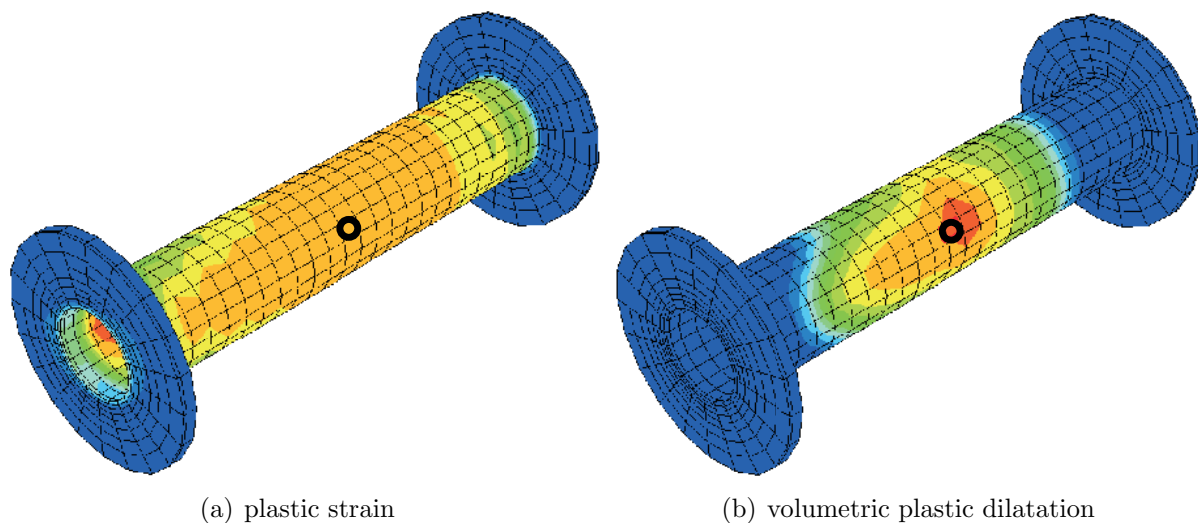Figure 10.13.: Distribution of accumulated plastic strain and porosity in an unfilled via at position 3, (maxima: red, minima: blue)

The exponent c is known as the fatigue ductility exponent, commonly ranging from -0.5 to -0.7 for metals.

Different sources report that the ductility of electrodeposited copper is smaller than the ductility of bulk copper, [17, 245, 278, 149]. Thus, we assume here a maximal ductility of 20%.

We now apply relation (10.30) to the results of Section 10.4. The plastic strain increment is found by averaging the plastic strain from step 2 to step 5. The first step is skipped because the strain induced by the initial cooling gives no information about a typical strain increment.

The region with maximum straining of the via is marked in Figure 10.13 and 10.14 by a circle. Here we get (averaged over the integration points of the element) for the unfilled via at position 4 $\Delta\varepsilon^p_{\mathsf{ave}} = 0.005737$ and for the soft-filled via $\Delta\varepsilon^p_{\mathsf{ave}} = 0.002876$. Applying Equation (10.30) gives a live expectation of $N_f = 591$ and $N_f = 1867$ for the unfilled and filled via, respectively. The same procedure applied to the vias at position 3 results in $N_f = 1084$ for the unfilled and $N_f = 525$ for the filled via.

The calculated numbers of cycles are low with respect to the required life expectation of at least 4000 cycles, i.e., $N_f = 8000$. Moreover, this approach does not account for the fact that the absolute value of ε^p is higher in case of a filling in the vias. Also, additional information about crack or pore growth are not consulted for life time estimation.

(a) plastic strain   (b) volumetric plastic dilatation

Figure 10.14.: Distribution of accumulated plastic strain and porosity in an unfilled via at position 4, (maxima: red, minima: blue)

To answer the question of how reliable this simple traditional approach is, we study in the following the mechanical response of the vias over a longer period of time and analyze the plastic strain as well as the expected pore growth. To this end, 20 steps of temperature cycling after the initial cooling are computed. Because of the significant computational effort we analyze here only the maximal loaded vias at position 3 and 4, the conclusion for the remaining via positions are analogous. In case of the hard-filled vias we do not observe additional straining after the first cool down. Therefore, and because hard filling is of somewhat artificial nature, we investigate in the following only the unfilled and soft-filled vias.

The distribution of plastic variables after 21 temperature steps is shown in Figure 10.13 and Figure 10.14 for vias at position 3 and 4, respectively. During continued temperature cycling the location of the maximal values of plastic strain and plastic pore growth changes. The displayed distribution nicely reflects the loading of the via. In position 4 bending dominates and the accumulated plastic strain and, in particular, the plastic volumetric dilatation show a localization on the corresponding sides of the via. In position 3 (direct underneath the chip) the via is mainly stretched along its axis and the distribution of plasticity in circumferential direction is basically homogeneous. The highest plastic straining is accumulated in the upper half of the copper tube, whereas the pores and voids grow increasingly towards the lower half. If we consider superposition of both defects there seems to be a higher probability of failure within the middle parts of the
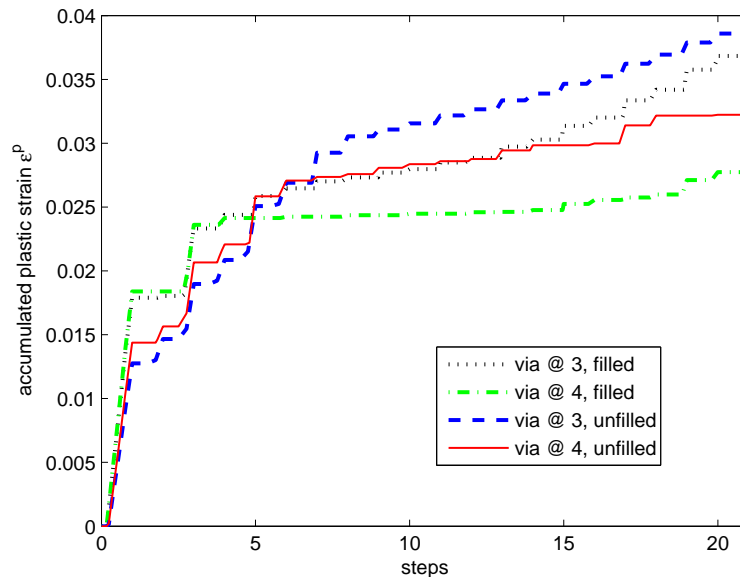
Figure 10.15.: Temporal development of plastic straining within 21 temperature steps
for unfilled and soft-filled vias

vias. Clearly, here is some need to substantiate such an effect experimentally.

The strain values at inner and outer side of the via wall become similar. Moreover, starting after about 8 steps the rising of temperature starts to cause a small increase in plastic strain also for the soft-filled vias. Pore growth as modeled here can only happen in a tension dominated state, i.e., during heating.

To account for both plastic straining and increasing porosity the temporal development of the plastic variables is plotted in the Figures 10.15 — 10.18 for the position marked in Figure 10.14. The values computed at this locus are close to the absolute maxima of $\varepsilon^p, \vartheta^p$ for all analyzed vias. In order to additionally avoid numerical artifacts all plotted values are averaged within the finite elements.

For all studied vias the cooling from manufacturing temperature of 456 K down to 233 K initiates an formidable amount of plastic strain with amplitudes higher in the filled than in the unfilled vias. Within the next temperature steps the increments of plastic strain are still large but around step 6 the plastic straining shows saturation. Then it depends on the position of the via how much the strain increments reduces. To illustrate this, Figure 10.16 shows the strain increments within the steps. We clearly see that the increment of plastic strain computed from a FEA of 5 temperature steps is not representative for the rest of the life cycle. The increment $\Delta\varepsilon^p$ is in the first

(a) vias at position 3   (b) vias at position 4
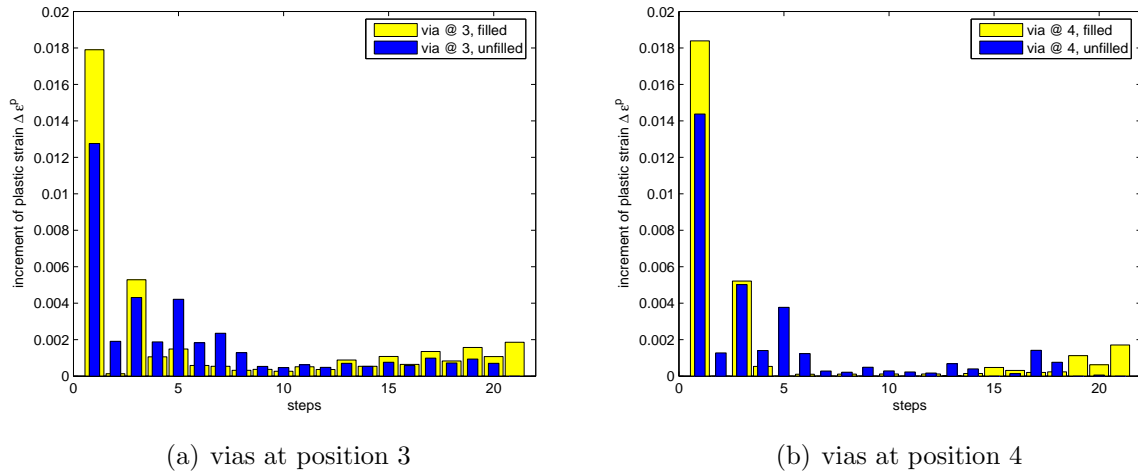
Figure 10.16.: Increments of plastic strain $\Delta\varepsilon^p$ within the temperature steps for unfilled and soft-filled vias

steps significantly higher than the average of steps 6 to 21. In particular, the influence of the fillings in the vias is inverse. In case of no filling we get an average strain of $\Delta\varepsilon^p{}_{\mathtt{ave}} = 0.000798$ (with filling $\Delta\varepsilon^p{}_{\mathtt{ave}} = 0.000664$) in position 4, resulting in $N_f = 15818$ and $N_f = 21490$, respectively. The corresponding numbers of the unfilled and filled via at position 3 are $N_f = 4529$ and $N_f = 4942$. Note that the computed live expectations are by an order of magnitude larger than above.

Figure 10.17 displays the temporal development of the maximal possible void growth, i.e., the volumetric plastic dilatation ϑ^p. Nearly constant increments $\Delta\vartheta^p$ are observed after each heating step. Because the volumetric plastic dilatation as a function of time (or steps) shows an almost linear slope it may reach a critical value after a certain number of steps. Ductile metals are known to fail by fracture when the porosity reaches a volume fraction of at most 0.3, [343]. Extrapolating the function in Figure 10.17, this critical porosity would be reached after $150\ldots300$ temperature steps. This number is a not necessarily realistic because by equation (7.190) we allow the pores to open in tension but not to shrink in compression. Consequently, ϑ^p can be considered an auxiliary value which at best gives an upper limit for the realistic porosity.

Henceforth, lets follow the constitutive model outlined in Section 10.3 which allows also for pore closure. To this end, we introduce the variable $\tau^p = \ln(J_p)$ to measure plastic volume change, i.e., to account for the growth and shrinkage of voids and keep ϑ^p to be an internal variable accounting for volumetric plasticity and for work hardening but now without its physical meaning of pore growth. To ensure that the pores must not

210
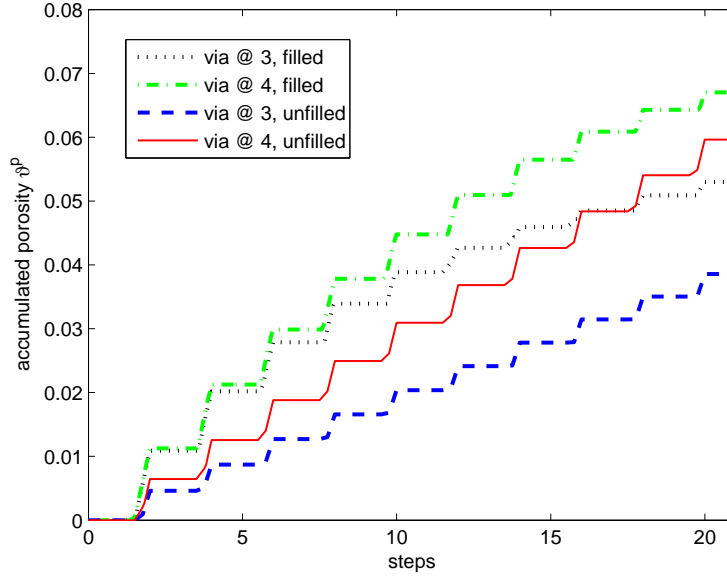
Figure 10.17.: Temporal development of monotonically assumed void growth within 21 temperature steps for unfilled and soft-filled vias

get smaller that their initial size within the virgin material we constrain $\tau^p \geq 0$.

Figure 10.18 monitors the volumetric growth (and shrinkage) in the vias during 21 temperature steps. In all vias the first heating steps cause a significant growth in porosity. Then, similar to the plastic straining, a certain saturation is reached after approximately 6 steps. Thenceforward pores in the copper material open and close with every temperature cycle. The resulting porosity shows a slight increase in every cycle.

To estimate the life time of a materials from its porosity an empirical equation like (8.1) is not known. Therefore we apply the following strategy to calculate the number of cycles when the resulting porosity reaches a critical value. First we determine the porosity after the first few cycles, here we choose step 6. For the unfilled via at position 3 we get $\tau^p_{\text{ini}} = 1.187 \cdot 10^{-4}$, for the filled via $\tau^p_{\text{ini}} = 2.003 \cdot 10^{-4}$. Now we compute the average increase of porosity within every temperature cycle from step 6 to 21 ($\Delta\tau^p = 1.499 \cdot 10^{-4}$ / $\Delta\tau^p = 2.2135 \cdot 10^{-4}$) and extrapolate that increase in a linear manner until the resulting porosity reaches the critical value.

$$\Delta\tau^p = (\tau^p_{\text{crit}} - \tau^p_{\text{ini}})N_f^{-1} \tag{10.31}$$

The number of cycles $(2N_f)$ corresponds to the life expectation. Table 10.3 summarizes the results for both, plastic straining and resulting porosity computed with 21

211
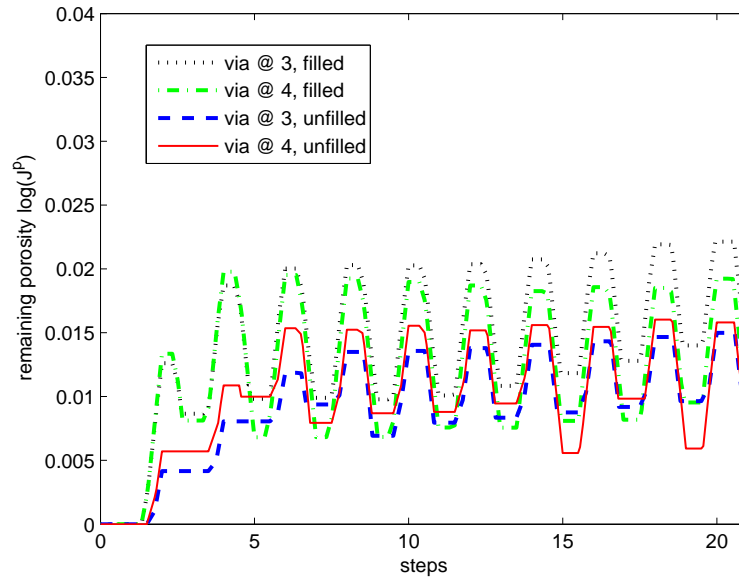
Figure 10.18.: Temporal development of pore opening and closure within 21 temperature steps for unfilled and soft-filled vias

via position		$N_f(\varepsilon^p)$	$N_f(\tau^p)$
3	no filling	4529	1293
3	soft-filling	4942	1864
4	no filling	15818	6172
4	soft-filling	21490	14125

Table 10.3.: Life expectation in the different via positions.

temperature steps. Both criteria yield qualitatively equal results and show the unfilled via at position 3 being the most likely to fail. The lower numbers for the porosity criterion is likely to be caused by the linear way of extrapolation (equation (10.31) vs. equation (10.30)). Fillings support the vias, in particular, in a tension-compression dominated state. An experimental verification of the observed correlations (as well as of the relatively high fatigue ductility) was not available to us and is left for future research.

The presented analysis of plated through vias shows that both mechanisms, plastic straining and the growth of pores within the copper via have an essential influence on the life time expectation of the vias and, consequently, the whole circuit unit. The actual accumulated damage depends on the position of the via on the PC Board and on the filling.

The extrapolated number of cycles until failure of the units depends on the number of temperature cycles considered in the numerical analysis. In particular, a realistic life time estimate needs to base on a finite element analysis of at least 20 temperature steps. Considering less steps gives rather accidental results influenced, e.g., by the initial reference state. Furthermore, after few temperature cycles it is not yet possible to estimate wether the filling of a copper via supports plastic straining or prevents it.

Presumed that the input to the finite element analysis, in particular the material properties of the electrolytically deposited copper and the failure criteria, reflect the actual situation, the introduced FEA-based strategy can serve as a predictive tool for the plated through holes and vias. This reduces the need of highly repetitive and costly experimental failure tests, resulting in significant cost savings to the industry.

A strategy to calibrated material parameter using experimental measurements will be sketched in the remaining of this Chapter.

10.6. Experimental parameter identification for solder alloys

Solder joints are essential components in microelectronic devices, see Figure 10.1, 10.2. Fields of solder balls are used to join different electronic components and, concurrently, to realize electric conductivity. A single solder ball is small, typical only a few hundred micrometers in size. Due to the ubiquitous miniaturization and depending on the technology applied, solder balls of less than 50 μm in diameter are today's state of the art. Traditionally, solder is made of lead alloys but for environmental reasons plumbiferous solder needs to be replaced by lead-free materials, e.g., alloys made of tin, silver and copper. Unfortunately, these new materials tend to form cracks and micro-voids, resulting in reduced load-carrying capacity and loss of conductivity. The remote goal of our work is to numerically analyze the life cycle of lead-free solder joints. This, in turn, requires the knowledge of the basic material parameters such as Young modulus, initial yield stress, hardening law, critical straining as well as the time dependency of the parameter.

10.6.1. Uniaxial tension test of solder paste

The classical experiment to determine the mechanical parameter describing elasticity, plasticity and failure of a material is the uniaxial tension test. We conducted uniax-
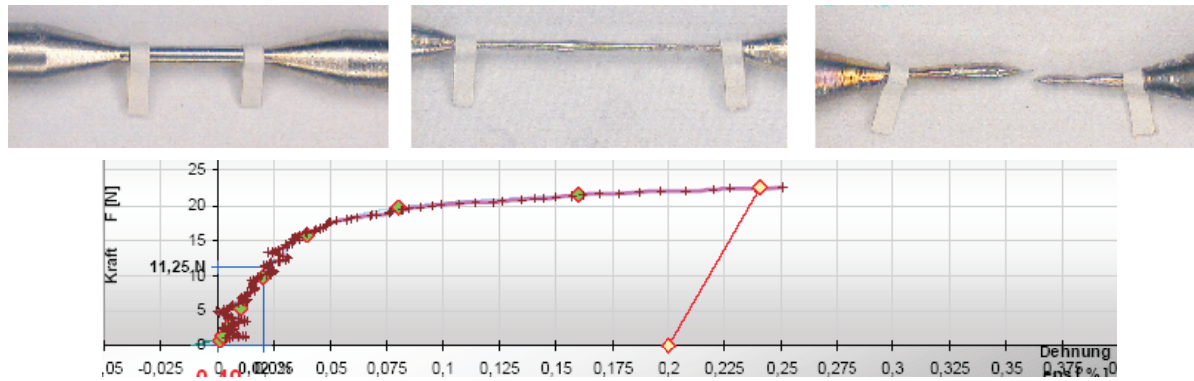
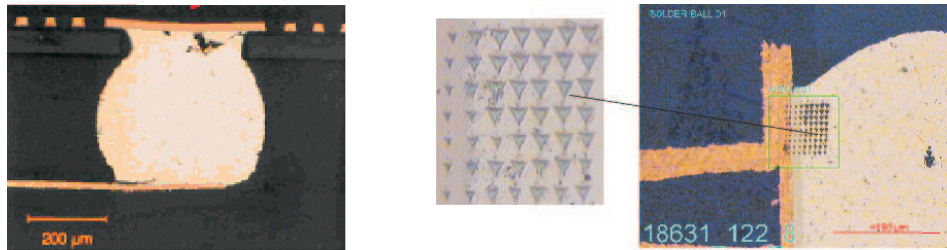Figure 10.19.: Uniaxial tension test of a Sn95.5Ag4.5Cu0.5-solder alloy.

Figure 10.20.: Solder ball and indents on the nano scale.

ial tension tests on different lead-free solder alloys. Though the specimens are small (with a typical length of 5mm) a uniaxial tension test is a macroscopic test. Thus, the specimens here are made of solder paste, where we can only hope that the mechanical properties are exactly the same as in the epoxy embedded $500 - 50\mu$m sized solder balls of a circuit board. Figure 10.19 shows the results of a uniaxial tension tests on a specimen of Sn95.5Ag4.5Cu0.5-solder paste. Clearly, the material is of high ductility and, moreover, the elastic range can hardly be distinguished from the beginning plastic deformation. The problem in case of the very soft solder paste are large deviations in the measurements (up to 100 %). Therefore, and to account for the size of the actual solder balls, mechanical properties of lead-free alloys are determined by nanoindentation experiments, Figure 10.20, see [4, 170, 369].
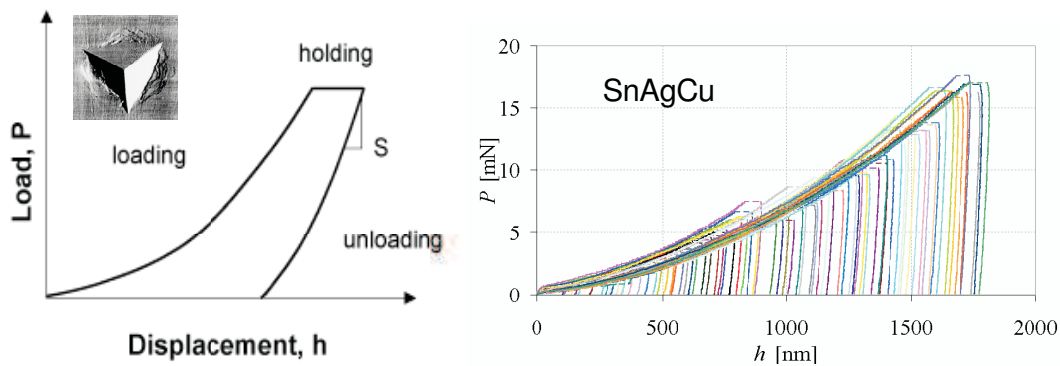
Figure 10.21.: Typical load-indentation depth curves, schematic plot and experimental results for Sn95.5Ag4.5Cu0.5-solder

10.6.2. Nanoindentation experiments

Almost as common as uniaxial tension tests are indentation tests, i.e., experiments where a hard tip, typically a diamond, is pressed into a material sample. After some time the load is removed and the residual indentation area in the sample is measured. The maximum load is divided by the indentation area to determine the hardness of the material. Nanoindentation in particular exploits the fact that the contact area between tip and material sample (and thus the volume of material that is tested) can be made arbitrarily small. The problem of measuring the microscopic small area of contact is solved by depth sensing indentation. In this method, the load and the displacement of the indenter are recorded during the indentation process. The recorded data are analyzed to determine the mechanical properties of the sample. In opposite to classical indentation experiments like the Vickers- or Brinell-Test, one can obtain much more information than just the hardness of the material.

A typical quasi-static load-displacement curve of a depth-sensing indentation experiment is shown in Figure 10.21. As the load is applied, the indenter sinks into the material due to both elastic and plastic deformation. If the load is held constant, the indenter may continue to sink due to time-dependent deformation, i.e. creep. During unloading the material recovers by a process that is primarily elastic. Methods have been developed to analyze all the three parts, loading, holding and unloading, of the load-displacement curves. However, the results obtained depend on the model chosen and can be very sensitive to the details of the analysis, see [144] for a detailed study.

We use a Microsystems-Nanoindenter Machine and apply standard techniques to extract
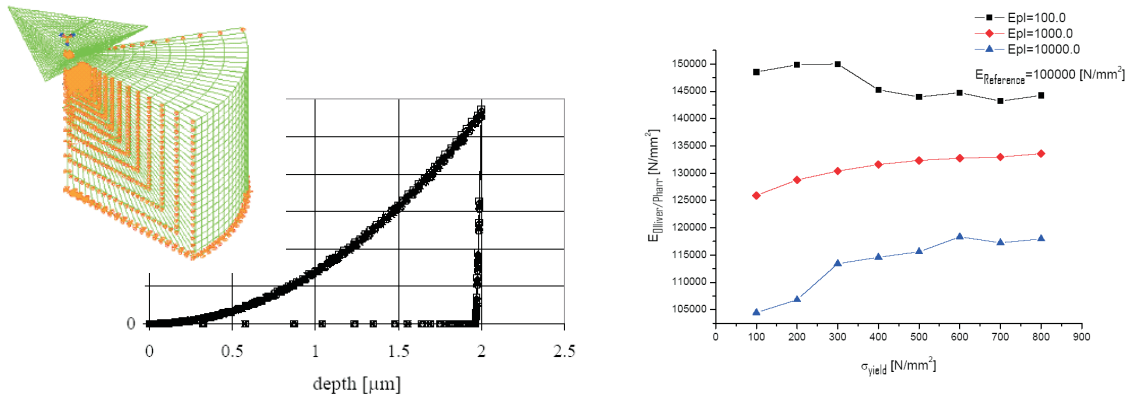
Figure 10.22.: Fe simulation of indentation experiments in solder using a Berkovich indenter and error of the experimentally determined Young modulus $E_{\text{Oliver/Pharr}}$ vs. initial yield stress σ_{yo} for different plastic tangents E_{pl}.

the material properties from the measured load-indentation depth curves. Without going into detail, the Young modulus of the sample is determined by the Oliver-Pharr method [248] out of the unloading slope, see, e.g., [115]. The initial yield stress is extracted following the approach of Tabor [318]. Note that the underlying assumption of an elastic-ideal plastic material results in a very rough estimate of the initial yield stress and, moreover, precludes the specification of plastic hardening.

The typical indenter tip in nanoindentation experiments is a three-side pyramidal shaped diamond (Berkovich diamant). This indenter is self-similar, i.e., the projected area of contact A scales with the remaining indentation depth h_c,

$$A = 3\sqrt{3}h_c^2 \tan^2 \theta = c^* h_c^2, \qquad (10.32)$$

where the opening angle $\theta = 65.3^o$. In experiments the factor c^* is calibrated to the actual machine and may deviate from theory. The load and indentation depth of a typical SnAgCu solder sample recorded during the indentation process result in a load-displacement curve as displayed in Figure 10.21.

To assess the quality of our experimental results we model and analyze the experimental setup by finite element computations and compare the real (input) material data with the results determined from the load-displacement curves. The load-displacement curve of a typical sample recorded during the computed indentation process are shown in Figure 10.22. The material data are $E = 35000$MPa, $\nu = 0.3$, $\sigma_{yo} = 50$MPa and $E_{pl} = 3000$MPa, where the latter is the plastic tangent modulus of a bilinearly modeled
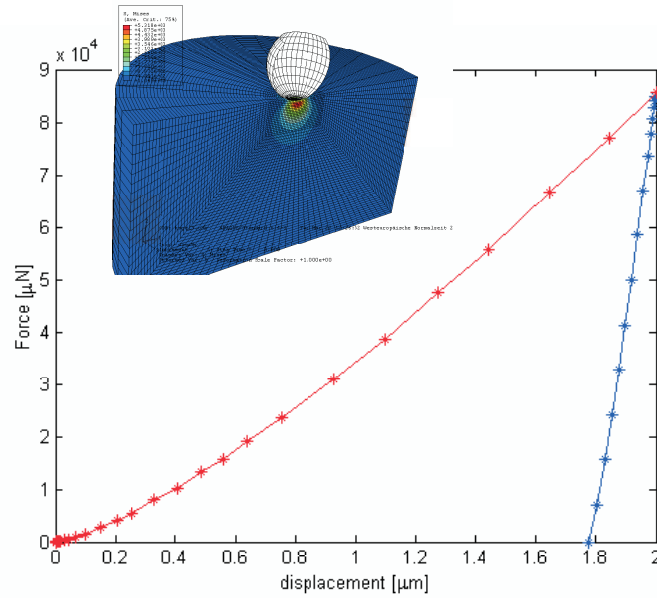
Figure 10.23.: Load-indentation depth curve computed with same material data as above using a spherical indenter.

elastic-plastic material law,

$$\sigma_y = E_{pl}\varepsilon^p. \tag{10.33}$$

It can be seen from Figure 10.22 (as well as from experimental recordings in Figure 10.21), that the indent is almost completely plastic; the slope of the unloading branch is steep and the elastic recovery of the indentation depth (i.e., the difference of maximal and remaining displacement) is small.

Figure 10.22 also illustrates that for the very soft and ductile solder material the standard techniques result in a considerably large error. In the diagram on the right hand side the elastic Young modulus determined from the (computed) load-displacement curve with the Oliver–Pharr method, $E_{\text{Oliver/Pharr}}$, is plotted versus the initial yield stress, σ_{yo}, for different plastic tangents $E_{pl} = 100, 1000, 10000$MPa. The Young modulus of the material is $E = 100000$MPa. Especially for low hardening materials the error of the experimentally determined Young modulus can be significant, e.g., an error of about 50% is observed for $E_{pl} = E/1000$ and a low yield stress $\sigma_{yo} = 100$MPa.

Therefore, and to collect additional information out of the measured load-displacement curve, we apply an inverse analysis technique. To this end we model and compute the experimental setup by finite elements, Fig. 10.22, and compare the input material data

with the results determined from the load-displacement curve. By means of a controlling optimization algorithm due to Powell [274] we minimize the error and adapt the material data of the bilinear elastic-plastic material law to the reference (experimentally measured) load displacement curve.

Unfortunately, the approach allows to vary only two out of the three material data E, σ_{yo} and E_{pl}. By the self-similar geometry of the Berkovich indenter a variation of the load results only in a variation of the total and remaining indentation depth, the area of contact is a dependent variable. This renders the problem not unique, varying E, σ_{yo}, E_{pl} independently results in meaningless load-displacement curves. One way to solve this unsatisfying situation is to include hardening information obtained from the macroscopic uniaxial tension tests of Section 10.6.1. Another way seems the choice of another indenter, in particular a spherical indenter. A spherical indenter is not self similar, here,

$$A \propto h_c R, \tag{10.34}$$

where R is the radius of the sphere. This relation gives us an additional parameter to control (but may cause experimental difficulties, especially in calibration). The three parameter E, σ_{yo}, E_{pl} may now be determined by the inverse analysis technique. A load-indentation depth curve computed with a spherical indenter of radius $R = 10\mu$m and same material data as above is displayed in Figure 10.23. We observe a bigger elastic range, the unloading branch clearly shows differences to the Berkovich indenter curve in Figure 10.22. For pure elastic contact we can derive a load-displacement relationship from Hertz-Contact theory [168],

$$P = \frac{4}{3}\frac{E}{1-\nu^2}h^{3/2}\sqrt{R}. \tag{10.35}$$

When the load is plotted versus the indentation depth in a log-log diagram we get a strait line. A deviation from the strait line indicates the onset of plasticity. The sphere may be enlarged to see the different (elastic and plastic) regimes during the nano-testing procedure more clearly. Moreover, additional work needs to be done to analyze the time dependence (creep) of solder material out of the measured load-indentation depth curves.

11. Shock Wave Induced Damage in Kidney Tissue

In shock-wave lithotripsy — a medical procedure to fragment kidney stones — the patient is subjected to hypersonic waves focused at the kidney stone. Although this procedure is widely applied, the physics behind this medical treatment, in particular the question of how the injuries the surrounding kidney tissue arise, is still under investigation. To contribute to the solution of this problem several numerical simulations of a human kidney under shock-wave loading are summarized in this chapter.

11.1. Shock-wave lithotripsy

Extracorporeal shock-wave lithotripsy (ESWL) is the most common treatment for kidney stone disease. The idea of this non-invasive procedure to comminute kidney stones is to generate a number of high intensity pressure waves (shock waves) outside the patient and to focus it on the stone within the kidney. This form of therapy was developed over twenty years ago, and has proven to be fast, effective, and relatively free from the trauma and expense associated with surgery.

The focal point of the shock wave is fixed, and the patient is moved so that the stone (imaged by fluoroscopy or ultrasound) rests at the focal point. The urologist controls three parameters: the number of shock waves administered, the repetition rate, and the voltage (or energy) of the shock wave generator. The latter is directly associated to the amplitude of

Figure 11.1.: The idea of ESWL

the pressure wave. As a rule, stones of a size of 10mm are best treated with ESWL, stones

greater than 20mm in most cases need surgery. Typically, from one to three thousand shock waves are fired onto the stone at a rate of around one per second. The treatment is monitored by imaging and terminated when it is judged that residual fragments are small enough to be voided in the urine or grasped and removed using transurethral or percutaneous probes. The appropriate intensity of shock waves for a particular treatment is based on size, shape, composition, and location of the stone — and on the experience of the medical doctors.[1]. Actually, because stone imaging is limited, the urologists tend to overtreat patients to avoid them coming back with residual stones [209].

Electro-hydraulic

Electro-mechanical

Acoustic lens

Acoustic lens focusing

Piezoelectric emitters

Piezoelectric
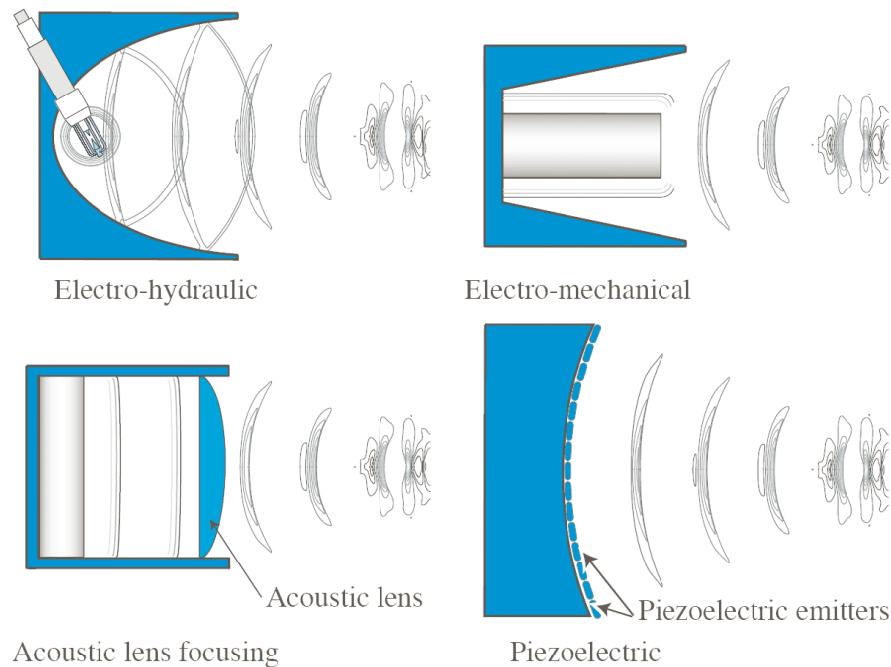
Figure 11.2.: Different types of lithotripters used in ESWL

A very important factor in the treatment is the lithotripter device. Different types of lithotripters have been approved for clinical use. They are classified by the type of shock wave source they utilize. Figure 11.2 illustrates some particular configurations; for a comparison of the different devices and historical details of ESWL see, e.g., [323, 324, 373].

The most common lithotripters are electro-hydraulic devices which generate shock waves by underwater spark discharge. Widely used is the Dornier HM3 which has been proven by clinical experience to be most efficacious [196]. Here, the shock waves are focused by a brass ellipsoidal reflector to a geometric focal point (F2) approximately 13.5 cm

---

[1]Images of Figure 11.1 found at http://members.aol.com/geometrie11/koorgeom/lithotr1.htm.

above the rim of the reflector. Investigators have used ultrasonic hydrophones to map the pressure field in HM3s at the focal point with the result that the pressure impulse is a zone roughly cylindrical in shape (precisely: a tapered cylinder), approximately 10-15 mm in diameter and 80-90 mm long. The peak pressures is typical in the range of 30-50 MPa, up to 100 MPa. Widely used are also electro-magnetic lithotripters which often have a smaller focal area ($\approx$ 2mm in diameter) and a higher peak pressure. Less common are acoustic and piezo-electric lithotripters.

The pressure field in a lithotripter can be decomposed into several components. That is illustrated in Figure 11.3 for the wave propagation in a typical electro-hydraulic lithotripter. The initial shock wave is generated by the discharge across a spark gap located at the first focus (F1) of the ellipsoidal reflector. Since the reflector is not a complete enclosure, part of the shock wave is reflected towards the second focal point (reflected wave) while the rest expands unhindered (incident wave). A diffraction or "edge" wave is created as the shock wave reaches the edge of the reflector. For more details see [320], where we also took the pictures aside from.

Because of difficulties in accessing clinical machines, at the California Institute of Technology, Pasadena, USA, a research lithotripter was designed after the HM3 [88]. A typical measurement for the pressure at the focus (F2) of the Caltech
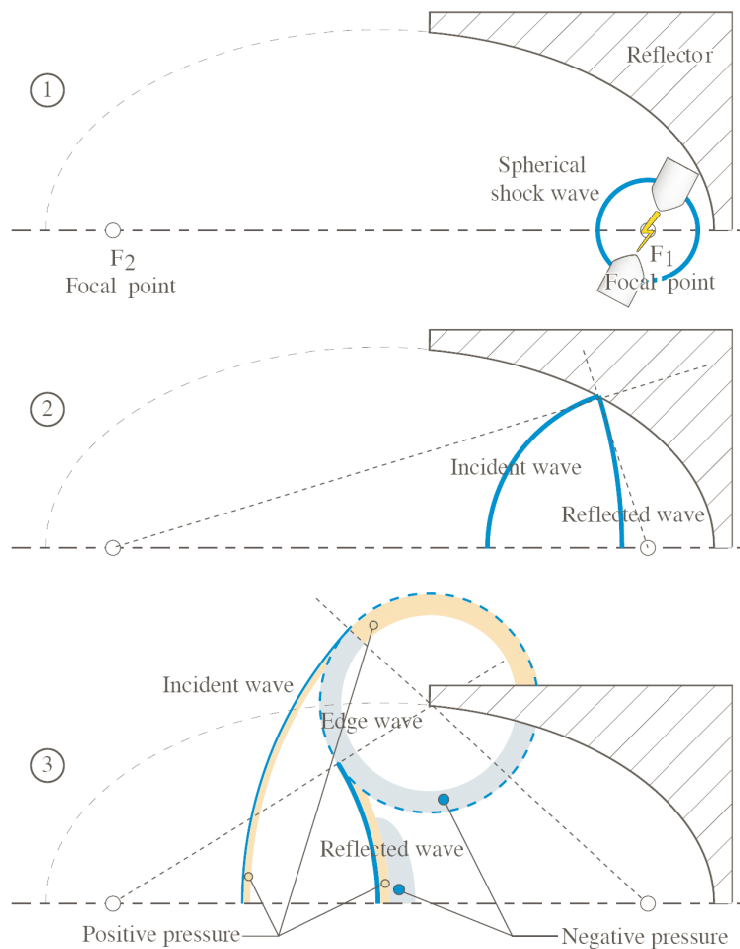

Figure 11.3.: Shock wave propagation.

device is shown in Figure 11.4^2. Although the pressure profile can vary significantly from lithotripter to lithotripter, the basic shape remains essentially the same. A narrow positive pressure spike with short rise time and rapid fall ($< 1\mu$s) are followed by a significant negative pressure, the so called "tension tail".
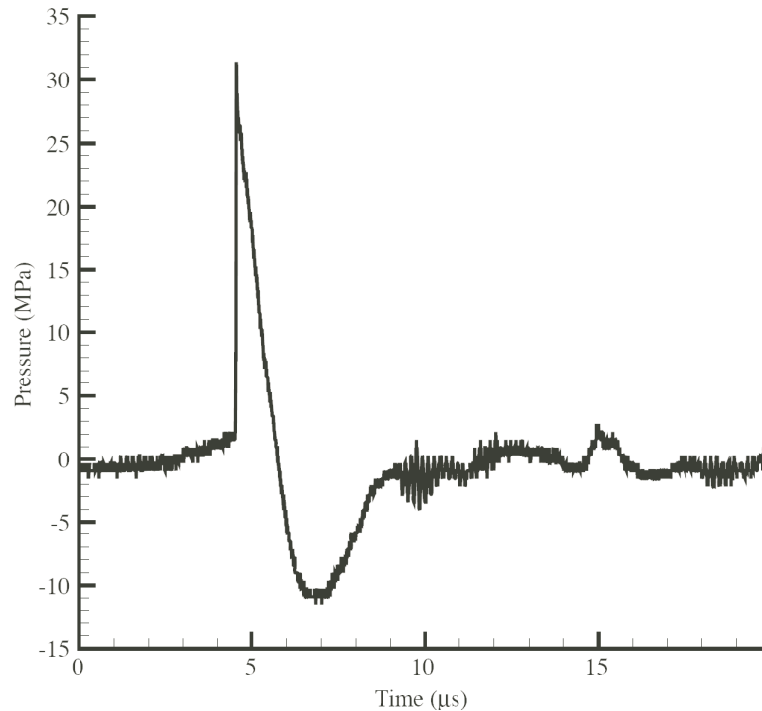

Figure 11.4.: Experimental pressure measurement at the focal point of a DH3 lithotripter.

The widespread use of lithotripsy has originated numerous research efforts aimed at understanding the physics of ESWL. Nonetheless, the exact mechanisms of stone comminution are still a topic of debate. Figure 11.5 illustrates two mechanisms that have been substantiated by empirical observation: spallation and erosion by cavitation.

Spallation is a material failure caused by tensile stress produced as the compressive part of the pressure wave is reflected by the distal stone–tissue interface as a tensile wave. This reflected wave combines with the tensile tail of the incident wave to produce a plane of maximum tensile stress that can cleave the stone. In the case of a cylindrical or cuboid artificial stone that happens at about 2/3 of its length [379]. The typical duration of a spallation process is in the range of some μs.

Erosion by cavitation is caused by the action of cavitating bubbles near the stone. The

---

^{2}Data courtesy of Michael R. Bailey, Center for Industrial and Medical Ultrasound, Applied Physics Lab, University of Washington, Seattle.

tensile component of a lithotripsy shock wave typically generates cavitation, i.e., bubbles (or clouds of bubbles) that oscillate in size and finally collapse violently after the passage of the wave. During the violent collapse a local (secondary) shock wave is ejected. This phenomena, named micro-jetting, is likely to be responsible for the pitted surface of the desintegrated stone. Empirical evidence suggests that cavitation is an important comminution mechanism [99, 294, 91, 11]. Note that the cavitation of bubbles until final collapse may take several ms, see [293] for illustrative pictures.
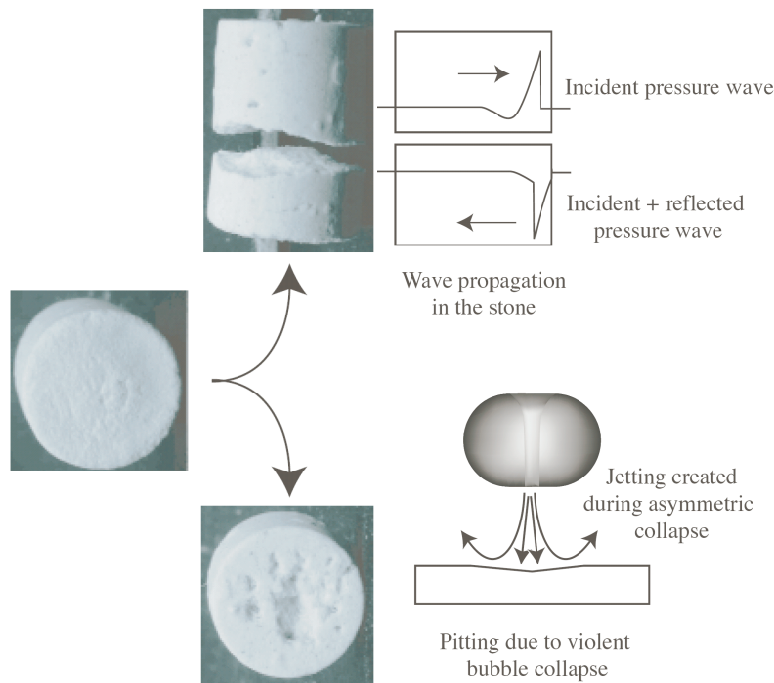
Figure 11.5.: Mechanisms of stone comminution.(Photographs courtesy of Erin Hatt, Department of Anatomy and Cell Biology, Indiana University School of Medicine, IA, USA.)

Although effective in breaking kidney stones, ESWL can also cause significant short- and long-term damage to the kidneys. The first study of side effects during ESWL was published in [81]. The extend of kidney injuries depends on many factors, as e.g., the size of the kidney, the blood pressure, the age of the patient etc. Early studies reported only minor or temporary effects on the kidney tissue [172, 176, 179] but meanwhile it is established knowledge that damage can been observed on both cellular and systemic level, see [9, 55, 110, 314, 374] and others. A common side effect of a lithotripsy treatment is the
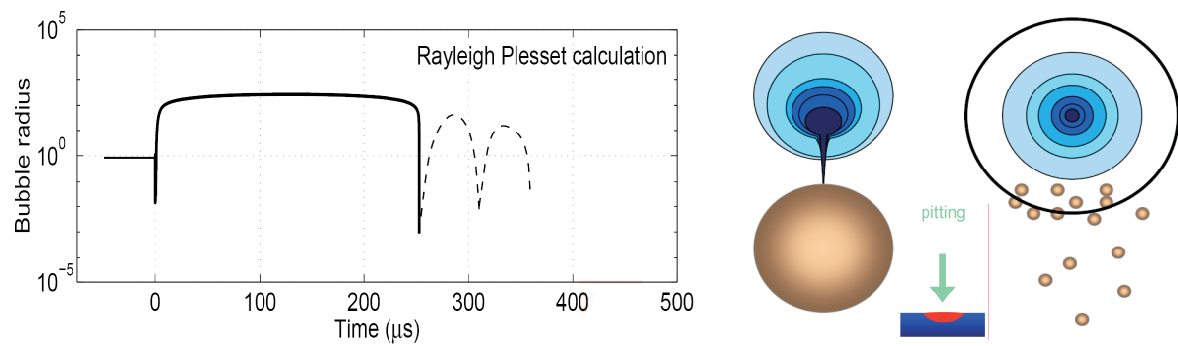
Figure 11.6.: Typical solution of the Rayleigh-Plesset equations describing the oscillating bubbles (left) and illustration of asymmetric and symmetric oscillation resulting in bubble collapse (left).

presence of blood in the urine (hematuria). Typical legions in the kidney are bruising, renal and perirenal hemorrhage and kidney enlargement. Experimental investigations on rats and pigs followed [39, 56, 94, 102] with the aim to understand the mechanisms and reasons for damage caused by shock waves. In Figure 11.7 two pig kidneys after ESWL treatment are displayed. Two mechanical effects seem to be of essential influence: shear induced stretching and cavitation induced rupture of capillaries.

Shearing of tissue. The compressive wave of the SWL impulse needs a high peak pressure to induces cracks and, by internal reflection, spallation in the stone. But the focused wave front also causes shearing along its way in the kidney tissue which may be responsible for kidney injuries in the pre-focal area of the pressure wave [315, 92, 313].

Tension by cavitation. The compressive front is followed by a tension tail and, therefore, bubble cavitation is induced which is thought to assist in stone comminution. Bubbles nucleate, expand up to several micrometer in size and finally collapse. During bubble expansion the surrounding vessels and capillaries dilate and may rupture [387, 386]. This mechanism causes irreversible changes of the kidney tissue material due to hydrostatic tension.

Furthermore, experimental evidence suggests that tissue damage is solely caused by subjecting the kidney tissue to shock waves, their amplitude and number is responsible for the extend of lesions [55, 154]. The presence or absence of a kidney stone does not affect the side effects [375].
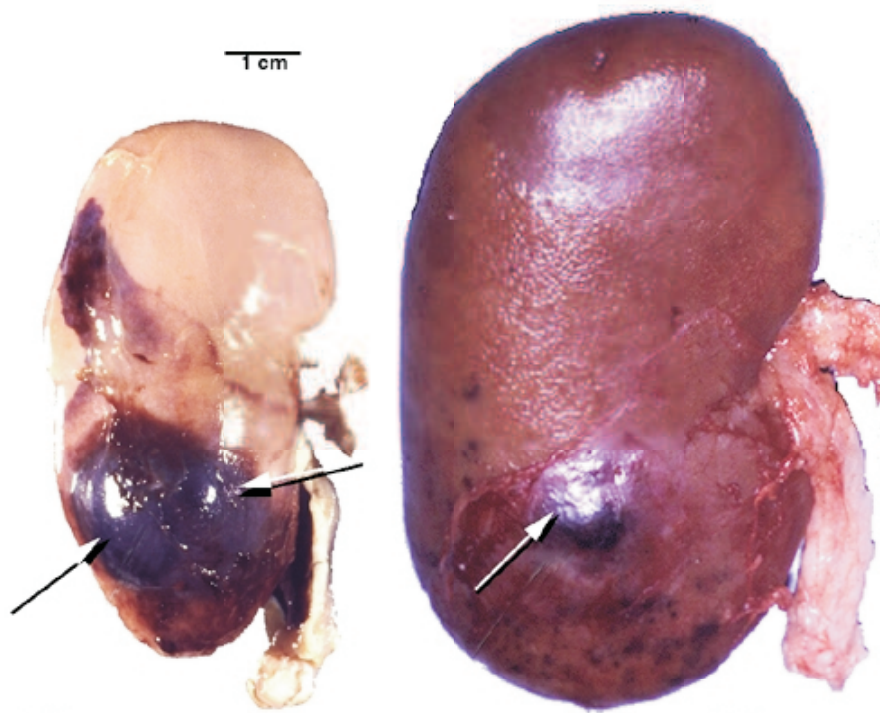
Figure 11.7.: Typical kidney injuries after an ESWL treatment observed on a juvenile (left) and an adult (right) pig kidney [39].

11.2. The human kidney

The kidneys are part of the urinary system; a human being has two of these life ensuring organs. In filtering blood and forming urine the kidneys perform several functions, see e.g. [337] for details, which can roughly be summarized by:

- regulation of blood volume and composition,

- regulation of blood pressure,

- contributions to metabolism.

The paired kidneys are reddish, kidney-bean shaped organs located just above the waist in the abdomen. A typical kidneys in an adult is 10-12 cm long, 5-7 cm wide and 3 cm thick and has a mass of 135-150 g. The concave medical border of each kidney faces the vertebral column; near the center is a deep vertical fissure through which the ureter, blood vessels, lymphatic vessels, and nerves leave the kidney, see Figure 11.2. A thin
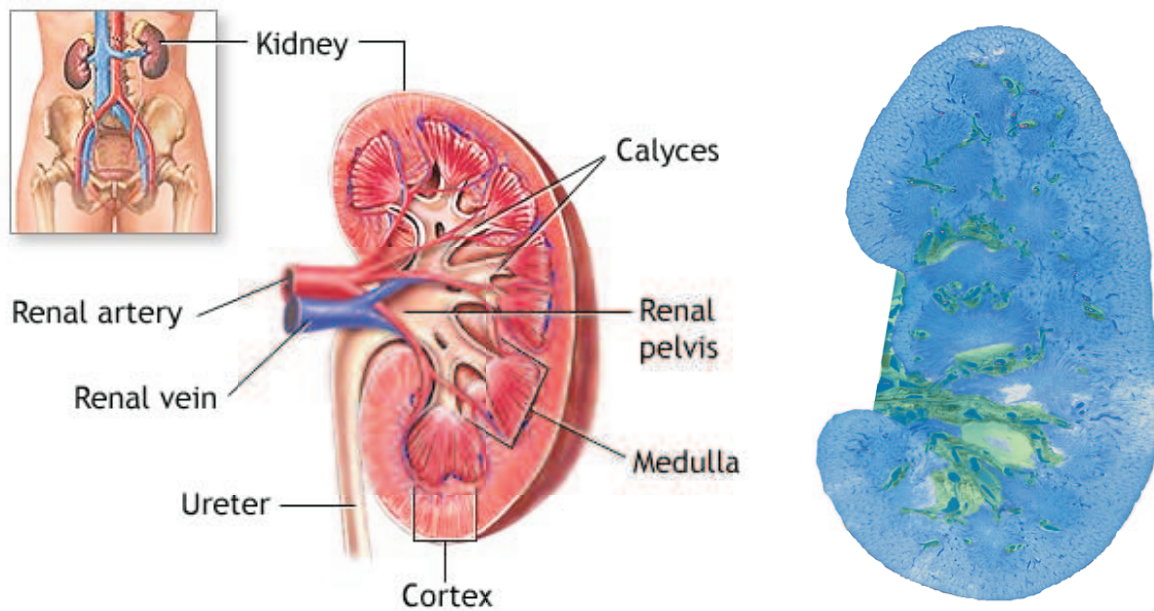
Figure 11.8.: Anatomy of a human kidney and frontal section of a left kidney (Photograph courtesy of Dr. A. Evans, Department of Anatomy, Indiana University School of Medicine, IA, USA.)

renal capsule, i.e., a smooth, transparent membrane composed of dense irregular tissue surrounds the kidney and holds it firmly in place within the abdomen.

A frontal section through the kidney reveals two distinct regions: a superficial, smooth-textured reddish area called renal cortex (cortex = rind or bark) and a deep, reddish-brown region called the renal medulla (medulla = inner portion). The medulla consists of 6-10 cone shaped renal pyramids. The wider end of each pyramid faces the renal cortex and its narrow end, called renal papilla, points towards the center of the kidney. Those portions of the renal tissue that extend between the renal pyramids are sometimes called renal columns.

The renal pyramids within the medulla constitute the functional portion of the kidney. On the microscopic level, the functional units located here are about 1 million structures called nephrons. The nephrons engage in the three basic processes: filtering blood, returning useful substances to blood so that they are not lost from the body, and removing substances from the blood that are not needed by the body. As a result, nephrons maintain the homeostasis of blood and urine is produced.

(a) surface data

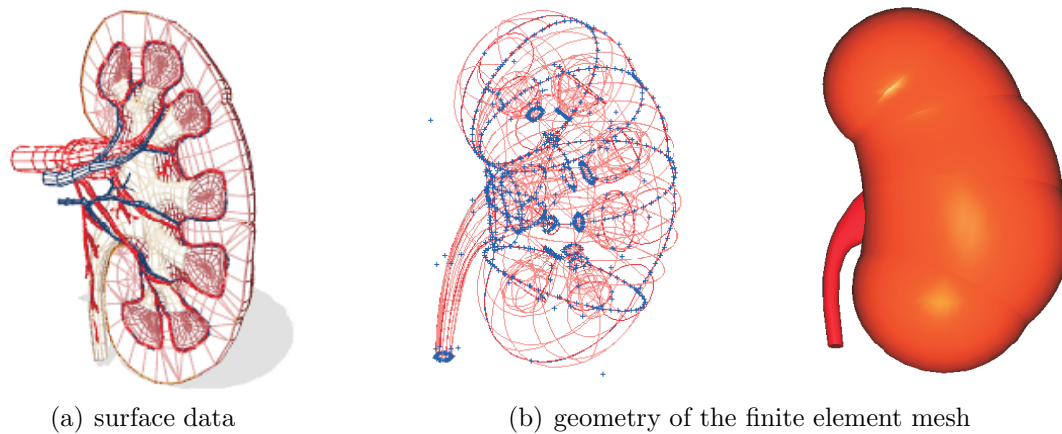(b) geometry of the finite element mesh

Figure 11.9.: Geometrical model of one half of a human kidney and simplified geometry of the finite element model.

The urine formed by the nephrons then drains into cuplike structures at the narrow end of the pyramids called calyces, and from there into a single large cavity, the renal pelvis, and finally out through the ureter into the urinary bladder.

To study ESWL by finite element analysis we have initiated an effort aimed at the development of anatomically correct models of the kidney. To begin, we purchased geometrical data from a company[3] which specializes in the visualization of complex structures, see Figure 11.9 left. With the help of these surface data a finite element mesh including the gross anatomical details was built. It should be noted that the geometrical data, as purchased, do not fulfill appropriate requirements for a finite element mesh, e.g. non-overlapping, non-distorted tetrahedral elements with positive volume. The three-dimensional finite element model generated here thus required significant manual manipulation to bring it even to a level suitable for coarse calculations. Finally, the geometry of the finite element mesh was set up using the CAE software of IDEAS [162], see Figure 11.9 mid and right and 11.11 for the results. In the continuing research the present model will be greatly refined. Furthermore, a simplified two-dimensional model including the main anatomical details was build, it is illustrated in Figure 11.10.

The kidney model is completely embedded in body tissue to avoid mismatching effects from the models boundaries. Moreover, the kidney is modeled without a stone. Four regions of functional tissue are distinguished, representing renal cortex, pyramids, surrounding medulla tissue and ureter with renal pelvis. Each of them a different material

---

[3]Viewpoint Corporation, New York; www.viewpoint.com

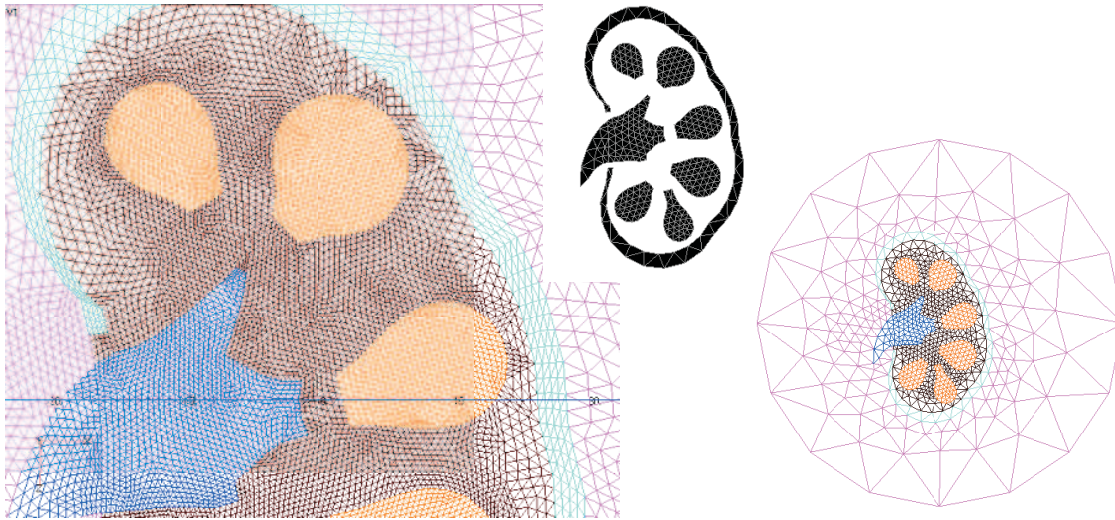Figure 11.10.: Two-dimensional finite element mesh of a kidney.

behavior can be assigned, Figure 11.10 and 11.11. Note that these different region are defined in the three-dimensional model as well, although they can not be distinguished on the picture.

11.3. Material properties of kidney tissue

The material properties of biological tissue are subject of increasing interest. Recently, several works on methods of testing and suitable experimental setup for soft bio-materials including kidney tissue were reported, cf. [220, 271, 259]. Detailed experimental investigations on kidney tissue can be found in [111, 219, 212, 239]. The intentions of the reported experiments are different but all available experiments have in common, that they focus on the elastic and viscoelastic properties for "the" kidney, i.e., the whole organ is considered to be made of an isotropic and homogenized material. The first assumption — isotropy — is justified by the irregular and non-uniformly textured tissue, see [239]. On the other hand, the assumption of one homogenized material is not helpful for our investigation. As mentioned above we want to distinguish between different regions of the kidney with different sensitivity to stress and straining.

The first and only available in vivo experiments on high speed straining were performed on (anaesthetized) rhesus monkeys by Melvin [212] and re-reported in [219]. With the aim to understand the mechanisms of injury during impact loading, compression tests
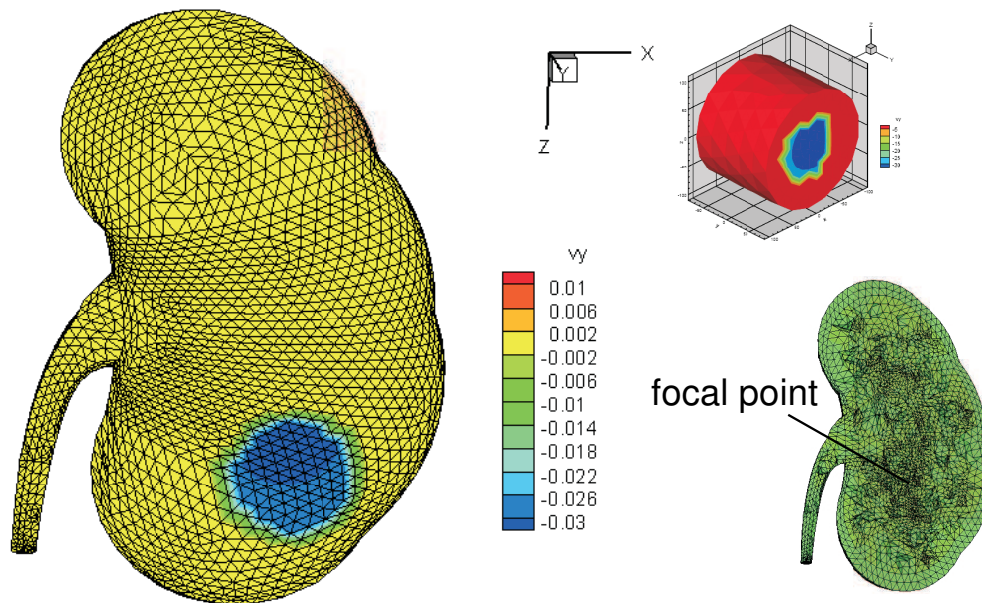
Figure 11.11.: Three-dimensional finite element mesh of a kidney.

with strain rates of $0.38s^{-1} \ldots 38s^{-1}$ were performed. The kidneys material response is clearly non-linear, the resistance of the material increases with deformation. Data on shear or tension are not available.

In vitro experiments are reported using pig [239, 111, 112] and rat [259] kidneys. In particular, the pig kidney is similar in structure and function to a human kidney, thus making it a useful model for understanding the human kidney.

Farshad et al. [111] conducted different uniaxial as well as triaxial tests on kidneys of fresh (less than 12 hours dead) pigs. Tensile tests were performed on the renal capsule (the hull of the kidney); they showed an increase of the rupture stress with an increase in the loading rate. For compression and shear tests the samples have been taken from the renal cortex, i.e., the outer part of the kidney, see Figure 11.12. In contrast to other investigations and models Farshad et al. found the renal tissue to be slightly *compressible*. Therefore, the measured data were adapted to describe the whole organ by means of a Blatz & Ko model, cf. Chapter 3.4, for the circumferential and radial directions of the kidney.

Moreover, the long term compression test showed an instantaneous straining followed by a viscous response of the tissue. For characterization of the time depended behavior
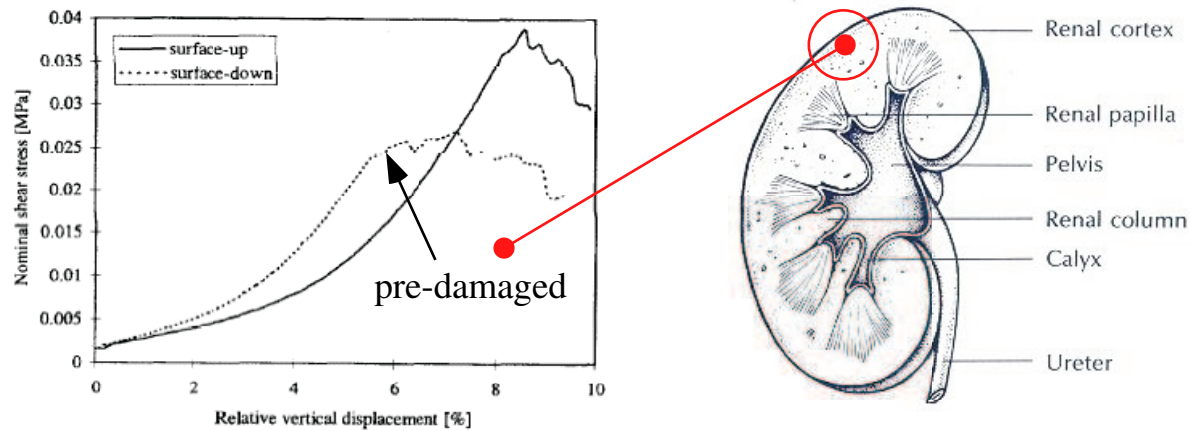
Figure 11.12.: Nominal shear stress vs. relative vertical displacement measured by [111] in a small punch test of slowly loaded cortex samples (loading rate 5 mm/min).

a linear visco-elastic model was employed in [111]. The instantaneous elastic modulus was found to be 4.8 MPa and reduces in the range of several seconds but the detailed long term response is not of interest for us.

Shear tests were performed in [111] by punching a cylinder into a slice of $8 - 10$mm thickness and 40mm in diameter. The punch tests were conducted on the undisturbed outer surface of the kidney (with the capsula being removed) and on the pre-damaged cut section of the cortex. The corresponding rupture stress is 0.035 MPa and 0.025 MPa, see Figure 11.12, whereby generally an increase of the loading rate leads to increase of rupture stress. Note that the pre-damaged specimen show somewhat like a "plastic" region before rupture. Moreover, the reported stress level required for shear rupture is lower than the average rupture stress for cortex material in compression, where in radial and circumferential direction 0.25 MPa and 0.18 MPa are reported.

Nasseri et al. report in [239] experiments on fresh kidneys of 3-6 month pigs with a weight of about 180g. The samples have also been taken from the renal cortex. Dynamic shear tests with small amplitude oscillatory motion (cycles) and shear rates between $0.01s^{-1}$ and $2.5s^{-1}$ were performed. The data are adapted to a non-linear differential material model originally developed for brain tissue and here applied for the kidney (describing a non-linear Maxwell material combined with Mooney-Rivlin elasticity). We do not apply this model because the viscous effects are in the range of several seconds but we refer to the measured data. Of particular interest for us is the observed rupture stress in shear ranging from 100 Pa up to 1000 Pa, see Figure 11.13. Again, an increase of rupture
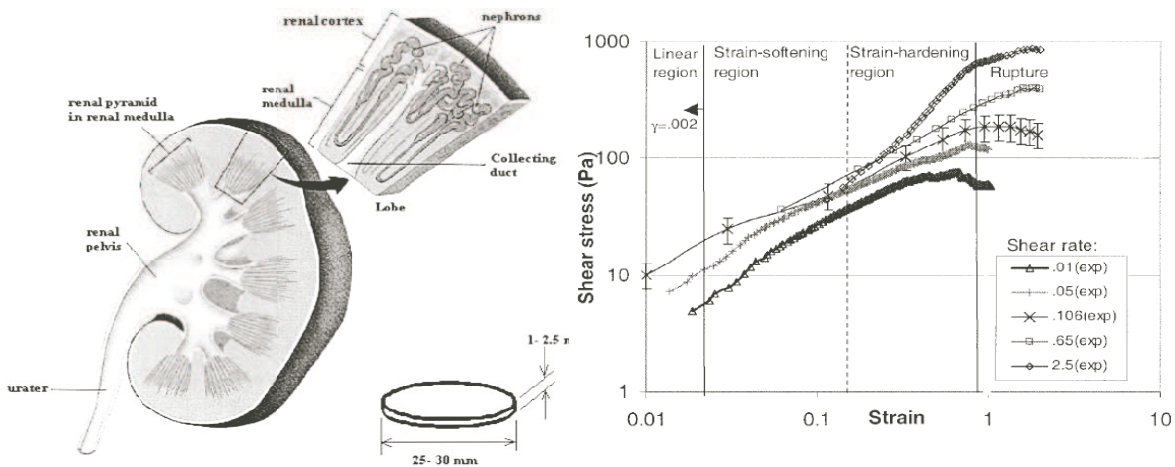
Figure 11.13.: Shear stress vs. strain curves for pig kidney under different shear rates according to [239].

stress with the increase of shear rate can be observed from the plot[4]. However, all values are significantly lower than the values reported in [111]. On the other hand, the rupture stress of renal tubulus (capillaries with $25 - 50\mu$m in diameter) was determined in [371, 372] to be in the range of 1.8-2 MPa. Moreover, investigations of our own group observed renal damage in ESWL when the peak negative pressure exceeds 1.5-3.5 MPa [92].

Note that the interior of the kidney is likely to be softer tissue than the renal cortex but detailed measurements are lacking. A diagram in [111] shows that sustained uniaxial compression of 0.015MPa yield to a straining of about 40-45 % in cortex and about 65-70 % in the (unspecified) medulla tissue. Correspondingly, the elastic modulus of medulla tissue would be $\approx 2/3$ of that of the cortex.

However, significant variations in the experimentally measured material data are observed. For example, slowly applied tension on specimen of the renal capsula results in rupture at $5\ldots14$ MPa, the results for cortex tissue varies from $0.45\ldots0.14$ MPa, [111]. Moreover, the difference of in vitro and in vivo measurements are pointed out in [120] and [201]. The latter work compares the speed of sound and the elastic modulus of several human organs, here especially the high deviation of in vitro measured data is remarkable.

Concluding from these and further sources (e.g. [209, 117, 272]) we assume the threshold

---

[4]Please note that according to [239] the data after onset of rupture have been removed from the plot.

for damaging stresses within the kidney to be in the range of $0.5\ldots1.5$MPa, where the cortex is less sensitive than the medulla and the (liquid filled) ureter is unlikely to be damaged at all. Similar, the cortex is stiffer than the medulla. The overall elastic modulus of the kidney is about 1MPa. Here we account already for the observed rate dependency, in rapid loading Young's modulus is up to 10 times higher than in slow loading [118, 239]. The poisson number will be determined by means of the sound velocity (see below), which was measured in [201] to be 1540m/s. The density of pig kidney tissue was found to be slightly above that of water [111, 201], for our calculations we set $\rho_0 = 1050$kg/m^3. Viscosity of the kidney is not expected to play a role here but we choose 0.005Pa.s; for comparison, water has a viscosity of 0.001Pa.s and blood has 0.007Pa.s [118].

11.4. Wave propagation

Physically, a shock wave is a type of propagating disturbance typically associated with a high stress intensity. Like a regular wave, a shock wave carries energy and can propagate through a medium (or, precisely, through a field). A shock wave is very intense and travels through the medium at a speed higher than a regular wave. However, depending on the specific medium, the energy of a shock wave may be dissipates relatively quickly with the distance. Thus, over time the shock wave can change from a nonlinear wave into a linear wave, degenerating into a conventional sound wave.
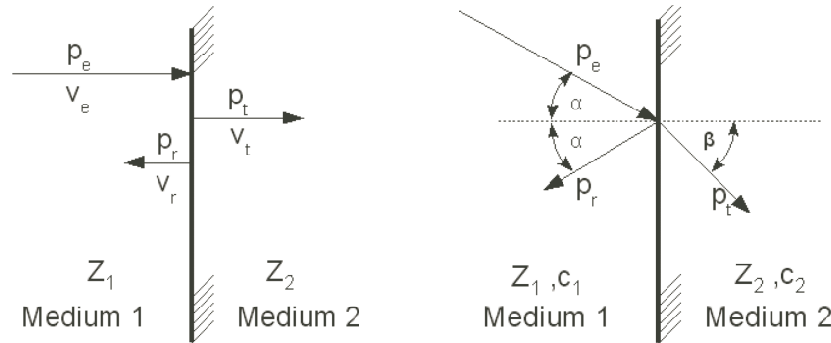

Figure 11.14.: Wave reflection and transmission, $\sin\alpha/c_1 = \sin\beta/c_2$.

The speed of sound is a fundamental material property and denoted here with c. In linearized theory it is related the compressive stiffness of the material κ (bulk modulus)

and the material density ρ_0 by

$$c = \sqrt{\frac{\kappa}{\rho_0}}. \tag{11.1}$$

The acoustic impedance describes how a material absorbs and reflects sound and is given by the ratio of sound pressure p to the absolute value of particle velocity v.

$$z = \frac{p}{|v|} = \rho_0 c. \tag{11.2}$$

Figure 11.14 illustrates the reflection and transmission of a sound wave at the interface of two media. The left figure illustrates a wave hitting the interface orthogonally. With indices e, r, t for entering, reflected and transmitted wave it holds

$$\begin{aligned} p_e &= p_r + p_t\,, \\ |v_e| &= |v_r| + |v_t|\,, \end{aligned}$$

and we define the reflection r by

$$r = \frac{p_r}{p_e} = \frac{z_2 - z_1}{z_1 + z_2}. \tag{11.3}$$

Clearly, it holds $-1 < r < 1$. The cases with $r < 0$ are called soft reflection (or soft transmission), whereas $r > 0$ describes hard reflection which is additionally characterized by phase inversion. Three limit cases are to distinguish.

- $r = 1$: total reflection, no phase inversion

- $r = 0$: no reflection

- $r = -1$: total reflection, phase inversion

Figure 11.14 on the right illustrates the reflection in an ideal fluid where $\sin\alpha/c_1 = \sin\beta/c_2$. In a real medium, and in particular in solids, the inclined interface causes not only reflection but transversal waves to arise. Consequently we observe a decay of magnitude and, after several reflections, a scattering of the travelling wave.

During ESWL the reflection at boundaries of the different organs and at tissue inhomogeneities as well as the interaction with cavitating bubbles influences the travelling pressure wave. This is illustrated in Figure 11.15 where two representative wave forms of lithotripsy shocks measured on the anterior surface of pig kidneys are shown (reported in [89]). The peak pressure recorded in the living tissue (right picture) is only 2/3 of the amplitude recorded in the experimental setup with dead kidney material. This effect may in part be caused by the methods of measurements but the wave tail in the
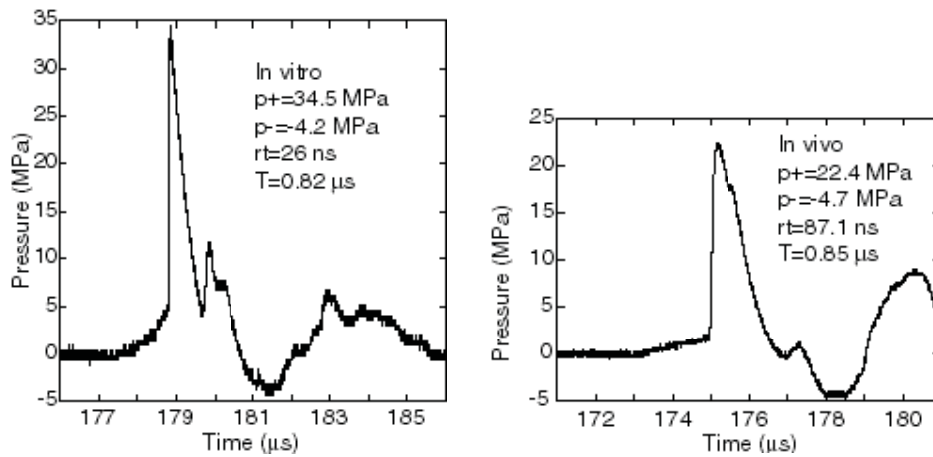
Figure 11.15.: Experimental measurements of ESWL pressure waves on the anterior kidney surface.

right picture clearly indicates reflection. However, a significant decay of amplitude with the wave propagation was not observed in [89]. That is in opposite to experiments of [113, 112], see Figure 11.16. Here the form of an ESWL impulse (measured as an electrical impulse) after penetrating 10 mm of calf kidney samples shows a visible smearing (left). The amplitude of the shock impulse after penetration of kidney samples of 5 mm, 10 mm, 25 mm and 40 mm thickness decays of about 60% (after 40 mm). It is interesting to note that numerical results for the interaction of pressure wave and energy release by cavitation of [321, 322] suggest that the exact details of the lithotripter waveform are not as important as the maximum bubble size (which, in turn, is related to maximal tension).

An analytical expression of an ESWL pressure impulse is given by [155]

$$p(t) = \begin{cases} 2p_{\max} \exp^{-\frac{t}{\tau_1}} \cos\left(\frac{t}{\tau_2} + \frac{\pi}{3}\right) & 0 < t < \frac{7\pi}{6}\tau_2 \\ 0 & \text{otherwise.} \end{cases} \qquad (11.4)$$

Time τ_1 characterizes the decay of the impulse whereas time τ_2 determines the duration. Following [11] we choose here $\tau_1 = 1.1$ μs, $\tau_2 = 1.96$ μs and, in this Section, $p_{\max} = 100$ MPa.

With the measured data of $c = 1540$m/s and $\rho_0 = 1050$ kg/m^3 (cf. Section 11.3) and equation (11.1) we can directly determine the bulk modulus of the kidney to be $\kappa = 2500$ MPa. Note that this value is slightly above the compressibility of water $\kappa_{H2O} = 2250$ MPa and above that of fat tissue $\kappa_{fat} = 1300$ MPa ($c = 952$m/s, $\rho_0 = $
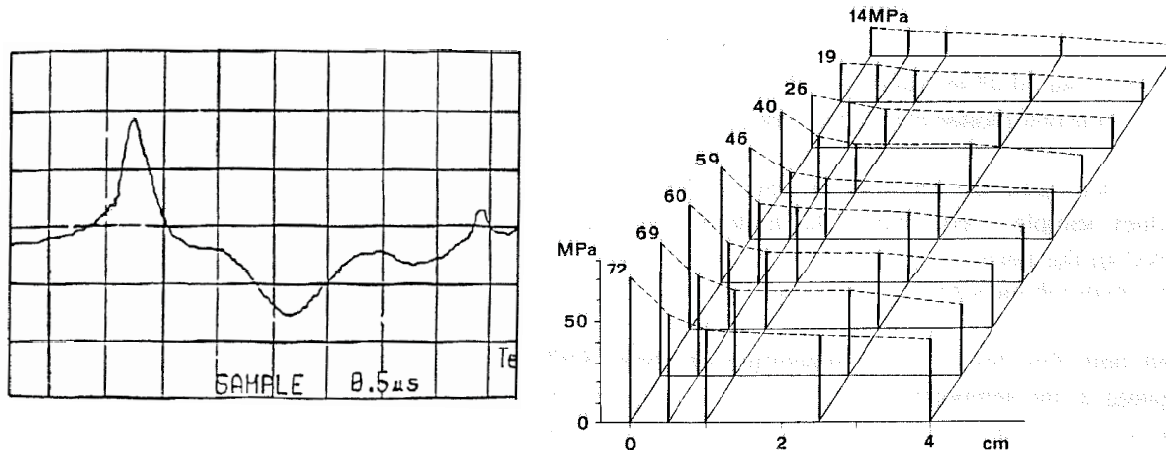
Figure 11.16.: Shock wave pulse recorded in [113] after penetration of a 10 mm thick calf kidney sample (grid spacing vertical 20mV, horizonal 0.5μs) and peak positive pressure measured in [112] after penetration of kidney samples of different thickness up to 40 mm.

1450 kg/m³, [182, 273]). Considerations of [319] which, with a similar approach, lead to a significant smaller bulk modulus are not plausible. Moreover, assuming for the kidney an average elastic modulus of $E = 1$ MPa our simple estimate leads to a Poisson number of $\nu = 0.49994$.

To evaluate our finite element analyzes we start studying the propagation of a pressure impulse in a homogeneous uniaxial model meshed with triangular plain strain elements, see Figure 11.17 and Figure 11.18a. The elastic sample is free in axial but constraint in lateral direction. To apply the loading impulse we use the linear relation between pressure and particle velocity (11.2) to prescribe the pressure field as a nodal velocity on the marked left boundary, Figure 11.18a,

$$v = \frac{p}{\varrho_0\, c} = \frac{100 \cdot 10^6 \frac{\text{N}}{\text{m}^2}}{1050 \frac{\text{kg}}{\text{m}^3} \cdot 1550 \frac{\text{m}}{\text{s}}} = 61.444 \cdot 10^{-3} \frac{\text{mm}}{\mu\text{s}}. \tag{11.5}$$

For a relatively coarse mesh of about 2500 linear triangles with typical element size $l_e = 1.5$ mm we observe after 10 mm wave travelling already a significant decay in amplitude and high oscillations following the initial impulse, Figure 11.17a. A finer mesh with $l_e = 0.5$ mm and quadratic shape functions reduces this effect but still shows high frequency oscillations, Figure 11.17b.

Therefore, we introduced an artificial viscosity in our model. Artificial (bulk) viscosity is thought to damp oscillations in the highest element frequency, a damping which is
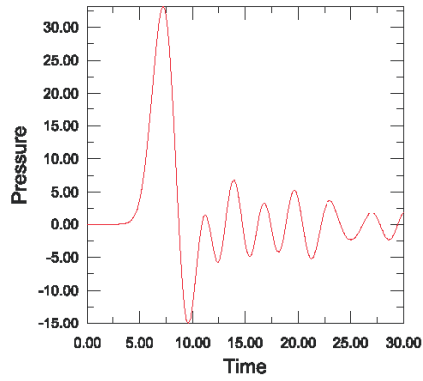
(a) linear elements of size 1.5 mm after 10 mm propagation
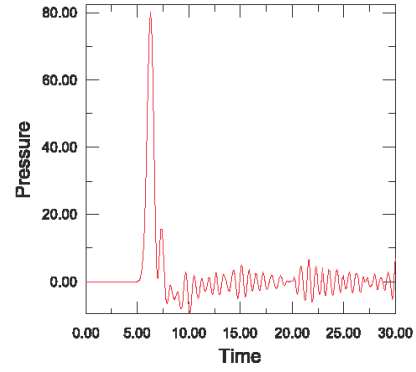
(b) quadratic elements of size 0.5 mm after 10 mm propagation
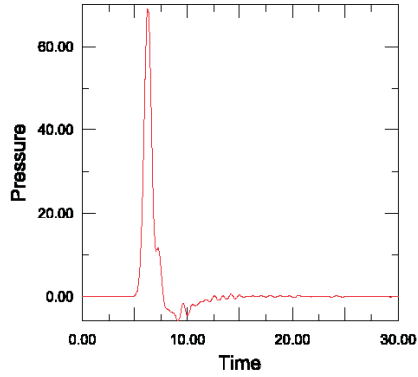
(c) quadratic elements of size 0.5 mm with viscosity $\alpha = 0.06$ after 10 mm propagation
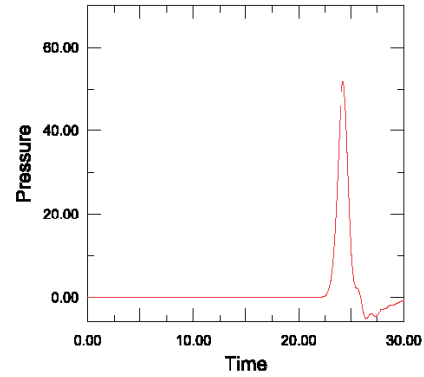
(d) quadratic elements of size 0.5 mm with viscosity $\alpha = 0.06$ after 40 mm propagation
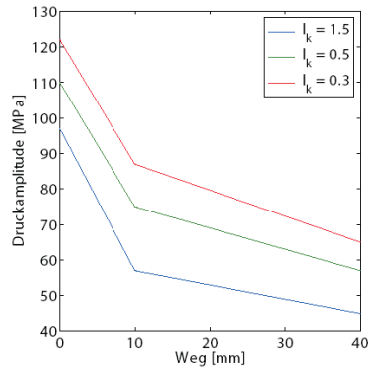
(e) decay of pressure maxima for different mesh size with viscosity $\alpha = 0.06$ after 10 mm propagation
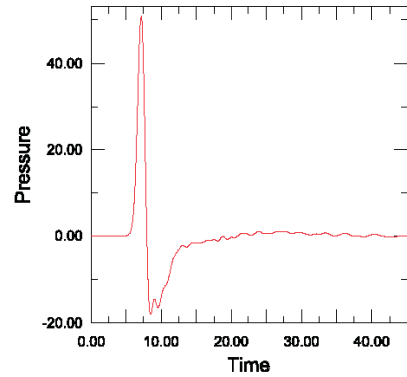
(f) kidney mesh with typical size of 0.5 mm $\alpha = 0.06$ after 10 mm propagation

Figure 11.17.: Pressure impulse after propagation into homogeneous elastic tissue.

236

sometimes referred to as truncation frequency damping. It generates a viscosity pressure that is linear in the volumetric strain rate $\dot{\vartheta}$,

$$p_{\mathrm{damp}} = \alpha_d \rho c l_e \dot{\vartheta} \tag{11.6}$$

where is α a damping coefficient ρ is the current material density, l_e is an element characteristic length, and c is the current (dilatational) wave speed. For acoustic elements, the bulk viscosity pressure can also be obtained from the above equation by using relation (11.2) with the result

$$p_{\mathrm{damp}} = \alpha \frac{l_e \dot{p}}{c} \tag{11.7}$$

where $\dot{p}$ and c are the pressure rate and the speed of sound in the fluid, respectively. Note that we only apply a linear bulk viscosity but not forms of artificial viscosity which are designed to smear a shock front across several elements and to prevent elements from collapsing under extremely high velocity gradients. Figure 11.17c and d show the pressure after 10 mm and 40 mm propagation for $\alpha = 0.06$; the high frequency oscillations but also the pressure amplitudes are damped. Therefore we studied the proper choice of parameter α carefully, with best results for $\alpha = 0.06$, cf. [273]. Note that pressure propagation still requires a fine discretization. In Figure 11.17e the maximum amplitude after 10 mm travelling is plotted for different mesh sizes. Clearly, a further mesh refinement improves the results but for a two and three-dimensional kidney model such refinement is limited by computational capacity.

In Figure 11.17f the propagated pressure impulse is plotted after 10 mm propagation into the two-dimensional kidney model. We employ the model of Figure 11.10 and distribute the load as indicated in Figure 11.20 like a Gaussian distribution; this correlates with measured data of [89]. Note that the mesh in Figure 11.20 is then ultimately refined to a typical element size of $l_e = 0.5$ mm, the small interior (green, braun red) elements are subdivided into 16 elements, the larger elements into 32.

Figure 11.18 illustrates soft and hard transitions at an orthogonal material interfaces with different compressibility. To this end we distinguish three regions of material in our simplified model of Figure 11.18a. We set for the first and second material $E_1 = E_2 = E$ and vary the third, all other data remain constant as above. Soft reflection is realized with $r = -\frac{1}{2}$, it follows by (11.1-11.3): $E_3 = \frac{1}{9}E$; hard reflection is realized with $r = \frac{1}{2}$: $E_3 = 9E$. Figure 11.18b and d show the initial (6μs) and reflected (12.5μs) pressure at the marked point 2. Clearly the amplitude decays with reflection and plot c also shows phase reflection, further maxima follow from additional reflections. Figure 11.18c and e illustrate the transitive waves at material point 3.

At last we use the full test model of Figure 11.18a to vary the material parameter for the different regions of the kidney to better map its different elastic properties. The
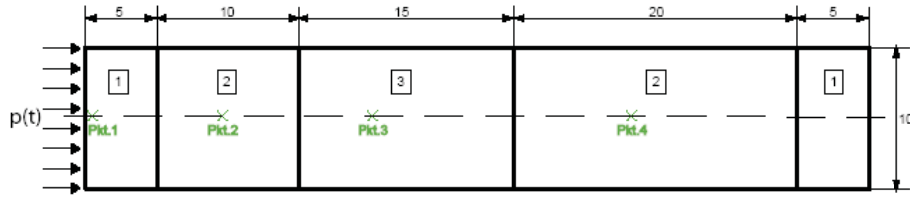
(a) Model for simple uniaxial tests with different material regions
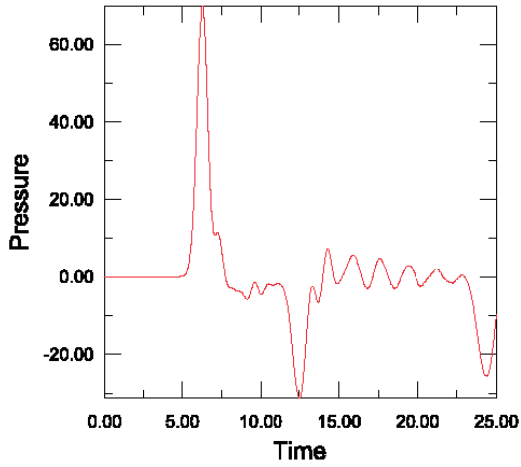
(b) pressure at 2 after soft transition
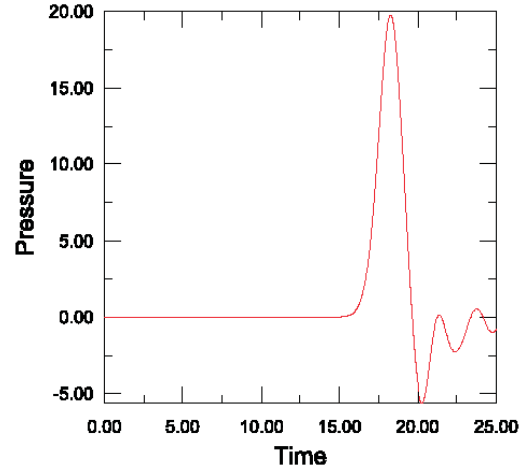
(c) pressure at 3 after soft transition
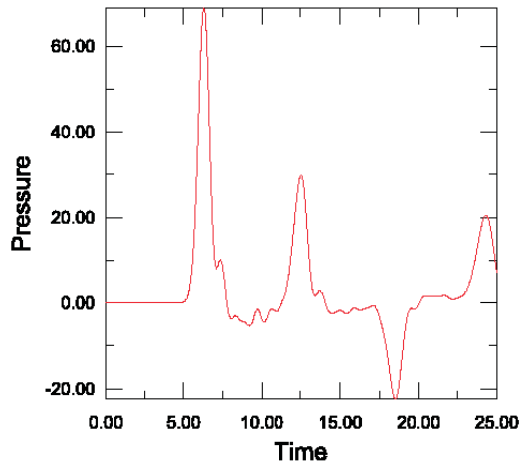
(d) pressure at 2 after hard transition
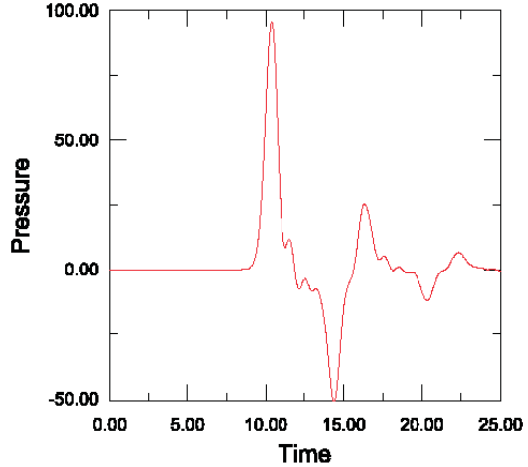
(e) pressure at 3 after hard transition

Figure 11.18.: Reflection and transmission of pressure waves at interface between material 2 and 3.
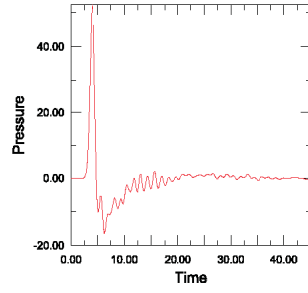
(a) pressure after 5 mm
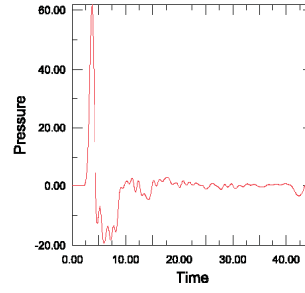
(b) pressure after 5 mm
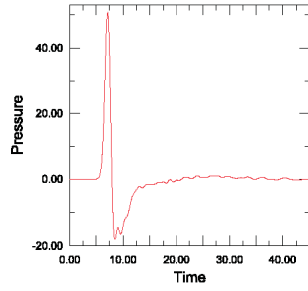
(c) pressure after 10 mm
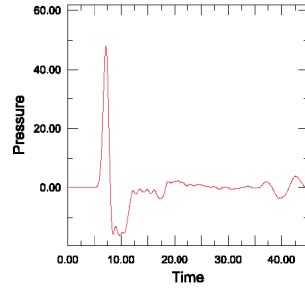
(d) pressure after 10 mm
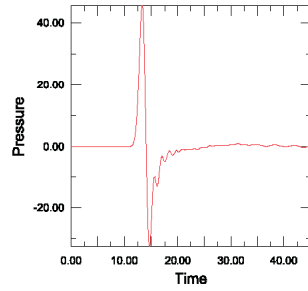
(e) pressure after 20 mm
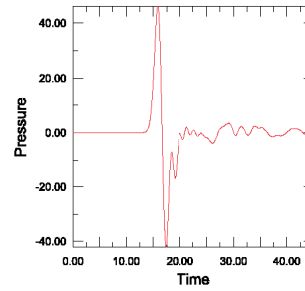
(f) pressure after 20 mm
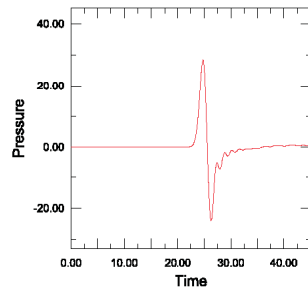
(g) pressure after 40 mm
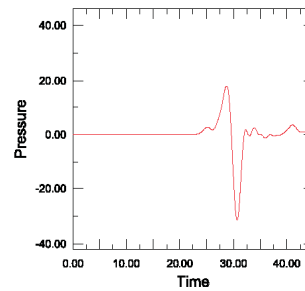
(h) pressure after 40 mm

Figure 11.19.: Pressure waves propagating into the kidney modeled as homogeneous material (left) and with different elastic parameters (right).
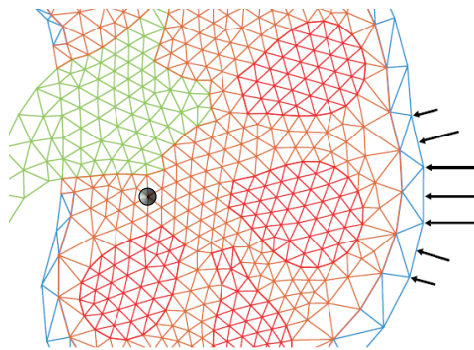
Figure 11.20.: Loading of the two-dimensional kidney model, focus (F2, "stone") marked with •.

volumes of the materials in the test model correspond to the volume fractions of cortex (1), renal medulla (2) and pyramidal (3) tissue a ESWL impulse will pass. Assuming sound speed as a lower limit for the pressure waves propagation speed a time of at most $c/l_{\mathrm{model}} = 35.5\mu$s is needed to pass the model. Knowing that the cortex is stiffer than the average kidney whereas the pyramids are softer and summarizing different variations we set: $E_1 = 1.2$ MPa, $E_2 = 1.0$ MPa, $E_3 = 0.55$ MPa to get a realistic wave speed within the whole kidney, see also [273].

11.5. Material model

At first we decided to study the effect of shock waves on the cellular level. In opposite to the whole kidneys properties, many information on cells are available. The mechanical properties of (living) cells have been studied with various techniques including atomic force microscope [147, 150, 211] or micropipet aspiration [134, 135]. Cells of the body are not only able to withstand high (cyclic) stresses (with peak magnitudes exceeding 10 MPa [135]) but respond to mechanical stresses as signals to regulate their metabolic activity and gene expression. We are not able to simulate signal response or transmission but just looked on the mechanical stress state. To this end, a two-dimensional, simplified material model of an array of nine cells was build using size and material data found in the above cited references and the response to a shock wave impulse was studied. Although the cell is a composite system, made of a membrane surrounding a complex fluid it is modeled here as a solid with elastic material properties. Because of the very simplified cell geometry a qualitative assessment of the results is not meaningful. The main result of these computation is that we clearly observe a high hydrostatic pressure

within the cell and a high shearing of the cell walls, see Figure 11.21.
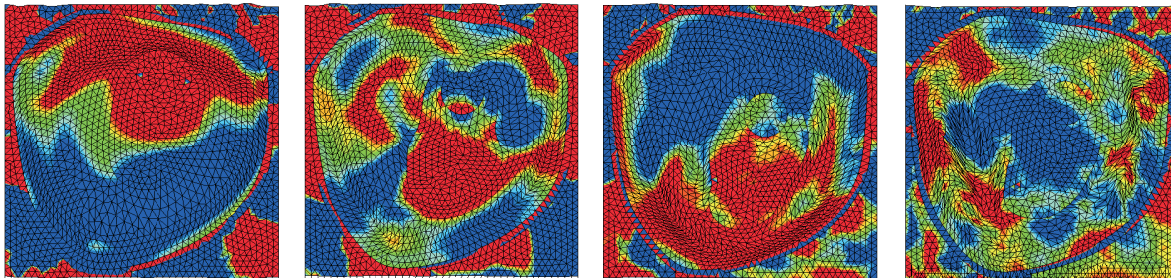
Figure 11.21.: Pressure (blue) and tension (red) in a cell 5, 10, 15 and $30\mu s$ after an ESWL impulse hit the model from above.

However, tissue is not just a macroscopic generalization of the cells microscopic properties. Clearly, to model a whole organ a macroscopic constitutive relation needs to be derived modelling the tissue as a kind of homogenized material. Because an approach going from the microscopic to the macroscopic level is not yet realistic (see [352] for the state of the art) such a constitutive relation is empirical. Therefore, we employed for the kidney a two-parametric general Ogden material, cf. Chapter 3, where the coefficients $\alpha_1 = 5$, $\alpha_2 = -5$ and $\mu_1 = \mu/15$, $\mu_2 = -\mu/3$ are adapted to experiments with brain tissue [221]. The sum $(\alpha_1\mu_1 + \alpha_2\mu_2)/2$ is chosen in a way, that it corresponds to the elastic shear modulus measured for the kidney and varied for the different regions. Furthermore, the model is extended to the compressible range using the ansatz $W^{\text{vol}} = \kappa(\ln J)^2/2$, see also Figure 3.3 of Chapter 3.

The elasticity of the material is bounded, above a certain bearable stress some kind of damage will occur. Typical damage of shock waves is illustrated in Figure 11.22 for a thin cellophane foil subjected to an ESWL impulse. This experiment, conducted by Lokhandwalla [197] with the Caltech electro-hydraulic lithotripter illustrates how the tissue is damaged by shearing (resulting in tearing of the film) as well as by hydrostatic tension (resulting in holes).

The medical literature shows that in a living kidney scarring occurs with damaged tissue [240]. The way that scarring occurs can proceed to progressive renal damage and correlates closely with a fall in renal function and the onset of hypertension. The reason for these effects are the special way a kidney works - which is, of course, more than a pure mechanical response on straining or shearing. One typical feature, cf. [284], is the accumulation of extracellular matrix in the glomerulus (the essential parts of the nephrons) and eventual collapse of capillary walls resulting in a loss of glomerular function. Scarring in and around the nephrons is characterized by tubular atrophy and an
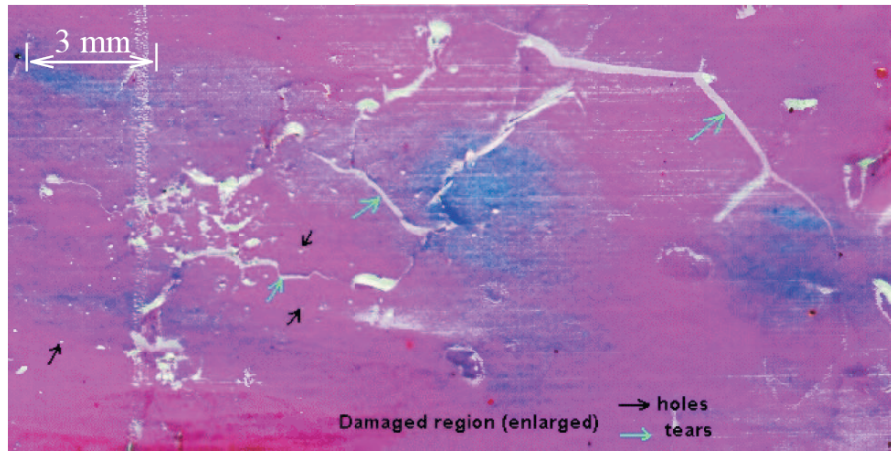
Figure 11.22.: Cellophane film after 100 shocks at 1Hz: holes and tears [197].

accumulation of interstitial matrix. As the interstitial space continues to enlarge due to the increase in matrix material, more glomeruli or tubules and micro-vessels are working inaccurately causing further tissue injury. This results in the release of more enzymes which stimulate more scar formation and an additional loss of functional tissue. Thus, a vicious cycle may be triggered that eventually ends in extensive kidney damage. (Note that this is a very different process than what happens in normal wound healing where there is controlled degradation of any extra matrix material.)

Translated in mechanical terms this means that the elasticity of the tissue is not necessarily lost but an impairment of renal function occurs. This effect, together with the measured stress strain curve of [111] motivated us to model the kidney damage as a kind of plasticity, i.e., the material undergoes a non-reversible deformation. The stresses are bounded by an upper limit but the elastic properties are unaltered.

Let the equilibrium response of the material be characterized by a free-energy density per unit undeformed volume of the form

$$A = A(\boldsymbol{F}, \boldsymbol{F}^p, \varepsilon^i, \vartheta^i) \tag{11.8}$$

where $\boldsymbol{F}$ is the deformation gradient, $\boldsymbol{F}^p$ is the plastic part and $\boldsymbol{F}^e = \boldsymbol{F}\boldsymbol{F}^{p-1}$ the elastic part of the deformation. The plastic deformation rate is assumed to obey the flow rule

$$\dot{\boldsymbol{F}}^p \boldsymbol{F}^{p-1} = \dot{\varepsilon}^i \boldsymbol{M} + \dot{\vartheta}^i \boldsymbol{N} \tag{11.9}$$

where ε^i and ϑ^i are scalar variables accounting for *irreversible* (plastic) deformation. Their rates are subjected to the constraints

$$\dot{\varepsilon}^i \geq 0 \quad \text{and} \quad \dot{\vartheta}^i \geq 0. \tag{11.10}$$

The tensors $\boldsymbol{M}$ and $\boldsymbol{N}$ set the direction of the deviatoric (unimodular) and volumetric plastic deformation rates, respectively. Tensor $\boldsymbol{M}$ is assumed to be trace-free and normalized but otherwise unknown whereas tensor $\boldsymbol{N}$ is fixed,

$$|\boldsymbol{M}|^2 = \frac{3}{2} \ , \quad \text{tr}(\boldsymbol{M}) = 0 \quad \text{and} \quad \boldsymbol{N} = \frac{1}{3}\boldsymbol{I}. \tag{11.11}$$

In that way tensor $\boldsymbol{N}$ corresponds to volumetric expansion only, in compression the elastic deformation will not be bounded, see Figure 11.24a.
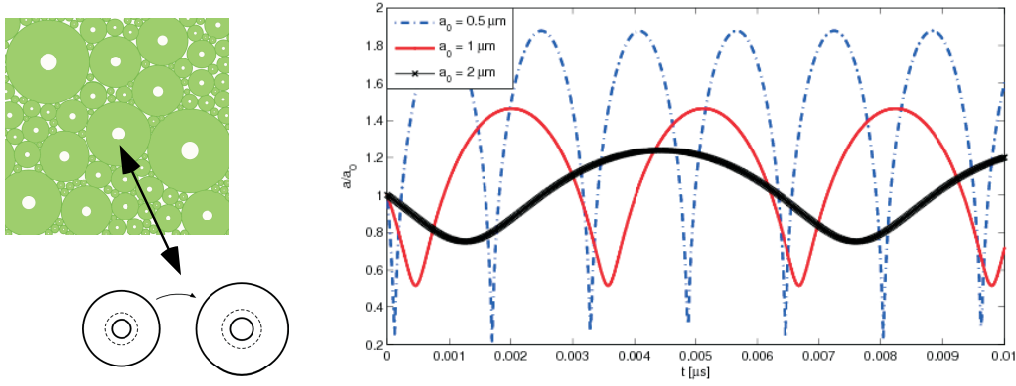
Figure 11.23.: Model of tissue with bubbles of different sizes (left) and bubble oscillations (radius vs. time) after ESWL impulse (right).

For the cavitation of bubbles we apply the spherical shell model of Chapter 7.1, see Figure 11.23. The oscillation of (empty) bubbles modeled in a non-linear elastic material and described in Chapter 7.3.2 are similar to the bubble oscillations described by Rayleigh-Plesset equations (Figure 11.6), although the underlying model is different. For interest of us is here the maximum radius of the growing bubbles - which is likely to overstrain the surrounding vessels and capillaries.

In order to formulate a complete set of constitutive relations, the free-energy density (11.8) and appropriate rate equations for the internal variables ε^i and ϑ^i must be specified. At first we link the mechanism of bubble expansion causing irreversible damage to the macroscopic material parameter. To this end we consider a representative undeformed material of volume V_0 and deformed volume V and determine the local volume fraction of bubbles in the deformed configuration as

$$f = N_V \frac{V_0}{V} \frac{4\pi \bar{a}^3}{3}, \tag{11.12}$$

where $\bar{a}$ is current average bubble radius and N_V is the referential bubble density, i. e., the number of bubbles per unit volume. The volumes V_0 and V are related through $V = JV_0$ where

$$J \equiv \det \boldsymbol{F} = \det(\boldsymbol{F}^e \boldsymbol{F}^p) = \det \boldsymbol{F}^e \det \boldsymbol{F}^p \equiv J^e J^p \qquad (11.13)$$

is the local Jacobian of the deformation and J^e and J^p are the corresponding elastic and plastic components. Using these relations we have

$$J^p = V(J^e V_0)^{-1} = (1 - f_0)/(1 - f). \qquad (11.14)$$

This relation allows f to be computed from J^p and, using (11.12), equation (11.14) may be recast in terms of the average bubble radius $\bar{a}$, with the result

$$J^p = 1 - f_0 + \frac{V}{J^e V_0} f = 1 - N_V \frac{4\pi \bar{a}_0^3}{3} + N_V \frac{4\pi \bar{a}^3}{3 J^e}. \qquad (11.15)$$

It is worth to note that $J^e \cong 1$ for the (almost) incompressible tissue material, and (11.15) simplifies to

$$J^p = 1 + \frac{4\pi}{3} N_V (\bar{a}^3 - \bar{a}_0^3) \quad \text{and} \quad \bar{a} = \left[\frac{3}{4\pi} \frac{1}{N_V} (J^p - 1) + \bar{a}_0^3 \right]^{1/3} \qquad (11.16)$$

which allows $\bar{a}$ to be computed from J^p. Moreover, the variable ϑ^i is a measure of the accumulated *irreversible volumetric deformation* and coincides (up to a constant) with $\ln J^p$.

Without loss of generality, the elastic strain-energy density can be expressed in terms of the logarithmic elastic strain $\boldsymbol{\epsilon}^e = \frac{1}{2} \ln(\boldsymbol{C}^e)$, i.e., $W^e = W^e(\boldsymbol{C}^e, T) = W^e(\boldsymbol{\epsilon}^e, T)$, cf. Chapter 3. We denote by $\boldsymbol{\sigma}$ the stress conjugate to $\boldsymbol{\epsilon}^e$, namely,

$$\boldsymbol{\sigma} = \frac{\partial W^e}{\partial \boldsymbol{\epsilon}^e}(\boldsymbol{\epsilon}^e). \qquad (11.17)$$

The first Piola-Kirchhoff stress tensor $\boldsymbol{P}$ follows from Coleman's relations as $\boldsymbol{P} = \partial A/\partial \boldsymbol{F}$ and can be evaluated to result in

$$\boldsymbol{P} = \frac{\partial W^e}{\partial \boldsymbol{F}} = \frac{\partial W^e}{\partial \boldsymbol{\epsilon}^e} \frac{\partial \boldsymbol{\epsilon}^e}{\partial \boldsymbol{C}} \frac{\partial \boldsymbol{C}}{\partial \boldsymbol{F}}. \qquad (11.18)$$

By application of (11.18) follows

$$p = \kappa \left(\ln J^e \right), \qquad (11.19)$$

i. e., the pressure in the tissue is linear in the elastic logarithmic volumetric strain. Additional stress contributions may result from viscosity.

(a) stress-strain curve   (b) pitting   (c) pressure   (d) stress vs. elongation
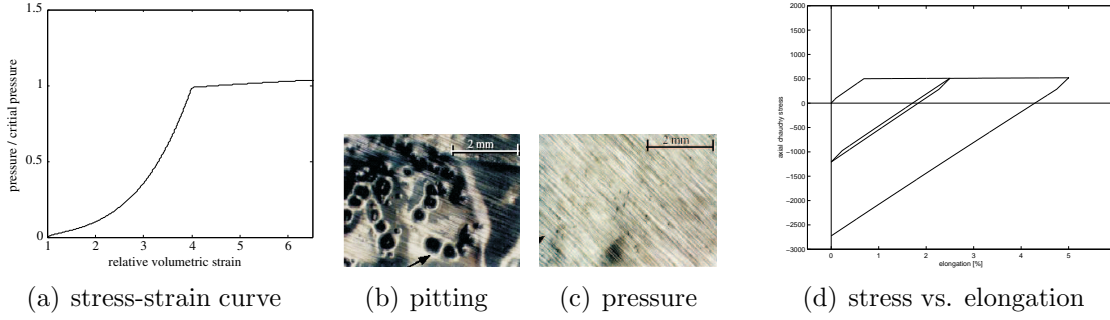
Figure 11.24.: effective stress-strain curve for volumetric expansion, effect of cavitation in tension (pitting) and pressure (no effect) experimentally studied in [197], and axial Cauchy stresses computed in two cycles of a uniaxial strain test

A plastic energy function can be formulated by an additive decomposition into volumetric and volume preserving components. The latter is solely a function of the effective irrevesible deviatoric strain, ε^i, and is here of the form

$$W^p(\varepsilon^i) = \frac{\sigma_0 \varepsilon_0^i}{n+1} \left(\left(1 + \frac{\varepsilon^i}{\varepsilon_0^i} \right)^{n+1} - 1 \right), \tag{11.20}$$

where σ_0 is the initial critical stress, and ε_0^i is a reference parameter. Depending on the choice of the exponent, function (11.20) may account for hardening of the critical stress, $0 < n \leq 1$, as well as for its softening, $-1 \leq n < 0$.

The volumetric part of the dissipated energy function is attributed directly to the bubble growth. In the dilute limit, the total energy dissipated by expanding bubbles is the first moment of the energy dissipated by each individual bubble. Following the strategy outlined in Chapter 7, considering an average bubble radius $\bar{a}$ and inserting function (11.20) lead to

$$W^p(\varepsilon^i, \vartheta^i) = W^p(\varepsilon^i) +$$
$$\frac{\sigma_0 \varepsilon_0^i}{(n+1)} \frac{N_V 4\pi \bar{a}^3}{3} \left(\frac{2}{3\varepsilon_0^i} \right)^{n+1} \int_1^{1/f} \left\{ \ln \frac{x}{x - 1 + [1 + (e^{\vartheta^i} - 1)/f_0]^{-1}} \right\}^{n+1} dx. \tag{11.21}$$

Aside of conventional newtonian viscosity two more types of rate effects may be considered: rate sensitivity in the irreverible deformations and micro-inertia due to rapidly expanding bubbles. To ensure a variational structure in the presence of rate sensitivity a dual kinetic potential $\psi^*(\dot{\varepsilon}^i, \dot{\vartheta}^i)$ needs be postulated such that the thermodynamic forces

conjugate to $\dot{\varepsilon}^i$ and $\dot{\vartheta}^i$ can be derived from ψ^*, cf. Chapter 7. Micro-inertia as a dissipative energy term renders the equations of motion for the growth of the bubbles of second order in time. Neglecting the interaction of bubbles, the total micro-inertia attendant to the growth of the bubble ensemble is the weighted sum of the kinetic energies due to the expansion of each individual bubble. For spherical bubbles in an incompressible material this micro-kinetic energy and can be computed readily in terms of the averaged bubble radius $\bar{a}$, with the result

$$L(\bar{a}, \dot{\bar{a}}) = 2\pi N_V \varrho_0 \bar{a}^3 \dot{\bar{a}}^2, \tag{11.22}$$

where ϱ_0 is the mass density per unit volume. In order to formulate updates possessing a variational structure, a change of variables in function (11.22) is required to result in a system with quadratic inertia and constant mass, see equations (7.174) and (7.177-7.185) of Chapter7.

For implementation of the material model in our finite-element code we employ a time-incremental procedure as described in Chapter 6 and Chapter 7. The internal state variables, ε_{n+1}^i and ϑ_{n+1}^i, are updated in every time step $t_{n+1} - t_n$ by recourse to an incremental objective function $f_n = f_n(\boldsymbol{F}_{n+1}, \varepsilon_{n+1}^i, \vartheta_{n+1}^i, \boldsymbol{M}, \boldsymbol{N})$. This function includes the free energy of the material, as well as the dissipated energy, the micro-kinetic energy and the dual kinetic potential. These contributions, subject to the constraints (11.11), compete in energetic terms, and the optimal internal process is that one which minimizes the function f_n. This may be expressed in variational form as

$$W_n(\boldsymbol{F}_{n+1}) = \min_{\varepsilon_{n+1}^i, \vartheta_{n+1}^i, \boldsymbol{M}, \boldsymbol{N}} f_n. \tag{11.23}$$

11.6. Numerical results

The results of three-dimensional finite element analyzes are summarized in Figure 11.25 and Figure 11.26. In all computations the kidney is modeled without a stone. This approach is backed by experimental studies showing that injuries are caused by ESWL treatment and hardly influenced by stone fragmentation [90].

For numerical computation we distinguish regions of functional (sensitive) kidney tissue and non-functional tissue (renal pelvis and ureter). The latter part is modeled as a neo-hookean material with an elastic shear modulus of 0.5334 MPa. The sensitive structures, i.e., the cortex, the renal pyramids and the surrounding medulla tissue are modeled with the presented material model and the elastic data adapted in Section 11.4. Solely for the cortex we set $\nu = 0.4999$ to match the compressibility of the surrounding body tissue.
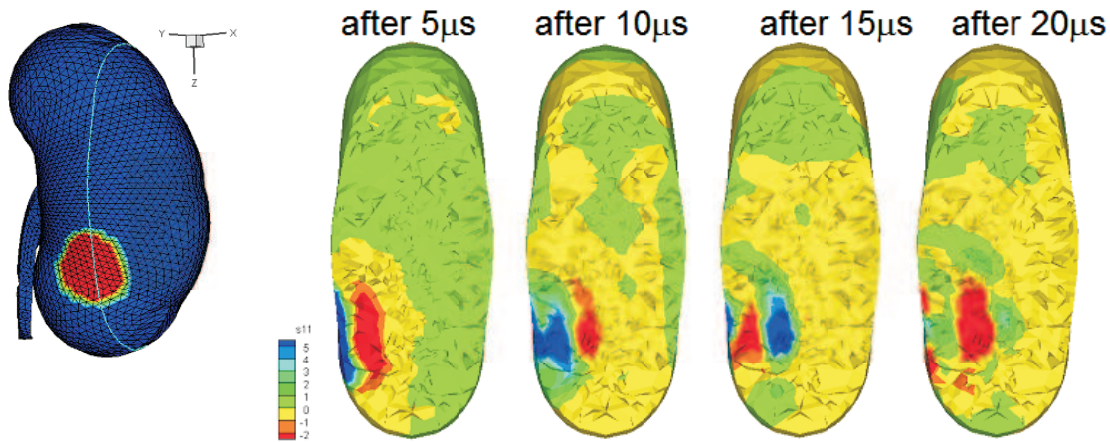
Figure 11.25.: ESWL impulse travelling through the kidney (blue: pressure, red: tension).

In terms of initial bulk κ and shear modulus μ that means for the cortex $\kappa = 2$ GPa, $\mu = 0.8$ MPa, the medulla tissue $\kappa = 2.78$ GPa, $\mu = 0.6667$ MPa and for the pyramids $\kappa = 1.5$ GPa, $\mu = 0.3667$ MPa. Note that in contrast to former results [368, 364] the kidney is surrounded here by an acoustic material with $K = 2$ GPa.

The pressure impulse is applied on the anterior kidney surface as a nodal velocity. The impulse is focused in the meridional section at $x = 0$, $y = 0$, $z = 10$mm. The spatial distribution of the impulse is centered at the anterior surface with $x = 1$mm, $y = 0$, $z = 17$mm. In the loading area the velocity is distributed in such a way that $v = v(t)$ in the center decaying to $v = 0.5v(t)$ at radius $r = 5$mm and zero at $r \geq 11$mm away from the center point. The model is not supported. It is subjected to one impulse of form (11.4) with $p_{\max} = 50$MPa and then released. For time integration we apply an explicit Newmark scheme with adaptive time step size over a period of 100μs.

The irreversible deformation starts at a certain critical stress σ_0. For the sensitive parts of the kidney we choose here $\sigma_0 = 1$MPa in the cortex, $\sigma_0 = 80$Pa in the medulla tissue and $\sigma_0 = 2.5$Pa within the renal pyramids. Exponent n of equation 11.21 is set 0.1, density $\rho = 1050$kg/m^3 and viscosity $\eta = 0.005$Pa s.

After all we know the applied critical stress can considered to be a lower bound of the materials rupture stress. Nonetheless, we choose the data in that way to see a significant effect of one shock. In practise, there are several hundred shocks applied and the damage within the kidney accumulates. However, with today's available computer we are not yet able to compute the time period of several shocks to simulate the process of ESWL.
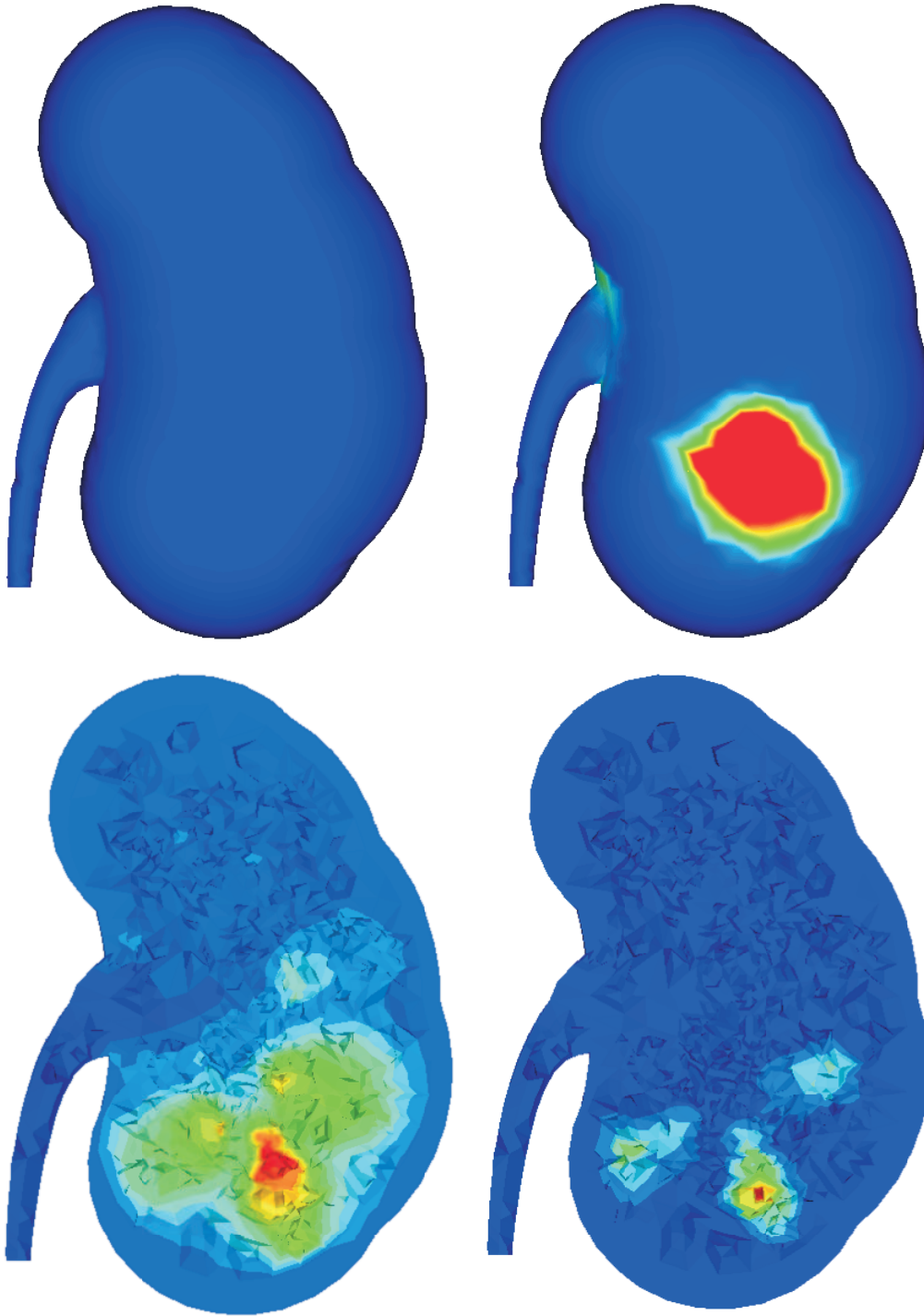
Figure 11.26.: The effective irreversible deformation computed in the kidney (blue: zero, red: maximum) indicates deviatoric straining (ε^i, left) and irreversible volumetric expansion (ϑ^i, right); the upper pictures show the exterior view, the lower pictures show the meridional section of the kidney.

Although a quantitative assessment of the results is difficult to give, we observe a good agreement of localized damaged with medical and experimental results. Common shock wave induced lesions are kidney enlargement, bruising and hemorrhage in the pre-focal area, see [92] and the photograph of ESWL subjected pig kidneys in Figure 11.7. The location of injuries correlates to the area of peak negative pressure and greatest cavitation. This effect is well captured by our kidney model. Moreover, shear induced damage is observed in our model only within the kidney and not in the renal cortex, see Figure 11.26.

For completeness we computed the three-dimensional kidney model with a purely elastic material model. Figure 11.25 shows the stress propagating into the kidney with magnitudes of $-2\ldots5$ MPa. This corresponds very well to observations of [92] where a peak negative pressure of $1.5 - 3.5$ MPa is considered to be the threshold for damage caused by ESWL.

249

Part III.

Appendix

Appendix 1:

Notation

Here we summarize the basic forms of vectors and tensors employed in the text. For more details we refer to literature on vector and tensor algebra, e.g., [54, 32, 46, 57, 295]. Being aware that we loose some of the theories beauty and generality we restrict ourselves in this work to the use of cartesian-coordinate systems with orthonormal base vectors $\boldsymbol{e}_i$. The range of lowercase latin indices is $1, 2, 3$. Moreover we adopt Einstein's summation convention according to which any expression in which an index appears repeatedly is understood to be a sum over the range of this index.

1.1. Scalars

Formally scalars are zeroth-order tensors. Scalars are written here mainly in lowercase greek letters, $\alpha, \beta, ...$ Exemtions are made for some physical quantities, e.g., the temperature is denoted by T.

1.2. Vectors

First-order tensors are vectors. Vectors are denoted here by boldface lowercase letters, $\boldsymbol{a}, \boldsymbol{b}, ...$ and have both direction and length. The corresponding vector spaces are denoted by cursive uppercase letters, i.e., $\boldsymbol{a} \in V$, $\boldsymbol{b} \in W$. In components a vector is written as

$$\boldsymbol{a} = a_i \boldsymbol{e}_i = a_1 \boldsymbol{e}_1 + a_2 \boldsymbol{e}_2 + a_3 \boldsymbol{e}_3 \equiv \begin{bmatrix} a_1 & a_2 & a_3 \end{bmatrix}^T . \tag{1.1}$$

Vector algebra is well known and may be looked up in many standard mathematical textbooks (e.g. [57, 299]). We focus here only on the properties of the different products of vectors.

The **scalar product** (or dot product or inner product) of two vectors $\boldsymbol{a}$ and $\boldsymbol{b}$ is denoted by $\boldsymbol{a} \cdot \boldsymbol{b}$ or equivalently $\langle \boldsymbol{a}, \boldsymbol{b} \rangle$ and gives a scalar quantity with magnitude $a_i b_i = a_1 b_1 + a_2 b_2 + a_3 b_3$. Properties of the scalar product are (here $\boldsymbol{o}$ is the zero vector):

$$\boldsymbol{a} \cdot \boldsymbol{b} = \boldsymbol{b} \cdot \boldsymbol{a} \tag{1.2}$$

$$\boldsymbol{a} \cdot \boldsymbol{o} = 0 \tag{1.3}$$

$$\boldsymbol{a} \cdot \boldsymbol{a} > 0 \quad \Leftrightarrow \quad \boldsymbol{a} \neq \boldsymbol{o} \tag{1.4}$$

$$\boldsymbol{a} \cdot \boldsymbol{a} = 0 \quad \Leftrightarrow \quad \boldsymbol{a} = \boldsymbol{o} \tag{1.5}$$

$$\boldsymbol{a} \cdot \boldsymbol{b} = 0 \quad \Leftrightarrow \quad \boldsymbol{a} \text{ is orthogonal to } \boldsymbol{b}. \tag{1.6}$$

The **length** of a vector is

$$|\boldsymbol{a}| = \left(\boldsymbol{a} \cdot \boldsymbol{a} \right)^{\frac{1}{2}}. \tag{1.7}$$

A unit vector has length 1, i.e., for the bases vectors of our cartesian coordinates hold

$$\boldsymbol{e}_i \cdot \boldsymbol{e}_j = \delta_{ij}, \tag{1.8}$$

where the **Kronecker delta** δ_{ij} equals 1 if $i = j$ and is zeros otherwise. The length of a vector works as a vector norm. In general, a **norm** $||\boldsymbol{a}||$ is a non-negative real number with properties

$$\|\boldsymbol{a}\| = 0 \quad \Leftrightarrow \quad \boldsymbol{a} = \boldsymbol{o} \tag{1.9}$$

$$\|\boldsymbol{a}\| < \infty. \tag{1.10}$$

The **vector product** or (cross product) of two vectors $\boldsymbol{a}$ and $\boldsymbol{b}$ is written as $\boldsymbol{a} \times \boldsymbol{b}$ and produces a new vector orthogonal to the plane spanned by $\boldsymbol{a}$ and $\boldsymbol{b}$ with components

$$(\boldsymbol{a} \times \boldsymbol{b})_i = \epsilon_{ijk} a_j b_k, \tag{1.11}$$

where e_{ijk} is the permutation symbol[5]. Another way to compute the cross product easily is given by

$$\boldsymbol{a} \times \boldsymbol{b} = \det \begin{pmatrix} \boldsymbol{e}_1 & \boldsymbol{e}_2 & \boldsymbol{e}_3 \\ a_1 & a_2 & a_3 \\ b_1 & b_2 & b_3 \end{pmatrix}. \tag{1.12}$$

Note that the magnitude of the resulting vector measures the area spanned by the vectors $\boldsymbol{a}$ and $\boldsymbol{b}$, i.e., $|\boldsymbol{a} \times \boldsymbol{b}| = \text{span}(\boldsymbol{a}, \boldsymbol{b})$.

---

[5] $e_{ijk} = 1$ for $ijk = 123, 231, 312$ and $e_{ijk} = -1$ for $ijk = 132, 213, 321$ and $\epsilon_{ijk} = 0$ for coincident indices.

Properties of cross products are:

$$\boldsymbol{a} \times \boldsymbol{b} = -\boldsymbol{b} \times \boldsymbol{a}, \tag{1.13}$$

$$\boldsymbol{a} \times \boldsymbol{b} = \boldsymbol{o} \quad \Leftrightarrow \quad \boldsymbol{a}\|\boldsymbol{b}, \text{ i.e., } \boldsymbol{a} \text{ and } \boldsymbol{b} \text{ are linearly dependent,} \tag{1.14}$$

$$\boldsymbol{a} \cdot (\boldsymbol{b} \times \boldsymbol{c}) = \boldsymbol{b} \cdot (\boldsymbol{c} \times \boldsymbol{a}) = \boldsymbol{c} \cdot (\boldsymbol{a} \times \boldsymbol{b}), \tag{1.15}$$

The last line states a **parallelepipedic product** (or box product) of the three vectors $\boldsymbol{a}, \boldsymbol{b}, \boldsymbol{c}$. The expression $\boldsymbol{a} \cdot (\boldsymbol{b} \times \boldsymbol{c})$ represents the volume of a parallelepiped spanned by the vectors. The volume is zero if and only if the vectors are linearly dependent. The box product may conveniently be calculated by

$$(\boldsymbol{a} \times \boldsymbol{b}) \cdot \boldsymbol{c} = \det \begin{pmatrix} a_1 & b_2 & c_1 \\ a_2 & b_2 & c_2 \\ a_3 & b_3 & c_3 \end{pmatrix}. \tag{1.16}$$

The **dyadic product** (or tensor product) of two tensors is denoted by $\boldsymbol{a} \otimes \boldsymbol{b}$. The resulting **dyad** is a second order tensor with components

$$(\boldsymbol{a} \otimes \boldsymbol{b})_{ij} = a_i b_j = \begin{pmatrix} a_1 b_1 & a_1 b_2 & a_1 b_3 \\ a_2 b_1 & a_2 b_2 & a_2 b_3 \\ a_3 b_1 & a_3 b_2 & a_3 b_3 \end{pmatrix}. \tag{1.17}$$

For the dyadic product the following relations hold:

$$(\boldsymbol{a} \otimes \boldsymbol{b})\boldsymbol{c} = \boldsymbol{a}(\boldsymbol{b} \cdot \boldsymbol{c}) = (\boldsymbol{b} \cdot \boldsymbol{c})\boldsymbol{a}, \tag{1.18}$$

$$(\alpha\boldsymbol{a} + \beta\boldsymbol{b}) \otimes \boldsymbol{c} = \alpha(\boldsymbol{a} \otimes \boldsymbol{c}) + \beta(\boldsymbol{b} \otimes \boldsymbol{c}), \tag{1.19}$$

$$(\boldsymbol{a} \otimes \boldsymbol{b})(\boldsymbol{c} \otimes \boldsymbol{d}) = (\boldsymbol{b} \cdot \boldsymbol{c})\boldsymbol{a} \otimes \boldsymbol{d} = \boldsymbol{a} \otimes \boldsymbol{d}(\boldsymbol{b} \cdot \boldsymbol{c}). \tag{1.20}$$

Note that in general,

$$\boldsymbol{a} \otimes \boldsymbol{b} \neq \boldsymbol{b} \otimes \boldsymbol{a}, \tag{1.21}$$

i.e., the dyadic product is not commutative. Also, a dyad can not necessarily be expressed as a single tensor product.

$$\boldsymbol{a} \otimes \boldsymbol{b} + \boldsymbol{c} \otimes \boldsymbol{d} \neq \boldsymbol{x} \otimes \boldsymbol{y} \text{ for some } \boldsymbol{x}, \boldsymbol{y}. \tag{1.22}$$

1.3. Second-Order Tensors

Tensors of second order $\boldsymbol{A} \in (W \otimes V)$ are linear operators that act on a vector $\boldsymbol{a} \in V$ to generate a vector $\boldsymbol{b} \in W$. For notation we use boldface latin capitals.

$$\boldsymbol{A} : V \longrightarrow W$$

$$\boldsymbol{u} \mapsto \boldsymbol{A}\boldsymbol{a}. \tag{1.23}$$

253

Equation (A 1.23 is commonly written as (cf. remarks in Section 1.5)

$$\boldsymbol{u} = \boldsymbol{A}\boldsymbol{a}. \tag{1.24}$$

Any second order tensor may be expressed as a dyad, e.g.,

$$\boldsymbol{A} = A_{ij}\boldsymbol{e}_i \otimes \boldsymbol{e}_j. \tag{1.25}$$

The nine components of (the matrix of) tensor $\boldsymbol{A}$ are

$$(\boldsymbol{A})_{ij} = \begin{pmatrix} A_{11} & A_{12} & A_{13} \\ A_{21} & A_{22} & A_{23} \\ A_{31} & A_{32} & A_{33} \end{pmatrix}. \tag{1.26}$$

Sum, difference, multiplication with a scalar and further operations of second order tensors are defined analogously to vector and matrix algebra. For example, the transpose of tensor $\boldsymbol{A}$ in equation (A 1.25), $\boldsymbol{A}^\top$, is given by

$$\boldsymbol{A}^\top = A_{ij}\boldsymbol{e}_j \otimes \boldsymbol{e}_i \equiv (\boldsymbol{A})_{ji} = \begin{pmatrix} A_{11} & A_{21} & A_{31} \\ A_{12} & A_{22} & A_{32} \\ A_{13} & A_{23} & A_{33} \end{pmatrix}. \tag{1.27}$$

The **magnitude** of Tensor $\boldsymbol{A}$ is defined as the Frobenius norm of its matrix represention, i.e.,

$$|\boldsymbol{A}| := \|(\boldsymbol{A})_{ij}\|_F = (A_{ij}A_{ij})^{\frac{1}{2}}. \tag{1.28}$$

The second order unit (or identity) tensor is defined by $\boldsymbol{I}$, the corresponding zero tensor is $\boldsymbol{O}$. Additional properties of second order tensors are summarized in Section 2.1.

The **double scalar product** (contractive product) is denoted by $\boldsymbol{A} : \boldsymbol{B}$ or equivalently $\langle \boldsymbol{A}, \boldsymbol{B} \rangle$ and yields a scalar. In components the scalar product evaluates to

$$(\boldsymbol{A} : \boldsymbol{B})_{ij} = A_{ij}B_{ij}. \tag{1.29}$$

Note that for the double scalar product holds

$$\boldsymbol{A} : \boldsymbol{B} = \boldsymbol{B} : \boldsymbol{A} \equiv \langle \boldsymbol{A}, \boldsymbol{B} \rangle = \langle \boldsymbol{B}, \boldsymbol{A} \rangle, \tag{1.30}$$

and, moreover,

$$\boldsymbol{A} : (\boldsymbol{B} : \boldsymbol{C}) = (\boldsymbol{B}^\top \boldsymbol{A}) : \boldsymbol{C} = (\boldsymbol{A}\boldsymbol{C}^\top) : \boldsymbol{B} \tag{1.31}$$

$$\boldsymbol{A} : (\boldsymbol{a} \otimes \boldsymbol{b}) = \boldsymbol{a} \cdot \boldsymbol{A}\boldsymbol{b} \tag{1.32}$$

$$(\boldsymbol{a} \otimes \boldsymbol{b})(\boldsymbol{c} \otimes \boldsymbol{d}) = (\boldsymbol{a} \cdot \boldsymbol{b})(\boldsymbol{c} \cdot \boldsymbol{d}). \tag{1.33}$$

A special case of the last equation is

$$(\boldsymbol{e}_i \otimes \boldsymbol{e}_j)(\boldsymbol{e}_k \otimes \boldsymbol{e}_l) \quad = \quad (\boldsymbol{e}_i \cdot \boldsymbol{e}_j)(\boldsymbol{e}_k \cdot \boldsymbol{e}_l) = \delta_{ij}\delta_{kl}. \tag{1.34}$$

The **tensor product** (or dot product) of two second order tensors is written as by $\boldsymbol{AB}$ (here as commonly written without a dot). The result is again a second order tensor with components

$$(\boldsymbol{AB})_{ij} = A_{ik}B_{kj}. \tag{1.35}$$

The matrix product is not commutative, i.e., in general

$$\boldsymbol{AB} \neq \boldsymbol{BA}. \tag{1.36}$$

Moreover holds

$$(\boldsymbol{AB})^\top = \boldsymbol{B}^\top \boldsymbol{A}^\top. \tag{1.37}$$

The **dyadic product** of two second order tensor consequently generates a **fourth order tensor**. The definition and properties of the dyadic product follow analogously to equation (1.18-1.22). Computed in components we write

$$(\boldsymbol{A} \otimes \boldsymbol{B})_{ijkl} \quad = \quad C_{ijkl} = A_{ij}B_{kl}, \tag{1.38}$$

resulting in $3^4 = 81$ entries for the result C_{ijkl}.

1.4. Higher-Order Tensors

Generally, a third order tensor, $^{<3>}\mathbf{D}$, has 27 components D_{ijk} and a fourth order tensor, $\overset{<4>}{C}$, has 81 components C_{ijkl}. This sequence can be continued but tensors of order higher than four are not subject of this work.

For further use we define here the corresponding unit and zero tensor of order four, $\overset{<4>}{I}$ and $\overset{<4>}{O}$, respectively. Finally we note that a fourth order tensor may be expressed with the help of the three Cartesian basis vectors as

$$\overset{<4>}{C} \quad = \quad C_{ijkl}\boldsymbol{e}_i \otimes \boldsymbol{e}_j \otimes \boldsymbol{e}_k \otimes \boldsymbol{e}_l. \tag{1.39}$$

1.5. Remark

Throughout this work equations are formulated in tensor notation, in matrix notation and sometimes indicial notation. For readability we use the same notation for matrices as for tensors but we will not use connective symbols. Moreover, for finite element implementation tensors are often converted into matrices and vectors by using the Voigt-matrix notation, cf. e.g. [159, 390]. To illustrate the notations we formulate here an energy-like scalar expression in the different ways.

$$\underbrace{\boldsymbol{x} \cdot \boldsymbol{A} \boldsymbol{x}}_{tensor} \equiv \underbrace{\boldsymbol{x}^{\top} \boldsymbol{A} \boldsymbol{x}}_{Voigt-matrix} \equiv \underbrace{x_{ij} A_{ijkl} x_{kl}}_{indicial}. \tag{1.40}$$

Appendix 2:

Some Rules of Tensor Algebra and Calculus

In this chapter some fundamental rules of tensor manipulations in the 3D-Euclidian space are summarized for reference. All statements are given without proof. For more details consult the textbooks [32, 121, 376] among others.

2.1. Decompositions, invariants and eigenvalues of tensors

Here we summarize operations on tensors of second order $\boldsymbol{A} \in \mathbb{R}^3 \times \mathbb{R}^3$ applied within this work. If necessary, the extension to tensors of higher order is straightforward.

Determinate, inverse, orthogonality, symmetry and antisymmetry

The **determinate** of a tensor is given by the determinate of its matrix representation in equation (A 1.26), $\det \boldsymbol{A} = \det(\boldsymbol{A})_{ij}$, with properties

$$
\begin{aligned}
\det \boldsymbol{A}^\top &= \det \boldsymbol{A} & (2.1) \\
\det(\alpha \boldsymbol{A}) &= \alpha^3 \det \boldsymbol{A} & (2.2) \\
\det(\boldsymbol{A}\boldsymbol{B}) &= \det \boldsymbol{A} \ \det \boldsymbol{B}. & (2.3)
\end{aligned}
$$

Presuming a non-singular tensor, i.e., $\det \boldsymbol{A} \neq 0$, than exists an unique **inverse** $\boldsymbol{A}^{-1}$ of tensor $\boldsymbol{A}$ satisfying the relation

$$
\boldsymbol{A}^{-1}\boldsymbol{A} = \boldsymbol{A}\boldsymbol{A}^{-1} = \boldsymbol{I}. \tag{2.4}
$$

Some fundamental rules for the inverse of a tensor are

$$(\boldsymbol{A}^{-1})^{-1} = \boldsymbol{A} \tag{2.5}$$

$$(\alpha\boldsymbol{A})^{-1} = \frac{1}{\alpha}\boldsymbol{A}^{-1} \tag{2.6}$$

$$(\boldsymbol{AB})^{-1} = \boldsymbol{B}^{-1}\boldsymbol{A}^{-1} \tag{2.7}$$

$$\boldsymbol{A}^{-2} = \boldsymbol{A}^{-1}\boldsymbol{A}^{-1} \tag{2.8}$$

$$\det\boldsymbol{A}^{-1} = \frac{1}{\det\boldsymbol{A}}. \tag{2.9}$$

Moreover we defined an abbreviation,

$$A^{-\top} := (\boldsymbol{A}^{-1})^{\top} = (\boldsymbol{A}^{\top})^{-1}. \tag{2.10}$$

For the Inverse of a second-order tensor holds the **Sherman-Morrison-Formula**.

$$(\boldsymbol{A} + \boldsymbol{a} \otimes \boldsymbol{b})^{-1} = \boldsymbol{A}^{-1} - \frac{\boldsymbol{A}^{-1}\boldsymbol{a} \otimes \boldsymbol{b}\,\boldsymbol{A}^{-1}}{\boldsymbol{I} + \boldsymbol{b}\,\boldsymbol{A}^{-1}\boldsymbol{a}}. \tag{2.11}$$

A second order tensor $\boldsymbol{R}$ is said to be **orthogonal** if

$$\boldsymbol{R}\boldsymbol{R}^{\top} = \boldsymbol{R}^{\top}\boldsymbol{R} = \boldsymbol{I}. \tag{2.12}$$

This implies, $\boldsymbol{R}^{-1} = \boldsymbol{R}^{\top}$ and, additionally, $(\det\boldsymbol{R})^2 = 1$.

If $\det(\boldsymbol{R}) = 1$ tensor $\boldsymbol{R}$ prescribes a **rotation** ($\boldsymbol{R} \in SO3$), if $\det(\boldsymbol{R}) = -1$ then tensor $\boldsymbol{R}$ prescribes a reflection. Hence, a linear transformation with an orthogonal tensor satisfies the condition

$$\boldsymbol{R}\boldsymbol{u} \cdot \boldsymbol{R}\boldsymbol{v} = \boldsymbol{u} \cdot \boldsymbol{R}^{\top}\boldsymbol{R}\boldsymbol{v} = \boldsymbol{u} \cdot \boldsymbol{v} \tag{2.13}$$

for all vectors $\boldsymbol{u}$ and $\boldsymbol{v}$. This states the well known property of two vectors that their length as well as the angle between them is preserved during rotation.

Any tensor $\boldsymbol{A}$ can uniquely be decomposed into a **symmetric** and an **antisymmetric tensor**.

$$\boldsymbol{A} = \mathrm{sym}(\boldsymbol{A}) + \mathrm{skew}(\boldsymbol{A}) \tag{2.14}$$

where we define

$$\mathrm{sym}(\boldsymbol{A}) = \frac{1}{2}\big(\boldsymbol{A} + \boldsymbol{A}^{\top}\big), \tag{2.15}$$

$$\mathrm{skew}(\boldsymbol{A}) = \frac{1}{2}\big(\boldsymbol{A} - \boldsymbol{A}^{\top}\big). \tag{2.16}$$

Then for any second order tensor $\boldsymbol{A}$ and $\boldsymbol{B}$ holds

$$\text{sym}(\boldsymbol{A}) : \boldsymbol{B} = \text{sym}(\boldsymbol{A}) : \boldsymbol{B}^\top = \text{sym}(\boldsymbol{A}) : \text{sym}(\boldsymbol{B}), \tag{2.17}$$

$$\text{skew}(\boldsymbol{A}) : \boldsymbol{B} = -\text{skew}(\boldsymbol{A}) : \boldsymbol{B}^\top = \text{skew}(\boldsymbol{A}) : \text{skew}(\boldsymbol{B}), \tag{2.18}$$

$$\text{sym}(\text{skew}(\boldsymbol{A})) = \text{skew}(\text{sym}(\boldsymbol{A})) = 0. \tag{2.19}$$

Finally lets state that a second order tensor is said to be **positive definite** if for all $\boldsymbol{x} \neq \boldsymbol{o}$

$$\boldsymbol{x} \cdot \boldsymbol{A}\boldsymbol{x} > 0. \tag{2.20}$$

Positive definite tensors are symmetric and have, as a consequence of $\det \boldsymbol{A} > 0$, only positive entries on the main diagonal. The tensor is **positive semi-definite** if

$$\boldsymbol{x} \cdot \boldsymbol{A}\boldsymbol{x} \geq 0, \tag{2.21}$$

and negative (semi)-definite otherwise.

Trace and deviator of a second-order tensor

Every second-order tensor $\boldsymbol{A}$ can be decomposed into a spherical tensor $\alpha \boldsymbol{I}$ and a deviatoric tensor dev $\boldsymbol{A}$.

$$\boldsymbol{A} = \alpha \boldsymbol{I} + \text{dev}\,\boldsymbol{A}. \tag{2.22}$$

The spherical tensor is related to the trace of tensor $\boldsymbol{A}$ which is a scalar denoted by tr$\boldsymbol{A}$. The trace is given by

$$\text{tr}\boldsymbol{A} = A_{11} + A_{22} + A_{33} = A_{ii}. \tag{2.23}$$

Then the decomposition reads

$$\boldsymbol{A} = \frac{1}{3}\,\text{tr}\boldsymbol{A}\,\boldsymbol{I} + \text{dev}\,\boldsymbol{A}. \tag{2.24}$$

The trace has the properties

$$\text{tr}\boldsymbol{A} = \text{tr}\boldsymbol{A}^\top, \tag{2.25}$$

$$\text{tr}(\boldsymbol{A} + \boldsymbol{B}) = \text{tr}\boldsymbol{A} + \text{tr}\boldsymbol{B}, \tag{2.26}$$

$$\text{tr}(\alpha\boldsymbol{A}\boldsymbol{B}) = \alpha\,\text{tr}(\boldsymbol{A}\boldsymbol{B}) = \alpha\,\text{tr}(\boldsymbol{B}\boldsymbol{A}), \tag{2.27}$$

$$\text{tr}(\boldsymbol{A}^\top\boldsymbol{B}) = \text{tr}(\boldsymbol{A}\boldsymbol{B}^\top) = \text{tr}(\boldsymbol{B}^\top\boldsymbol{A}) = \text{tr}(\boldsymbol{B}\boldsymbol{A}^\top). \tag{2.28}$$

The trace of a tensor may equivalently be computed by the double scalar product

$$\text{tr}\boldsymbol{A} = \boldsymbol{A} : \boldsymbol{I} = \boldsymbol{I} : \boldsymbol{A}. \tag{2.29}$$

In other words, the deviatoric part of tensor $\boldsymbol{A}$ is defined from equation2.24 by

$$\operatorname{dev} \boldsymbol{A} = \boldsymbol{A} - \frac{1}{3} \operatorname{tr} \boldsymbol{A}\, \boldsymbol{I}, \tag{2.30}$$

or, in components,

$$\operatorname{dev} A_{ij} = A_{ij} - \frac{1}{3} A_{ij} \delta_{ij}. \tag{2.31}$$

Invariants, eigenvalues and spectral decomposition

Let a general Tensor $\boldsymbol{A}$ have n eigenvalues $\{\lambda_\alpha,\ \alpha = 1, \ldots n\}$. Correspondingly there are n right eigenvectors $\{\boldsymbol{u}_\alpha,\ \alpha = 1, \ldots n\}$, and n left eigenvectors $\{\boldsymbol{v}_\alpha,\ \alpha = 1, \ldots n\}$. Thus,

$$\boldsymbol{A}\boldsymbol{u}_\alpha = \lambda_\alpha \boldsymbol{u}_\alpha, \quad \alpha = 1, \ldots, n, \tag{2.32}$$
$$\boldsymbol{v}_\alpha \boldsymbol{A} = \boldsymbol{A}^T \boldsymbol{v}_\alpha = \lambda_\alpha \boldsymbol{v}_\alpha, \quad \alpha = 1, \ldots, n, \tag{2.33}$$

The set of homogeneous algebraic equations to determine the eigenvalues λ_α and the right eigenvectors $\boldsymbol{u}_\alpha$ is the well known **characteristic equation**

$$\big(\boldsymbol{A} - \lambda_\alpha \boldsymbol{I}\big)\boldsymbol{u}_\alpha = 0, \tag{2.34}$$

which may be stated analogously for (2.33). Then the **spectral representation** of $\boldsymbol{A}$ reads

$$\boldsymbol{A} = \sum_{\alpha=1}^{n} \lambda_\alpha \boldsymbol{u}_\alpha \otimes \boldsymbol{v}_\alpha. \tag{2.35}$$

The components A_{ij} of tensor $\boldsymbol{A}$ relative to a basis of **principal directions** form a diagonal matrix where the eigenvalues of $\boldsymbol{A}$ are the diagonal elements

$$(\boldsymbol{A})_{ij} = \begin{pmatrix} \lambda_1 & 0 & 0 \\ 0 & \lambda_2 & 0 \\ 0 & 0 & \lambda_3 \end{pmatrix}. \tag{2.36}$$

The **characteristic polynomial**, also known as the Cayley-Hamilton polynomial, for a second-order tensor, is the equation resulting from the eigenvalue problem (2.34), i.e., $\det\big(\boldsymbol{A} - \lambda_\alpha \boldsymbol{I}\big) = 0$, giving

$$\boldsymbol{\lambda}_\alpha^3 - I_1^A \boldsymbol{\lambda}_\alpha^2 - I_2^A \boldsymbol{\lambda}_\alpha - I_3^A = \boldsymbol{0}. \tag{2.37}$$

The scalar coefficients of the characteristic polynomial are the principal invariants of tensor $\boldsymbol{A}$. The explicit expressions for the three **principal invariants** of a second-order tensor are

$$
\begin{aligned}
I_1^A &= \text{tr}\boldsymbol{A} & (2.38) \\
I_2^A &= \frac{1}{2}\big((\text{tr}\boldsymbol{A})^2 - \text{tr}(\boldsymbol{A}^2)\big) = \text{tr}\boldsymbol{A}^{-1}\det\boldsymbol{A} = \text{tr}(\text{cof}\boldsymbol{A}) & (2.39) \\
I_3^A &= \det\boldsymbol{A}. & (2.40)
\end{aligned}
$$

Equivalently, we can claim that for every second-order tensor the principal invariants fulfil the **Cayley-Hamilton equation**:

$$
\boldsymbol{A}^3 - I_1^A\boldsymbol{A}^2 - I_2^A\boldsymbol{A} - I_3^A\boldsymbol{I} = \boldsymbol{0}, \tag{2.41}
$$

or, explicitly,

$$
\boldsymbol{A}^3 - \text{tr}\boldsymbol{A}\,\boldsymbol{A}^2 - \text{tr}(\text{cof}\boldsymbol{A})\boldsymbol{A} - \det\boldsymbol{A}\boldsymbol{I} = \boldsymbol{0}. \tag{2.42}
$$

The principle invariants of tensor $\boldsymbol{A}$ expressed with the eigenvalues are given with

$$
\begin{aligned}
I_1^A &= \lambda_1 + \lambda_2 + \lambda_3 & (2.43) \\
I_2^A &= \lambda_1\lambda_2 + \lambda_1\lambda_3 + \lambda_2\lambda_3 & (2.44) \\
I_3^A &= \lambda_1\lambda_2\lambda_3. & (2.45)
\end{aligned}
$$

The principal invariant do — by definition — not depend on the coordinate system. Note that the definition of an invariant is not unique, e.g., a multiplication of an invariant with any scalar factor yields another invariant value. Widely used are also the so-called **basic invariants**, the invariants of a tensor $\boldsymbol{A}$ defined as the traces of powers of $\boldsymbol{A}$,

$$
\begin{aligned}
\hat{I}_A &= \text{tr}\boldsymbol{A} = \boldsymbol{I} : \boldsymbol{A} & (2.46) \\
\hat{II}_A &= \text{tr}(\boldsymbol{A}^2) = \boldsymbol{I} : \boldsymbol{A}^2 & (2.47) \\
\hat{III}_A &= \text{tr}(\boldsymbol{A}^3) = \boldsymbol{I} : \boldsymbol{A}^3. & (2.48)
\end{aligned}
$$

Because of their practical importance we re-formulate the second invariant (2.39) here in terms of the tensor components

$$
I_2^A = \alpha\big(A_{ii}A_{jj} - A_{ji}A_{ij}\big) \tag{2.49}
$$

where we denote by α a factor which is $\frac{1}{2}$ in equation (2.39) but may also be determined by the physical nature of the referring tensor.

261

Finally, we state that for the **invariants of the deviatoric part** of tensor $\boldsymbol{A}$ the following relations hold:

$$J_1^A \equiv I_1^{devA} \;=\; 0 \tag{2.50}$$

$$J_2^A \equiv I_2^{devA} \;=\; -\frac{1}{2}\operatorname{tr}(\operatorname{dev}\boldsymbol{A})^2 \tag{2.51}$$

$$J_3^A \equiv I_3^{devA} \;=\; \det(\operatorname{dev}\boldsymbol{A}) = \frac{1}{3}\operatorname{tr}(\operatorname{dev}\boldsymbol{A})^3, \tag{2.52}$$

or, applying equation (2.38–2.40),

$$J_2^A \;=\; I_2^A - \frac{1}{3}(I_1^A)^2 \tag{2.53}$$

$$J_3^A \;=\; I_3^A - \frac{1}{3}I_1^A I_2^A + \frac{2}{27}(I_1^A)^3. \tag{2.54}$$

Derivatives of a second order tensor

The derivatives of the principal invariants of a second order tensor with respect to the tensor itself are given here for reference:

$$\frac{\partial \boldsymbol{I}_1^A}{\partial \boldsymbol{A}} = \boldsymbol{I} \quad \text{or} \quad \frac{\partial I_1^A}{\partial A_{ij}} = \delta_{ij} \tag{2.55}$$

$$\frac{\partial \boldsymbol{I}_1^A}{\partial \boldsymbol{A}} = \boldsymbol{I} \quad \text{or} \quad \frac{\partial I_1^A}{\partial A_{ij}} = \delta_{ij} \tag{2.56}$$

$$\frac{\partial \boldsymbol{I}_1^A}{\partial \boldsymbol{A}} = \boldsymbol{I} \quad \text{or} \quad \frac{\partial I_1^A}{\partial A_{ij}} = \delta_{ij} \tag{2.57}$$

Some rules of transformation for the deformation gradient

The deformation gradient works between current and reference placement, is a two point tensor and thus denoted with a small and a capital index as in (1.14). Within a cartesian coordinate system the deformation gradient $\boldsymbol{F} = \partial \boldsymbol{x}/\partial \boldsymbol{X}$ and its inverse relation $\boldsymbol{F}^{-T} = \partial \boldsymbol{X}/\partial \boldsymbol{x}$ can also be written as:

$$\boldsymbol{F} = F_{iJ} \;=\; \frac{\partial x_i}{\partial X_J}\boldsymbol{e}_J \otimes \boldsymbol{e}_i \qquad \boldsymbol{F}^T = F_{Ji} = \frac{\partial x_i}{\partial X_J}\boldsymbol{e}_i \otimes \boldsymbol{e}_J \tag{2.58}$$

$$\boldsymbol{F}^{-1} = F_{iJ}^{-1} \;=\; \frac{\partial X_J}{\partial x_i}\boldsymbol{e}_J \otimes \boldsymbol{e}_i \qquad \boldsymbol{F}^{-T} = F_{Ji}^{-1} = \frac{\partial X_J}{\partial x_i}\boldsymbol{e}_i \otimes \boldsymbol{e}_J$$

Some useful differential relations for the deformation gradient are summarized here:

$$\frac{\partial \boldsymbol{F}}{\partial \boldsymbol{F}} = \overset{<4>}{I} \quad \text{or} \quad \frac{\partial F_{iJ}}{\partial F_{kL}} = \delta_{ik}\delta_{JL} \tag{2.59}$$

$$\frac{\partial \boldsymbol{F}^{-T}}{\partial \boldsymbol{F}} = -\boldsymbol{F}^{-T}\boldsymbol{F}^{-T} \quad \text{or} \quad \frac{\partial F_{Ji}^{-1}}{\partial F_{kL}} = -F_{Jk}^{-1}F_{Li}^{-1} \tag{2.60}$$

$$\frac{\partial \det(\boldsymbol{F})}{\partial \boldsymbol{F}} = \det(\boldsymbol{F})\boldsymbol{F}^{-T} \quad \text{or} \quad \frac{\partial \mathcal{J}}{\partial F_{iJ}} = \mathcal{J}F_{Ji}^{-1} \tag{2.61}$$

$$\frac{\partial \mathrm{tr}(\boldsymbol{F}^T \cdot \boldsymbol{F})}{\partial \boldsymbol{F}} = 2\boldsymbol{F} \quad \text{or} \quad \frac{\partial (F_{mN}F_{mN})}{\partial F_{iJ}} = 2F_{iJ} \tag{2.62}$$

Equation (2.59), (2.60) and (2.62) follow by direct calculation following the rules summarized in the appendix III. The proof of (2.61) is lengthy but can be found in [339].

2.2. Gauss's integral theorem and divergence theorem

Because of its importance in continuums mechanics we state here a general form of Gauss's integral theorem and a the special case known as divergence theorem. For proofs and more details consult the mathematical textbooks as, e.g., [121, 139].

A general version of Gauss's integral theorem reads

$$\int_{\Omega \backslash \Lambda} \mathrm{grad} \circ \boldsymbol{A}(\boldsymbol{x}) dV \;\; = \;\; \int_{\partial \Omega} \boldsymbol{n} \circ \boldsymbol{A}(\boldsymbol{x}) dS + \int_{\Lambda} \boldsymbol{n} \circ [\![\boldsymbol{A}(\boldsymbol{x})]\!] dS. \tag{2.63}$$

Equation (2.63) includes the classical theorems of Gauss and Stokes as special cases. In this version the tensorial fields $\boldsymbol{A}(\boldsymbol{x})$ defined in the region Ω may be discontinuous at a surface of discontinuity Λ. The function

$$[\![\boldsymbol{a}]\!] = \boldsymbol{a}^- - \boldsymbol{a}^+ \tag{2.64}$$

is the difference of the values of the field quantity $\boldsymbol{a}$ on both sides of the surface of discontinuity. The index " + " refers to the side with positive outward-pointing unit normal $\boldsymbol{n}$ and the index " - " refers to the opposite side, i.e., the side where the positive surface normal $\boldsymbol{n}$ points to. The symbol $\circ$ in equation (2.63) summarizes three different possible operations, namely: multiplication with a scalar field, scalar product with a vectorial or tensorial field, or vector (wedge) product with a vector field.

Let now Ω be a bounded open subset of $\mathbb{R}^n$ with smooth (or piecewise smooth) boundary $\partial\Omega$. Let $\boldsymbol{a} = [a_1 \ldots a_n]$ be a smooth vector (or tensorial) field defined in $\mathbb{R}^n$, or at least in $\Omega \cup \partial\Omega$. Again $\boldsymbol{n}$ be the unit outward-pointing normal of $\partial\Omega$. Then follows

$$\int_\Omega \operatorname{div} \boldsymbol{a} \ dV_0 = \int_{\partial\Omega} \boldsymbol{n}\boldsymbol{a} \ dS, \tag{2.65}$$

where as above dV is the element of volume in $\mathbb{R}^n$ and dS is the element of surface area on $\partial\Omega$. Equation (2.65) is cited in the text as **divergence theorem**.

2.3. Reynolds' transport theorem

To conclude this summary we present a fundamental theorem to evaluate a time derivative in some changing volume. The rate of any scalar or tensorial function $\Psi(\boldsymbol{x}, t)$ in a time depending volume $V(t)$ is

$$\frac{d}{dt} \int_{V(t)} \Psi(\boldsymbol{x}, t) \ dV = \frac{d}{dt} \int_{V_0} \Psi(\boldsymbol{\varphi}(\boldsymbol{X}, t), t) \, J(\boldsymbol{X}, t) \ dV \tag{2.66}$$

Evaluating the right hand side of 2.66[6], transferring it to the current placement and applying the divergence theorem gives **Reynolds' transport theorem**

$$\frac{d}{dt} \int_{V(t)} \Psi \ dV = \int_{V(t)} \frac{\partial\Psi}{\partial t} \, dV + \int_{\partial V(t)} \Psi \cdot \boldsymbol{v} \cdot \boldsymbol{n} \, dS, \tag{2.67}$$

where we dropped the arguments for readability. The first term in (2.67) denotes the local time rate of the spacial field $\Psi(\boldsymbol{x}, t)$, the second term characterizes the outward normal flux, i.e., the rate of transport of $\Psi \cdot \boldsymbol{v}$ across a fixed boundary ∂V of region $V(t)$. Assuming $\Psi(\boldsymbol{x}, t)$ to be sufficiently smooth, the local form of (2.67) is the **material time derivative**,

$$\frac{d}{dt} = \frac{\partial\Psi}{\partial t} + \operatorname{grad} \Psi \cdot \boldsymbol{v}. \tag{2.68}$$

---

[6]Note that $\dot{J}V_0 = \frac{\dot{J}}{J}V(t)$ and $\frac{\dot{J}}{J} = \operatorname{div}\boldsymbol{v}(\boldsymbol{x}, t)$.

Appendix 3:

Functional Spaces and Norms

Here we summarize some linear spaces and norms naturally to use in finite element approximations. The definitions are given for scalar functions. The analogous definition for vector valued functions are obtained by applying the definition to each one of the components. For more detailed expressions we refer to the mathematical literature, e.g., [48, 87, 126, 125]. Throughout this section let $\Omega \in \mathbb{R}^d$ be a bounded open set.

Let $u : \mathbb{R}^d \to \mathbb{R}$ and let α be a multi-index[7]. Then we write the partial derivatives of a function by

$$D^\alpha u = \frac{\partial^{|\alpha|} u}{\partial x_1^{\alpha_1} \ldots \partial x_d^{\alpha_d}}. \tag{3.1}$$

Definition: *Frobenius-norm.* Let $u \in \mathbb{R}^\alpha$ and let α be a multi-index. Then we define the norm

$$\|u\|_F = \sqrt{u_{\alpha_1}^2 + \cdots + u_{\alpha_d}^2}. \tag{3.2}$$

If $u \in \mathbb{R}^n$ is a vector definition (3.2) coincides with the definition of the Euclidian norm.

The **Lebesque-space** $L^p(\Omega)$, $p \geq 1$, is the linear space of functions $u : \Omega \to \mathbb{R}$ which are Lebesque-measurable, i.e., the ess $\sup_\Omega u < \infty$.

Definition: *L^p-norm.* Let $u \in L^p(\Omega)$, $p \geq 1$. Then we define the norm

$$\|u\|_p = \left(\int_\Omega u \, dx \right)^{1/p}. \tag{3.3}$$

According to custom we refer to functions $L^2(\Omega)$ as functions which are square integrable over Ω. All piecewise continuous functions u belong to $L^2(\Omega)$.

---

[7]A multi-index α of dimension d is an array $\{\alpha_1, \ldots, \alpha_d\}$ of nonnegative integers, $\alpha \in \mathbb{N}^d$. The degree $|\alpha|$ of the multi-index is the sum $\alpha_1 + \cdots + \alpha_d$. For example: a quadratic polynomial in two dimensions has $|\alpha| = 6$ independent coefficients with indices $\alpha = \{00\}, \{10\}, \{01\}, \{20\}, \{11\}, \{02\}$

The **Sobolev-space** $W^{m,p}(\Omega)$ is the linear space of functions $u : \Omega \rightarrow \mathbb{R}$ such that $D^\alpha u \in L^p(\Omega)$ in the distributional sense. In other words, these are functions in $L^p(\Omega)$ whose distributional derivatives up to order m are themselves in $L^p(\Omega)$.

Definition: *Sobolev Seminorm.* Let $u : \Omega \rightarrow \mathbb{R}$ be m-times continuously differentiable in Ω, $m \geq 0$. Then we define the seminorm

$$|u|_{m,p} = \Big(\sum_{|\alpha|=m} \int_\Omega |D^\alpha u|^p \, dx \Big)^{1/p} . \tag{3.4}$$

Definition: *Sobolev norm.* Let $u : \Omega \rightarrow \mathbb{R}$ be m-times continuously differentiable in Ω, $m \geq 0$. Then we define the norm

$$\|u\|_{m,p} = \Big(\sum_{k=0}^m \int_\Omega |u|_{k,p} \, dx \Big)^{1/p} . \tag{3.5}$$

The Sobolev space $W^{m,p}(\Omega)$ is a complete normed space, or Banach space, under the norm (3.5).

The **Hilbert space** $H^m(\Omega)$, $m \geq 0$ is the Sobolev-space $W^{m,2}(\Omega)$. The particular space $H^0(\Omega)$ coincides with the Lebesque space $L^2(\Omega)$.

For instance, all piecewise continuous functions u with piecewise continuous first derivatives belong to $H^1(\Omega)$.

Definition: *Hilbert norm.* Let $u : \Omega \rightarrow \mathbb{R}$ be m-times continuously differentiable in Ω, $m \geq 0$. Then we define the norm

$$\|u\|_m = \Big(\sum_{k=0}^m |u|_k^2 \Big)^{1/2} . \tag{3.6}$$

The Hilbert space $H^m(\Omega)$ the space of functions over Ω which can be obtained as limits of smooth functions under the norm $\| \cdot \|_m$. These limits may be thought of as functions which are square integrable over Ω and whose distributional derivatives of order up to m are themselves square integrable. In addition, the Hilbert spaces $H^m(\Omega)$ are spaces with the inner product

$$\big(u, v \big)_m = \sum_{|\alpha|=m} \int_\Omega D^\alpha u \cdot D^\alpha v \, dx . \tag{3.7}$$

Appendix 4:

Evaluation of the exponential and logarithmic mapping and their derivatives

Here algorithms for the computation of the exponential and logarithmic mapping and their first and second linearizations according to Radovitzky and Ortiz [276] are given.

Let $\boldsymbol{A} \in \mathbb{R}^{n \times n}$, $\boldsymbol{B} \in \mathbb{R}^{n \times n}$ be square matrices, not necessarily symmetric. The exponential of $\boldsymbol{A}$ is defined as

$$\exp(\boldsymbol{A}) = \sum_{k=0}^{\infty} \frac{1}{k!} \boldsymbol{A}^k \tag{4.1}$$

provided that the series converges. The logarithm of $\boldsymbol{B}$ is defined as

$$\ln(\boldsymbol{B}) = \sum_{k=1}^{\infty} \frac{(-1)^{k-1}}{k!} (\boldsymbol{B} - \boldsymbol{I})^k \tag{4.2}$$

provided that the series converges.

4.1. Spectral representation

Let $\boldsymbol{A}$ have eigenvalues $\{\lambda_\alpha, \ \alpha = 1, \ldots n\}$, right eigenvectors $\{\boldsymbol{u}_\alpha, \ \alpha = 1, \ldots n\}$, and left eigenvectors $\{\boldsymbol{v}_\alpha, \ \alpha = 1, \ldots n\}$. Thus,

$$\boldsymbol{A}\boldsymbol{u}_\alpha = \lambda_\alpha \boldsymbol{u}_\alpha, \quad \alpha = 1, \ldots, n, \tag{4.3}$$

$$\boldsymbol{A}^T \boldsymbol{v}_\alpha = \lambda_\alpha \boldsymbol{v}_\alpha, \quad \alpha = 1, \ldots, n, \tag{4.4}$$

and

$$\boldsymbol{A} = \sum_{\alpha=1}^{n} \lambda_\alpha \boldsymbol{u}_\alpha \otimes \boldsymbol{v}_\alpha \tag{4.5}$$

The exponential of $\boldsymbol{A}$ then admits the spectral representation

$$\exp(\boldsymbol{A}) = \sum_{\alpha=1}^{n} e^{\lambda_\alpha} \boldsymbol{u}_\alpha \otimes \boldsymbol{v}_\alpha \tag{4.6}$$

We wish to linearize the exponential mapping twice. To this end, we begin by recalling that the solution to the problem

$$\dot{\boldsymbol{x}}(t) = \boldsymbol{A}\boldsymbol{x}(t) + \boldsymbol{f}(t), \qquad t \geq 0 \tag{4.7}$$
$$\boldsymbol{x}(0) = \boldsymbol{x}_0 \tag{4.8}$$

in $\mathbb{R}^n$ is

$$\boldsymbol{x}(t) = \exp(t\boldsymbol{A})\boldsymbol{x}_0 + \int_0^t \exp((t-\tau)\boldsymbol{A})\boldsymbol{f}(\tau)\,d\tau, \qquad t \geq 0 \tag{4.9}$$

It therefore follows that $\exp(\boldsymbol{A})_{ij}$ is the ith component of the solution of the initial-value problem (4.7 - 4.8) at $t = 1$ with $\boldsymbol{f}(t) = \boldsymbol{0}$ and $\boldsymbol{x}_0 = \boldsymbol{e}_j \equiv j$th standard basis vector in $\mathbb{R}^n$.

Imagine now perturbing the matrix $\boldsymbol{A}$ to $\boldsymbol{A} + \delta\boldsymbol{A}$ in (4.7 - 4.8), resulting in a perturbed solution $\boldsymbol{x}(t) + \delta\boldsymbol{x}(t)$. To first order, $\delta\boldsymbol{x}(t)$ is the solution of the problem

$$\delta\dot{\boldsymbol{x}}(t) = \boldsymbol{A}\delta\boldsymbol{x}(t) + \delta\boldsymbol{A}\boldsymbol{x}(t), \qquad t \geq 0 \tag{4.10}$$
$$\delta\boldsymbol{x}(0) = \boldsymbol{0} \tag{4.11}$$

Using (4.9), the solution of this problem is found to be

$$\delta\boldsymbol{x}(t) = \int_0^t \exp((t-\tau)\boldsymbol{A})\delta\boldsymbol{A}\exp(\tau\boldsymbol{A})\,d\tau \tag{4.12}$$

But we also have

$$\boldsymbol{x}(t) + \delta\boldsymbol{x}(t) = \exp(t(\boldsymbol{A}+\delta\boldsymbol{A}))\boldsymbol{x}_0 \sim [\exp(t\boldsymbol{A}) + D\exp(t\boldsymbol{A})\delta\boldsymbol{A}]\boldsymbol{x}_0 + \text{hot} \tag{4.13}$$

Comparing (4.12) and (4.13) yields

$$D\exp(\boldsymbol{A})\delta\boldsymbol{A} = \int_0^1 \exp((1-\tau)\boldsymbol{A})\delta\boldsymbol{A}\exp(\tau\boldsymbol{A})\,d\tau \tag{4.14}$$

or, in components

$$Dexp(\boldsymbol{A})_{ijkl} = \int_0^1 \exp((1-\tau)\boldsymbol{A})_{ik} \exp(\tau\boldsymbol{A})_{lj} \, d\tau \qquad (4.15)$$

In order to evaluate this integral we may make use of representation (4.5) to write (4.15) in the form

$$Dexp(\boldsymbol{A})_{ijkl} = \sum_{\alpha=1}^{n} e^{\lambda_\alpha} \sum_{\beta=1}^{n} \left[\int_0^1 e^{\tau(\lambda_\beta - \lambda_\alpha)} \, d\tau \right] u_{\alpha i} v_{\alpha k} u_{\beta l} v_{\beta j} \qquad (4.16)$$

which evaluates to

$$Dexp(\boldsymbol{A})_{ijkl} = \sum_{\alpha=1}^{n} \sum_{\beta=1}^{n} f(\lambda_\alpha, \lambda_\beta) u_{\alpha i} v_{\alpha k} u_{\beta l} v_{\beta j} \qquad (4.17)$$

or, in invariant notation

$$Dexp(\boldsymbol{A}) = \sum_{\alpha=1}^{n} \sum_{\beta=1}^{n} f(\lambda_\alpha, \lambda_\beta) \boldsymbol{u}_\alpha \otimes \boldsymbol{v}_\beta \otimes \boldsymbol{v}_\alpha \otimes \boldsymbol{u}_\beta \qquad (4.18)$$

In these expressions we have written

$$f(\lambda_\alpha, \lambda_\beta) \;=\; \frac{e^{\lambda_\beta} - e^{\lambda_\alpha}}{\lambda_\beta - \lambda_\alpha} \quad \text{if} \quad \lambda_\beta \neq \lambda_\alpha \qquad (4.19)$$

$$f(\lambda_\alpha, \lambda_\alpha) \;=\; e^{\lambda_\alpha} \quad \text{otherwise} \qquad (4.20)$$

Note that the above expressions are valid even when eigenvalues are repeated.

In order to determine the second derivative of the exponential mapping we may differentiate (4.15) to obtain

$$
\begin{aligned}
D^2 exp(\boldsymbol{A})_{ijklmn} \;=\;\; & \int_0^1 (1-\tau) Dexp((1-\tau)\boldsymbol{A})_{ikmn} \exp(\tau\boldsymbol{A})_{lj} \, d\tau \\
& + \int_0^1 \tau \exp((1-\tau)\boldsymbol{A})_{ik} Dexp(\tau\boldsymbol{A})_{ljmn} \, d\tau
\end{aligned}
\qquad (4.21)
$$

Inserting (4.5) and (4.17) into this expression gives

$$D^2 exp(\boldsymbol{A})_{ijklmn} =$$

$$\sum_{\alpha=1}^{n} \sum_{\beta=1}^{n} \sum_{\gamma=1}^{n} \left[\int_0^1 (1-\tau) f((1-\tau)\lambda_\alpha, (1-\tau)\lambda_\beta) e^{\tau\lambda_\gamma} \, d\tau \right] u_{\alpha i} v_{\alpha m} u_{\beta n} v_{\beta k} u_{\gamma l} v_{\gamma j}$$

$$+ \sum_{\alpha=1}^{n} \sum_{\beta=1}^{n} \sum_{\gamma=1}^{n} \left[\int_0^1 \tau f(\tau\lambda_\alpha, \tau\lambda_\beta) e^{(1-\tau)\lambda_\gamma} \, d\tau \right] u_{\alpha l} v_{\alpha m} u_{\beta n} v_{\beta j} u_{\gamma i} v_{\gamma k} \qquad (4.22)$$

Defining

$$g(\lambda_\alpha, \lambda_\beta, \lambda_\gamma) = \int_0^1 \tau f(\tau\lambda_\alpha, \tau\lambda_\beta) e^{(1-\tau)\lambda_\gamma} \, d\tau \tag{4.23}$$

(4.22) simplifies to

$$D^2 \exp(\boldsymbol{A})_{ijklmn} =$$
$$\sum_{\alpha=1}^n \sum_{\beta=1}^n \sum_{\gamma=1}^n g(\lambda_\alpha, \lambda_\beta, \lambda_\gamma) v_{\alpha m} u_{\beta n} [u_{\alpha l} v_{\beta j} u_{\gamma i} v_{\gamma k} + u_{\alpha i} v_{\beta k} u_{\gamma l} v_{\gamma j}] \tag{4.24}$$

which is the sought expression.

The derivatives of the logarithmic mapping can be obtained directly from the previous expressions by recognizing that $\ln = \exp^{-1}$ and using the properties of inverse functions. This leads to

$$D\log(\boldsymbol{B})_{ijkl} = D\exp(\boldsymbol{A})_{ijkl}^{-1} \tag{4.25}$$
$$D^2\log(\boldsymbol{B})_{ijklmn} =$$
$$-D\exp(\boldsymbol{A})_{ijpq}^{-1} D\exp(\boldsymbol{A})_{rskl}^{-1} D\exp(\boldsymbol{A})_{tumn}^{-1} D^2\exp(\boldsymbol{A})_{pqrstu} \tag{4.26}$$

where $\boldsymbol{A} = \exp(\boldsymbol{B})$. The first of these expressions evaluates to

$$D\log(\boldsymbol{B})_{ijkl} = \sum_{\alpha=1}^n \sum_{\beta=1}^n f(\mu_\alpha, \mu_\beta) u_{\alpha i} v_{\alpha k} u_{\beta l} v_{\beta j} \tag{4.27}$$

where $\{\mu_\alpha, \ \alpha = 1, \ldots n\}$ are the eigenvalues of $\boldsymbol{B}$, $\{\boldsymbol{u}_\alpha, \ \alpha = 1, \ldots n\}$ are its right eigenvectors, and $\{\boldsymbol{v}_\alpha, \ \alpha = 1, \ldots n\}$ its left eigenvectors. In invariant notation

$$D\log(\boldsymbol{B}) = \sum_{\alpha=1}^n \sum_{\beta=1}^n f(\mu_\alpha, \mu_\beta) \boldsymbol{u}_\alpha \otimes \boldsymbol{v}_\beta \otimes \boldsymbol{v}_\alpha \otimes \boldsymbol{u}_\beta \tag{4.28}$$

where we write

$$f(\mu_\alpha, \mu_\beta) = \frac{\log\mu_\beta - \log\mu_\alpha}{\mu_\beta - \mu_\alpha} \quad \text{if} \quad \mu_\beta \neq \mu_\alpha \tag{4.29}$$

$$f(\mu_\alpha, \mu_\alpha) = \frac{1}{\mu_\alpha} \quad \text{otherwise} \tag{4.30}$$

Note that the above expressions are valid even when eigenvalues are repeated.

4.2. Taylor series expansion

For small $\boldsymbol{A}$ it may be cheaper to evaluate the exponential mapping and its derivatives directly from its series expansion (4.1). Likewise, for $\boldsymbol{B}$ close to the identity it may be cost-effective to use (4.2) directly. To this end, it proves convenient to express (4.1) in the form

$$\exp(\boldsymbol{A}) = \sum_{k=0}^{\infty} \exp^{(k)}(\boldsymbol{A}) \tag{4.31}$$

where the terms $\exp^{(k)}(\boldsymbol{A})$ in the expansion follow from the recurrence relation

$$\exp^{(0)}(\boldsymbol{A}) = \boldsymbol{I} \tag{4.32}$$

$$\exp^{(k+1)}(\boldsymbol{A}) = \frac{1}{k+1}\exp^{(k)}(\boldsymbol{A})\boldsymbol{A}, \quad k = 0, \dots \tag{4.33}$$

Here $\boldsymbol{I}$ is the identity matrix. It follows from this representation that

$$D\exp(\boldsymbol{A}) = \sum_{k=1}^{\infty} D\exp^{(k)}(\boldsymbol{A}) \tag{4.34}$$

where

$$D\exp^{(1)}(\boldsymbol{A}) = D\boldsymbol{A} \tag{4.35}$$

$$D\exp^{(k+1)}(\boldsymbol{A}) =$$
$$\frac{1}{k+1}[D\exp^{(k)}(\boldsymbol{A})\boldsymbol{A} + \exp^{(k)}(\boldsymbol{A})D\boldsymbol{A}], \quad k = 1, \dots \tag{4.36}$$

In components

$$D\exp^{(1)}(\boldsymbol{A})_{ijkl} = \delta_{ik}\delta_{jl} \tag{4.37}$$

$$D\exp^{(k+1)}(\boldsymbol{A})_{ijkl} =$$
$$\frac{1}{k+1}[D\exp^{(k)}(\boldsymbol{A})_{ipkl}A_{pj} + \exp^{(k)}(\boldsymbol{A})_{ik}\delta_{jl}], \quad k = 1, \dots \tag{4.38}$$

Likewise

$$D^2\exp(\boldsymbol{A}) = \sum_{k=2}^{\infty} D^2\exp^{(k)}(\boldsymbol{A}) \tag{4.39}$$

where

$$D^2\exp^{(2)}(\boldsymbol{A}) = \tfrac{1}{2}D^2\boldsymbol{A}^2 \tag{4.40}$$

$$D^2\exp^{(k+1)}(\boldsymbol{A}) =$$
$$\frac{1}{k+1}\{D^2\exp^{(k)}(\boldsymbol{A})\boldsymbol{A} + 2\mathrm{sym}[D\exp^{(k)}(\boldsymbol{A})D\boldsymbol{A}]\}, \quad k = 2, \dots \tag{4.41}$$

In components

$$D^2\exp^{(2)}(\boldsymbol{A})_{ijklmn} = \tfrac{1}{2}(\delta_{ik}\delta_{lm}\delta_{jn} + \delta_{im}\delta_{kn}\delta_{jl}) \tag{4.42}$$

$$D^2\exp^{(k+1)}(\boldsymbol{A})_{ijklmn} = \tfrac{1}{k+1}[D^2\exp^{(k)}(\boldsymbol{A})_{ipklmn}A_{pj} +$$

$$D\exp^{(k)}(\boldsymbol{A})_{imkl}\delta_{jn} + D\exp^{(k)}(\boldsymbol{A})_{ikmn}\delta_{jl}], \quad k = 2,\ldots \tag{4.43}$$

The logarithmic mapping can be given a similar treatment. Begin by expressing (4.2) in the form

$$\log(\boldsymbol{B}) = \sum_{k=1}^{\infty} \log^{(k)}(\boldsymbol{B}) \tag{4.44}$$

where the terms $\log^{(k)}(\boldsymbol{B})$ in the expansion follow from the recurrence relation

$$\log^{(1)}(\boldsymbol{B}) = \boldsymbol{B} - \boldsymbol{I} \tag{4.45}$$

$$\log^{(k+1)}(\boldsymbol{B}) = -\frac{k}{k+1}\log^{(k)}(\boldsymbol{B})(\boldsymbol{B} - \boldsymbol{I}), \quad k = 1,\ldots \tag{4.46}$$

It follows from this representation that

$$D\log(\boldsymbol{B}) = \sum_{k=1}^{\infty} D\log^{(k)}(\boldsymbol{B}) \tag{4.47}$$

where

$$D\log^{(1)}(\boldsymbol{B}) = D\boldsymbol{B} \tag{4.48}$$

$$D\log^{(k+1)}(\boldsymbol{B}) =$$

$$-\tfrac{k}{k+1}[D\log^{(k)}(\boldsymbol{B})(\boldsymbol{B} - \boldsymbol{I}) + \log^{(k)}(\boldsymbol{B})D\boldsymbol{B}], \quad k = 1,\ldots \tag{4.49}$$

In components

$$D\log^{(1)}(\boldsymbol{B})_{ijkl} = \delta_{ik}\delta_{jl} \tag{4.50}$$

$$D\log^{(k+1)}(\boldsymbol{B})_{ijkl} =$$

$$-\tfrac{k}{k+1}[D\log^{(k)}(\boldsymbol{B})_{ipkl}(B_{pj} - \delta_{pj}) + \log^{(k)}(\boldsymbol{B})_{ik}\delta_{jl}], \quad k = 1,\ldots \tag{4.51}$$

Likewise

$$D^2\log(\boldsymbol{B}) = \sum_{k=2}^{\infty} D^2\log^{(k)}(\boldsymbol{B}) \tag{4.52}$$

where

$$D^2\log^{(2)}(\boldsymbol{B}) = \tfrac{1}{2}D^2\boldsymbol{B}^2 \tag{4.53}$$

$$D^2\log^{(k+1)}(\boldsymbol{B}) =$$

$$-\tfrac{k}{k+1}\{D^2\log^{(k)}(\boldsymbol{B})(\boldsymbol{A} - \boldsymbol{I}) + 2\text{sym}[D\log^{(k)}(\boldsymbol{B})D\boldsymbol{B}]\}, \quad k = 2,\ldots \tag{4.54}$$

272

In components

$$D^2\log^{(2)}(\boldsymbol{B})_{ijklmn} = \tfrac{1}{2}(\delta_{ik}\delta_{lm}\delta_{jn} + \delta_{im}\delta_{kn}\delta_{jl}) \tag{4.55}$$

$$D^2\log^{(k+1)}(\boldsymbol{B})_{ijklmn} = -\tfrac{k}{k+1}[D^2\log^{(k)}(\boldsymbol{B})_{ipklmn}(A_{pj} - \delta_{pj})+$$

$$D\log^{(k)}(\boldsymbol{B})_{imkl}\delta_{jn} + D\log^{(k)}(\boldsymbol{B})_{ikmn}\delta_{jl}], \quad k = 2,\dots \tag{4.56}$$

Bibliography

[1]

[2] H. J. Albrecht, J. Jendrny, W. H. Müller, and C. Wieand. Lebensdauervorhersagen für Vias und Mikrovias in HDI-Boards per FE-Simulation und ihre experimentelle Verifikation. In K. J. Wolter and S. Wiese, editors, *Interdisziplinäre Methoden in der Aufbau- und Verbindungstechnik*. ddp goldenbogen, Dresden, 2003.

[3] H. J. Albrecht, J. Jendrny, W. H. Müller, and C. Wieand. Lifetime Prediction by fe-Simulation and Experimental Verification for Vias and Microvias in HDI-Substrates. In *Proc. of Eighth Ann. Pan Pacific Microelectronic Simposium (SMTA)*, pages 201 – 208. Hawai, 2003.

[4] H.-J. Albrecht, A. Juritza, K. Müller, W.H. Müller, J. Sterthaus, J. Villain, and A. Vogliano. Interface reactions in microelectronic solder joints and associated intermetallic compounds: An investigation of their mechanical properties using nanoindentation. *Proceedings of the Electronics Packaging Technology Conference (EPTC)*, pages 726–731, 2003.

[5] J. Altenbach and H. Altenbach. *Einführung in die Kontinuumsmechanik*. Teubner Studienbücher, Stuttgart, 1995.

[6] H. Anderson. Analysis of a model for void growth and coalescence ahead of a moving crack tip. *Journal of the Mechanics and Physics of Solids*, 25:217–233, 1977.

[7] E. M. Arruda and Boyce M. C. A Three-Dimensional Constitutive Model for the Large Stretch Behavior of Rubber Elastic Materials. *Journal Mech. Physics Solids*, 41:389–412, 1993.

[8] M.F. Ashby, F.J. Blunt, and M. Bannister. Flow characteristics of highly constrained metal wires. *Acta Metallurgica*, 37(7):1847–1857, 1989.

[9] O. Atahan, T. Alkibay, U. Karaoglan, N. Deniz, and I. Bozkirli. Acute bioeffects of electromagnetic lithotripsy. *Scandinavian Journal Of Urology And Nephrology*, 30(4):269–272, 1996.

[10] I. Babuška and J. Melenk. The Partition of Unity Method. *International Journal for Numerical Methods in Engineering*, 40:727–758, 1997.

[11] M. Bailey, L. Crum, O. Sapozhnikov, A. Evan, J. McAteer, R. Cleveland, and T. Colonius. Cavitation in shock wave lithotripsy. In *In Proceedings of the 5th International Symposium on Cavitation, Osaka, Japan*, 2003.

[12] J.M. Ball. Convexity Conditions and Existence Theorems in Nonlinear Elasticity. *Arch. Rat. Mech. Anal.*, 63:337–403, 1977.

[13] J.M. Ball. Discontinuous equilibrium solutions and cavitation in non-linear elasticity. *Philosophical Transactions of the Royal Society of London Series A-Mathematical Physical and Engineering Sciences*, 306(1496):557–611, 1982.

[14] D. Balzani, P. Neff, J. Schröder, and G. Holzapfel. A polyconvex framework for soft biological tissues. adjustment to experimental data. *International Journal of Solids and Structures*, 1:1, 2005.

[15] D. Balzani, J. Schröder, D. Gross, and P. Neff. Modeling of anisotropic damage in arterial walls based on polyconvex stored energy functions. In *Computational Plasticity: Fundamentals and Applications, Proceedings of the 8th International Conference on Computational Plasticity*, 2005.

[16] T. W. Barbee, L. Seamann, R. Crewdson, and D. Curran. Dynamic fracture criteria for ductile and brittle metals. *Journal of the Materials*, 7:393–401, 1972.

[17] D.B. Barker and A. Dasgupta. Thermal analysis in plated-through-hole reliability. In *Thermal Stress and Strain in Microelectronic Packaging, editor J.H. Lau, van Nostrand Reinhold, New York*, 1993.

[18] G. I. Barrenblatt. The mathematical theory of equilibrium of cracks in brittle fracture. *Adv. Appl. Mech.*, 7:55–129, 1962.

[19] S. Bartels, C. Carstensen, K. Hackl, and U. Hoppe. Effective Relaxation for Microstructure Simulations: Algorithms and Applications. *Comput. Methods Appl. Mech. Engrg.*, 193:5143–5175, 2005.

[20] K. J. Bathe. *Finite Element Procedures*. Prentice-Hall, 1997.

[21] C. D. Beachem. Electron fractographic study of influence of plastic strain conditions upon ductile rupture processes in metals. *Transactions of the American Society of Metals*, 56:318–326, 1963.

[22] C. D. Beachem and G. R. Yoder. Elasto-plastic fracture by homogeneous microvoid

coalescence tearing along alternating shear planes. *Metallurgical Transactions*, 4:1145–1153, 1973.

[23] E. Becker and W. Bürger. *Kontinuumsmechanik*. B. G. Teubner Verlag, 1975.

[24] R. Becker. Ring fragmentation predictions using the gurson model with material stability conditions as failure criteria. *International Journal of Solids and Structures*, 39:3555–3580, 2002.

[25] R. Becker and A. Needleman. Effect of yield surface curvature on necking and failure in porous plastic solids. *Journal of Applied Mechanics-Transactions of the ASME*, 53(3):491–499, 1986.

[26] R. Becker and R.E. Smelser. Simulation of strain localization and fracture between holes in an aluminum sheet. *Journal of the Mechanics and Physics of Solids*, 42(5):773–796, 1994.

[27] W. Beitz and K. H. Küttner. *Dubbel—Taschenbuch für den Maschinenbau*. Springer–Verlag, 1990.

[28] J Belak. On the nucleation and growth of voids at high strain-rates. *Journal of Computer Aided Materials Design*, 5:193–206, 1998.

[29] J. Belak. How metals fail. *Lawrence Livermore National Laboratory, S&TR*, 7/8:317–327, 2002.

[30] T. Belytschko, N. Möes, S. Usui, and C. Parimi. Arbitrary discontinuities in finite elements. *International Journal for Numerical Methods in Engineering*, 50:993–1013, 2001.

[31] T. Belytschko, Y. Moran, and Y. Li. *Finite Element Methods*. Y, 2002.

[32] A. Bertram. *Elasticity and Plasticity of Large Deformations*. Springer, 2005.

[33] A. Bertram and B. Svendsen. On frame-indifference and form-invariance in constitutive theory. *Acta Mech.*, 132:195–207, 1999.

[34] A. Bertram and B. Svendsen. On material objectivity and reduced constitutive equations. *Arch. Mech.*, 53:653–675, 2001.

[35] J. Betten. *Kontinuumsmechanik. Elasto-, Plasto- und Kriechmechanik*. Springer-Verlag, Berlin, 1993.

[36] Kaushik Bhattacharya. *Microstructure of Martensite*. Oxford University Press, 2003.

[37] P. J. Blatz and W. L. Ko. Application of finite elasticity theory to the deformation of rubbery material. *Trans. of Soc. of Rheology*, 6:223–251, 1962.

[38] S. Blenk, H. Ehrentraut, and W. Muschik. Statistical foundation of macroscopic balances for liquid crystals in alignment tensor formulation. *Physica A*, 174:119–138, 1991.

[39] P.M. Blomgren, B.A. Connors, J.E. Lingeman, L.R. Willis, and A.P. Evan. Quantitation of shock wave lithotripsy-induced lesion in small and large pig kidneys. *Anatomical Record*, 249(3):341–348, 1997.

[40] H. Blumenauer and G. Pusch. *Technische Bruchmechanik*. Deutscher Verlag für Grundstoffindustrie Leipzig, 1982.

[41] Th. Böhme. Berechnung von steifigkeiten und höheren gradientenkoeffizienten für reinstoffe und binäre legierungen mit atomaren potentialen. Studienarbeit, TU Berlin, 2004.

[42] Th. Böhme and W.H. Müller. On the simulation of the spinodal decomposition process and phase growth in a leadfree brazing material. *Computational Materials Science, to appear*, 2006.

[43] Böhme, Th. and Dreyer, W. and Müller, W. H. Determination of stiffness and higher gradient coefficients for binary alloys with the embedded-atom method. *Continuum Thermodynamics, to appear*, 2006.

[44] R. de Borst, J. Pamin, R. H. J. Peerlings, and Sluys L. J. On gradient-enhanced damage and plasticity models for failure in quasi-brittle and frictional materials. *Computational Mechanics*, 17(1):130–141, 2001.

[45] et al Borvik. Shear plug formation in steel. 5:193–206, 2001.

[46] Ray M. Bowen and C.-C. Wang. *Introduction to Vectors and Tensors, Part A: Linear and Multilinear Algebra*. Plenum Press, 1976.

[47] D. Braess. *Finite Elemente*. Springer–Verlag, 1992.

[48] S. Brenner and L. Scott. *The Mathematical Theory of Finite Element Methods*. Springer, New York, 1994.

[49] W. Brocks. What does Materials Characterization Mean - Testing or Modelling? Technical Note GKSS/WMS/00/13, 2000.

[50] W. Brocks. FEM-Analysen von Rissproblemen bei nichtlinearem Materialver-

halten. DVM-Weiterbildungsseminar Anwendung numerischer Methoden in der Bruchmechanik Freiberg, Technical Note GKSS/WMS/02/01, 2002.

[51] W. Brocks and J. Olschewski. Bruchmechanik I. Technical Note GKSS/WMS-04/04, Vorlesungsmanuskript Technische Universität Berlin (Nachdruck WS1988/89), 2004.

[52] W. Brocks, D.Z. Sun, and A. Honig. Verification of micromechanical models for ductile fracture by cell model calculations. *Computational Materials Science*, 7(1-2):235–241, 1996.

[53] I. N. Bronstein and K. A. Semendjajew. *Taschenbuch der Mathematik*. Teubner Verlagsgesellschaft, Leipzig, 1983.

[54] I. N. Bronstein and K. A. Semendjajew. *Ergänzende Kapitel zum Taschenbuch der Mathematik*. Teubner Verlagsgesellschaft, Leipzig, 1988.

[55] S.A. Brown, R. Munver, F.C. Delvecchio, R.L. Kuo, P. Zhong, and G.M. Preminger. Microdialysis assessment of shock wave lithotripsy- induced renal injury. *Urology*, 56(3):364–368, 2000.

[56] F. Brummer, T. Brauner, and D.F. Hulser. Biological effects of shock-waves. *World Journal Of Urology*, 8(4):224–232, 1990.

[57] K Burg, H. Haf, and I. Wille. *Höhere Mathematik für Ingenieure, Band I - V*. B. G. Teubner Verlag, 1997.

[58] K. Burth and W. Brocks. *Plastiziät*. Vieweg, 1992.

[59] Carstensen C., Hackl K., and Mielke A. Nonconvex potentials and microstructures in finite-strain plasticity. *Proceedings of the Royal Society London A*, 458:299–317, 2002.

[60] Miehe C. Computational micro-to-macro transitions for discretized microstructures of heterogeneous materials at finite strains based on the minimization of averaged incremental energy. *Computer Methods in Applied Mechanics and Engineering*, 192:559–591, 2003.

[61] Miehe C., Schotte J., and Lambrecht M. Homogenization of inelastic solid materials at finite strains based on incremental minimization principles. Application to the texture analysis of polycrystals. *Journal of the Mechanics and Physics of Solids*, 50:2123–2167, 2002.

[62] Miehe C. and Lambrecht M. A two-scale finite element relaxation analysis of shear bands in non-convex inelastic solids: Small-strain theory for standard dissipative

materials. *Computer Methods in Applied Mechanics and Engineering, 192:, 2003.*, 192:473–508, 2003.

[63] Simo J. C. and Tarnow N. The discrete energy momentum method. Conserving algorithms for nonlinear elastodynamics. *Zeitschrift fuer Angewandte Mathematik und Physik*, 43:757–792, 1992.

[64] Simo J. C., Tarnow N., and Wong K. Exact energy-momentum conserving algorithms and symplectic schemes for nonlinear dynamics. *Computer Methods in Applied Mechanics and Engineering*, 100:63–116, 1992.

[65] J. W. Cahn. Spinodal Decomposition. *Transactions of the Metallurgical society of AIME*, 242:166–180, 1968.

[66] John W. Cahn and John E. Hilliard. Free Energy of a Nonuniform System. I. Interfacial Free Energy. *The Journal of Chemical Physics*, 28(2):258–267, 1958.

[67] J.W. Cahn. Free energy of a non-uniform system.I. Interfacial free energy. *J Chem Phys*, 30:258–267, 1958.

[68] J.W. Cahn. Free energy of a non-uniform system.II. Thermodynamic basis. *J Chem Phys*, 30:1121–1124, 1959.

[69] J.W. Cahn and J. E. Hilliard. Free energy of a non-uniform system. III. Nucleation in a two-component incompressible fluid. *J Chem Phys*, 31:688–699, 1959.

[70] G.T. Camacho and M. Ortiz. Computational modelling of impact damage in brittle materials. *International Journal of Solids and Structures*, 33(20-22):2899–2938, 1996.

[71] G.T. Camacho and M. Ortiz. Adaptive lagrangian modelling of ballistic penetration of metallic targets. *Computer Methods in Applied Mechanics and Engineering*, 142(3-4):269–301, 1997.

[72] M. M. Carroll and A.C. Holt. Static and dynamic pore-collapse relations for ductile porous materials. *Journal of Applied Physics*, 43:1626–1636, 1998.

[73] C. Carstensen. *Wissenschaftliches Rechnen — Finite Elemente*. Universität Kiel, 1999.

[74] C. Carstensen. Some remarks on the history and future of averaging techniques in finite element error analysis. *Z. Angew. Math. Mech.*, 84:0–0, 2004.

[75] C. Carstensen. Ten remarks on nonconvex minimisation for phase transition simulations. *Comput. Methods Appl. Mech. Engrg.*, 194:169–193, 2005.

279

[76] C. Carstensen and K. Weinberg. Calculating the energy-norm fem-error for Reissner-Mindlin plates without known reference solution. *Computational Mechanics*, 26(6):566–570, 2000.

[77] C. Carstensen and K. Weinberg. Adaptive mixed finite element method for Reissner-Mindlin plates. *Computer Methods in Applied Mechanics and Engineering*, 190(51-52):6895–6908, 2001.

[78] C. Carstensen and K. Weinberg. An adaptive nonconforming finite element method for Reissner-Mindlin Plates. *Int. J. Numerical Methods in Engineering*, 56:2313–2330, 2003.

[79] P.P. Castaneda and P. Suquet. Nonlinear composites. *Advances in Applied Mechanics, Vol 34*, 34:171–302, 1998.

[80] P. Chadwick. *Continuum Mechanics - Concise Theory and Problems*. G. Allen & Unwin, 1976.

[81] C. Chaussy, E. Schmiedt, D. Jocham, W. Brendel, B. Forssmann, and V. Walther. First clinical experience with extracorporeally induced destruction of kidney stones by shock waves (reprinted from j urol, vol 127, pg 417-420, 1981). *Journal Of Urology*, 167(5):1957–1960, 2002.

[82] A.V. Cherkaev, K.A. Lurie, and G.W. Milton. Invariant properties of the stress in plane elasticity and equivalence classes of composites. *Proceedings of the Royal Society of London Series A-Mathematical Physical and Engineering Sciences*, 438(1904):519–529, 1992.

[83] R.M. Christensen. Effective properties of composite-materials containing voids. *Proceedings of the Royal Society of London Series A-Mathematical Physical and Engineering Sciences*, 440(1909):461–473, 1993.

[84] R.M. Christensen. Two theoretical elasticity micromechanics models. *Journal of Elasticity*, 50(1):15–25, 1998.

[85] C.C. Chu and A. Needleman. Void nucleation effects in biaxially stretched sheets. *Journal of Engineering Materials and Technology- Transactions of the ASME*, 102(3):249–256, 1980.

[86] P. G. Ciarlet. *The Finite Element Method for Elliptic Problems*. North-Holland, Amsterdam, 1978.

[87] P. G. Ciarlet and J. L. Lions, editors. *Handbook of Numerical Analysis*. Finite Element Methods. Elsevier Science Publishers B.V. (North–Holland), 1991.

[88] R.O. Cleveland, M.R. Bailey, N. Fineberg, B. Hartenbaum, M. Lokhandwalla, J.A. McAteer, and B. Sturtevant. Design and characterization of a research electrohydraulic lithotripter patterned after the dornier hm3. *Review Of Scientific Instruments*, 71(6):2514–2525, 2000.

[89] R.O. Cleveland, D.A. Lifshitz, B.A. Connors, A.P. Evan, L.R. Willis, and L.A. Crum. In vivo pressure measurements of lithotripsy shock waves in pigs. *Ultrasound In Medicine And Biology*, 24(2):293–306, 1998.

[90] R.O. Cleveland, D.A. Lifshitz, B.A. Connors, A.P. Evan, L.R. Willis, and L.A. Crum. In vivo pressure measurements of lithotripsy shock waves in pigs. *Ultrasound In Medicine And Biology*, 24(2):293–306, 1998.

[91] A. Coleman and J. Saunders. A review of the physical-properties and biological effects of the high amplitude acoustic fields used in extracorporeal lithotripsy. *Ultrasonics*, 31:75–89, 1993.

[92] A.J. Coleman, T. Kodama, M.J. Choi, T. Adams, and J.E. Saunders. The cavitation threshold of human tissue exposed to 0.2-mhz pulsed ultrasound - preliminary measurements based on a study of clinical lithotripsy. *Ultrasound In Medicine And Biology*, 21(3):405–417, 1995.

[93] B. D. Coleman and W. Noll. Material symmetry and thermostatic inequalities in finite elastic deformations. *Arch. Rational Mech. Anal.*, 15:87–111, 1964.

[94] B.A. Connors, A.P. Evan, L.R. Willis, P.M. Blomgren, J.E. Lingeman, and N.S. Fineberg. The effect of discharge voltage on renal injury and impairment caused by lithotripsy in the pig. *Journal Of The American Society Of Nephrology*, 11:310–318, 2000.

[95] R. Cortes. Dynamic growth of microvoids under combined hydrostatic and deviatoric stresses. *International Journal of Solids and Structures*, 29(13):1637–1645, 1992.

[96] R. Cortes. The growth of microvoids under intense dynamic loading. *International Journal of Solids and Structures*, 29(11):1339–1350, 1992.

[97] R. Cortes and M. Elices. Numerical modeling of ductile spall fracture. *International Journal of Impact Engineering*, 16(2):237–251, 1995.

[98] G.R. Cowper. Gaussian Quadrature Formulas for Triangles. *International Journal for Numerical Methods in Engineering*, 7:405–408, 1973.

[99] L. Crum. Cavitation microjets as a contributory mechanism for renal calculi disintegration in ESWL. *Journal of Urology*, 140:1587–1590, 1988.

[100] B. Dacorogna. *Direct methods in the calculus of variations*. Springer, 1989.

[101] E. Dekel, S. Eliezer, Z. Henis, E. Moshe, A. Ludmirsky, and I.B. Goldberg. Spallation model for the high strain rates range. *Journal of Applied Physics*, 84(9):4851–4858, 1998.

[102] Y.L. Deng, D.Z. Luo, and H.G. Chen. Effects of high-energy shock-waves on testes of wistar rats. *Journal Of Endourology*, 7(5):383–386, 1993.

[103] J.C DiTomasso. Stress Analysis of Vias within General Electric's Multichip Modules. University of Massachusetts at Amherst, MA, report provided on the web, http://www.ecs.umass.edu/mie/ labs/mda/fea/ditomaso/Main.htm, 2000.

[104] W. Dreyer and W. H. Müller. A study of coarsening in tin/lead solders. *Int. J. Solid and Structures*, 37:3841–3871, 2000.

[105] W. Dreyer and W. H. Müller. Toward Quantitative Modeling of Morphology Changes in Solids with Phase Field Theories: Atomistic Arguments for the Determination of Higher Gradient Coefficients. *Key Eng. Mater.*, 240:113–126, 2003.

[106] W. Dreyer, W. H. Müller, and W. Weiss. Tales of thermodynamics and obscure applications of the second law. *Continuum Mech. Thermodyn.*, 12:151–184, 2000.

[107] W. Dreyer and B. Wagner. Sharp-interface model for eutectic alloys Part I: Concentration dependend surface tension. *Interfaces Free Bound.*, 7:199–227, 2005.

[108] D. S. Dugdale. Yielding of steel sheets containing clits. *J. Mech. Phys. Solids*, 8:100–104, 1960.

[109] W. Ehlers. *Porous Media*. Springer, 2002.

[110] A.P. Evan, L.R. Willis, J.E. Lingeman, and J.A. McAteer. Renal trauma and the risk of long-term complications in shock wave lithotripsy. *Nephron*, 78(1):1–8, 1998.

[111] M. Farshad, M. Barbezat, P. Flueler, F. Schmidlin, P. Graber, and P. Niederer. Material characterization of the pig kidney in relation with the biomechanical analysis of renal trauma. *Journal Of Biomechanics*, 32(4):417–425, 1999.

[112] L. Filipczynski, J. Etienne, and T. Kujawska. Shock-wave pulse pressure after penetration of kidney tissue. *Ieee Transactions On Ultrasonics Ferroelectrics And Frequency Control*, 41(1):130–133, 1994.

[113] L. Filipczynski, J. Etienne, and M. Piechocki. An attempt to reconstruct the lithotriptor shock- wave pulse in kidney - possible temperature effects. *Ultrasound In Medicine And Biology*, 18(6-7):569–577, 1992.

[114] U. Fischer and W. Stephan. *Prinzipien und Methoden der Mechanik*. Fachbuchverlag Leipzig, 1972.

[115] Anthony C. Fischer-Cripps. *Nanoindentation*. Springer Verlag, 2002.

[116] L. B. Freund. *Dynamic Fracture Mechanics*. Cambridge University Press, 1998.

[117] T. Funami, H. Yada, and Y. Nakao. Curdlan properties for application in fat mimetics for meat products. *Journal of food science*, 63:283–287, 1998.

[118] Y.C. Fung. *Biomechanics, Mechanical Properties of Living Tissues*. Springer Verlag, 1993.

[119] M. Garajeu, J.C. Michel, and P. Suquet. A micromechanical approach of damage in viscoplastic materials by evolution in size, shape and distribution of voids. *Computer Methods in Applied Mechanics and Engineering*, 183(3-4):223–246, 2000.

[120] A. Gefen and S.S. Margulies. Are in vivo and in situ brain tissues mechanically similar? *Journal of Biomechanics*, 37:1339–1352, 2004.

[121] E. Gekeler. *Mathematische Methoden zur Mechanik*. Springer, Berlin (to appear), 2006.

[122] Y. Germain and A. Molinari. Creep failure analysis of bars sustaining constant tensile loads. *Mechanics of Time-Dependent Materials*, 4(1):57–79, 2000.

[123] R. Gilmore. The growth or collapse of a spherical bubble in a viscous compressible liquid. Technical Report Rep. No. 26-4, California Institute of Technology, 1952.

[124] B.L. Glushak, S.V. Koritskaya, and I.R. Trunin. Numerical analysis of damage accumulation in copper under dynamic load. *Chemical Physics Reports*, 18(10-11):1835–1841, 2000.

[125] H. Goering, H. G. Roos, and L. Tobiska. *Finite Element Methode*. Akademie–Verlag, Berlin, 1988.

[126] A. Göpfert and T. Riedrich. *Funktionalanalysis. In: Mathematik für Ingenieure, Naturwissenschaftler, Ökonomen und Landwirte. Bd.22*. Teubner Verlagsgesellschaft, Leipzig, 1980.

[127] D. E. Grady and Kipp M. E. Dynamic fracture and fragmentation. In J. R. Asay; M. Shahinpoor, editor, *High pressure shock compression of solids.* Springer-Verlag, 1993.

[128] D. E. Grady and M.E. Kipp. *Dynamic Fracture and Fragmentation. in J. R. Asay; M. Shahinpoor (Eds.): High pressure shock compression of solids.* Springer-Verlag, 1993.

[129] D.E. Grady and D.A. Benson. Fragmentation of metal rings by electromagnetic loading. *Exp. Mech.*, 23(4):393–400, 1983.

[130] K. Graeff-Weinberg. Ein Finite–Element–Konzept zur lokalen Netzverdichtung und seine Anwendung auf Koppel- und Kontaktprobleme. Universität Magdeburg, 1995.

[131] M. Gross. *Conserving Time Integrators for Nonlinear Elastodynamics.* phdthesis, University of Kaiserslautern, 2004. PhD thesis.

[132] P.R. Guduru, A.J. Rosakis, and G Ravichandran. Dynamic shear bands: an investigation using high speed optical and infrared diagnostics. *Mechanics of Materials*, 33:371–402, 2001.

[133] T. Guennouni and D. Francois. Constitutive-equations for rigid plastic or viscoplastic materials containing voids. *Fatigue and Fracture of Engineering Materials and Structures*, 10(5):399–418, 1987.

[134] F. Guilak, W. Jones, H. P. Ting-Beall, and G. M. Lee. The deformation behavior and mechanical properties of chondrocytes in articular cartilage. *Osteoarthritis and Cartilage*, 7:59–70, 1999.

[135] F. Guilak, J. R. Tedrow, and R. Burgkart. Viscoelastic Properties of the Cell Nucleus. *Biochemical and Biophysical Research Communications*, 269:781–786, 2000.

[136] J. Gurland and J. Plateau. Mechanism of ductile rupture of metals containing inclusions. *Transactions of the american society of metals*, 56:442–455, 1963.

[137] A. L. Gurson. Continuum theory of ductile rupture by void nucleation and growth: Part 1 - yield criteria and flow rules for porous ductile media. *Journal of Engineering Materials and Technology- Transactions of the ASME*, 99(1):2–15, 1977.

[138] M.E. Gurtin. *Introduction to Continuums Mechanics.* Springer, 1981.

[139] W. Hackbusch. *Theorie und Numerik elliptischer Differentialgleichungen.* Teubner–Verlag, 1992.

[140] K. Hackl. Generalized standard media and variational principles in classical and finite strain elastoplasticity. *Journal of the Mechanics and Physics of Solids*, 45(5):667–688, 1997.

[141] W. Han and D. Reddy. *Plasticity*. Springer, 1999.

[142] S. Hao and W. Brocks. The Gurson-Tvergaard-Needleman-model for rate and temperature-dependent materials with isotropic and kinematic hardening. *Computational Mechanics*, 20(1-2):34–40, 1997.

[143] F. Hartmann and C. Katz. *Statik mit Finiten Elementen*. Springer-Verlag, Berlin, 2002.

[144] A. Häse. Mininiaturmesverfahren zur Bestimmung mechanischer Kennwerte in mikroelektronischen Werkstoffen (in German). TU Berlin, Inst. F. Mech., 2006.

[145] Z. Hashin. The elastic moduli of heterogeneous materials. *ASME, Journal of Applied Mechanics*, 29:143–150, 1962.

[146] Z. Hashin. Analysis of composite-materials - a survey. *Journal of Applied Mechanics-Transactions of the ASME*, 50(3):481–505, 1983.

[147] E. A. Hassan, W.F. Heinz, M. Antonik, S. DCosta, N. P. Nageswaran, C. Schoenenberger, and J. H. Hoh. Relative Microelastic Mapping of Living Cells by Atomic Force Microscopy. *Biophysical Journal*, 74:1564–1578, 1998.

[148] P. Haupt. *Continuum Mechanics and Theory of Materials*. Springer, 2002.

[149] C. Hayes. Characterization of electrodeposited copper for dynamic flex applications (part 2). *INSIGHT, International Disk Drive Equipment and Materials Association*, 3-4:34–36, 2001.

[150] R. M. Henderson and H. Oberleithner. Pushing, pulling, dragging, and vibrating renal epithelia by using atomic force microscopy. *Am J Physiol Renal Physiol*, 278:F689–F701, 2000.

[151] R. Hill. A self-consistent mechanics of composite materials. *Journal of the Mechanics and Physics of Solids*, 13(4):213–222, 1965.

[152] G. Holzapfel. *Nonlinear Solid Mechanics*. Wiley & Sons, 2000.

[153] M. Hori and S. Nematnasser. Dynamic-response of crystalline solids with microcavities. *Journal of Applied Physics*, 64(2):856–863, 1988.

[154] D. Howard and B. Sturtevant. In vitro study of the mechanical effects of shockwave lithotripsy. *Ultrasound In Medicine And Biology*, 23(7):1107–1122, 1997.

[155] L. Howle, D. G. Schaefer, M. Shearer, and P. Zhong. Lithotripsy: The Treatment Of Kidney Stones With Shock Waves. *SIAM*, 40:356–371, 1998.

[156] Y. Huang, J.W. Hutchinson, and V. Tvergaard. Cavitation instabilities in elastic plastic solids. *Journal of the Mechanics and Physics of Solids*, 39(2):223–241, 1991.

[157] T.J.R. Hughes. Stability, convergence, and growth and decay of energy of the average accelerations method (a.k.a. Newmark/trapezoidal) in nonlinear structural dynamics. *Computers and Structures*, 6:313–324, 1976.

[158] T.J.R. Hughes. Generalization of selective integration procedures to anisotropic and nonlinear media. *International Journal for Numerical Methods in Engineering*, 15:1413—1418, 1980.

[159] T.J.R. Hughes. Analysis of transient algorithms with particular reference to stability behaviour, 1983.

[160] T.J.R. Hughes. Analysis of transient algorithms with particular reference to stability behaviour. In *Computational Methods for Transient Analysis*. North Holland: Amsterdam, 1983.

[161] ABAQUS Inc. Finite element code: Abaqus 6.5.1 standard & explicit, 2005.

[162] SRC Inc. Finite element code: Ideas 9.1, 2004.

[163] Miehe C.and Schröder J. and Becker M. Computational homogenization analysis in finite elasticity. Material and structural instabilities on the microand macroscales of periodic composites and their interaction. *Computer Methods in Applied Mechanics and Engineering*, 191:4971–5005, 2002.

[164] S. Jana, U. Ramamurtya, K. Chattopadhyay, and Y. Kawamura. Subsurface deformation during Vickers indentation of bulk metallic glasses. *Materials Science and Engineering A*, 375:1191–1195, 2004.

[165] Y. Jinyun. Symmetric gaussian quadrature formulae for tetrahedronal regions. *Computer Methods in Applied Mechanics and Engineering*, 43:349–353, 1984.

[166] M. Jirasek and T. Belytschko. Computational resolution of strong discontinuities. In H.A. Mang, F.G. Rammersdorfer and J. Eberhardsteiner, editor, *Proceedings of the Fifth World Congress on Computational Mechanics (WCCM V)*. Vienna, 2002.

[167] J.N. Johnson. Dynamic fracture and spallation in ductile solids. *Journal of Applied Physics*, 52(4):2812–2825, 1981.

[168] K.L. Johnson. *Contact mechanics*. Cambridge University Press, 1987.

[169] S. Jun and S. Im. Multiple-scale meshfree adaptivity for the simulation of adiabatic shear band formation. *Comp. Mech.*, 25:257–266, 2000.

[170] A. Juritza, J. Sterthaus, W. H. Müller, and K. Weinberg. Modeling and Verifying Nanoindentation Tests of Pb-free Solder Alloys by Numerical Methods. *PAMM, Proc. Appl. Math. Mech.*, 4(DOI 10.1002/ pamm.2004100xx), 2004.

[171] M. L. Kachanow. *Introduction to continuum damage mechanics*. Dortricht, 1986.

[172] M. Kallerhoff, K. Mullersiegel, R. Verwiebe, M.H. Weber, K. Wassmann, M. Blech, F. Scheler, and R.H. Ringert. Localization and degree of tissue-damage by extracorporeal shock-wave lithotripsy. *Urologe-Ausgabe A*, 30(2):85–88, 1991.

[173] N. Kambouchev, J. Fernandez, and R. Radovitzky. Polyconvex Model for Materials with Cubic Anisotropy. *arXiv:cond-mat/0505178 v1 7 May*, 5:2–28, 2005.

[174] C. Kane, J.E. Marsden, and M. Ortiz. Symplectic energy momentum integrators. *Journal of Mathematical Physics*, 40:3353–3371, 1999.

[175] C. Kane, J.E. Marsden, M. Ortiz, and M. West. Variational integrators and the newmark algorithm for conservative and dissipative mechanical systems. *Int. J. Numer. Meth. Engng.*, 49:1295–1325, 2000.

[176] T. Kishimoto, M. Senju, T. Sugimoto, K. Yamamoto, W. Sakamoto, M. Iimori, T. Kanasawa, S. Wada, and M. Maekawa. Effects of high-energy shock-wave exposure on renal-function during extracorporeal shock-wave lithotripsy for kidney-stones. *European Urology*, 18(4):290–298, 1990.

[177] D. Krajcinowicz. *Damage Mechanics*. Elsevier Science, North Holland, Amsterdam, 1996.

[178] D. Krajcinowicz and J. Lemaitre. *Continuum Damage Mechanics, CISM Courses and Lectures No. 295*. Springer–Verlag, Berlin, 1987.

[179] S. Krysiewicz. Complications of renal extracorporeal shock-wave lithotripsy reviewed. *Urologic Radiology*, 13(3):139–145, 1992.

[180] D. Kuhl and M.A. Crisfield. Energy Conserving and Decaying Algorithms in Non-Linear Structural Dynamics. *International Journal for Numerical Methods in Engineering*, 45:569–599, 1999.

[181] E. Kuhl. Habilitation. Technical report, University of Kaiserlautern, 2004.

[182] H. Kuttruff. *Physik und Technik des Ultraschalls*. S. Hirzel Verlag Stuttgart, 1988.

[183] Lu L. and R. Schwaiger, Z.W. Shan, M. Dao, K. Lu, S. Suresh. Nano-sized twins induce high rate sensitivity of flow stress in pure copper. *Acta Materialia*, 53:2169–2179, 2005.

[184] J.B. Leblond, G. Perrin, and J. Devaux. An Improved Gurson-Type Model for Hardenable Ductile Metals. *European Journal of Mechanics A-Solids*, 14(4):499–527, 1995.

[185] J.B. Leblond, G. Perrin, and P. Suquet. Exact results and approximate models for porous viscoplastic solids. *International Journal of Plasticity*, 10(3):213–235, 1994.

[186] J.B. Leblond and G. Roy. A model for dynamic ductile behavior applicable for arbitrary triaxialities. *Comptes Rendus de l Academie des Sciences Serie II Fascicule B-Mecanique Physique Astronomie*, 328(5):381–386, 2000.

[187] E.H. Lee. Elastic-plastic deformation at finite strain. *J. Appl. Mech.*, 36:1–6, 1969.

[188] K. J. Lee and R. A. Westerman. Elastic properties pf hollow-sphere-reinforced composites. *J. Composite Mat.*, 4:242–252, 1970.

[189] J. Lemaitre and J.-L. Chaboche. *Mechanics of solid materials*. Cambridge University Press, 1998.

[190] Y. Leroy and M. Ortiz. Localization analysis under dynamic loading. *Inst. of Phys. Conf. Series*, 102:257–265, 1987.

[191] Y. Leroy and M. Ortiz. Finite element analysis of transient strain localization phenomina in frictional solids. *Int. J. Num. Ana. Meth. Geomech.*, 14:93–124, 1990.

[192] A. Lew, J.E. Marsden, M. Ortiz, and M. West. Asynchronous variational integrators. *Arch. Rational Mech. Anal.*, 167:85–146, 2003.

[193] S. Li, W.K. Liu, D. Qian, P.R. Guduru, and A.J. Rosakis. Dynamic shear band propagation and micro-structure of adiabatic shear bands. *Comput. Methods Appl. Mech. Engrg.*, 191:73–92, 2001.

[194] S. Li, W.K. Liu, A.J. Rosakis, T. Belytschko, and W. Hao. Mesh-free galerkin simulations of dynamic shear band propagation and failure mode transition. *Int. J. Solids and Structures*, 39:1213–1240, 2002.

[195] I. M. Lifshitz and V. V. Slyozov. The kinetics of precipitation from supersaturated solid solutions. *Journal Phys Chem Solids*, 19:35–50, 1961.

[196] J.E. Lingeman and Safar F. S. Lithotripsy systems: In smith a.d., badlani g.h., bagley d.h., clayman r.v., jordan g.h., kavoussi l.r., lingeman j.e., preminger g.m., segura j.w. (eds); smith's textbook of endourology. St Louis, Quality Medical Publishers, 1996.

[197] M. Lokhandwalla. Damage Mechanisms in Shock Wave Lithotripsy. California Institute of Technology, 2001. PhD thesis.

[198] J. Lubliner. On the thermodynamic foundations of non-linear solid mechanics. *Int. J. Non-Linear Mech*, 7:237–254, 1972.

[199] J. Lubliner. *Plasticity Theory*. Macmillan Publishing Company, NewYork, 1990.

[200] Ortiz M. and Repetto E.A. Nonconvex energy minimization and dislocation structures in ductile single crystals. *Journal of the Mechanics and Physics of Solids*, 47:397–462, 1999.

[201] H. Maass and U. Kuehnapfel. Noninvasive Measurement of Elastic Properties of Living Tissue. Institut für Angewandte Informatik, Forschungszentrum Karlsruhe, 1999.

[202] P.E. Magnusen, E.M. Dubensky, and D.A. Koss. The effect of void arrays on void linking during ductile fracture. *Acta Metallurgica*, 36(6):1503–1509, 1988.

[203] P.E. Magnusen, D.J. Srolovitz, and D.A. Koss. A simulation of void linking during ductile microvoid fracture. *Acta Metallurgica et Materialia*, 38(6):1013–1022, 1990.

[204] L. Malvern. *Introduction to the Mechanics of a Continuous Medium*. Prentice-Hall, 1969.

[205] A. Marchand and J. Duffy. An experimental-study of the formation process of adiabatic shear bands in a structural steel. *J. Mech. Phys. Solids*, 36:261–281, 1988.

[206] J. Marsden and T.J.R. Hughes. *Mathematical Foundations of Elasticity*. Prentice-Hall, Englewood Cliffs, NJ, 1983.

[207] J.J. Mason, A.J. Rosakis, and G. Ravichandran. On the strain and strain-rate dependence of plastic work converted to heat–an experimental study using high-speed infrared detectors and the Kolsky bar. *Mech. Mater.*, 17:135–145, 1994.

[208] G. Maugin. *The Thermodynamics of Plasticity and Fracture.* Cambridge University Press, 1992.

[209] J. McAteer, J. Williams, L. Willis, and A. E. Evans. Personal communication with the autor (k.w.) at the swl group meeting. Indianapolis, IA, 2002.

[210] F. A. McClintock. A criterion for ductile fracture by the grows of holes. *Journal of Applied Mechanics*, 35:363–371, 1968.

[211] M. McElfresh, E. Baesu, R. Balhorn, J. Belak, M. J. Allen, and R.E. E. Rudd. Combining constitutive materials modeling with atomic force microscopy to understand the mechanical properties of living cells. 2001.

[212] J. W. Melvin, R. L. Stalnaker, and V. L. Roberts. Impact injury mechanisms in abdominal organs. *SAE Transactions (cited in Miller 2000)*, 700968:115–126, 1973.

[213] S. Mercier and A. Molinari. Micromechanics of void growth at high rates. *Journal de Physique IV*, 10(P9):415–420, 2000.

[214] J. Mergheim, E. Kuhl, and P. Steinmann. A finite element method for the computational modelling of cohesive cracks. *Int. J. Numer. Methods Engng.*, 2004. accepted for publication.

[215] S. Michlin. *Variationsmethoden der mathematischen Physik.* Akademie–Verlag, Berlin, 1962.

[216] C. Miehe. Exponential map algorithm for stress updates in anisotropic multiplicative elastoplasticity for single crystals. *International Journal for Numerical Methods in Engineering*, 39(19):3367–3390, 1996.

[217] C. Miehe. Exploitation of incremental energy minimization principles in computational multiscale analyses of inelastic solids. In *XXI ICTAM, 15.-21. August 2004, Warsaw, Poland*, 2004.

[218] C. Miehe and N. Apel. Anisotropic elastic-plastic analysis of shells at large strains: A comparison of multiplicative and additive approaches to enhanced finite element design and constitutive modeling. *International Journal for Numerical Methods in Engineering*, 61(2):2067–2113, 2004.

[219] K. Miller. Constitutive modelling of abdominal organs. *J. of Biomechanics*, 33:367–376, 2000.

[220] K. Miller. How to test very soft bilogical tissue in extension? *J. of Biomechanics*, 34:651–657, 2001.

[221] K. Miller, K. Chinzei, G. Orssengo, and P. Bednarz. Mechanical properties of brain tissue in-vivo: experiment and computer simulation. *J. of Biomechanics*, 33:1369–1376, 2000.

[222] G. W. Milton. *The Theory of Composites*. Cambridge University Press, 2002.

[223] G.W. Milton and A.V. Cherkaev. Which elasticity tensors are realizable? *Journal Of Engineering Materials And Technology- Transactions Of The Asme*, 117(4):483–493, 1995.

[224] A. Molinari and S. Mercier. Micromechanical modelling of porous materials under dynamic loading. *Journal of the Mechanics and Physics of Solids*, 49(7):1497–1516, 2001.

[225] J.F. Molinari and M. Ortiz. Three-dimensional adaptive meshing by subdivision and edge-collapse in finite deformation dynamic-plasticity problems with application to adiabatic shear banding. *Int. J. Numer. Meth. Engng.*, 53:1001–1026, 2002.

[226] C.B. Morrey. Quasi-convexity and the lower semicontinuity of multiple integrals. *Pacific J. Math.*, 2:25–53, 1952.

[227] E. Moshe, S. Eliezer, Z. Henis, M. Werdiger, E. Dekel, Y. Horovitz, S. Maman, I.B. Goldberg, and D. Eliezer. Experimental measurements of the strength of metals approaching the theoretical limit predicted by the equation of state. *Applied Physics Letters*, 76(12):1555–1557, 2000.

[228] A. Mota, Yang. J, K. Weinberg, and M. Ortiz. Fragmentation. In *Proc. of the Annual ASCII Meeting*, 2004.

[229] I. Müller and P. Strehlow. *Rubber and Rubber Balloons*. Springer Verlag, 2004.

[230] Ingo Müller. *Thermodynamics*. Pitman, 1985.

[231] Ingo Müller. *Grundzüge der Thermodynamik*. Springer Verlag, 2001.

[232] S. Müller. *Variational models for microstructure and phase transitions*. MPI Leipzig, 1996.

[233] W.H. Müller and J. Jendrny. Zwischenbericht, Siemens, ZT MF6, (in german). TU Berlin, Institute of Mechanics, 2002.

[234] W. Muschik. *Aspects of Non-Equilibrium Thermodynamics*. World Scientific, Singapore, 1990.

[235] W. Muschik. Material frame and objectivity. *Technische Mechanik*, 15:127–137, 1998.

[236] W. Muschik, C. Papenfuss, and H. Ehrentraut. Theory of liquid crystals. *Journal of Non-Equilibrium Thermodynamics*, 29:75–106, 2000.

[237] W. Muschik, C. Papenfuss, and H. Ehrentraut. A sketch of continuum thermodynamics. *Journal of Non-Newtonian Fluid Mechanics*, 96:255–290, 2001.

[238] W. Muschik, C. Papenfuss, and H. Ehrentraut. Mesoscopic theory of liquid crystals. *Journal of Non-Equilibrium Thermodynamics*, 29(1):75–106, 2004.

[239] S. Nasseri, L.E. Bilston, and N. Phan-Thien. Viscoelastic properties of pig kidney in shear, experimental results and modelling. *Rheol Acta*, 41:180–192, 2002.

[240] K.A. Nath. Tubulointerstitial changea as a major determinant in the progression of renal damage. *Am J Kidney Dis*, 20:1–17, 1992.

[241] A. Needleman. An analysis of intersonic crack growth under shear loading. *Journal of Applied Mechanics*, 66:847–857, 1999.

[242] A. Needleman and M. Ortiz. Effect of boundaries and interfaces on shear-band localication. *International Journal of Solids and Structures*, 28(7):859–877, 1991.

[243] S. Nematnasser and M. Hori. Void collapse and void growth in crystalline solids. *Journal of Applied Physics*, 62(7):2746–2757, 1987.

[244] N.N.: Newmark. A method of computation for structural dynamics. *Proceedings of the ASCE Journal of the Engineering Mechanic Division 85 EM3*, pages 67–94, 1959.

[245] M. Niewczas and J. D. Embury. Approaching the Theoretical Strength in Ductile Copper. In *The Integration of Material, Process and Product Design, Zabaras et al. (eds)*, 1999.

[246] J.A. Nucci, R. R. Keller, D. P. Field, and Y. Shacham-Diamond. Grain boundary misorientation angles and stress-induced voiding in oxide passivated copper interconnects. *Appl. Phys. Lett.*, 70:1242–1244, 1997.

[247] R. W. Ogden. *Non-linear Elastic Deformations*. Dover, New York, 1997.

[248] W. C. Oliver and G. M. Pharr. Nanoindenation. *J. Mater. Res.*, 7:1564–1574, 1992.

[249] et al. Olsen. Dynamic ductile fracture. *Experiments*, 1:1, 2001.

[250] V.C. Orsini and M.A. Zikry. Void growth and interaction in crystalline materials. *International Journal of Plasticity*, 17(10):1393–1417, 2001.

[251] M. Ortiz. A constitutive theory for the inelastic behavior of concrete. *Mechanics of Materials*, 4:67–93, 1985.

[252] M. Ortiz and A. Cuitino. A material-independent method for extending stress update algorithms from small-strain plasticity to to finite plasticity with multiplicative kinematics. *Engrg. Comp.*, 9:437–451, 1992.

[253] M. Ortiz, Y. Leroy, and A. Needleman. A finite element for localized failure analysis. *Comput. Method Appl. Mech. and Engng.*, 61:189–214, 1987.

[254] M. Ortiz and A. Molinari. Effect of strain hardening and rate sensitivity on the dynamic growth of a void in a plastic material. *Transaction of the ASME*, 59:48–53, 1992.

[255] M. Ortiz and A. Pandolfi. A class of cohesive elements for the simulation of three-dimensional crack propagation. *International Journal for Numerical Methods in Engineering*, 44:1267–1282, 1999.

[256] M. Ortiz, R. Radovitzky, and E. A. Repetto. The computation of the exponential and logarithmic mappings and their first and second linearizations. *International Journal for Numerical Methods in Engineering*, 52:1431–1441, 2001.

[257] M. Ortiz and L. Stainier. The variational formulation of viscoplastic constitutive updates. *Computer Methods in Applied Mechanics and Engineering*, 171(3-4):419–444, 1999.

[258] W. Ostwald. Über die vermeintliche Isometrie des roten und gelben Quecksilberoxyds und die Oberflächenspannung fester Körper. *Zeitschrift f. Phys. Chemie*, 21:495–503, 1900.

[259] M. P. Ottensmeyer. In Vivo Measurement of Solid Organ Tissue Mechanical Properties. Simulation Group, CIMIT, 2002.

[260] M.Y. Pan, M. Gupta, A.A.O. Tay, and K. Vaidyanathan. Development of bulk nanostructured copper with superior hardness for use as an interconnect material in electronic packaging. *Microelectronics and Reliability*, doi:10.1016/j.microrel.2005.06.009, 2006.

[261] A. Pandolfi, S. Conti, and M. Ortiz. A recursive-faulting model of distributed damage in confined brittle materials. *Journal of the Mechanics and Physics of Solids*, 54:1972–2003, 2006.

293

[262] A. Pandolfi, P. R. Guduru, M. Ortiz, and A. J. Rosakis. Three-dimensional cohesive element analysis and experiments of dynamic fracture in c300 steel. *International Journal of Solids and Structures*, 37:3733–3760, 2000.

[263] A. Pandolfi, P. Krysl, and M. Ortiz. Finite element simulation of ring expansion and fragmentation. *International Journal of Fracture*, 95:279—-297, 1999.

[264] A. Pandolfi and F. Manganiello. A model for the human cornea: constitutive formulation and numerical analysis. *Biomechan Model Mechanobiol. DOI 10.1007/s10237-005-0014-x*, 10:0, 2006.

[265] A. Pandolfi and M. Ortiz. An efficient adaptive procedure for three-dimensional fragmentation simulations. *Engineering with Computers*, 18:148–159, 2002.

[266] C. Papenfuss. Theory of liquid crystals as an example of mesocopic continuum mechanics. *Computational Material Science*, 19:45–52, 2000.

[267] C. Papenfuß. *Mesoscopic theory of liquid crystals*. Habiliatation, TU Berlin, 2005.

[268] C. Papenfuss, P. Ván, and W. Muschik. Mesoscopic theory of microcracks. *Archives of Mechanics*, 55(5-6):459–477, 2003.

[269] T. Pardoen and J.W. Hutchinson. An extended model for void growth and coalescence. *Journal of the Mechanics and Physics of Solids*, 48(12):2467–2512, 2000.

[270] P. Perzyna. Internal state variable description of dynamic fracture of ductile solids. *International Journal of Solids and Structures*, 22(7):797–818, 1986.

[271] N. Phan-Thien, S. Nasseri, and L.E. Bilston. Oscillatory squeezing flow of a biological material. *Rheol Acta*, 39:409–417, 2000.

[272] P. Pipek and V Sinevic. Rheologische Eigenschaften grob zerkleinerten Fleisches. *Fleischwirtschfat*, 72:507–510, 1992.

[273] M. Plagemann. Numerische Untersuchungen zur Belastung der menschlichen Niere während einer Lithotripsie-Behandlung. Studienarbeit, Institut für Mechanik, TU Berlin, 2006.

[274] M. D. C Powell. Direct search algorithms for optimization calculations. *Acta Numerica*, 7:287—336, 1998.

[275] G. Pusch and M. Krempe. *Technische Stoffe*. Deutscher Verlag für Grundstoffindustrie Leipzig, 1982.

[276] R. Radovitzky and M. Ortiz. Error estimation and adaptive meshing in strongly nonlinear dynamic problems. *Computer Methods in Applied Mechanics and Engineering*, 172(1-4):203–240, 1999.

[277] L. Ratke and P.W. Voorhees. *Growth and Coarsening: Ostwald Ripening in Engineering Materials.* Springer, 2002.

[278] D. T. Read and Y.-W. Cheng, R. Geiss. Mechanical Behavior of Electrodeposited Copper Film at Elevated Temperatures. Talk at ASME IMECE 2004, Anaheim, CA, Nov. 15, 2004.

[279] S. Reese and D. Christ. Modelling Of Shape Memory Alloys In The Finite Deformation Range Considering Fatigue Under Cyclic Loading. COMPLAS VIII, CIMNE, Barcelona, 2005.

[280] T. Resseguier, S. Couturier, J. David, and G. Nierat. Spallation of metal targets subjected to intense laser shocks. *J. Appl. Phys.*, 82:2617–2620, 1997.

[281] J. R. Rice. Mathematical analysis in the mechanics of fracture, in h. liebowitz (ed.). In *Fracture*, pages 191–311. Academic Press, New York, 1968.

[282] J. R. Rice. Continuum mechanics and thermodynamics of plasticity in relation to microscale defomation mechanism. In A.S. Argon, editor, *Constitutive Equations in Plasticity*, pages 23–79. MIT Press, Cambridge, MA, 1975.

[283] J. R. Rice and D.M. Tracey. On the ductile enlargement of voids in triaxial stress fields. *Journal of the Mechanics and Physics of Solids*, 17:201–217, 1969.

[284] R.A. Risdon, J.A.C. Sloper, and de H.E. Wardener. Relatioship between renal function and histological changes found in renal biopsy specimens from patients with persistent glomerular nephritis. *Lancet*, 2:363–366, 1968.

[285] R. T. Rockafellar. *Convex Analysis, PrincetonMathematical Series 28.* Princeton University Press, 1970.

[286] H.C. Rogers. Adiabatic plastic deformation. *Annu. Rev. Mater. Sci.*, 9:283–311, 1979.

[287] J. H. Rose, J. Ferrante, and J. R. Smith. Universal binding energy curves for metals and bimetallic interfaces. *Phys. Rev. Lett.*, 47:675–678, 1981.

[288] J. Rösler, H. Harders, and M. Bäker. *Mechanisches Verhalten der Werkstoffe.* Teubner, 2006.

[289] G. Ruiz, M. Ortiz, and A. Pandolfi. Three-dimensional finite-element simulation of the dynamic brazilian tests on concrete cylinders. *International Journal for Numerical Methods in Engineering*, 48:963—994, 2000.

[290] G. Ruiz, M. Ortiz, and A. Pandolfi. Three-dimensional cohesive modeling of dynamic mixed-mode fracture. *International Journal for Numerical Methods in Engineering*, 52:97–120, 2001.

[291] Ogden R.W. . *Proc R Soc Lond A*, 326:565–84, 1972.

[292] Ogden R.W. Elastic deformations of rubberlike solids. In *Mechanics of Solids (The Rodney Hill 60th Anniversary Volume)*, pages 499–538. Wheaton and Co, 1982.

[293] W. Sass, M. Braunlich, H. Dreyer, E. Matura, W. Folberth, Preismeyer H., and J. Seifert. The mechanisms of stone disintegration by shock waves. *Ultrasound in Medicine and Biology*, 17:239–243, 1991.

[294] W. Sass, H. Dreyer, S. Kettermann, and J. Seifert. The role of cavitational activity in fragmentation processes by lithotripters. *Journal of Stone Disease*, 4:193–207, 1992.

[295] H. Schade. *Tensoranalysis*. Walter de Gruyter, Berlin, 1997.

[296] J. Schiotz and T. Vegge, F. D. Di Tolla, K. W. Jacobsen. Atomic-scale simulations of the mechanical deformation of nanocrystalline metals. *PHYSICAL REVIEW B*, 60:11971–, 1999.

[297] J. Schröder and P. Neff. Invariant Formulation of Hyperelastic Transverse Isotropy Based on Polyconvex Free Energy Functions. *International Journal of Solid and Structures*.

[298] H. R. Schwarz. *Methode der finiten Elemente*. Teubner Verlagsgesellschaft, Stuttgart, 1991.

[299] H. Schwetlick and H. Kretzschmar. *Numerische Verfahren für Naturwissenschaftler und Ingenieure*. Fachbuchverlag Leipzig, 1991.

[300] B. R. Seth. Generalized strain measure with applications to physical problems. In D. Abir M. Reiner, editor, *Second-Order Effects in Elasticity, Plasticity and Fluid Dynamics*, pages 162–172. Pergamon Press, Oxford, 1964.

[301] T. Siegmund and W. Brocks. A numerical study on the correlation between the work of separation and the dissipation rate in ductile fracture. *Engineering Fracture Mechanics*, 67:139–154, 2000.

[302] T. Siegmund and W. Brocks. The role of cohesive strength and separation energy for modeling of ductile fracture. In *Fatigue and Fracture Mechanics: 30th Volume. K.L. Jerina, P.C. Paris, eds*, pages 139–151. American Society for Testing and Materials. Special Technical Publication 1360, 2000.

[303] J. C. Simo and T.J.R. Hughes. *Computational Inelasticity*. Springer Verlag, 1998.

[304] J.C. Simo and C. Miehe. Assocative coupled thermoplasticity at finite strains: Formulation, numerical analysis and implementation. *Comput Methods Appl Mech Eng*, 98:41–104, 1992.

[305] J.C. Simo, J. Oliver, and F. Armero. An analysis of strong discontinuities induced by strain-softening in rate-independent inelastic solids. *Comput. Mech.*, 12:277–296, 1993.

[306] J. J. Skrzypek and R. B. Hetnarski. *Plasticity and Creep*. CRC Press, 2000.

[307] SRC. Femap, 2001.

[308] D. Steglich and W. Brocks. Micromechanical Modelling of the behavior of ductile materials including particles. *Comp. Mat. Science*, 9:7–17, 1997.

[309] D. Steglich and W. Brocks. Micromechanical modelling of damage and fracture of ductile materials. *Fatigue and Fracture of Engineering Materials and Structures*, 21(10):1175–1188, 1998.

[310] P. Steinmann and J. Mergheim. Novel fe discretisation method for the computation of strong and weak discontinuities at finite strains. In D. Braess, C. Carstensen, and K. Hackl, editors, *Gemischte und nicht-standard Finite-Elemente-Methoden mit Anwendungen*. Mathematisches Forschungsinstitut Oberwolfach, Report No. 5/2005, 2005.

[311] J. Stoer. *Numerische Mathematik*. Springer–Verlag, 1989.

[312] A. Strachan, T. Cagin, and Goddard W. A. Critical behavior in spallation failure of metals. *Physics Review B*, 63:060103, 2001.

[313] B. Sturtevant. Shock wave effects in biomechanics. *Sadhana-Academy Proceedings In Engineering Sciences*, 23(5-6):579–596, 1998.

[314] B. Sturtevant and D. Howard. The mechanical effects of focused shock waves on tissue-like structures. *J. Acoust. Soc. Am.*, 98:2942–3000, 1995.

[315] B. Sturtevant and M. Lokhandwalla. Biomechanical effects of eswl shock waves. *J. Acoust. Soc. Am.*, 103:3037–3053, 1998.

[316] C.W. Sun, S.P. Feng, S.M. Zhuang, and X.P. Long. Dynamic fracture feature in metals under very high strain rate induced by shock loading. *Fracture and Strength of Solids, Pts 1 and 2*, 145-9:273–278, 1998.

[317] B. A. Szabò and I. Babuška. *Finite Element Analysis*. Verlag John Wiley and Sons, 1991.

[318] D. Tabor. *The Hardness of Metals*. Oxford, 1951.

[319] M. Tamagawa and T. Akamatsu. Effects of shock waves on living tissues (numerical analysis of a propagating pressure wave toward living tissue). *International Journal Series B-Fluids And Thermal Engineering*, 39(4):714–720, 1996.

[320] M. Tanguay. Computation of bubbly cavitating flow in shock wave lithotripsy. PhD-Thesis, California Institute of Technology, 2004.

[321] M. Tanguay and T. Colonius. Numerical investigation of bubble cloud dynamics in shock wave lithotripsy. In *Proc. of FEDSM02, ASME, Montreal, Canada, July 14-18*, 2002.

[322] M. Tanguay and T. Colonius. Progress in modeling and simulation of shock wave lithotripsy (swl). In *Proc. 5th Inter. Symposium on Cavitation, Osaka, Japan, published electronically at http://iridium.me.es.osaka-u.ac.jp/cav2003/index1.html: paper OS-2-1-010*, 2003.

[323] M. Thiel. Application of shock waves in medicine. *Clinical Orthopaedics And Related Research*, 387:18–21, 2001.

[324] M. Thiel, M. Nieswand, and M. Dorffel. The use of shock waves in medicine - a tool of the modern or: an overview of basic physical principles, history and research. *Minimally Invasive Therapy and Allied Technologies*, 9(3-4):247–253, 2000.

[325] W. R. Thissell, A. K. Zurek, D. L. Tonks, and R. S. Hixon. Experimental quantitative damage measurements and void growth model predictions in the spallation of tantalum. *AIP Conference Proceedings*, 550(1):451–454, 2000.

[326] W.R. Thissell, A.K. Zurek, D.A.S. Macdougall, and D. Tonks. Damage evolution and damage model validation in spalled tantalum. *Journal de Physique IV*, 10(P9):769–774, 2000.

[327] T.Y. Thomas. Extended compatibility conditions for the study of surfaces of discontinuity in continuum mechanics. *J. Math. Mech.*, 6:311–322, 1957.

[328] P.F. Thomason. *Ductile Fracture of Metals*. Pergamon Press, 1990.

[329] P.F. Thomason. A view on ductile-fracture modelling. *Fatigue and Fracture of Engineering Materials and Structures*, 21(9):1105–1122, 1998.

[330] P.F. Thomason. Ductile spallation fracture and the mechanics of void growth and coalescence under shock-loading conditions. *Acta Materialia*, 47(13):3633–3646, 1999.

[331] A.W. Thompson. Modeling of local strains in ductile fracture. *Metallurgical Transactions A-Physical Metallurgy and Materials Science*, 18(11):1877–1886, 1987.

[332] P. Thoutireddy, J.F. Molinari, E.A. Repetto, and M. Ortiz. Tetrahedral composite finite elements. *International Journal for Numerical Methods in Engineering*, 53(6):1337–1351, 2002.

[333] S.P. Timothy. The structure of adiabatic shear bands in metals: A critical review. *Acta Metall.*, 35:301–306, 1987.

[334] W. Tong and G. Ravichandran. Inertial effects on void growth in porous viscoplastic materials. *Journal of Applied Mechanics-Transactions of the ASME*, 62(3):633–639, 1995.

[335] S. Torquato. *Random Heterogeneous Materials*. Springer, 2001.

[336] S. Torquato and F. Lado. Effective properties of 2-phase disordered composite media .2. evaluation of bounds on the conductivity and bulk modulus of dispersions of impenetrable spheres. *Physical Review B*, 33(9):6428–6435, 1986.

[337] G. J. Tortora. *Principles of Human Anatomy*. John Wileys & Sons, 2002.

[338] L. R. G. Treloar. Stress-strain data for vulcanized rubber under various types of deformation. *Proc of the Faraday Soc*, 40:59–70, 1944.

[339] C. Truesdell and W Noll. *The Non-Linear Field Theories of Mechanics. In Flügge, S.: Handbuch der Physik. Volume III/3*. Springer-Verlag, Berlin, 1965.

[340] C. Truesdell and R. A. Toupin. *The Classical Field Theories. In Flügge, S.: Handbuch der Physik. Volume III/1*. Springer-Verlag, Berlin, 1960.

[341] V. Tvergaard. Influence of voids on shear band instabilities under plane-strain conditions. *International Journal of Fracture*, 17(4):389–407, 1981.

[342] V. Tvergaard. Material failure by void coalescence in localized shear bands. *International Journal of Solids and Structures*, 18(8):659–672, 1982.

[343] V. Tvergaard. Material failure by void growth to coalescence. *Advances in Applied Mechanics*, 27:83–151, 1990.

299

[344] V. Tvergaard, Y. Huang, and J.W. Hutchinson. Cavitation instabilities in a power hardening elastic-plastic solid. *European Journal of Mechanics A-Solids*, 11(2):215–231, 1992.

[345] V. Tvergaard and J.W. Hutchinson. Effect of initial void shape on the occurrence of cavitation instabilities in elastic-plastic solids. *Journal of Applied Mechanics-Transactions of the ASME*, 60(4):807–812, 1993.

[346] V. Tvergaard and A. Needleman. Analysis of the cup-cone fracture in a round tensile bar. *Acta Metallurgica*, 32(1):157–169, 1984.

[347] V. Tvergaard and A. Needleman. Effects of nonlocal damage in porous plastic solids. *International Journal of Solids and Structures*, 32(8-9):1063–1077, 1995.

[348] R.L.J.M. Ubachs, P.J.G. Schreurs, and M.G.D. Geers. A nonlocal diffuse interface model for microstructure evolution in tin-lead solder. *J Mech Phys Solids*, 52:1763–1792, 2004.

[349] R.L.J.M. Ubachs, P.J.G. Schreurs, and M.G.D. Geers. Phase field dependent viscoplastic behaviour of solder alloys. *International Journal of Solid and Structures*, 42:2533–2558, 2005.

[350] P. Ván, C. Papenfuss, and W. Muschik. Mesoscopic dynamics of microcracks. *Physical Review E*, 62(5):6206–6215, 2000.

[351] P. Ván, C. Papenfuss, and W.Muschik. Griffith cracks in the mesoscopic microcrack theory. *Journal of Physics A: Mat. Gen.*, 37:5315–5328, 2004.

[352] C. Verdier. Rheological Properties of Living Materials. From Cells to Tissues. *Journal of Theoretical Medicine*, 5:67–91, 2003.

[353] R. Verfürth. *A review of a posteriori error estimation and adaptive mesh-refinement techniques*. Wiley-Teubner, 1996.

[354] C. Wagner. Theorie der Alterung von Niederschlagen durch Umlösen (Ostwald-Reifung). *Zeitschrift Fur Elektrochemie*, 65(7-8):581–591, 1961.

[355] K. Washizu. *Variational Methods in Elasticity and Plasticity*. Pergamon Press, Tokyo, 1982.

[356] G. Weber and L. Anand. Finite deformation constitutive-equations and a time integration procedure for isotropic, hyperelastic viscoplastic solids. *Computer Methods in Applied Mechanics and Engineering*, 79(2):173–202, 1990.

[357] K. Weinberg. Adaptive Computation of Elasto-Plastic Plates by a Locking Free Finite Element Method. In T. Sonar and I. Thomas, editors, *Notes on Num. Fluid Mechanics*, pages 227–239. Logos, Berlin, 2001.

[358] K. Weinberg. An adaptive Finite Element Approach for a Mixed Reissner-Mindlin Plate Formulation. *Computer Methods in Applied Mechanics and Engineering*, 190(37-38):4999–5008, 2001.

[359] K. Weinberg. Localization of Failure in Shock-Loaded Metals. In R. Mahnken, R. Hermann, and E. Schnack, editors, *Proc. 17. Workshop-AG Composite*. Paderborn, 2004.

[360] K. Weinberg. Finite-Element Simulation of Failure under Shock-Loading. In D. Braess, C. Carstensen, and K. Hackl, editors, *Gemischte und nicht-standard Finite-Elemente-Methoden mit Anwendungen*. Mathematisches Forschungsinstitut Oberwolfach, Report No. 5/2005, 2005.

[361] K. Weinberg. Methode der finiten elemente i: Lineare probleme. Skript zur Vorlesung WS 2005/06, Technische Universität Berlin, 2005.

[362] K. Weinberg and T. Böhme. Mesoscopic Modeling for Continua with Pores: Biological Soft Tissue. *to appear in: Non-Equilibrium Thermodynamics*, 2006.

[363] K. Weinberg and T. Böhme. Mesoscopic Modeling for Continua with Pores: Dynamic Void Growth in Visco-Plastic Metals. *to appear in: Non-Equilibrium Thermodynamics*, 2006.

[364] K. Weinberg, T. Colonius, and M. Ortiz. A Model for Kidney Tissue Damage under High Speed Loading. *PAMM, Proc. Appl. Math. Mech.*, 4(DOI 10.1002/ pamm.200410098):234–235, 2004.

[365] K. Weinberg, A. Mota, and M. Ortiz. A Variational Constitutive Model for Porous Metal Plasticity. *Computational Mechanics*, 37(2):142 – 152, 2006.

[366] K. Weinberg and W. H. Müller. A Strategy for Damage Assesment of Thermally Stressed Copper Vias in Microelectronic Printed Circuit Boards. *submitted to: Microelectronics & Reliability*, 2006.

[367] K. Weinberg and M. Ortiz. A Variational Formulation of Porous Plasticity and its Application to the Taylor Impact Test. In H.A. Mang, F.G. Rammersdorfer and J. Eberhardsteiner, editor, *Proceedings of the Fifth World Congress on Computational Mechanics (WCCM V)*. Vienna, 2002.

[368] K. Weinberg and M. Ortiz. Shock Wave Induced Damage in Kidney Tissue. *Computational Material Science*, 32:588–593, 2005.

[369] K. Weinberg, J. Sterthaus, and W. H. Müller. Material Identification by Nanoindentation. *PAMM, Proc. Appl. Math. Mech.*, 5, 2005.

[370] Weinberg, K. and Gabbert, U. . An Adaptive pNh-Technique for Global-Local Finite Element Analysis. *Engng. Comp.: Int. J. Comp.-Aided Engng and Software*, 19:485–500, 2002.

[371] L. W. Welling and J. J. Grantham. Physical properties of isolated perfused renal tubules and tubular basement membranes. *J Clin Invest.*, 51:1063–1075, 1972.

[372] LW Welling, MT Zupka, and DJ Welling. Mechanical Properties of Basement Membrane. *News Physiol Sci*, 10(1):30–35, 1995.

[373] O. Wess. Physikalische Grundlagen der Stoßwellentherapie. *J. Mineralstoffwechsel*, 4:7–18, 2004.

[374] L.R. Willis, A.P. Evan, B.A. Connors, P. Blomgren, N.S. Fineberg, and J.E. Lingeman. Relationship between kidney size, renal injury, and renal impairment induced by swl. *Journal Of The American Society Of Nephrology*, 10:1753–1762, 1999.

[375] W.T. Wilson, J.S. Morris, D.A. Husmann, and G.M. Preminger. Extracorporeal shock-wave lithotripsy - comparison between stone and no-stone animal-models of swl. *Journal Of Endourology*, 6(1):33–36, 1992.

[376] P. Wriggers. *Nichtlineare Finite-Elemente-Methode*. Springer, Berlin, 2001.

[377] P. Wriggers and S. Reese. A note on enhanced strain methods for large deformations. *Computer Methods in Applied Mechanics and Engineering*, 135:201–2–9, 1996.

[378] B. Wunderle, R. Dudek, B. Michel, and H. Reich. Thermo-Mechanical Reliability of Power Flip-Chip Cooling Concepts. In *Proc. of Electronic Components and Technology Conference,IEEE*, pages 427–437, 2004.

[379] X. Xi and P. Zhong. Dynamic photoelastic study of the transient stress field in solids during shock wave lithotripsy. *J. Acoust. Soc. Am.*, 109:1226–1239, 2001.

[380] X. P. Xu and A. Needleman. Numerical simulations of dynamic interfacial crack growth allowing for crack growth away from the bond line. *Int. J. Fracture*, 74:253–275, 1995.

[381] X. P. Xu and A. Needleman. Numerical simulations of dynamic crack growth along interface. *Int. J. Fracture*, 74:289–324, 1996.

[382] J. Yang, A. Mota, and M. Ortiz. Variational strain-localisation finite elements. *Int. J. Numer. Methods Engrg.*, 52:1431–1441, 2001.

[383] C. Yu, M. Ortiz, and A. J. Rosakis. 3d modelling of impact failure in sandwich structues. *Fracture of Polymers. Composite of Adhesives II*, pages 527–537, 2003.

[384] C. Yu, A. Pandolfi, M. Ortiz, D. Coker, and A.J. Rosakis. Three-dimensional modeling of intersonic shear-crack growth in asymmetrically loaded unidirectional composite plates. *International Journal of Solids and Structures*, 39:6135–6157, 2002.

[385] Z.L. Zhang, C. Thaulow, and J. Odegard. A complete gurson model approach for ductile fracture. *Engineering Fracture Mechanics*, 67(2):155–168, 2000.

[386] P. Zhong, Y. Zhou, and S. Zhu. Dynamics of bubble oscillation in constrained media and mechanisms of vessel rupture in shock wave lithotripsy. CAV2001:sessionA5.005, 2001.

[387] P. Zhong, Y. Zhou, and S. Zhu. Dynamics of bubble oscillation in constrained media and mechanisms of vessel rupture in swl. *Ultrasound in Med. and Biol.*, 27:119–134, 2001.

[388] M. Zhou, G. Ravichandran, and A.J. Rosakis. Dynamically propagating shear bands in impact-loaded prenotched plates–ii. numerical simulations. *J. Mech. Phys. Solids*, 44:1007–1032, 1996.

[389] M. Zhou, A.J. Rosakis, and G. Ravichandran. Dynamically propagating shear bands in impact-loaded prenotched plates–i. experimental investigations of temperature signature and propagation speed. *J. Mech. Phys. Solids*, 44:981–1006, 1996.

[390] O. C. Zienkiewicz and R. L. Taylor. *The Finite Element Method. Vol. 1-3.* McGraw–Hill Book Company, 2003.

[391] A.K. Zurek, W.R. Thissell, D.L. Tonks, R. Hixson, and F. Addessio. Quantification of damage evolution for a micromechanical model of ductile fracture in spallation of tantalum. *Journal de Physique IV*, 7(C3):903–908, 1997.

[392] R. Zurmühl. *Praktische Mathematik für Ingenieure und Physiker.* Springer–Verlag, 1984.